



## 3-D Vector Flow Imaging

Holbek, Simon

*Publication date:*  
2016

*Document Version*  
Publisher's PDF, also known as Version of record

[Link back to DTU Orbit](#)

*Citation (APA):*  
Holbek, S. (2016). *3-D Vector Flow Imaging*. Technical University of Denmark, Department of Electrical Engineering.

---

### General rights

Copyright and moral rights for the publications made accessible in the public portal are retained by the authors and/or other copyright owners and it is a condition of accessing publications that users recognise and abide by the legal requirements associated with these rights.

- Users may download and print one copy of any publication from the public portal for the purpose of private study or research.
- You may not further distribute the material or use it for any profit-making activity or commercial gain
- You may freely distribute the URL identifying the publication in the public portal

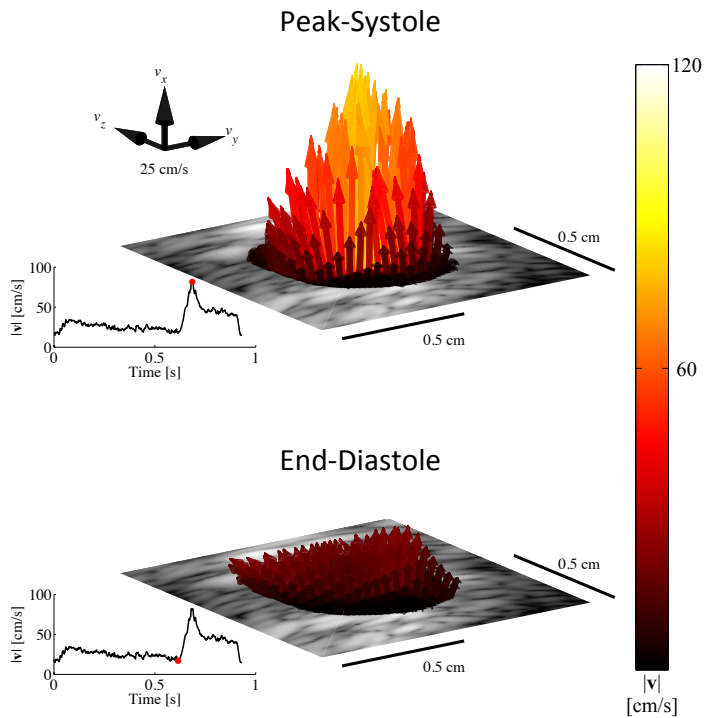
If you believe that this document breaches copyright please contact us providing details, and we will remove access to the work immediately and investigate your claim.

# 3-D Vector Flow Imaging

Simon Holbek

Supervised by: Professor Jørgen Arendt Jensen, PhD, Dr. Techn.

Co-supervised by: Associate Professor Matthias Bo Stuart, PhD



Cover image: 3-D vector flow *in vivo*

**Technical University of Denmark**  
**Department of Electrical Engineering**  
**Center for Fast Ultrasound Imaging (CFU)**

Ørsteds Plads 349

2800 Kgs. Lyngby

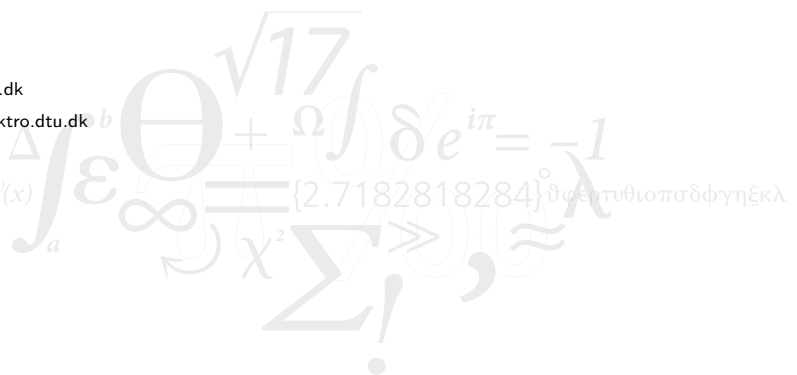
DENMARK

Tel: (+45) 4525 5832

Web: [www.bme.elektro.dtu.dk](http://www.bme.elektro.dtu.dk)

Author e-mail: [sholbek@elektro.dtu.dk](mailto:sholbek@elektro.dtu.dk)

$$f(x+\Delta x) = \sum_{i=0}^{\infty} \frac{(\Delta x)^i}{i!} f^{(i)}(x)$$



# Contents

<b>Preface</b>	vii
<b>Summary</b>	ix
<b>Resumé</b>	xi
<b>Acknowledgements</b>	xiii
<b>Abbreviations</b>	xv
<b>1 Introduction</b>	1
1.1 Motivation . . . . .	1
1.2 Objective . . . . .	3
1.3 Scientific contributions . . . . .	3
1.4 Outline of the thesis . . . . .	6
<b>2 Blood Velocity Estimation in Medical Ultrasound Imaging</b>	9
2.1 Purpose . . . . .	9
2.2 1-D Methods . . . . .	9
2.3 Vector flow methods . . . . .	12
2.4 Discussion . . . . .	17
<b>3 Transverse Oscillation Methods</b>	19
3.1 Purpose . . . . .	19
3.2 Basic principles . . . . .	19
3.3 Transverse oscillation method . . . . .	20
3.4 Filtering in the Fourier domain . . . . .	23
3.5 Directional transverse oscillation . . . . .	25
3.6 Additional methods and applications . . . . .	25
3.7 Discussion . . . . .	26

<b>4</b>	<b>2-D Transducer Setups</b>	27
4.1	Purpose . . . . .	27
4.2	Generating the ultrasound . . . . .	27
4.3	2-D mimicking setups . . . . .	29
4.4	2-D transducers . . . . .	30
<b>5</b>	<b>3-D Vector Flow With a Fully Addressed Matrix Probe</b>	35
5.1	Purpose . . . . .	35
5.2	Background . . . . .	35
5.3	Continuous data acquisition . . . . .	36
5.4	Data acquisition & processing . . . . .	37
5.5	Experimental setup . . . . .	43
5.6	Measurements . . . . .	44
5.7	Comparison to MRI . . . . .	49
5.8	Additional applications . . . . .	50
5.9	Conclusion and perspectives . . . . .	51
<b>6</b>	<b>Row-Column 3-D Vector Flow</b>	55
6.1	Purpose . . . . .	55
6.2	Background . . . . .	55
6.3	TO on an RC array . . . . .	56
6.4	Transmission sequence . . . . .	57
6.5	Parametric simulation study . . . . .	60
6.6	Experimental setup . . . . .	67
6.7	Measurements . . . . .	67
6.8	Conclusion and perspective . . . . .	71
<b>7</b>	<b>Row-Column 3-D Volumetric Vector Flow</b>	75
7.1	Purpose . . . . .	75
7.2	Background . . . . .	75
7.3	Introduction . . . . .	76
7.4	Plane-by-plane 3-D volumetric vector flow . . . . .	76
7.5	Flow-rig measurements . . . . .	78
7.6	Synthetic aperture 3-D volumetric vector flow . . . . .	79
7.7	Results . . . . .	85
7.8	Conclusion and perspective . . . . .	85
<b>8</b>	<b>Project Conclusion and Perspectives</b>	89
8.1	Perspective . . . . .	90
	<b>Bibliography</b>	91
	References from Chapter 1 . . . . .	91

---

References from Chapter 2 . . . . .	91
References from Chapter 3 . . . . .	94
References from Chapter 4 . . . . .	96
References from Chapter 5 . . . . .	98
References from Chapter 6 . . . . .	99
References from Chapter 7 . . . . .	100
<b>Paper I: 3-D Vector Flow Estimation with Row-Column Addressed Arrays</b>	<b>103</b>
<b>Paper II: Ultrasonic 3-D Vector Flow Method for Quantitative <i>in vivo</i> Peak Velocity and Flow Rate Estimation</b>	<b>121</b>
<b>Paper III: 3-D Velocity Estimation for Two Planes <i>in vivo</i></b>	<b>133</b>
<b>Paper IV: <i>In vivo</i> 3-D Vector Velocity Estimation with Continuous Data</b>	<b>139</b>
<b>Paper V: 3-D Vector Velocity Estimation with Row-Column Addressed Arrays</b>	<b>145</b>
<b>Paper VI: 3-D Vector Flow Using a Row-Column Addressed CMUT Array</b>	<b>151</b>
<b>Paper VII: Experimental 3-D Vector Flow Estimation with Row-Column Addressed Arrays</b>	<b>161</b>
<b>Patent I: 3-D Imaging Using RC-Addressed Transducer Arrays: Two-Way Focusing and 3-D VFI</b>	<b>167</b>
<b>Paper A: 3-D Flow Estimation using Row-Column Addressed Transducer Arrays</b>	<b>191</b>
<b>Paper D: Row-column Addressed 2-D Array with a Double Curved Surface</b>	<b>215</b>



# Preface

This PhD thesis has been submitted to the Department of Electrical Engineering at the Technical University of Denmark in partial fulfillment of the requirements for acquiring the PhD degree. The research providing the foundation for the thesis has been conducted over a period of three years from November 1st, 2013, to October 31st, 2016 at the Center for Fast Ultrasound Imaging (CFU), Department of Electrical Engineering. The project has been supervised by Prof. Jørgen Arendt Jensen, PhD, Dr. Techn, and co-supervised by Assoc. Prof. Matthias Bo Stuart, PhD. The project was financially supported by grant 82-2012-4 from the Danish National Advanced Technology Foundation and by BK Ultrasound Aps, Denmark.

During my three years, I have had the opportunity to meet fellow researchers and present my research at conferences in Chicago, Helsingborg, Allinge, Taipei, San Diego, Tours and Chicago. Travelling to these conferences has been a huge experience as it has broadened my horizon regarding technical and clinical aspects of ultrasound.

As a side benefit of working in an experimental lab and having a relative low BMI, I have participated in more scans and experiments on a voluntary basis, that any healthcare system could ever have provided. I believe that all my organs and major vessels have been viewed by several medical doctors (and engineers) at least ones on average. It has been a pleasure to receive compliments about having "*a beautiful liver*" or having "*some very nice flow in your kidney*" on a rainy Monday morning. It is very uplifting to know, that even if my own research will not make an impact in the community, hopefully my organs and arteries will do so, as they are immortalized in several journals.

My office mate had the mantra, that the work as a PhD student was similar to run a 100m hurdle - blindfolded. You never know when you hit an obstacle, but certainly you will, so remember to enjoy the times when everything runs seamlessly. I have truly enjoyed my three years of research, and especially the periods following in the wake of overcoming large obstacles. I consider these "*ahaa*"-moments as one of the greatest privileges one can have as a researcher, which maintains the curiosity and justifies the large effort put in the work.

Simon Holbek  
Kgs. Lyngby, Denmark, October 2016



# Summary

For the last decade, the field of ultrasonic vector flow imaging has gotten an increasingly attention, as the technique offers a variety of new applications for screening and diagnostics of cardiovascular pathologies. The main purpose of this PhD project was therefore to advance the field of 3-D ultrasonic vector flow estimation and bring it a step closer to a clinical application.

A method for high frame rate 3-D vector flow estimation in a plane using the transverse oscillation method combined with a 1024 channel 2-D matrix array is presented. The proposed method is validated both through phantom studies and *in vivo*. Phantom measurements are compared with their corresponding reference value, whereas the *in vivo* measurement is validated against the current golden standard for non-invasive blood velocity estimates, based on magnetic resonance imaging (MRI). The study concludes, that a high precision was achieved and that estimates were comparable with MRI derived results. However, the large channel count of the applied transducer hinders a commercial implementation of the 3-D method for two main reasons: The large and heavy connection cable is impractical for clinical use, and the high channel count hampers the task of real-time processing.

In a second study, some of the issue with the 2-D matrix array are solved by introducing a 2-D row-column (RC) addressing array with only  $62 + 62$  elements. It is investigated both through simulations and via experimental setups in various flow conditions, if this significant reduction in the element count can still provide precise and robust 3-D vector flow estimates in a plane. The study concludes that the RC array is capable of estimating precise 3-D vector flow both in a plane and in a volume, despite the low channel count. However, some inherent new challenges are introduced with the array. The major disadvantage with an RC transducer, is the limited field-of-view, which is restricted to the forward looking array. It is discussed, that this drawback may be solved with a diverging lens, providing a larger field-of-view, due the the dispersion of the energy.

Based on the presented results it is concluded that 3-D vector flow using TO is a feasible method for obtaining angle-independent estimates of e.g. peak velocities and flow rates at a high frame rate for clinical applications. Moreover, the RC array offers a setup allowing for real-time processing

x

---

# Resumé

(Summary in Danish)

Hastighedsestimering ved brug af medicinsk ultralyd har i de senere år tiltrukket stor interesse, da teknikken har mange anvendelsesmuligheder inden for diagnosticering af kardiovaskulære sygdomme. Hovedformålet med dette Ph.D.-projekt har derfor været at bringe 3-D vektor hastighedsestimering ved brug af ultralyd et skridt nærmere klinisk anvendelse.

Et af hovedprojekterne i denne afhandling har været implementeringen af *transverse oscillation* (TO)-metoden på en 1024 element 2-D matrix transducer for at estimere 3-D vektor hastigheder ved høje *frame rates*. Metoden blev valideret både i fantommålinger og *in vivo*. Fantommålinger blev holdt op mod referenceværdier, hvorimod *in vivo* resultater blev sammenlignet med tilsvarende resultater opnået med magnetisk resonans billed-dannelse (MRI) modaliteten, hvilket anses som værende den gyldne standard. Studiet konkluderer, at metoden giver en høj præcision og er sammenlignelig med MRI resultater. Den benyttede transducer var imidlertid behæftet med en række ulemper så som: et tungt og upraktisk kabel, der er svært at benytte i klinikken i praksis, samt at det høje antal kanaler hindrer realtids-processering af data.

Et andet studie forsøgte at løse disse problemstillinger, ved at adressere elementerne i en 2-D transducer langs enten rækker eller søjler. Således kunne en transducer med kun 62 + 62 elementer benyttes. I simuleringstudier og eksperimentelle forsøg, blev effekten på 3-D hastighedsestimaterne af så kraftig en reduktion i antallet af elementer undersøgt. Studiet viste, at på trods af den signifikante reduktion i antallet af elementer, var det stadig muligt at estimere præcise og nøjagtige 3-D vektor hastigheder i både et plan og i et volumen. Række-søjle adressering af transducerelementerne løste en del af problemerne, men introducerede ligeledes andre. Således kunne hastigheder kun estimeres i transduceroverfladens fremadskuende retning. Afslutningsvist diskuterer denne afhandling muligheden for at løse dette problem ved at montere en divergerende linse på transduceren, hvilket giver et udvidet synsfelt grundet spredningen af den udsendte ultralyd.

Baseret på de præsenterede resultater konkluderes det, at 3-D vektor hastighedsestimering med TO er en potent kandidat, der i fremtiden vil kunne bruges til at estimere vinkelafhængige makshastigheder og flow rater ved høje *frame rates*. Ydermere åbner række-søjle teknologien op for procesering i realtid.



# Acknowledgements

First and foremost I would like to extend my sincere thanks to my supervisor, Prof. Jørgen Arendt Jensen, and my co-supervisor, Assoc. Prof. Matthias Bo Stuart, PhD. I am grateful that both believed in my qualification and personality and offered me the PhD position. Under their guidance, I have learned to approach various challenges with an open mind but with a critical sense.

As a new employee in a not yet known field, Michael Pihl took the time and the patience to introduce me to his previous work and discuss the current issues. I truly admire the effort he spent in giving me as good a start as possible.

Thanks to all the medical doctors, for insights full discussions about real life applications of ultrasound, and for removing the bell jar that we engineers tend to navigate inside from time to time.

I also want to thank all of my fellow PhD-students for the very pleasant working environment you all have contributed to. I have appreciated your company when travelling to different places around the world, and for always taking the time to discuss personal or working-related issues. A special thank should here go to my office mate Jacob Olesen, whom I had the pleasure to share office with for three years.

On behalf of all the readers and myself, I would like to thank Nina Kjærgaard for the valuable help of proofreading the dissertation.

Whenever SARUS did not collaborate, Borislav Tomov never hesitated to help. Neither did Elna Sørensen, and I'm thankful for her patience when explaining me over and over again, how the administrative tasks should be handled.

I would also like to thank my parents, Henning and Barbara Holbek, for their unconditional support and for always encouraging me to follow my dreams in every aspects of life. Last, but definitely not least, I would like to thank Louise Aaris Kønigsfeldt. Even though you have given ear to countless of complaining about SARUS or welcomed me home very late numerous of times, I have always felt your support and love throughout the project.



# Abbreviations

2-D	Two-Dimensional
3-D	Three-Dimensional
CVD	Cardiovascular disease
CFM	Color flow map
DTU	Danmarks Tekniske Universitet (Technical University of Denmark)
ECG	Electrocardiogram
FDA	Food and Drug Administration
FOV	Field of view
HRP	High resolution plane
HRV	High resolution volume
MRI	Magnetic Resonance Imaging
PRF	Pulse Repetition Frequency
PSF	Point spread function
RF	Radio frequency
RC	Row-column
Rx	Receive
SAFI	Synthetic aperture flow imaging
SAI	Synthetic aperture imaging
SARUS	Synthetic aperture real-time ultrasound system
SNR	Signal to Noise Ratio
Std	Standard deviation
TO	Transverse oscillation
Tx	Transmit
US	Ultrasound
VFI	Vector flow imaging



## 1.1 Motivation

Cardiovascular disease (CVD) is a common description of diseases related to heart and blood vessels, which account for 30 % of global deaths (WHO 2011). CVD includes coronary artery diseases, heart valve diseases, abnormal heart rhythm, vascular disease, etc. A large fraction of these diseases are related to lifestyle, as smoking, lack of exercise, obesity or excessive alcohol consumption can have a direct or indirect impact of the severity of the disease. The diseases are usually treated via invasive procedures, which are associated with high risk, due to the potential complications of a surgery. It is therefore crucial that such invasive procedures are performed only when strictly required and preferable based on trustworthy non-invasive screening techniques which can identify potential pathologies.

The presence of a CVD can be expressed in several ways, depending on the disease in question. Often, the blood flow dynamics can reveal pathologies, when examining disease specific characteristics based on applied fluid dynamic theories. As an example, one can examine the flow of an incompressible fluid through a vessel, Fig.1.1. Initially the fluid is flowing from left to right within a pipe of area  $a_1$  at a mean velocity of  $v_1$ . The pipe gradually narrows and reaches a constriction at a certain position. At this position, the area of the pipe is  $a_2$  and the mean velocity of the fluid is  $v_2$ . By introducing the concept of mass conservation on our setup, we get from the continuity principle that the mass entering the pipe must be the same as the mass going out of the pipe, i.e.  $a_1v_1 = a_2v_2 = Q$ . This means, that at the constriction, where  $a_2 < a_1$ , the reduced area size must be compensated by a proportional increase in  $v_2$ .

These principles can be directly translated to a stenotic region in an artery, where accumulation of plaque can result in a constriction. Since blood can be considered an incompressible fluid and mass conservation is present, a relative increase in the blood velocity measured at a stenotic region compared with a site before it, can determine the degree of severity, and whether action should be taken.

Among other imaging modalities used for screening and identification of cardiovascular diseases is the ultrasound (US) modality. The US modality is cheap, can be applied at the bedside and offers examination in real-time. The early usage of US displayed a gray-scale anatomical image (B-mode) of the scanned region. Later it became possible to estimate 1-D blood flow within a small range gate via 1-D spectral Doppler, but with the rapid development, color flow mapping (CFM) got accessible and provided 1-D blood

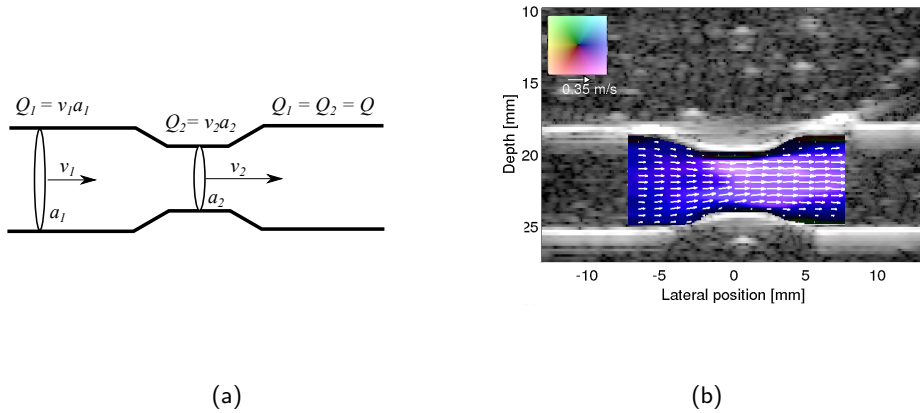


**Figure 1.1:** a) flow rate estimation when mass conservation is applied for an incompressible fluid. The flow rate  $Q_1$ , given by the cross-sectional area  $a_1$  and the mean velocity  $v_1$  perpendicular to the surface area, is equal to the flow rate estimated during the constriction where a smaller area  $a_2$  is compensated by an increased mean velocity  $v_2$ . b) experimental validation of the continuity principles in a constriction phantom. From (J. Jensen, Stuart, and J. A. Jensen 2015).

velocity information super-imposed on top of the B-mode image.

With 1-D velocity estimator methods well established, the development continued towards 2-D vector flow estimation. One of the approaches was the transverse oscillation (TO) method, which was the first 2-D technique to be implemented on a commercial scanner. Access to 2-D vector flow information offers an additional tool for examining the complexity of the blood flow, which can be used to identify pathologies that could not be revealed with previous 1-D methods. One example is the examination of the blood flow turbulence measured in patients with aortic stenosis both before and after replacement of the aortic valves, with reference measurements made to volunteers with a healthy ascending aorta (Hansen et al. 2016). The study showed that aortic stenosis had an increased flow complexity/turbulence compared with healthy individuals, and that the turbulence was significantly reduced after valve replacement, see Fig. 1.2.

Thus, application of 2-D vector flow in the clinic can be used to 1) identify and evaluate the necessity for making an invasive intervention, and 2) examine and monitor the effect of an intervention.

Both 1-D and 2-D blood flow estimation relies on several assumptions when used in the clinic for estimating peak velocities, volumetric flow rates, flow dynamics, etc. as well as several operator specific decisions are required. Many of these assumptions can be neglected when angle independent 3-D vector flow estimates are present, which also

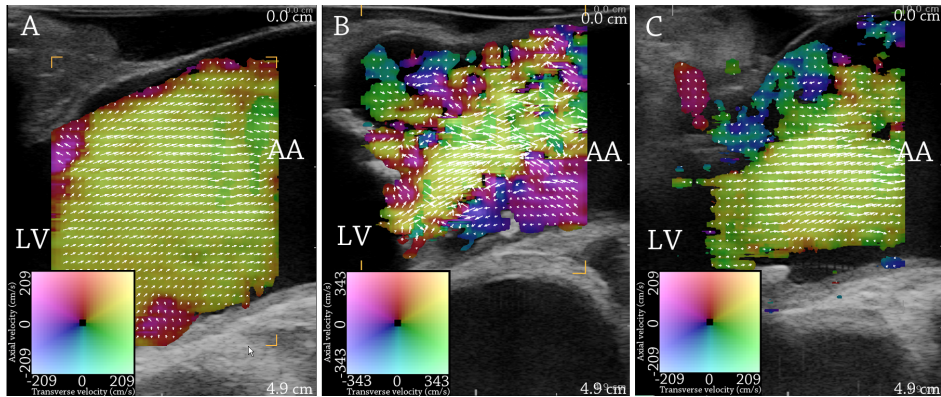


**Figure 1.2:** a) Long axis view of the systolic flow in a patient with normal aortic valves, b) in a patient with an aortic valve stenosis before replacement and c) after the replacement. LV = left ventricle. AA = ascending aorta. From (Hansen et al. 2016)

limits the number of operator manoeuvres, so that focus can be maintained on scanning the region of interest. With the extra flow dimension, new and unexplored applications may be discovered both for screening and surveillance of CVD, but before this can be implemented in the clinic, reliable 3-D methods and techniques need to be developed.

## 1.2 Objective

This thesis seeks to develop and validate methods for estimating 3-D vector flow on various transducer geometries. The methods are validated through simulations and in experimental setups. Transducers certified for clinical scans are used to validate the developed and optimized methods *in vivo* on healthy volunteers.

## 1.3 Scientific contributions

The main purpose of this PhD project is to develop ultrasonic methods for 3-D vector flow imaging. The motivation is to advance the field of velocity estimation in ultrasound, which plays an important role in the clinic. The velocity of blood has components in all three spatial dimensions, yet conventional methods can estimate only the axial component.

The thesis compiles the research presented in two manuscripts that have been submitted for publication in ISI journals, and a patent applications that was taken up by Analogic. Additionally, five conference proceedings are included in the project. Besides the included papers, the author has contributed to two filed patent applications, as well as

four journals and two proceedings. A full publication list is given below along with the scientific contribution.

### 1.3.1 Journal papers

- I **S. Holbek**, T. L. Christiansen, M. B. Stuart, C. Beers, E. V. Thomsen and J. A. Jensen. 3-D Vector Flow Estimation with Row-Column Addressed Arrays. Accepted for publication in *IEEE Trans. Ultrason., Ferroelec., Freq. Contr.*
- II **S. Holbek**, C. Ewertsen, H. Bouzari, M. J. Pihl, K. L. Hansen, M. B. Stuart, C. Thomsen, M. B. Nielsen and J. A. Jensen. Ultrasonic 3-D Vector Flow Method for Quantitative *in vivo* Peak Velocity and Flow Rate Estimation. Under review for *IEEE Trans. Ultrason., Ferroelec., Freq. Contr.*

### 1.3.2 Conference papers

- III **S. Holbek**, M. J. Pihl, C. Ewertsen, M. B. Nielsen and J. A. Jensen. 3-D Velocity Estimation for Two Planes *in vivo*. In *Proc. IEEE Ultrason. Symp.*, p. 1706-1709, 2014.
- IV **S. Holbek**, M. J. Pihl, C. Ewertsen, M. B. Nielsen and J. A. Jensen. *In vivo* 3-D Vector Velocity Estimation with Continuous Data. In *Proc. IEEE Ultrason. Symp.*, p. 1-4, 2015.
- V **S. Holbek**, T. L. Christiansen, M. F. Rasmussen, M. B. Stuart, E. V. Thomsen and J. A. Jensen. 3-D Vector Velocity Estimation with Row-Column Addressed Arrays. In *Proc. IEEE Ultrason. Symp.*, p. 1-4, 2015.
- VI **S. Holbek**, T. L. Christiansen, M. Engholm, A. Lei, M. B. Stuart, C. Beers, L. N. Moesner, J. P. Bagge, E. V. Thomsen and J. A. Jensen. 3-D Vector Flow Using a Row-Column Addressed CMUT Array. In *Proc. SPIE Ultrasound Imaging. Symp.*, Vol 9790, p. 979005-979005-8, 2016.
- VII **S. Holbek**, M. B. Stuart, and J. A. Jensen. Experimental 3-D Vector Velocity Estimation with Row-Column Addressed Arrays. In *Proc. IEEE Ultrason. Symp.*, p. 1-4, 2016.

### 1.3.3 Patent application

- I **S. Holbek**, H. Bouzari, M. Engholm, J. Jensen, M.B. Stuart, E. V. Thomsen, J. A. Jensen. 3-D Imaging Using Row-Column-Addressed Transducer Arrays: Two-way Focusing and Volumetric 3-D Vector Flow Imaging, Patent proposal in preparation. Expected to be filed ultimo 2016.

### 1.3.4 Additional papers and patents

Additional publications are listed here in chronological order.

#### 2015

- A** T. L. Christiansen, **S. Holbek**, M. F. Rasmusen, E. V. Thomsen, J. A. Jensen. 3-D Flow Estimation using Row-Column Addressed Transducer Arrays, International Patent Application, January, 2015, US application number: 14/599,857

**Contribution:** Concept development.

#### 2016

- B** J. A. Jensen, M. F. Rasmussen, M. J. Pihl, **S. Holbek**, C. A. Villagomez-Hoyos, D. P. Bradway, M. B. Stuart, B. G. Tomov. Safety Assessment of Advanced Imaging Sequences, I: Measurements. *IEEE Trans. Ultrason., Ferroelec., Freq. Contr.*, Vol. 63, No. 1, 2016, p. 110-119.

**Contribution:** Development and improvement of calibration scripts.

- C** T. Bechsgaard, K. L. Hansen, A. H. Brandt, **S. Holbek**, L. Lönn, L. Strandberg, C. Bækgaard, N. Nielsen, M. B. Jensen, and J. A. Jensen. Vector Volume Flow in Arteriovenous Fistulas. *Proc. SPIE Ultrasound Imaging. Symp.*, Vol 9790, p. 979003-979003-8, 2016.

**Contribution:** Development of MATLAB code to process data acquired from a commercial BK 5000 scanner.

- D** H. Bouzari, T. L. Christiansen, **S. Holbek**, M.B. Stuart, E. V. Thomsen, J. A. Jensen. Row-column Addressed 2-D Array with a Double Curved Surface, filed June 8, 2016, number: PCT/IB2016/053367

**Contribution:** Concept development for applications of a diverging lens for vector flow estimation.

- E** C. A. Villagomez-Hoyos **S. Holbek**, M. B. Stuart, and J. A. Jensen. High Frame Rate Synthetic Aperture 3D Vector Flow Imaging. In *Proc. IEEE Ultrason. Symp.*, p. 1-4, 2016.

**Contribution:** Design of transmit sequence and experimental setup

- F** A. H. Brandt, K. L. Hansen, C. Ewertsen, **S. Holbek**, J. B. Olesen, R. Moshavegh, C. Thomasen, J. A. Jensen, M. N. Bachmann. Carotid Artery Velocity: Comparison of Vector Velocity, Spectral Doppler and Magnetic Resonance. Draft.

**Contribution:** Development of MATLAB interface for automated processing of MRI data.

**G** J. A. Jensen, C. A. Villagomez-Hoyos, **S. Holbek**, K. L. Hansen. Velocity Estimation in Medical Ultrasound Systems. *Submitted in IEEE Signal Processing Magazine*, 2016.

**Contribution:** *In vivo* 3-D vector flow results.

**H** T. Bechsgaard, K.L. Hansen, A.H. Brandt, **S. Holbek**, J. L. Forman, C. Strandberg, N. Bækgaard, J. A. Jensen, M.N. Nielsen. First Comparison of Velocities in the Proximal Deep Veins of the Lower Extremities Estimated with Doppler and Vector Ultrasound. Draft.

**Contribution:** Development of MATLAB code to process data acquired from a commercial BK 5000 scanner.

## 1.4 Outline of the thesis

The thesis is divided into two parts. The first part (Chapter 2-4), assembles the relevant literature and theory for the reader, that is required for understanding the second part, which encounters the scientific contributions and conclusions (Chapter 5-8). The scientific part is suggested to be read chronically, as the presented challenges and limitations of a method described in one chapter are attempted to be solved in the following chapter.

**Chapter 2** Introduces previous published literature in the field of velocity estimation. The various methods are presented along with their advantages and drawbacks. Furthermore, the angle dependency problem is introduced to justify the need for 2-D and 3-D vector flow methods.

**Chapter 3** Explains the basic concept and requirement for a transverse oscillation velocity estimator. Special attention is made to the approach proposed by Jensen and Munk in 1998 (J. A. Jensen and Munk 1998), which founds the basis for the method applied throughout this thesis. This chapter also addresses additional TO methods as filtering in the Fourier domain and directional transverse oscillation.

**Chapter 4** Presents a large selection of transducer setup for acquiring volumetric data. The reviewed methods encounters both 2-D transducers capable of acquiring volumetric data in real-time as well as 2-D mimicking transducer setups, which lack the real-time acquisition properties.

**Chapter 5** Describes how 3-D vector flow in a plane was achieved with a 1024 channel matrix probe. The method is validated in experimental setups, through *in vivo* measurements of the common carotid artery, and finally, against MRI derived through-plane velocities. The Chapter is based on Paper II, III and IV.

**Chapter 6** Explores the performance of 3-D vector flow estimation when replacing a fully populated  $N \times N$  matrix array with an  $N + N$  row-column addressing array containing a factor  $N/2$  less elements. A parametric simulation study investigates the performance and identifies where the estimator deteriorates significantly. Experimental measurements are furthermore presented to validate the method. The work is presented in Paper I, V, VI and VII and is based on the ideas proposed in Paper A.

**Chapter 7** Expands the 3-D vector flow method to contain multiple planes or an entire volume. The first approach is an extension of the method presented in Chapter 6 and relies on focused emission. The second method has the potential of estimating 3-D vector flow at every point in a volume using a synthetic aperture approach and diverging waves. The ideas presented in this chapter emanate from Patent I.

**Chapter 8** Concludes the projects and discusses the perspectives and ideas on future work.



## CHAPTER 2

# Blood Velocity Estimation in Medical Ultrasound Imaging

---

**Summary** *Ever since the first example of blood velocity estimation using ultrasound was presented in 1957 by Satomura, the field has been developing rapidly. A wide range of techniques for displaying 1-D blood movement on commercial ultrasound scanners are well established and utilized on a daily basis for diagnostics and surveillance in the clinic. However, as blood movement is not unidirectional, several methods have been proposed to estimate the second and the third velocity component. This chapter describes the present angle dependency problem related to 1-D velocity estimators as well as a review on the leading vector flow techniques.*

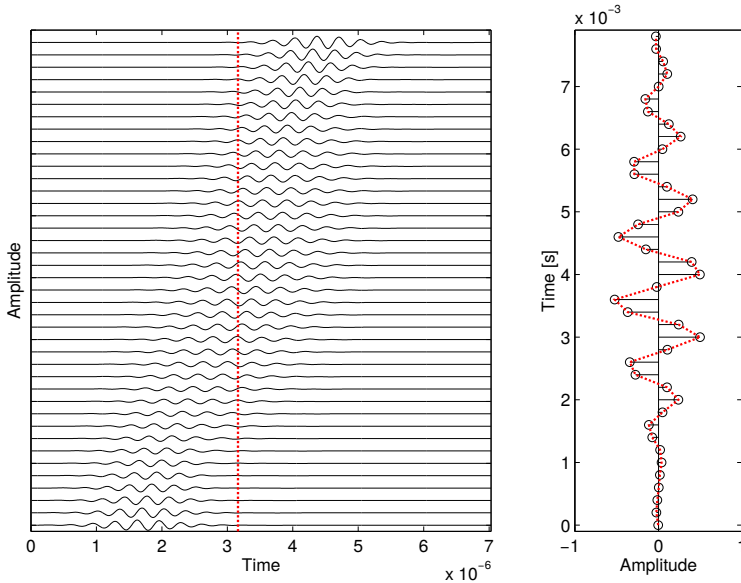
## 2.1 Purpose

Blood velocity estimation using medical ultrasound has become an important tool in the clinic for diagnosis of CVD and surveillance of patients. The field has advanced from simple 1-D velocity estimates along one direction to cover an entire plane with 2-D or 3-D vector flow methods. The purpose of this chapter, is to review some of the most important 1-D, 2-D and 3-D velocity estimation methods that have been proposed in the literature. The transverse oscillation (TO) method is not mentioned here, as a thorough review of the conventional estimator and the further developments are described in Chapter 3.

## 2.2 1-D Methods

### 2.2.1 Spectral estimator

A spectral 1-D estimator relies on sampling a slow time oscillating pattern at a fixed depth. The oscillating pattern arises when a scatterer having an axial velocity component is sampled from several pulse emissions, Fig. 2.1. The oscillating frequency of this temporal sampled signal is related to the magnitude of the axial displacement between each consecutive emission. The mean frequency content of the sampled signal can then reveal the magnitude and the direction of the movement.



(a)

**Figure 2.1:** The left figure shows the sampled signal obtained from a single scatterer moving away from the transducer for several pulse emissions. On the right image, a single sample is taken out at the red line for each pulse to generate the sampled signal. A spectral estimator exploits the relation between the frequency content of this signal and the axial movement. From (Jensen 1996).

### 2.2.2 Phase shift estimator

The first approach of a phase shift velocity estimator was the autocorrelation approach introduced by K. Namekawa *et. al* in 1982 (Namekawa et al. 1982) and later expanded by Kasai *et. al* in 1985 (Kasai et al. 1985). The autocorrelation method exploits the fact, that the mean phase shift between a consecutive amount of emissions can be translated to the mean axial velocity of the blood scatterer at a specific depth.

Consider a measurement setup where data are sampled at a certain depth,  $z_0$ , from a single RF sinusoid, as shown in Fig 2.2. Between two consecutive acquisitions, the magnitude of the velocity can be determined through the phase shift rate and by knowing the center frequency  $f_0$  of the sinusoidal. However, the direction of the movement is ambiguous since the same signal could be sampled whether the propagation was towards the left or the right. By sampling data from two distinct positions, at  $z_0$  and at  $z_0 - \delta$

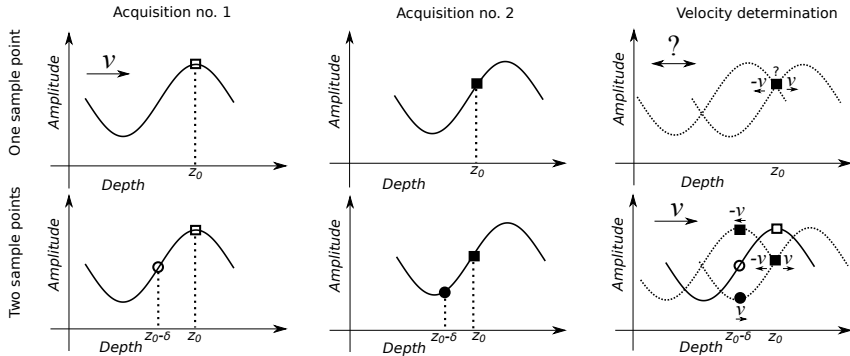


**Figure 2.2:** The figure shows the necessity of sampling a signal at two spatially separated points or by having IQ data, when determining the magnitude and direction of a displacements. The upper row shows the case, when only one point is sampled at every acquisition. At the velocity determination stage (rightmost figure), the magnitude can be estimated correctly, but the initial direction of the movement can be in either direction, since the second acquisition could have been obtained on either side of the sinusoid. In the lower row, spatial separated data are sampled at each acquisition. Independently, each pair of observations (circles or squares) can only determine the magnitude of the movement, but when combined, the direction is given unambiguously.

simultaneously, it is possible to determine both the direction and the magnitude of the movement uniquely.

In commercial scanners, this can be achieved directly by sampling data at four times the transmitted center frequency, which corresponds to a quarter of the wavelength  $\lambda_z$  i.e. a  $\pi/2$  phase shift. In signal processing, a  $\pi/2$  phase shifted imaginary signal can also be obtained by performing the Hilbert transformation  $\mathcal{H}\{\cdot\}$ . The original signal is denoted the in-phase signal, whereas the Hilbert transform of the in-phase signal yields the quadrature signal. When combined, these two signals form the in-phase and quadrature signal (IQ). The in-phase and quadrature signal form a pair, which possesses similar advantages as if it were sampled from two distinct positions simultaneously.

The autocorrelation velocity estimator relies on the receiving signals being narrowband (pure sinusoidal) and that the transmitted center frequency is similar to the frequency of the received signal. This requirement is often approached by transmitting a long pulse containing several sinusoidal cycles, but due to scattering effects, tissue attenuation etc. the received signal will most often not match completely.

### 2.2.3 Time shift estimator

The time shift estimator also denoted as the cross-correlation estimator, does not rely on any assumptions about the frequency content and only considers the most likely time shift

between the received signal from two consecutive transmit events. It was first proposed by Dotti *et al.* (Dotti et al. 1976) and further developed by Bonnefous and Pesqué, (Bonnefous and Pesqué 1986). The cross-correlation function in the time domain from the two consecutive signals  $r_1$  and  $r_2$  is defined as

$$R_{12}(\tau) = \frac{1}{2T} \int_T r_1(t)r_2(t + \tau)dt, \quad (2.1)$$

where  $T$  is the observation period and  $\tau$  is the lag. A cross-correlation estimator utilizes that the function  $R_{12}(\tau)$  reflects the relative correlation between the two signals at different time shifts/lags  $\tau$ . The peak value in  $R_{12}(\tau)$  is expected to represent the most likely direction and magnitude of blood movement, and can be revealed from the specific  $\tau$  and the time between the two transmit events. The time shift estimator does not have an upper limit for the detectable velocity range, but depends highly on, that the correlation is maintained between consecutive emissions. Only a minority of commercial scanners have implemented the time shift estimator, which can be attributed to the computational load of the technique.

#### 2.2.4 The angle dependency problem

Currently, velocity estimation in most commercial scanners is limited to only estimating the axial velocity component  $v_z$ , which is parallel to the ultrasound beam. The axial velocity is given by

$$v_z = |\mathbf{v}|\cos \theta, \quad (2.2)$$

where  $|\mathbf{v}|$  is the in-plane velocity magnitude and  $\theta$  is the beam-to-flow angle. The estimator has some inherent drawbacks as it breaks down when  $\theta$  approaches  $90^\circ$ , as illustrated in Fig. 2.3. A work-around to this angle dependency problem is to either physically angulate the transducer or apply delays electronically for steering the sonification angle at a preferable  $60^\circ$  to obtain the most accurate axial estimate. The manual angle corrections are performed by the operator to obtain the true velocity magnitude  $|\mathbf{v}|$ , which is subject to critical errors in the velocity estimation (Picot and Embree 1994). The angle correction assumes that  $\theta$  is constant in space and time, which can be correct in a straight vessel but collapses when the flow angle varies in space and time. For instance, in a vortex the flow will move around in  $360^\circ$ , which invalidates the assumption of a single correction angle. Due to these issues, the field evolved towards developing 2-D and 3-D angle independent velocity estimators.

### 2.3 Vector flow methods

The angle dependency problem can be solved when vector flow methods are applied to estimate 2-D or 3-D velocities. The sonification angle is in principle inconsiderable for

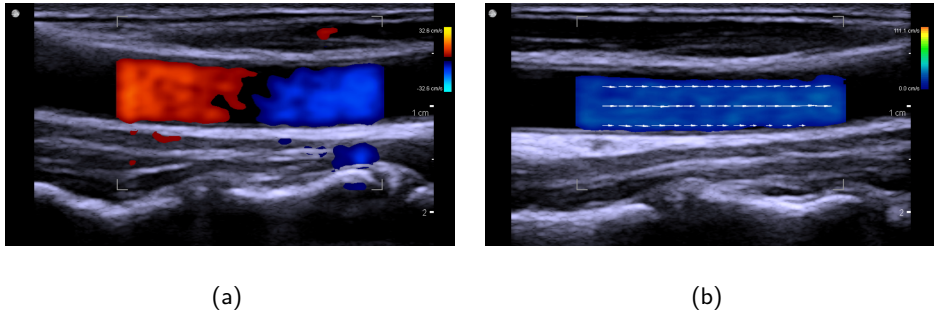


**Figure 2.3:** a) Color flow mappings of the common carotid artery at a  $90^\circ$  beam-to-flow angle. No flow can be detected in the center of the image, since the flow is orthogonal to the ultrasound beam. b) With 2-D vector flow techniques, the correct magnitude and direction can be retrieved, even when the flow is orthogonal to the beam. Here, the direction and magnitude of the flow is illustrated by the arrows and the colormap.

vector flow methods, although the actual performance might be reflected in the beam-to-flow angle. This section reviews the current leading vector flow techniques that are either developed for 2-D or 3-D applications.

### 2.3.1 Speckle tracking

In 1987, Trahey *et al.* (Trahey, Allison, and Ramm 1987) introduced the concept of speckle tracking for velocity estimation. By defining a small 2-D target kernel/speckle region in one image and performing a 2-D cross-correlation with the next image, the displacement having the highest correlation coefficient was expected to represent the most likely propagation of the speckle region. Since the speckle pattern reflects the underlying local composition of blood cell scatterer, the method requires a relative short time span between each frame to maintain a high temporal correlation between the speckle pattern of consecutive frames.

One of the major advantages with speckle tracking, compared with phase shift estimators, is the theoretical lack of an upper limit on the detectable velocity range. Despite this, it is a computational expensive method, which requires several compromises to provide an acceptable processing time. Furthermore, the choice of kernel size affects both the processing time and the spatial velocity resolution. By having a large kernel size, an improved performance can be obtained, as it is likely that the correct displacement can be detected. A large kernel size, however, results in a reduced spatial resolution of velocity estimates, as the average kernel movement is identified. On the other hand, reducing the kernel size can result in false estimates due to the likelihood of the search kernel being found elsewhere in the image than expected. Nevertheless, a better spatial resolution can

be obtained since the average kernel movement reflects a smaller area.

Several successful implementations with speckle tracking have been achieved for blood flow estimation (Udesen et al. 2008; K. L. Hansen et al. 2009; Fadnes, Nyrnes, et al. 2014) and recently for intra-cardiac volumetric 3-D vector flow imaging (Wigen and Løvstakken 2016).

### 2.3.2 Directional beamforming

In contrast to the majority of the proposed velocity estimation techniques, where RF data are beamformed in the direction of the propagating ultrasound waves, directional beamforming breaks with this standard. Here, the RF data are beamformed in the expected direction of the moving blood scatterer. With this approach, the interframe signal correlation along the flow direction is expected to be very high. By cross-correlating two lines beamformed along the same direction from consecutive emissions, the blood movement can be determined. The high interframe signal correlation allows the method to search for the highest cross-correlation coefficient at larger displacements with a reduced risk of detecting erroneous false peaks.

Although directional beamforming has provided convincing and impressive results, first by phantom studies and early *in vivo* measurements (S. I. Nikolov and Jensen 2001; Jensen and S. I. Nikolov 2004; Jensen, S. Nikolov, et al. 2006) and later by (Villagomez-Hoyos et al. 2016), the method still faces some challenges before implementation in a commercial scanner seems realistic. The major issues regarding directional beamforming are, as with speckle tracking, that a large amount of computational expensive cross-correlations have to be performed. Furthermore, the correct direction/angle at which the flow is propagating needs to be estimated before beamforming the desired lines (Jensen and Oddershede 2006; Kortbek and Jensen 2006; Villagomez-Hoyos et al. 2016).

### 2.3.3 Vector Doppler

Multi-beam Doppler, (one variant of vector Doppler), relies on the theoretical principle that the axial component  $v_z$  can be derived from the blood velocity vector  $\vec{v}$ , at any direction, as long as the beam-to-flow angle is known. By having two or three of these independent Doppler systems at different sonifications angles, triangulation of the derived respective axial velocity components can be used to obtain 2-D or 3-D vector Doppler velocities. The early approaches by Fahrback, 1970 (Fahrback 1970) used two transmitters/receiver (transcievers) arranged at a  $90^\circ$  angle to each other, to estimate 2-D vector Doppler from the orthogonal cross-beam. Extension of the method to 3-D was made shortly thereafter by (P. L. Hansen, Cross, and Light 1974) who generated a cross-beam from three transcievers. The proposed techniques could provide angle independent 2-D and 3-D velocity estimates, but only at the intersection point of the crossing beams.

With the advancement of transducer technology, the larger amount of elements allowed splitting the aperture into sub-apertures (Phillips, Kadi, and Ramm 1995; Scabia et al.

2000), as well as obtaining vector flow in a plane (Capineri, Scabia, and Masotti 2002; Pastorelli et al. 2008).

The vector Doppler technique was further improved by the use of plane waves, originally proposed for 2-D tissue motion estimation (Tanter et al. 2002). Crossing beams were now replaced by overlapping regions of steered plane waves, where vector Doppler could be applied. Several groups have contributed to the field of vector Doppler using plane waves, which both increased the field-of-view and the frame rate significantly. (Flynn et al. 2011; Ekroll et al. 2013; Provost et al. 2014; Ricci, Bassi, and Tortoli 2014; Yiu, Lai, and Yu 2014; Fadnes, Ekroll, et al. 2015; Correia et al. 2016).

One of the challenges with vector Doppler is when the autocorrelation approach is applied to determine the axial velocity component from different angles. As the transmitted pulse often has a relative short wavelength, this must be compensated by a high pulse repetition frequency to avoid reaching the aliasing limit. Moreover, the time between similar transmit events must be short, which limits the number of steering transmit angles. As a last consequence, the high pulse repetition frequency will lead to higher intensities and result in transducer heating, which can inhibit compliance with FDA limits.

### 2.3.4 Synthetic aperture imaging

Synthetic aperture imaging (SAI) originates from the field of radar systems, Sherwin *et al.* (Sherwin, Ruina, and Rawcliffe 1962). The principles were later adapted for ultrasound imaging (Bennett et al. 1982; Peterson and Kino 1984; Ylitalo and Ermert 1994; S. I. Nikolov 2001; S. I. Nikolov and Jensen 2002). One approach of SAI is illustrated in Fig. 2.4, where a spherical wave is transmitted from a single element emission. The backscattered signals are then beamformed in the receive stage with the full aperture. This creates an image, equally focused in the entire plane, which is referred to as a low resolution image, due to the unfocused transmission. By repeating the procedure for multiple various transmitting elements, several slightly different low resolution images can be created. Viewed in isolation, each low resolution image has a poor lateral resolution and a low SNR, but when added a high resolution image that is equally focused in the entire plane is obtained. The high resolution image is said to be focused synthetically in transmit and has a superior lateral resolution and SNR compared with an individual low resolution image (S. I. Nikolov and Jensen 2002).

The method is not limited to single-element transmissions as proposed by Bae and Jeong, 2000 (Bae and Jeong 2000), where a sub-aperture containing multiple transducer elements was used in the transmit stage to increase the strength of the generated acoustic field. By placing the virtual source behind the transducer, diverging waves are generated whereas plane waves are obtained when the virtual source is placed in front infinitely far away. Regardless of the position of the virtual source, a high resolution image can be achieved in a field-of-view, where the low resolution images are overlapping.

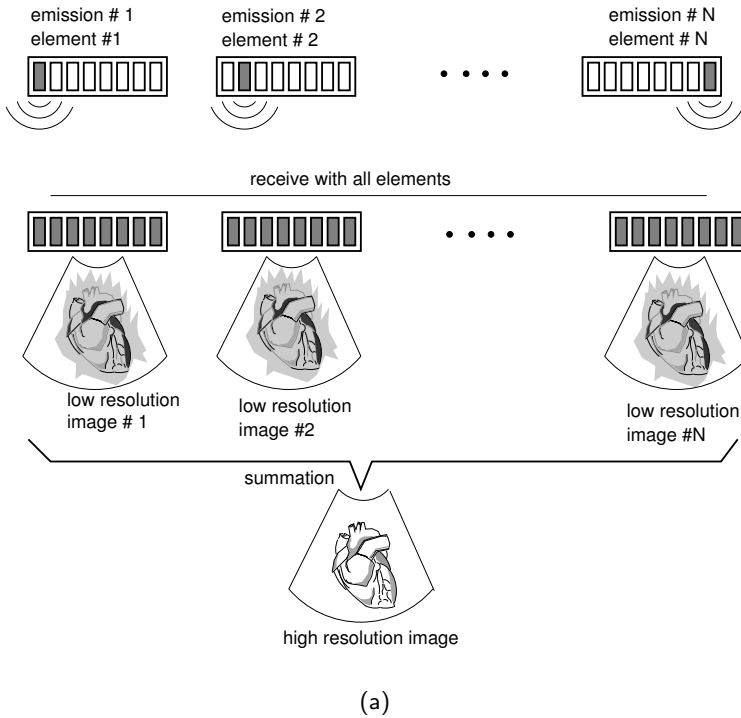


**Figure 2.4:** The basic principles of synthetic aperture imaging (SAI), where multiple unfocused low resolution images are coherently summed to form a high resolution image. From (S. I. Nikolov 2001).

### SYNTHETIC APERTURE FLOW IMAGING

Synthetic aperture flow imaging relies on the principles of SAI. The first attempts of blood flow estimation using SAI was made by Jensen and Nikolov 2002, (Jensen and S. I. Nikolov 2002). Directional beamforming was performed in each high resolution image and a cross-correlation was made line by line between each interframe to determine the magnitude of the movement. The method is associated with a high computational load, but an impressive high frame rate can be achieved, due to the few emissions needed for creating the next high resolution image.

Flow estimation using synthetic aperture imaging is not restricted to the actual position of the virtual source or a specific estimator - in fact any technique that can take advantage of high resolution images equally focused in every image point is a potential candidate for synthetic aperture flow imaging.

## 2.4 Discussion

This brief review demonstrates that several vector flow methods have been proposed in the literature, which all solve the angle dependency problem. The individual methods come with distinct advantages and drawbacks, as well as optimization procedures that can be applied, usually at the cost of sacrificing resolution, frame rate, computational speed etc. All of this has to be taken into account when settling on which technique to apply and for which application. One vector flow method widely used, that was not reviewed in this chapter, is the transverse oscillation (TO) method. A thorough examination of this method is presented in the next chapter, as this was also the estimator of choice in this project.



## CHAPTER 3

# Transverse Oscillation Methods

---

**Summary** *This chapter introduces the transverse oscillation (TO) velocity estimator proposed by Jensen and Munk, 1998. A short introduction to the basic principles are presented as well as how the method was expanded to estimate 3-D vector flow. Additional TO approaches and strategies are described with applications to tissue elasticity, motion estimation, and vector flow estimation.*

### 3.1 Purpose

The purpose of this chapter is to introduce the basic concept of the transverse oscillation (TO) method. Section 3.3 describes the TO method, which is applied in the studies presented in Chapter 5 and 6, whereas Sections 3.4 and 3.5 review some of the principles applied in Chapter 7. The chapter is not intended to give the reader an in-depth introduction to the field, but to point to the relevant literature, where a more thorough theoretical explanation can be found.

### 3.2 Basic principles

Conventional Doppler velocity estimators, as, e.g. the autocorrelation approach, rely on an oscillating pressure field in the direction of the transmitted pulse, from which the axial velocity can be determined. The pressure field is only oscillating in one dimension, and hence only a phase shift in the axial direction can be estimated. If, however, an oscillation can be generated or synthesized in the lateral dimension of the pressure field, similar techniques can be applied to estimate the phase shift in the direction transverse to the propagating pulse, and hence, the lateral velocity component. The TO method takes advantage of this by generating a double oscillating pressure field, from which the axial and lateral velocity components can be derived. The TO technique was proposed by Jensen and Munk (J. A. Jensen and Munk 1998), which was expanded in later work (J. A. Jensen 2001). A similar approach was suggested by Anderson (Anderson 1998).

The double oscillating field can be better understood by referring to the pattern arising when pounding two separated fingers (point sources) into still water. Around each finger, an oscillating wave front will propagate in all directions. The oscillating wave fronts will eventually meet and create an interference pattern, as illustrated in Fig. 3.1. In certain regions, the interference pattern will create a double oscillating field characterized by the two wavelenghts  $\lambda_z$  and  $\lambda_x$ .

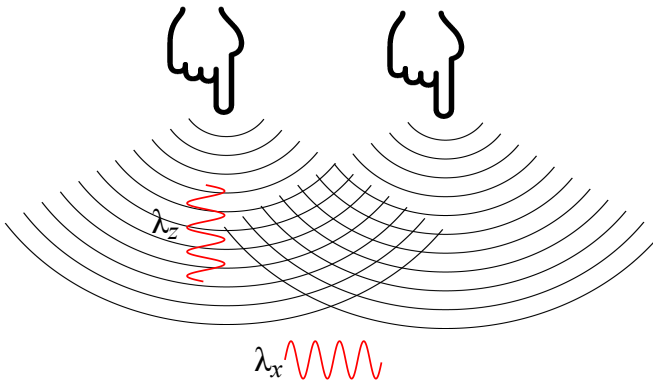


**Figure 3.1:** Illustration of how a double oscillating field can be created. The wavelengths  $\lambda_z$  and  $\lambda_x$  depend on the oscillation frequency and the separation distance between the two sources.

The analogy of generating a double oscillating field from two fingers pounding in water can be directly translated to ultrasound if the fingers are substituted with two transducer elements oscillating and generating ultrasonic waves.

A small propagating scatterer will be affected by the present pressure field. As the scatterer traverses the field, it will move up and down depending on the scatterer's initial position in the interference pattern. By recording the initial displacement caused by the interference pattern at different time instances, and by knowing the lateral wavelength  $\lambda_x$ , it is possible to estimate the propagation speed of the scatterer in the transverse direction.

In the conventional TO estimator, a weakly focused beam is emitted, and the double oscillating field is synthesized in the receive stage by having two apodization peaks of width  $w$  separated by a distance  $d_x$ . The width and the distance of the peaks determine the actual lateral wavelength  $\lambda_x$ . Generating the double oscillating field in receive rather than in transmit provides a larger flexibility, as the lateral wavelength can be chosen as desired.

### 3.3 Transverse oscillation method

#### 3.3.1 Beamforming

As described in Section 2.2.2, the conventional axial phase shift estimator relies on sampling a synthesized signal separated by a distance of  $\pi/2 = \lambda_z/4$  from the original signal. This is achieved either by sampling at four times the transmitted center frequency or by performing a Hilbert transformation on the sampled signal. The autocorrelation phase shift estimator can also be applied to estimate the lateral velocity component, but

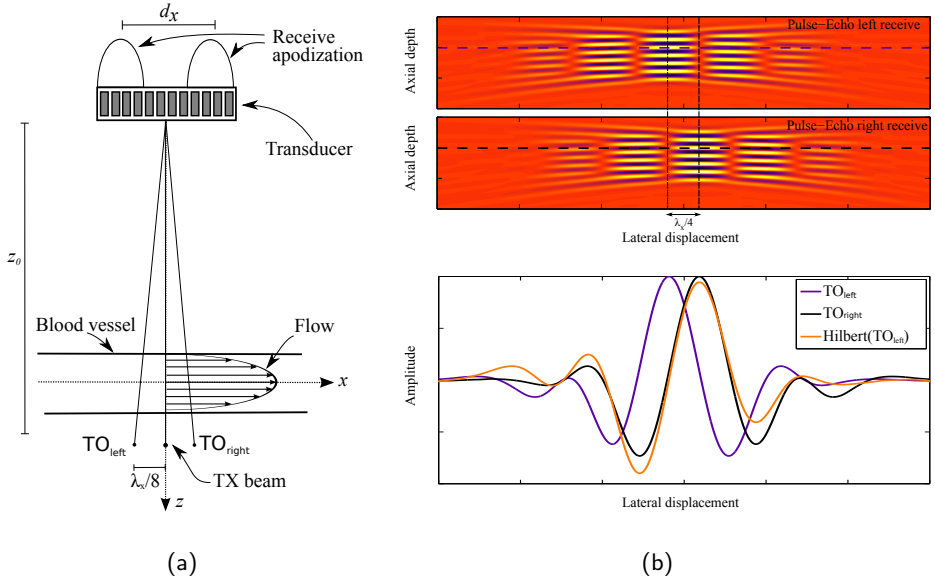


**Figure 3.2:** a) TO Beamforming setup where two lines  $TO_{left}$  and  $TO_{right}$  are beamformed with a spatial separation of  $\lambda_x/4$ . The double oscillating field is generated from the two peaks in the receive apodization. Modified from (Pihl, Marcher, and J. A. Jensen 2012). b) the upper figure shows the two double oscillating fields with a spatial displacement of  $\lambda_x/4$  illustrated by the vertical dotted lines. The two sampled signals from the same specified depth, illustrated by the horizontal lines, are plotted on top of each other along with a spatial Hilbert transformation of  $TO_{left}$ . A  $90^\circ$  phase-shift is obtained since  $TO_{right}$  and  $\mathcal{H}(TO_{left})$  are on top of each other.

requires that two signals, spatially shifted by a quarter of the lateral wavelength  $\lambda_x$ , can be sampled.

The spatial separated signals in the lateral dimension are obtained by beamforming the two lines  $TO_{left}$  and  $TO_{right}$  along the respective directions  $(-\lambda_x(z)/8, 0, z)$  and  $(\lambda_x(z)/8, 0, z)$ , see Fig. 3.2(a). The two lines are beamformed from the same transmit event, and the depth dependent lateral wavelength can theoretically be found as

$$\lambda_x(z) = 2\lambda_z \frac{z}{d_x}, \quad (3.1)$$

where  $\lambda_z$  is the wavelength of the emitted pulse,  $z$  is the axial depth of the beamformed

RF-line and  $d_x$  is the distance between the two peaks in the receive apodization. A simulation of two resultant pulse-echo fields are shown in Fig. 3.2(b) along with a plot of the signal amplitude in the lateral dimension at a fixed depth. The lower figure shows that the two fields are  $\pi/2$  phase-shifted, as the two sampled signals from the same specified depth,  $TO_{right}$  and  $\mathcal{H}(TO_{left})$ , are on top of each other. The two beamformed signals are said to form a spatial quadrature signal pair.

### 3.3.2 The velocity estimator

In principal, these two spatially separated signals are sufficient to estimate the lateral velocity component, but the robustness of an estimator relying entirely on these two inputs would deteriorate significantly as soon as the beam-to-flow angle deviates from  $90^\circ$ . The reason being, that since we have introduced a modulated lateral oscillation along with the present axial oscillation in the field, the sampled echo at any spatial position will contain information from both of these oscillations. This means, that when estimating the lateral velocity component, the results will be influenced by any scatterer propagating in the axial direction, which furthermore oscillates at a much higher frequency than in the lateral direction. To improve the performance for a non-transverse flow, the influence from the axial oscillations needs to be suppressed or decoupled in the estimator.

These were the considerations in the original derivation of the TO velocity estimator presented by Jensen, 2001 (J. A. Jensen 2001). Here it was shown, that the two quadrature signals could be combined to yield an expression for estimating a velocity component that was, theoretically, independent of phase changes caused by movement in the respective orthogonal direction:

$$v_x = \frac{\lambda_x f_{prf}}{2\pi 2k} \times \arctan \left( \frac{\Im\{R_1(k)\}\Re\{R_2(k)\} + \Im\{R_2(k)\}\Re\{R_1(k)\}}{\Re\{R_1(k)\}\Re\{R_2(k)\} - \Im\{R_2(k)\}\Im\{R_1(k)\}} \right) \quad (3.2)$$

$$v_z = \frac{\lambda_z f_{prf}}{2\pi 4k} \times \arctan \left( \frac{\Im\{R_1(k)\}\Re\{R_2(k)\} - \Im\{R_2(k)\}\Re\{R_1(k)\}}{\Re\{R_1(k)\}\Re\{R_2(k)\} + \Im\{R_2(k)\}\Im\{R_1(k)\}} \right), \quad (3.3)$$

where  $R_1(k)$  and  $R_2(k)$  are the autocorrelation functions with lag  $k$  for the two constructed signals derived in (J. A. Jensen 2001), and the  $f_{prf}$  is the pulse repetition frequency. It is here anticipated that  $f_{prf}$  is equal to the transmit frequency of a given emission type. The aliasing limit of the axial and transverse components are

$$v_{x_{max}} = \frac{\lambda_x f_{prf}}{4k} \quad (3.4)$$

$$v_{z_{max}} = \frac{\lambda_z f_{prf}}{8k}. \quad (3.5)$$

The axial velocity component can be estimated by using a conventional autocorrelation approach as (Kasai et al. 1985), as this method can estimate velocities in twice the range as the TO estimator. This requires an additional beamformed line created with a conventional receive apodization (Hanning, Tukey, etc.).

### 3.3.3 From 2-D to 3-D

The step from TO in 2-D to 3-D seems straightforward, at least in theory. Theoretically, it only requires a 2-D array, so that data from two lateral dimensions can be beamformed before the method can be expanded to estimate velocities in 3-D. The exact same equations can be reused when substituting  $\lambda_x$  with the modulated wavelength in the orthogonal dimension  $\lambda_y$ .  $\lambda_y$  also scales linearly with depth and depends on the position of the apodization peaks. Due to the increase in dimension of the array, the apodization profile is similarly expanded to cover the entire plane. If a symmetric 2-D array with similar receive apodization profiles is used, the two lateral wavelengths will be equal.

#### APODIZATION

The difficulties of 3-D TO arise when considering the physical dimensions of accessible 2-D arrays. Conventional 1-D linear arrays or phased arrays can contain at least 128 elements or more, allowing for a large flexibility in the transmit stage as well as the position and shape of the receive apodization profiles. Current fully sampled 2-D matrix arrays only span 32 elements in each dimension, resulting in a reduced flexibility when placing the receive apodization profile, see Fig. 3.3.

#### BEAMFORMING

To estimate the 3-D velocity vector along one propagation direction, a total of 5 unique beamformed lines are needed. One beamformed line for the axial velocity estimator, and two dedicated lines for each of the transverse and elevation velocity estimates, see Fig. 3.4. All five lines can either be beamformed in parallel from the same transmission or be combined from multiple consecutive transmission.

## 3.4 Filtering in the Fourier domain

One of the drawbacks with the conventional TO approach, is that the wavelength is depth dependent if a static apodization profile is applied. By using a dynamically adaptive depth dependent TO apodization profile, a constant lateral wavelength can be maintained within a limited range (J. A. Jensen, Brandt, and Nielsen 2015). However, changing the lateral wavelength requires a re-beamforming of the whole data set. This can be avoided

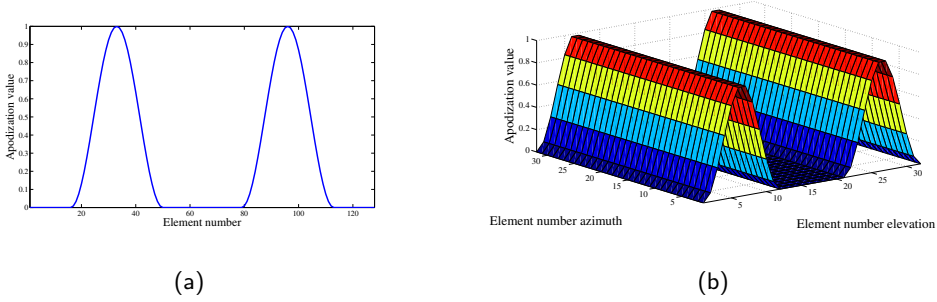


**Figure 3.3:** (a) Example of a 1-D TO apodization profile with two separated peaks applied on a 128 element transducer. b) Example of a 2-D TO apodization profile applied on a  $32 \times 32$  matrix array.

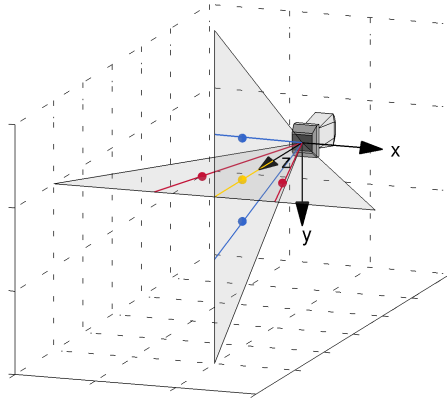


**Figure 3.4:** Illustration of the beamforming setup for estimating three velocity component along one direction  $(0, 0, z)$ . The axial velocity component  $v_z$  is estimated from the line beamformed along  $(0, 0, z)$  (yellow line). The transverse  $v_x$  component is derived from the two lines beamformed along  $(\pm\lambda_x(z), 0, z)$  (red lines), and the two beamformed lines  $(\pm\lambda_y(z), 0, z)$  (blues lines) are used for estimating  $v_y$ .

when generating the transverse oscillation by filtering a beamformed image in the Fourier domain, as proposed by Salles *et al.* 2015, (Salles, Chee, et al. 2015). Here, a constant lateral wavelength was achieved by multiplying a mask containing two separated Gaussian functions centred around the desired wavelength, with the 2-D Fourier transform of the image.

### 3.5 Directional transverse oscillation

As suggested by Bonnefous 1988, (Bonnefous 1988), beamforming could be made in lines transverse to the ultrasound beam. This idea was exploited by Jensen (J. A. Jensen 2015, 2016) to propose the idea of directional transverse oscillation (DTO). In DTO, multiple densely spaced lines are beamformed in the lateral dimensions to cover a region of interest. A traditional TO receive apodization profile with two peaks was used in the original work to create a lateral oscillation in the field. To obtain the quadrature signal needed for the TO estimator, a 2-D Hilbert transform can be performed in the lateral dimension along the laterally beamformed signals. The 2-D Hilbert transformation results in two fields phase-shifted by  $90^\circ$  only in the lateral dimension. From these two fields, an analytical wavelength  $\lambda_x$  can be estimated at each depth, which makes the method self-calibrating.

The method was later expanded by Jensen *et al.* 2015 (J. Jensen, Stuart, and J. A. Jensen 2015) who included filtering in the Fourier domain to obtain the lateral oscillation. The method was combined with plane wave imaging to obtain high frame rate 2-D vector flow estimates.

### 3.6 Additional methods and applications

Liebgott *et al.* 2005 and 2007 (Liebgott, Fromageau, et al. 2005; Liebgott, Wilhjelms, et al. 2007) applied a similar beamforming strategy as described in 3.3 with application for tissue elasticity imaging. The approach was expanded to a phased array for 2-D motion estimation in echocardiography (Liebgott, Salem, et al. 2009; Alessandrini et al. 2014). Another approach for 2-D displacement estimation using a transverse modulation method was proposed by Shiina *et al.* 2009 (Shiina, Kondo, and Yamakawa 2009) with applications on small apertures.

A method for tissue motion estimation using a full 3-D transverse oscillation in a volume has also been proposed by Salles *et al.* 2015, (Salles, Liebgott, et al. 2015), where the oscillation in one axial and two lateral dimensions were obtained simultaneously in an experimental setup with a 2-D array.

Two-dimensional *in vivo* vector flow imaging at high frame rates using transverse oscillation techniques and plane waves has also been reported in the literature (Lenge et al. 2015) with a phase-based block matching approach (Basarab et al. 2009).

An approach for Fourier domain beamforming for TO has also been proposed in the literature (Liebgott 2010). The technique improved the expected point spread functions when broadband signals were applied, compared with similar results obtained with a time domain beamformer.

### 3.7 Discussion

The original TO technique reviewed in this chapter is one of several approaches to estimate vector flow. What makes this vector flow estimator particularly interesting is the flexibility in the receive beamforming, which allows for varying the lateral wavelength to match the initial flow conditions. Furthermore, the TO estimator is based on the computational inexpensive autocorrelation function compared with the cross-correlation function which allowed for an implementation on a commercial BK Profocus scanner (BK Ultrasound, Herlev, DK) as the first vector flow technique, and hence, will ease a real-time implementation of 3-D TO. As reviewed in sections 3.4-3.6, developments in new optimization routines and approaches of generating the double oscillating field are still in progress and provide some very interesting alternative combinations for obtained vector flow in 2-D or 3-D. These techniques are further explored in Chapter 7.

To estimate 3-D vector flow using the TO method, a 2-D array is required. Next chapter reviews 2-D mimicking transducer setups and 2-D transducers applicable for 3-D TO vector estimation.

# CHAPTER 4

## 2-D Transducer Setups

---

**Summary** *The previous chapter described the transverse oscillation method and how vector flow estimates can be obtained in 2-D and 3-D. For 3-D vector flow imaging it is a necessity to acquire volumetric data. Volumetric data can either be obtained from 2-D mimicking transducer setups, including mechanical probes or free-hand scanning, both with 1-D transducers. However, a significantly higher frame rate can be achieved with 2-D arrays, as they can acquire real-time volumetric data. Various 2-D array constructions and designs are reviewed, regarding fully populated matrix arrays, micro beamformers, sparse arrays, and row-column addressed arrays, which all contain pros and cons with respect to commercial implementation, cost, flexibility and dimensions. It is concluded that 2-D arrays are preferred due to their properties of real-time volumetric data acquisition and increased frame rate.*

### 4.1 Purpose

The purpose of this chapter is to introduce the basic principles and technologies used in most of today's transducer elements. Furthermore, this chapter introduces various proposed ideas in the literature for creating an array from which volumetric data can be acquired. The chapter gives a brief introduction to a given method as well as presents its pros and cons. Special attention should be paid to the fully sampled matrix array in Section 4.4.1 and the row-column addressed array in Section 4.4.3, as two transducers based on these principles were used in work presented in Chapter 5, 6, and 7.

### 4.2 Generating the ultrasound

The fundamentals of medical ultrasound rely on the principles of having one or multiple vibrating transducer elements which can transmit and receive ultrasonic waves at frequencies in the MHz range. The ultrasonic waves are generated when a current is applied on the transducer elements which causes the elements to vibrate at amplitudes and frequencies specified by the current signal. Ideally, the impulse response to the transducer element is a single sinusoidal without any ringing effect. Conventionally, piezoelectric materials have been the preferred medium for making transducer elements since the very beginning of medical ultrasound. However, recent development in capacitive micromachined ultrasonic

transducers (CMUT) may be a possible game changer since CMUT's are cheaper to fabricate, are lead-free and provide a larger bandwidth.

### 4.2.1 Piezoelectric

One way of generating ultrasonic waves is by the use of piezoelectric materials. A piezoelectric material such as quartz has the ability to produce an electric charge related to the degree of material deformation. A similar reverse effect also exists, where a voltage drop across the medium will result in a deformation. The majority of ultrasonic transducer elements are therefore diced from piezoelectric material. The transducer elements exploit the piezoelectric effect alternately in the transmit and receive of ultrasonic imaging. During the transmit stage, a time varying voltage is applied across the elements generating propagating ultrasonic waves due to mechanical vibrations of the element. In the receive stage, the reverse properties are utilized in such a way that the back scattered echoes cause the piezoelectric materials to vibrate generating a current that is sampled by the imaging system.

### 4.2.2 Capacitive micromachined ultrasonic transducers (CMUT)

Transducer elements made up of piezoelectric materials are mechanically diced. This results in some limitations in the minimum distance between two neighboring elements (the kerf) as well as most of the piezoelectric materials contains lead. An alternative technique to fabricate transducer elements is the CMUT technology, performed in a cleanroom.

The CMUT technology must contain the same properties as the piezoelectric material, i.e. it should be feasible to generate controlled vibrations, creating ultrasonic waves in the transmit stage. For the receive stage, it should be possible to sample back-scattered ultrasonic echo signals. The ultrasonic waves in a CMUT are generated via multiple (thousands of) vibrating tiny cells. A cross-sectional view of such a single CMUT cell is seen in Fig. 4.1. The principles of the CMUT technology are as following; At rest, no voltage is applied to the electrodes and the top plate is unbent. Applying a DC-voltage across the top and bottom electrode "pulls in" the top electrode and works as the new starting point for the cell. The closer the top electrode can be pulled in, the higher the obtained sensitivity (unless a complete pull in is made, causing the cell to collapse). An ultrasound pressure field is generated by applying a sinusoidal AC-voltage across the cell, which induces a vibration on the top electrode. In receive the AC-voltage is disabled and the returning echo causes the top electrode to vibrate such that a signal is generated, which is sampled using the connected ultrasound system. Each element in a CMUT consists of several CMUT cells that can vibrate in phase to increase the transmitted pressure field. 1-D prototype CMUTs have been manufactured with success (Savoia, Caliano, and Pappalardo 2012), whereas 2-D CMUTs have until recently, only been reported for experimental use (Logan, Wong, and Yeow 2009; Christiansen et al. 2015; Rasmussen, Christiansen, et al. 2015).

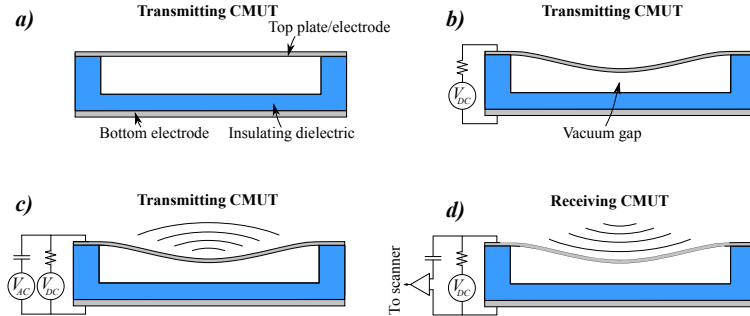


**Figure 4.1:** Cross section of a single circular CMUT cell. In a) the initial cell stage. b) A DC voltage is applied to pull the top electrode closer to the bottom electrode. The same DC voltage remains throughout both transmit and receive. c) An AC voltage is applied on the top electrode, which leads to oscillations around the starting point and ultrasound is transmitted. d) The returned pressure echo will result in a vibrating top electrode which induces a current, that can be sampled in the ultrasound scanner. From paper (Holbek et al. 2016)

CMUTs are lead free and fabricated using microelectromechanical systems (MEMS) technology, where structures in the order of microns can be manufactured. This technology offers the possibility of developing nearly kerf-less transducers with almost any choice of pitch, customized geometries, broadbanded transducers with high sensitivity, and at much lower fabrication cost.

### 4.3 2-D mimicking setups

It is not a necessity to use a 2-D array for volumetric ultrasound imaging as long as a 2-D transducer setup can be mimicked. In fact, data for volumetric imaging with a 1-D transducer can be obtained in two ways: Either by mechanical probes or by free-hand scanning combined with high precision tracking monitoring.

By mechanical probes or wobbling arrays, the basic idea is to mechanically rotate or translate a 1-D array to obtain multiple 2-D imaging planes, which can be mapped to form a volume, based on the transducer orientation at the acquisition time (Merz, Bahlmann, and Weber 1995; Lockwood, Talman, and Brunke 1998). The quality of the constructed volume relies highly on the accuracy of the mechanical positioning, and the usability depends on how fast the array can be repositioned and how often.

In free-hand scanning a tracking system is tracking the initial probe position and angulation via a tracker attached to the probe (Iversen et al. 2013). During a free-hand scan every acquired frame is translated according to the probe orientation and mapped into a volume. As the scan progresses at various positions and angles, an entire volume

can be mapped. The method can be combined with electrocardiogram (ECG) gating to provide a temporal dimension to the volumetric data. The method can benefit from all the advantages that come with 1-D arrays, but the precision and limitations inevitably lie in the accuracy of the sensing system.

For a thorough review of 3-D ultrasound systems, the reader is encouraged to read the review by Karadayi, Managuli and Kim 2009 (Karadayi, Managuli, and Kim 2009).

The limitations of a 2-D mimicking setup is, that a very low volume rate can be achieved due to the lack of real-time volumetric data acquisition. Therefore, 2-D transducers are of the essence when high volume rates are required as these transducers can obtain real-time volumetric data.

## 4.4 2-D transducers

### 4.4.1 Fully populated matrix arrays

The first fully populated 2-D arrays were presented in 1991 (Smith, Pavy and Ramm) (Smith, Pavy, and Ramm 1991; von Ramm, Smith, and Pavy 1991), with the transducer elements arranged in a rectangular grid. Due to the limitations of the imaging systems at the time being only 32 channels in transmit and 32 channels in receive could be used. The 2-D matrix array usually insonates a pyramid-shaped volume and offers the possibility of electronic two-way focusing, which can be steered in two perpendicular directions (elevation and azimuth).

Due to the exponential number of channels in an  $N \times N$  element matrix array, access to all individual channel data has been limited to a few research scanners such as SARUS (Jensen et al. 2013), which can handle 1024 channels in both transmit and receive provided with the  $32 \times 32$  phased matrix array (Vermon S.A., Tours, France). With a similar transducer Provost *et al.* 2014 (Provost et al. 2014) were able to transmit on all 1024 channels and receive from 512 using a multiplexor on their research scanner. A fully sampled matrix array offers a wide range of flexibility both in the transmit stage and in the processing. However, the large number of connections entails a thick and heavy main cable as seen in Fig. 4.2. The thick and heavy cable results in a reduced manoeuvrability, which is not a sustainable solution for an operator working with the equipment for several hours every day.

#### MICRO BEAMFORMING

For large fully populated arrays, it becomes impossible to connect all the individual elements to a conventional imaging system. One way to maintain the benefits of having a probe with thousands of elements and to keep the number of connections to the imaging system at a reasonable level is by applying micro beamformers (Savord and Solomon 2003; Halvorsrod, Luzi, and Lande 2005). In micro beamforming a large matrix array is divided into several sub-apertures in which a preliminary beamforming stage takes place. All channel data in the sub-aperture are summed according to a specified delay curve



**Figure 4.2:** The  $32 \times 32$  Vernon phased matrix array with all its cables and connectors.

based on the focal point and the out-put is reduced to a single channel. Each sub-aperture thereby reduces the data flow significantly and the resulting outputs from all sub-apertures are handled by the imaging system where a final delay and summation takes place.

Implementation of the electronics for micro-beamforming is rather expensive and external cooling can be necessary due to the comprehensive heat production. However, the technology is implemented in the current state-of-the-art 9.212 element fully sampled phased matrix array X6-1 PureWave xMATRIX probe from Phillips (Eindhoven, Netherlands).

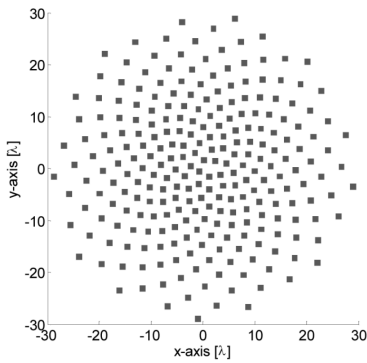
#### 4.4.2 Sparse arrays

To reduce the number of transducer elements, the idea of using a sparse or thinned array emerged first for 1-D arrays (Lockwood, Li, et al. 1996) and later for 2-D arrays (Davidsen, Jensen, and Smith 1994; Austeng and Holm 2002). From a fully populated or dense array a different sub sample of elements are used in the transmit state compared with the elements used in the receive stage. This approach maintains the advantages of having an effective 2-D array with a reduced number of element, however the reduced number of applied elements leads to a higher side-lobe level and a poorer SNR.

The elements can also be distributed according to off-axis templates, as presented beautifully by Ramalli *et al.* (Ramalli et al. 2015), where a simulated annealing optimization algorithm suggested a spiraling (sunflower) Fibonacci array pattern, see Fig. 4.3.

#### 4.4.3 Row-column addressed arrays

Another idea of creating a 2-D array with a low channel count was the row-column (RC) addressing approach introduced by Morton and Lockwood 2003 (Morton and Lockwood 2003) and further developed by Demoré (Demoré et al. 2009). An RC addressed array can



(a)



(b)

**Figure 4.3:** (a) Example of a sparse array proposed by Ramalli *et al.* 2015 where a spiralling pattern was suggested after optimization, from (Ramalli *et al.* 2015). (b) Sunflower with a similar spiralling seed pattern as proposed for the array element distribution. Image credit: brilliantbotany.com

be viewed as two orthogonally quadratic 1-D arrays with tall elements, mounted on top of each other. Compared with an  $N \times N$  matrix array, the total number of interconnections in an  $N + N$  RC array is reduced by a factor of  $N/2$ , which eases the interconnect and opens up for transducers with both a large footprint and a small pitch. An illustration of the of the two separated arrays and the effectively merged 2-D RC array is shown in Fig. 4.4.

Several versions and layouts of 2-D RC arrays have been presented for both piezo arrays (Seo and Yen 2006; Yen *et al.* 2009) and CMUTs (Chen *et al.* 2011; Sampaleanu *et al.* 2014; Christiansen *et al.* 2015). The first presented array for experimental use was a  $64+64$  element RC array reported by (Seo and Yen 2006) with a later version containing  $256+256$  elements (Seo and Yen 2007, 2008). In 2015 Christiansen *et al.* (Christiansen *et al.* 2015) manufactured a  $62+62$  element CMUT array with integrated apodization for suppressing ghost echoes for experimental use. A CMUT and a piezoelectric transducer with similar properties were later assembled to prototypes compatible with a commercial scanner (BK 5000 scanner, BK Ultrasound, Herlev, Denmark) in collaboration with Sound Technology, Inc. (State College, PA, USA).

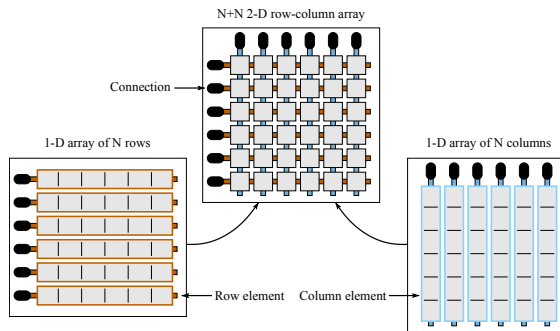


**Figure 4.4:** An RC array is composed of two  $1 \times N$  and  $N \times 1$  1-D one-way focused linear arrays mounted orthogonally on top of each other to form an  $N + N$  array. Modified from (Rasmussen and Jensen 2013).



## CHAPTER 5

# 3-D Vector Flow With a Fully Addressed Matrix Probe

---

**Summary** *This chapter presents 3-D vector flow estimates in a plane obtained with a fully addressed 1024 element 2-D matrix probe. It furthermore introduces the principles of designing a transmission sequence for continuous data acquisition. Such a sequence can provide velocity estimates in the kHz range, which is demonstrated both in two phantom studies and in vivo. The presented phantom measurements are compared with their corresponding reference value, whereas the in vivo measurement is validated against the current golden standard for non-invasive blood velocity estimates, based on magnetic resonance imaging (MRI).*

## 5.1 Purpose

The purpose of this chapter is to introduce a method for high frame rate 3-D vector flow estimation in a plane. It is also demonstrated that the technique provides a high precision as well as high accuracy when compared with reference values and competing imaging modalities such as magnetic resonance imaging (MRI). Furthermore, the chapter validates that the method can be a valuable tool in the clinic since operator dependent interactions can be handled automatically, as e.g. no angle correction is required. The chapter is composed of Paper II, III and IV.

## 5.2 Background

As stated in Chapter 4, a 2-D transducer setup is required for 3-D vector flow estimation. This chapter presents work obtained using a  $32 \times 32$  channel fully sampled 2-D matrix array. A similar probe was used by Provost *et al.* 2014 (Provost et al. 2014) to estimate volumetric 1-D Doppler velocities and recently applied to achieve 3-D volumetric flow *in vivo* (Correia et al. 2016).

The presented method in this chapter is based on the TO principles suggested by Jensen and Munk (J. A. Jensen and Munk 1998) and Jensen (J. A. Jensen 2001), further developed by Pihl *et al.* (Pihl and J. A. Jensen 2014; Pihl, Stuart, Tomov, Rasmussen, et al. 2014) who implemented a 3-D version of the TO technique on a 2-D matrix probe. This project continues the work by Pihl, who presented the first experimental results of

3-D vector flow estimation in a plane. The method also provided the first *in vivo* 3-D vector flow estimates for which an M-mode of a common carotid artery was presented (Pihl, Stuart, Tomov, P. M. Hansen, et al. 2013). This study differs from the previous work by designing a transmit scheme for continuous data acquisition which increases the frame rate from 13 Hz to 1.1 kHz. Furthermore, the large tissue movement in the *in vivo* measurements required new and more advanced clutter filtering, which was implemented successfully. Finally, great effort has been put in validating the method, both in phantom studies and *in vivo*.

### 5.3 Continuous data acquisition

Conventional ultrasound systems produces color flow estimates at a frame rate of  $\sim 20$ -25 Hz. The frame rate can be increased significantly if a continuous data acquisition scheme is applied.

An emissions sequence, where all identical transmit events are spaced equally in time, can be considered a continuous data scheme (Nikolov and J. A. Jensen 2001, 2003). Continuous data can be obtained through synthetic aperture imaging, plane waves, focused emissions, or for any other setup, as long as the transmit sequence is designed according to the aforementioned requirements.

Color flow sequences on commercial scanners usually transmit 8-16 flow emissions in the same direction followed by the same number of emissions in another direction and so on, until the region of interest is covered. The number of emissions needed for each velocity estimate is denoted the ensemble length  $e$ . The total number of unique flow lines in a sequence can be defined as  $F_i$ , where  $i = 1, 2, \dots, N$  and the total number of emissions used to create the B-mode image as  $B_j$ , where  $j = 1, 2, \dots, M$ , see Fig. 5.1. A schematic representation of one full transmit cycle with a conventional emission sequence can be written as

$$\begin{array}{c}
 \text{Ensemble length, } e \\
 \overbrace{F_1 \rightarrow F_1 \cdots \rightarrow F_1} \\
 F_2 \rightarrow F_2 \cdots \rightarrow F_2 \\
 \vdots \quad \quad \quad \vdots \\
 F_N \rightarrow F_N \cdots \rightarrow F_N \\
 B_1 \rightarrow B_2 \cdots \rightarrow B_M
 \end{array}$$

With such a sequence, all flow estimates are made line by line and a color flow map is constructed after all transmit events have been fired. The same procedure is applied for creating the B-mode. The B-mode and flow estimates can only be updated when

a new cycle of all the transmit events has taken place. The frame rate for this type of transmit sequence is highly dependent on the ensemble length. A large  $e$  is desired as it improves the performance of the clutter filter and the robustness of the velocity estimator, since averaging can be performed on more samples, but reduces the frame rate. It is also possible to obtain a large field-of-view by increasing  $N$  at the expense of a lower frame rate.

The proposed sequence used in this study relies on the principles of continuous data acquisition and is a rearrangement of the aforementioned transmit order. Schematically it can be described in the following way

$$\begin{array}{ccccccc}
 F_1 \rightarrow F_2 \rightarrow F_3 \rightarrow F_4 \cdots \rightarrow F_N \rightarrow B_1 \rightarrow & & & & & & \\
 F_1 \rightarrow F_2 \rightarrow F_3 \rightarrow F_4 \cdots \rightarrow F_N \rightarrow B_2 \rightarrow & & & & & & \\
 \vdots & & \vdots & & \vdots & & \\
 F_1 \rightarrow F_2 \rightarrow F_3 \rightarrow F_4 \cdots \rightarrow F_N \rightarrow B_M \rightarrow & & & & & & 
 \end{array}$$

Here, the duration between two identical emissions is the same at all times and is achieved by emitting the flow lines  $F_{1 \rightarrow N}$  consecutively, followed by emitting the B-mode emission  $B_1$ . Next, the flow lines  $F_{1 \rightarrow N}$  are emitted, followed by the B-mode emission  $B_2$  etc. When the desired amount of unique B-mode emissions  $M$  have been fired, the sequence repeats itself from the beginning. This type of sequence design significantly increases the frame rate, as a sliding window in the temporal direction is applied in the velocity estimator. This is achievable in practice, since data from latest transmit event replaces data from the oldest event in the data ensemble. Moreover, the ensemble length is not fixed and can vary according to the actual temporal variation of the flow at a specific spatial position. The actual frame rate of the sequence is given by

$$\text{fps} = \frac{f_{prf}}{N + 1} \quad (5.1)$$

where  $f_{prf}$  is the pulse repetition frequency, typically in the order of 10 kHz and the +1 comes from the interleaved B-mode emission. Although a high frame rate can be obtained, the challenge with this sequence is the trade-off between increasing the field-of-view (through a higher number of  $N$ ) while ensuring that the aliasing limit is not exceeded in the velocity estimates.

## 5.4 Data acquisition & processing

### 5.4.1 Beamforming

For each flow transmit event, a total of five lines were beamformed according to the principles of 3-D TO detailed in (Pihl and J. A. Jensen 2014; Pihl, Stuart, Tomov,

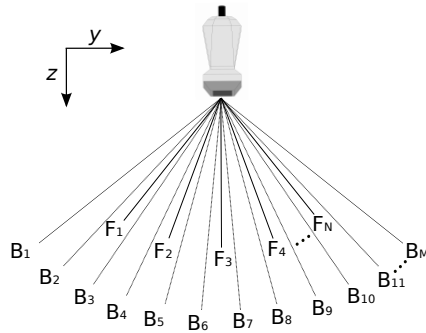


**Figure 5.1:** Illustration of the required flow lines  $F$  and B-mode emissions  $B$  needed for creating a color flow map. Depending of the order of the various transmit events, the sequence can be designed to acquire continuous data as described in 5.3. The spanned angles are only for illustrative purpose and not to scale. Obtained from (Holbek et al. 2016)

Rasmussen, et al. 2014) and Section 3.3.3. However, two different receive apodization profiles were used in this work, resulting in two rect profiles spanning respectively 8 and 10 elements, with a spacing of 24 elements for  $d_y$  and 22 elements for  $d_x$ . The shorter distance between the apodization peaks in  $x$  than in  $y$ , translated to a larger wavelength,  $\lambda_x$ , and thereby an increased velocity range for the  $v_x$  velocity component (see eq. 3.1). This is beneficial given the fact that the largest velocity magnitudes were expected to be along the  $x$ -axis, due to the orientation of the transducer.

### 5.4.2 Echo cancelling

As earlier mentioned, the presence of continuous data offers some new opportunities regarding removal of echoes from stationary tissue. In fact, we experienced that the usual preferred echo cancelling algorithms, the mean subtracting method and the linear regression fit (Hoeks et al. 1991), performed impeccably, more or less, for all our phantom setups. Even for *in vivo* measurements, reliable estimates were obtained at every other time instance than during the peak systole. The reason for this has its roots in the rapidly changing environment during peak systole, which includes both a significant vessel movement and a large temporal change in the flow magnitude. However, before the applied echo cancelling algorithm is explained, it is worth digging into the reasons for removing signals originating from surrounding tissue before further processing.

The point spread function (PSF) in an ultrasonic setup will always contain some sidelobes, which can be of different shapes and magnitudes. This means, that when we beamform a point in the middle of a vessel ( illustrated in Fig. 5.2), it is composed of the scattering echoes from small blood cells, the surrounding vessel wall, and noise. As we approach the vessel boundary, the relative difference in signal amplitude between back

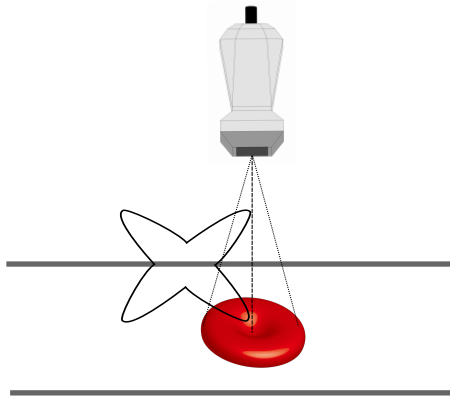


**Figure 5.2:** Sidelobes from the vessel walls affect the beamformed blood signal inside the vessel and require stationary echo cancelling before further processing.

scattered echoes from the vessel wall and the back scattering from blood cells and noise increases significantly.

As tissue echoes are 40-60 dB larger than the received signal from blood cells, it is crucial to clean the signal by removing contribution from tissue echoes before feeding it to the velocity estimator. This means, that even sidelobes levels  $-40$  dB at the center of the vessel are similar in amplitude to the blood signal or even higher. When no or very little tissue movement is present, stationary echo cancelling can easily be performed. Even though the tissue signal is very strong, the Fourier frequency domain at a fixed spatial position throughout time will reveal that only the DC component needs to be filtered (Fig. 5.3 top row).

When tissue movement is present, the frequency spectrum related to the tissue movement will broaden and the mean frequency will shift according to the displacement (Fig. 5.3 middle row). Subtraction of the mean signal in the time domain will only suppress tissue signal significantly at certain time instances and performing a linear regression of the movement and subtracting this from the signal will also provide similar results, when the acceleration gets too large. Yet another approach could be proposed, when defining a cut-off amplitude threshold in the frequency domain for which the influenced frequency components exceeding this value are set to 0 (Fig. 5.3 bottom row). If correctly defined, this effectively suppresses the strongest frequency components from the tissue movement. After the cut-off is applied, the inverse Fourier transformation is applied to the signal, serving as input to the velocity estimator. If a short ensemble length is present, as for a conventional emission sequence, the Fourier space needs to be represented by only 8-16 bins. It is therefore very likely that some bins will contain frequency information from both tissue, blood, and noise components. Having access to a larger ensemble length, as

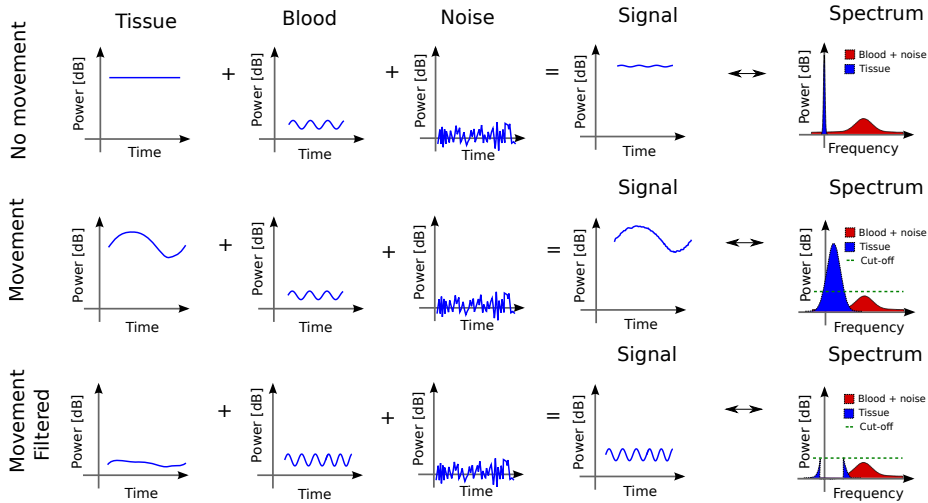


**Figure 5.3:** Illustration of the influence on the time varying signal and the Fourier space with and without tissue movement. When no tissue movement is present (upper row), the DC component in the Fourier frequency domain is related to the tissue movement and can easily be filtered with simple echo cancelling algorithms. When tissue movement is present (middle row), the spectrum related to the tissue broadens and overlaps with the frequency components related to blood movement. Bottom row, reconstructed signal when movement is present after energy-based frequency cut-off has been applied.

is the case with continuous data, the Fourier space can contain all the desired frequency components.

In this study, for every single beamformed line, at every spatial position, a Fourier transformation was made from 256 samples in the temporal direction. Frequency amplitudes above the specified threshold were put to zero and the inverse transformation was made afterwards. The filtered signal now contained 256 temporal data points from which an ensemble of the middle 16 data points were taken out and used to estimate the phase shift. This provided a good knowledge of present movement and future movement. Whenever data from a new emission was acquired, the ensemble was updated after a first-in-first-out procedure, meaning that the oldest of the 256 temporal data points was replaced by the newest and the sub sample taken out for the velocity estimator would, similarly, replace the oldest data point with the latest.

The applied echo cancelling algorithm relies on the work presented in (Villagomez-Hoyos 2016) and can be further improved, e.g. by introducing an adaptive threshold cut-off value.

### 5.4.3 Velocity estimator

The beamformed and echo-cancelled data were fed to the TO phase shift estimator as described in Chapter 3. With a continuous data acquisition sequence consisting of  $N$  flow emissions, a pulse repetition frequency of  $f_{prf}$ , and the two lateral wavelengths  $\lambda_x$  and  $\lambda_y$ , the maximum detectable velocities are

$$\begin{aligned} v_{x_{max}} &= \frac{\lambda_x}{4k} \frac{f_{prf}}{N+1} \\ v_{y_{max}} &= \frac{\lambda_y}{4k} \frac{f_{prf}}{N+1}, \end{aligned} \quad (5.2)$$

where  $k$  is the integer lag values used in the autocorrelation.

### 5.4.4 Phase shifting

The TO method is a phase shift estimator, which uses a four-quadrant inverse tangent operation in the calculations. Thus, there exists a limitation on the maximum detectable velocity, since the phase range spans from  $[-\pi : \pi]$ , which translates to  $[-v_{max} : v_{max}]$ , see Fig 5.4. Due to circular behavior of the operator, an angle of  $\pi + \delta\theta$  will correspond to  $-\pi + \delta\theta$ , which translates to a velocity estimate of  $v_{max} + \delta v$  will appear as  $-v_{max} + \delta v$ . This effect is denoted as aliasing. In computational science, the four-quadrant inverse tangent function is often denoted `atan2`.

This phase range can be shifted with a maximum of  $\pi$  in each direction. where it is most useful to increase the maximally detectable velocity without reaching the aliasing limit (J. A. Jensen 1996). In this study, the phase range was shifted by  $\pi/2$  to be at  $[-\frac{\pi}{2} ; \frac{3\pi}{2}]$ , this translates to a detectable velocity range of  $[-\frac{1}{2}v_{max} : \frac{3}{2}v_{max}]$  to match the expected velocities. A theoretical example of applying a  $\pi/2$  phase shift to avoid aliasing in the estimates is seen in Fig 5.4.

The phase shifting can be a maximum of  $\pi$  in either direction, which theoretically allows for a velocity range of  $[-2v_{max} : 2v_{max}]$ , if the shifting is made adaptively to match the initial flow conditions. Furthermore, the method could be extended to provide the proper phase shift at a given spatial position. Such an algorithm could map very complex flow at large velocities in e.g. stenotic regions or in the heart.

### 5.4.5 Angle estimation

The processed data provides the velocity components  $v_x, v_y$  and  $v_z$  along each steered direction. Hence, the direction of the flow, given by the angles  $\alpha$  and  $\beta$ , can be determined as

$$\alpha = \sin^{-1} \frac{v_z}{|\mathbf{v}|} \quad (5.3)$$

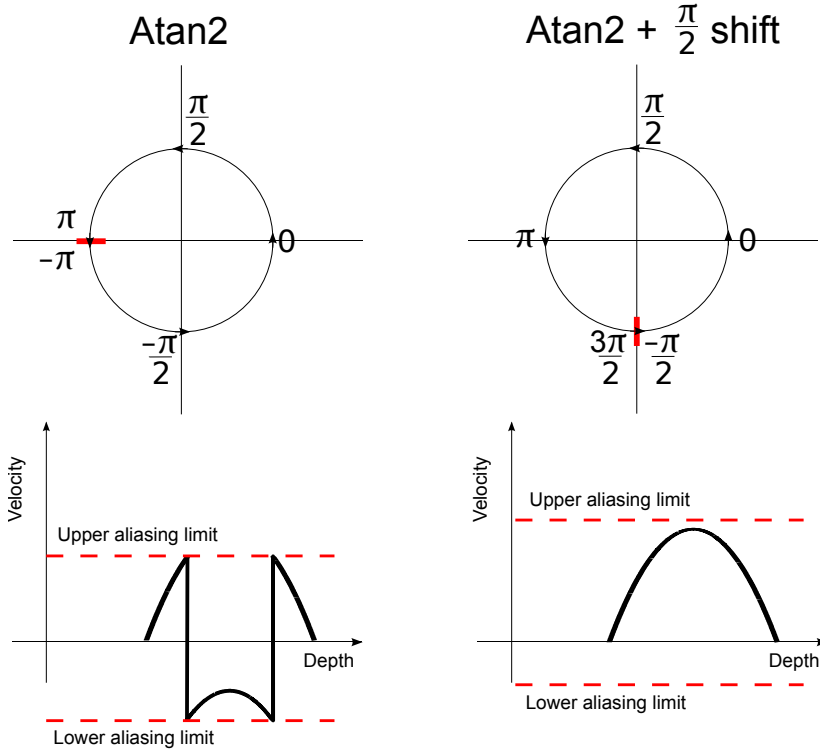


**Figure 5.4:** Upper row: Illustration of the `atan2` function (left) and `atan2` with a  $\pi/2$  phase shift (right). Bottom row: Example of aliasing, due to the position of the phase range (left), and the same velocity estimate when a  $\pi/2$  phase shift is applied, which shift the aliasing limit upwards to match the present velocities.

$$\beta = \arctan \frac{v_y/|\mathbf{v}|}{v_x/|\mathbf{v}|} = \arctan \frac{v_y}{v_x}, \quad (5.4)$$

where  $|\mathbf{v}|$  is the magnitude of the velocity,  $\alpha$  is the rotation around the  $y$ -axis and  $\beta$  the rotation around the  $z$ -axis, see Fig. 5.5. The estimated angles are used to estimate the direction of the flow in the *in vivo* measurement.

#### 5.4.6 Flow rate estimation

The instantaneous volumetric flow rate  $Q(t)$  is defined as

$$Q(t) = \sum_i A_i v_i(t), \quad (5.5)$$

where the cross-section of the blood vessel is divided into small areas of size  $A_i$  each with a velocity component  $v_i(t)$ , propagating perpendicularly to  $A_i$ . In this work, the index value  $i$  for the velocity component was replaced by the pixel values in  $(x_j, y_k)$  and the cross-sectional area  $A$  was the metric area of a pixel size which was constant. The flow rates at each pixel were calculated by multiplying the scan converted out-of-plane velocity component  $v_x(x_j, y_k)$  with the corresponding pixel value for the drawn mask  $M(x_j, y_k)$  and the cross-sectional area  $A$ . Mask values were either 0 or 1 and constant in time. The flow rate at time  $t$  was then

$$Q(t) = \sum_j \sum_k A v_x(x_j, y_k, t) M(x_j, y_k), \quad (5.6)$$

where the summation ran over all the  $j \times k$  pixels in the image.

In the experimental setup, flow rates were estimated based on a beamformed B-mode volume where the plane parallel to the flow transmissions was taken out for further processing. The B-mode image was used for manually delineating a mask of the cross sectional vessel. Only flow within this mask was examined in the further processing. After the delineation mask was drawn, the flow was processed, scan converted, interpolated and the mask was multiplied onto the final estimates. Within this mask, the flow rates, based on the velocity component perpendicular to the plane was calculated as a function of time.

## 5.5 Experimental setup

### 5.5.1 Equipment

The following describes the equipment used for the experimental and clinical scans

#### SARUS

The Synthetic Aperture Real-time Ultrasound System (SARUS) (J. A. Jensen, Holten-Lund, et al. 2013) is used for all experimental and clinical scans. The scanner is a 12 bit system capable of sampling raw RF data at a sampling frequency of 70 MHz from 1024 channels on 64 boards each with 2 GB of RAM.

#### 2-D MATRIX PROBE

A 3.5 MHz  $32 \times 32$  element 2-D phased array matrix probe with pitch = 0.3 mm (Vermon S. A., Tours, France) was connected to SARUS and used for the experiment. As a consequence of manufacturing issues, the actual physical dimensions of the probe was  $35 \times 32$ , where three rows positioned at row 9, 18, 27 in the largest dimension did not contain any elements.

### BK 5000 SCANNER

A commercial scanner (BK 5000, BK Ultrasound, Herlev, Denmark) and a linear 5.2 MHz probe (9032, BK Ultrasound, Herlev, Denmark), is used for reference measurements prior to experimental *in vivo* ultrasound measurements and the MRI measurement.

### FLOW-RIG SYSTEM

The flow-rig is an in-house built system used to validate velocity estimates in a steady laminar flow. The flow-rig contains a long inlet of 1.2 m, ensuring a steady laminar parabolic flow profile at the measuring site. Blood mimicking fluid is driven inside the vessel by a centrifugal pump in a closed loop circuit. At the measuring site, the rubber vessel ( $\varnothing = 12$  mm) is immersed into a water tank containing demineralized water. The volume flow  $Q$ , is measured with a MAG 1100 flow meter (Danfoss, Hasselager, Denmark), which, due to the assumption of a present laminar parabolic flow, can be translated to a peak velocity  $v_0$  via the relation  $v_0 = Q/(\pi R^2)$ , with  $R$  being the radius of the vessel. The expected velocity profile can then be calculated as  $v(r) = (1 - \frac{r^2}{R^2})v_0$ , where  $r$  is the distance from the center of the vessel.

### PULSATING FLOW PUMP SYSTEM

A second flow system (CompuFlow 1000, Shelley Medical Imaging Technologies, Toronto, Canada) is used to generate a pre-defined time-varying carotid flow waveform with user defined waveform, pulse duration, and flow rate. The manufacturer specified flow rate accuracy of the system is  $\pm 3\%$ . The flow pump is connected to a customized tissue mimicking phantom (Dansk Fantom Service, Frederiksund, Denmark), containing a straight-vessel ( $\varnothing = 8$  mm).

## 5.5.2 Measurement setup

For all measurements, the aim was to orient the transducer in such a way that a  $90^\circ$  beam-to-flow angle was obtained. This orientation could be obtained with certainty in the experimental setups, whereas for the *in vivo* measurements, the actual beam-to-flow angle was unknown until the data were processed. An illustration of the ideal measurement setup is shown in Fig. 5.5.

## 5.6 Measurements

In the following measurements, an interleaved continuous data acquisition sequence with  $M = 36$  and  $N = 10$  was designed. The 10 flow lines were steered from  $-15^\circ$  to  $15^\circ$  in steps of  $3.3^\circ$  with the focal point placed at 35 mm depth. The 36 B-mode emissions with virtual point sources placed at different locations behind the array, were applied to generate a  $60^\circ \times 60^\circ$  field-of-view volume using synthetic aperture imaging techniques. An ensemble length  $e$  of 16 for each velocity estimate was applied in the processing. The

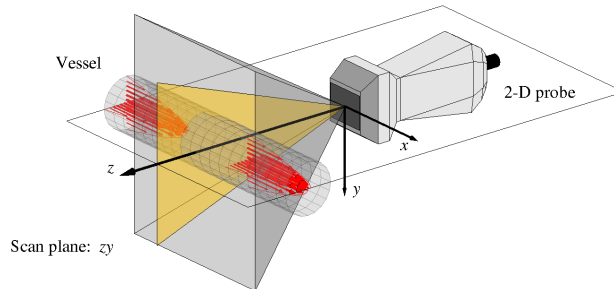


**Figure 5.5:** Ideal measurement setup, where the transducer is oriented to yield a  $90^\circ$  beam-to-flow angle. Flow data (yellow plane) are only obtained for the  $zy$ -plane, whereas B-mode (gray box) is present in a symmetric volume. Obtained from (Holbek et al. 2016).

processing and setup in the following described measurements were all the similar, unless otherwise stated.

### 5.6.1 Straight vessel steady flow measurements

At a  $90^\circ$  beam-to-flow angle, the transducer was oriented to acquire 3-D vector flow in a cross sectional scan plane, at a distance of 2.6 cm from transducer surface to the vessel center. A  $f_{prf}$  of 5 kHz and  $\pi/2$  phase shift, as described in 5.4.4, was used to match the expected velocity range.

#### RESULTS

A total of 15.8 seconds of data were acquired and processed. A manual segmentation of the vessel was made based on a B-mode image, where the delineated area was  $114 \text{ mm}^2$ , compared with the theoretical  $113 \text{ mm}^2$ . Flow rates within the delineated area was calculated at every time instance. Due to an ensemble length of 16, the temporal flow rate estimates were divided into sections of similar size, and the mean from each section was calculated. The standard deviation was calculated from the mean of all the sections. This gave an estimated flow rate of  $82.1 \pm 2.8 \text{ L h}^{-1}$  compared with the expected  $79.80 \text{ L h}^{-1}$ .

### 5.6.2 Straight vessel pulsating flow measurements

With the included CompuFlow 1000 System software, a carotid flow profile was generated with a cycle time of 0.84 s and a flow rate of  $2.57 \pm 0.08 \text{ mL/stroke} \pm 3\%$  as specified by the manufacturer.

An automated algorithm was developed to estimate the number of samples between each cycle. The basic step of the algorithm is to perform the autocorrelation on any input

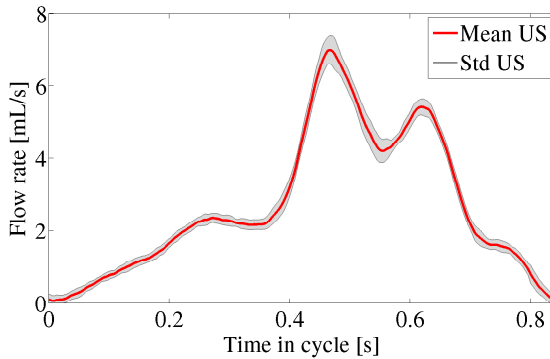


**Figure 5.6:** Mean cycle flow rate (red curve)  $\pm$  one standard deviation (grey area) estimated from 22 coherently aligned flow rate estimates.

signal which is expected to have a cyclic behavior, in our case, the estimated temporal flow rate. The distance between the two highest peaks from the autocorrelation is then expected to be the average number of samples between each new heart cycle. This routine is used both for the pulsating flow measurement and the *in vivo* measurement.

## RESULTS

A total of 18.9 seconds of data were acquired, and data processing was performed similarly to the flow-rig measurement. The automatic cycle-time algorithm estimated was 838 ms, which translates to 382 velocity estimates per cycle and 22 cycles in total. This was in agreement with the software specified true cycle time of 840 ms.

The data set was divided into 22 cycles which were coherently aligned. From the coherently alignment the mean cycle flow rate was estimated to  $2.68 \pm 0.04$  mL/stroke compared with the  $2.57 \pm 0.08$  mL/stroke specified by the pump settings, Fig. 5.6. A temporal waveform produced by the pump was accessible, but due to the long inlet, effectively acting as a low pass filter, the pump specified profile was not used as reference. The delineated vessel area was  $48.4 \text{ mm}^2$  compared with the expected area of  $50.3 \text{ mm}^2$  calculated from the specified vessel radius.

### 5.6.3 *In vivo*

Prior to the *in vivo* scans, intensity measurements were performed to ensure compliance with current FDA intensity regulations (FDA 2008). Intensity measurements were performed in accordance to the procedure described by Jensen 2016, (J. A. Jensen, Rasmussen, et al. 2016), which gave a derated mechanical index (MI) of 1.14 and an  $I_{spta.3} = 439 \text{ mW cm}^{-2}$ , when the system pulse repetition frequency  $f_{prf}$  was scaled to 12.6 kHz.

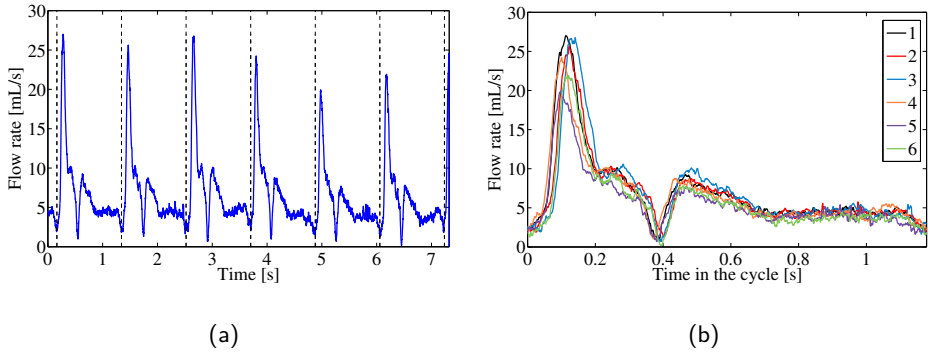


**Figure 5.7:** (a) Estimated flow rates (blue curve) with the applied heart cycle division (dotted lines). (b) Estimated flow rates of the coherently aligned heart cycles.

Both values complied with the FDA limits. At this  $f_{prf}$ , the temporal resolution of the velocity estimates were 14 ms.

The *in vivo* measurement was performed on a healthy 27-year old male. To ensure steady physiological flow conditions, the volunteer had been resting for 15 min before the measurements were conducted. The scan was performed by an experienced radiologist.

A  $\pi/2$  phase-shift was applied in the post processing to provide a detectable velocity range of  $[-45 ; 137]$   $\text{cm s}^{-1}$  at 2 cm depth, for the velocity component orthogonal to image plane. The cross sectional measurements were conducted 2-3 cm before the bifurcation in the common carotid artery.

## RESULTS

A total of 7.5 seconds of data were recorded in this scan. Given the fact, that no ECG gating was applied in this measurement and no reference heart rate was monitored, the automatic heart rate detection algorithm was applied on the time varying flow rate estimates. The average heart rate was estimated to be 50.9 beats per minute or 0.849 s/cycle, translating to 1350 estimates per cycle. The temporal flow rates could, thus, be divided into six complete heart cycles as shown in Fig. 5.7(a). Due to the short acquisition time, it was expected that the temporal flow rates during each cycle could be coherently aligned. Alignment of the flow rates are shown in Fig. 5.7(b).

It is seen that the flow rates from each cycle are not completely aligned, especially during the early systole. The temporal difference across all six cycles are, however, on a very small time scale of 20–30 ms. The average flow rate was  $6.5 \pm 0.6$  mL/cycle which translates to  $333 \pm 30$   $\text{mL min}^{-1}$ . The maximum peak systolic velocity magnitude, derived from the 3-D estimates for each cycle was  $99 \pm 3$   $\text{cm s}^{-1}$  compared with a value of

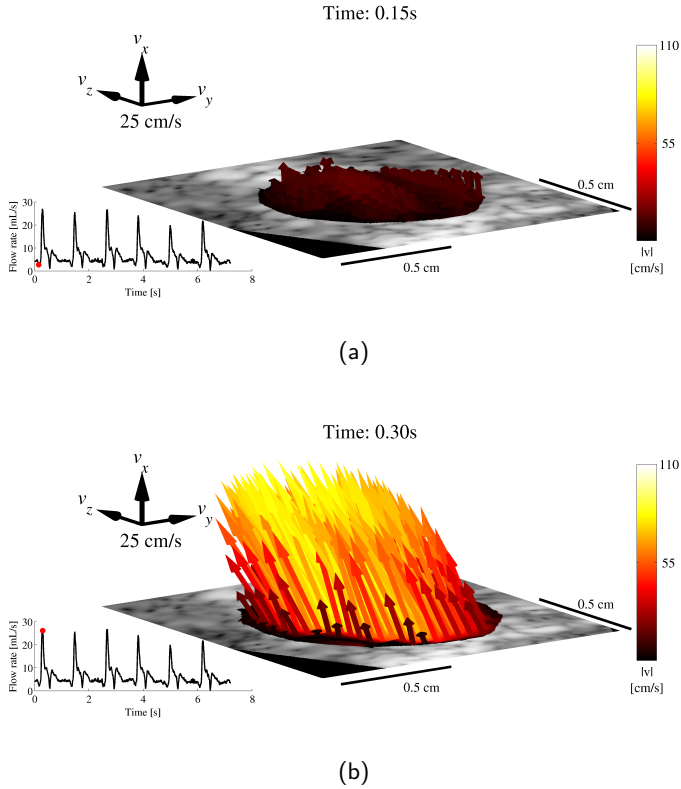


**Figure 5.8:** 3-D vector flow from the common carotid artery during the end-diastole a) and during peak-systole b). The colored arrows depict the direction of the flow and its magnitude. The velocity arrows are plotted on top of a B-mode image and only values within the delineated mask are shown. The bottom-left graph shows the flow rate at the time instance in the heart cycle indicated by the red dot. The scan was not conducted exactly cross-sectional to the vessel, which is revealed by the flow direction in b). Obtained from (Holbek et al. 2016).

$107 \pm 2 \text{ cm s}^{-1}$  obtained with 1-D spectral Doppler techniques prior to the measurement.

A 3-D vector representation of the cross sectional blood flow could also be constructed, based on the present data. Such an illustration is seen in Fig. 5.8, where both the flow during the end-diastole and peak-systole is displayed. The peak-systolic image reveals that the scan was not conducted exactly in a cross-sectional scan plane of the vessel, as the majority of the arrows have at least two non-zero velocity components. The

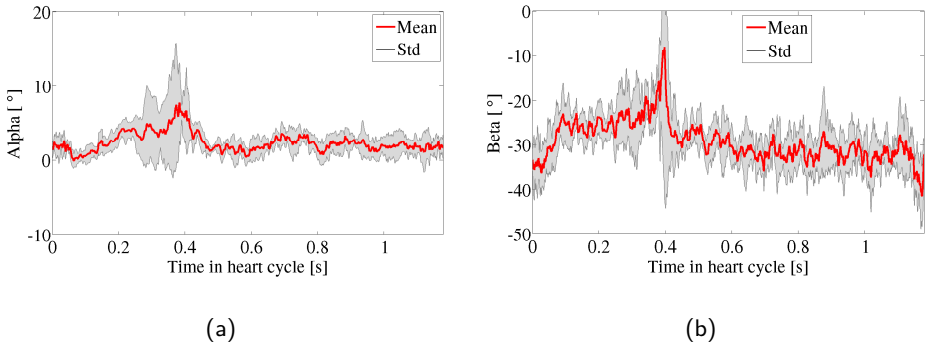


**Figure 5.9:** Estimated mean *in vivo* beam-to-flow angle  $\alpha$  and b) estimated mean flow direction  $\beta$ . Obtained from (Holbek et al. 2016).

actual direction of the blood flow movement could be estimated from the three velocity components as described in 5.4.5. The angles  $\alpha$  and  $\beta$  were calculated at every time instance in the heart cycle for all six cycles and subsequently coherently aligned, see Fig. 5.9. The largest deviation in  $\alpha$  was found during peak-systole and the early diastole. Similarly, the largest deviation in  $\beta$  was found at the early diastole. A flow entirely perpendicular to the scan plane (i.e. a  $90^\circ$  beam-to-flow angle) would result in  $\alpha = 0^\circ$  and  $\beta = 0^\circ$ . In this measurement, the mean precession values were  $\alpha = 2.4^\circ \pm 0.9^\circ$  and  $\beta = -29.1^\circ \pm 0.8^\circ$ , which were in accordance with the observations made from Fig. 5.8.

## 5.7 Comparison to MRI

Currently, MRI is often referred to as the golden standard for accurate non-invasive blood velocity estimation. Therefore, a comparison between the results obtained with US were made with similar quantities obtained with through-plane MRI blood flow estimates. A total of three ECG gated through-plane MRI measurements of the right common carotid artery were performed on the day before the experimental US measurements. Each measurement consisted of data retrieved from 210 heart beats. Prior to both the MRI scan and the US scan, a 1-D spectral Doppler measurement was performed with a commercial scanner as a reference. The materials used, the sequence specifications, and the applied method for data processing, are all described in details in the paper (Holbek et al. 2016).

### RESULTS

Data from the three measurements were processed to yield temporal peak velocities and flow rates based on the out-of-plane velocity component and the vessel area. The results

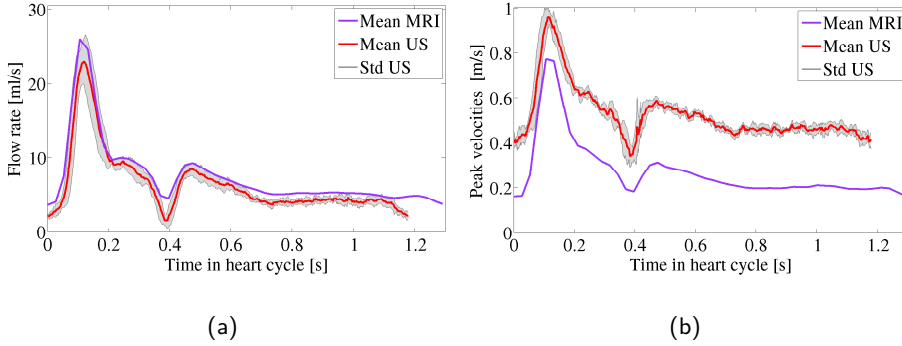


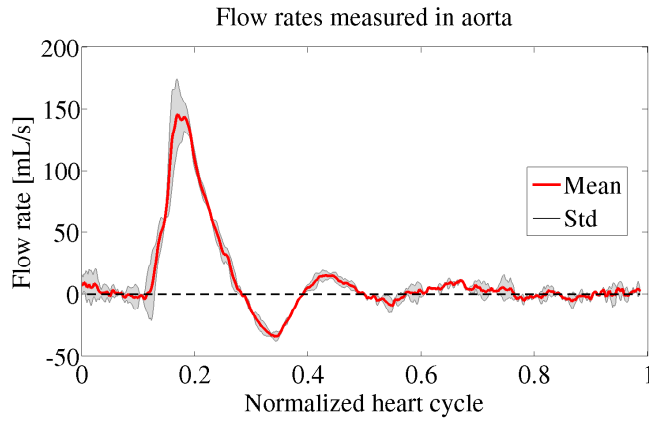
**Figure 5.10:** left: Mean volumetric flow rate throughout a heart cycle seen with MRI (purple curve) and US (red curve  $\pm$  one standard deviation). right) Peak through-plane velocities seen with MRI (purple curve) and US (red curve  $\pm$  one standard deviation). Obtained from (Holbek et al. 2016).

are presented in Fig. 5.10, together with the mean values obtained from the six heart cycles with US and their standard deviation. The peak velocity estimated with MRI was  $77 \pm 1 \text{ cm s}^{-1}$ . Spectral Doppler measurement obtained prior to the MRI scan was  $101 \pm 1 \text{ cm s}^{-1}$ , and  $107 \pm 2 \text{ cm s}^{-1}$  prior to US measurements. The mean flow rate was  $7.44 \pm 0.04 \text{ mL/stroke}$ . One heart cycle lasted 1.29 s, which translates to a flow rate of  $346 \text{ mL min}^{-1}$ . Similarly, for US, the heart cycle lasted 1.17 s, translating to  $333 \text{ mL min}^{-1}$ , which is 3.9% lower than that of MRI.

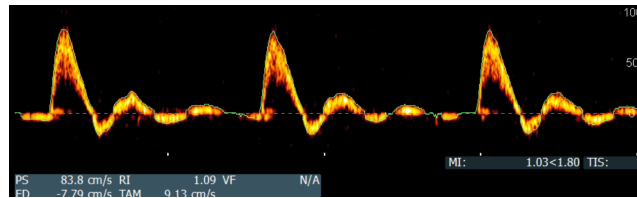
## 5.8 Additional applications

Application of the method in other vessels than the common carotid artery was explored by measuring in the abdominal aorta of a 30-year-old healthy volunteer. Due to the depth of the vessel and its dimensions ( $\varnothing = 2 \text{ cm}$ ), a larger sampling depth was required and the 10 flow directions were steered in a  $36^\circ$  field-of-view. Prior to the measurement, a spectral Doppler of the abdominal aorta was made with the commercial BK 5000 scanner. A total of 3.4 s of data were acquired, corresponding to 2 full heart cycles. The estimated flow rates with the 3-D method and the spectral Doppler velocities are shown in Fig. 5.11.

A peak flow rate of  $146 \text{ mL s}^{-1}$  or  $8.7 \text{ L min}^{-1}$  was found, whereas the largest retrograde flow was estimated to  $-34 \text{ mL s}^{-1}$  corresponding to  $2.0 \text{ L min}^{-1}$  in the diastolic phase. Mean flow rate during the cycle was  $11.0 \pm 0.3 \text{ mL/stroke}$ . The profile of the estimated flow rates was qualitatively in good agreement with the velocity profile obtained from spectral Doppler, but further validation is required.



(a)



(b)

**Figure 5.11:** (a) Estimated mean flow rates during a cycle in the abdominal aorta. The mean and standard deviations are found from two full heart cycles. (b). Spectral Doppler velocity estimates of the abdominal aorta obtained with a commercial scanner.

## 5.9 Conclusion and perspectives

The purpose of this study was to introduce an accurate method for high frame rate 3-D VFI using TO. The method should provide angle independent peak velocities and flow rate estimates, and preferably, yield similar results as the current golden standard MRI.

In this study, we gradually increased the complexity of the flow, starting with laminar parabolic flow in a flow-rig and ending with *in vivo* measurements of the common carotid artery. Results from the flow-rig and the pulsating flow showed a high precision and accuracy, indicating, that the method provided robust and reliable velocity estimates. *In vivo* results demonstrated the advantage of 3-D vector flow, since angle independent peak

velocities, similar to those derived from 1-D spectral Doppler, were obtained. Flow rates derived from six heart cycles had a precision of 9.1 % which was much higher than the 0.5 % for MRI. However, the acquisition time for all the MRI measurements were  $3 \times 210$  heart cycles  $\approx 14$  minutes. The measured flow rates between US and MRI only deviated 3.9 % when translating to  $\text{mL min}^{-1}$ . Whether any of the methods were overestimating or underestimating in the *in vivo* measurements cannot be concluded, since a ground truth could not be obtained, and measurements were conducted one day apart. However, the similarity of the two flow rate curves and peak velocities in Fig. 5.10 seems very high.

Based on the presented results, it can be concluded that 3-D VFI using TO can provide precise flow rates, comparable to similar quantities derived with through-plane MRI. The proposed method comes with several advantages compared with MRI: it has a much higher temporal and spatial resolution, ECG gating is not a necessity which eases measurements on patients with irregular heart rhythms, allowing for analysis of the instantaneous flow.

Compared with 1-D Doppler techniques and 2-D VFI methods, the proposed 3-D method eliminates several operator decisions and mathematical assumptions about geometry and flow angles, which otherwise lead to erroneous estimates of flow rates and peak velocities (J. Jensen et al. 2016).

One issue that needs to be addressed before the 3-D VFI technique can be implemented on a commercial setup is the heating of the probe. At a very high  $f_{prf}$ , almost the full aperture of the 2-D array is put into motion, resulting in an increased surface temperature due to e.g. the dissipation of kinetic energy into thermal energy. Although the measured thermal index (TI) of the sequence used for *in vivo* measurements was within current FDA limits for the actual scan duration, it will be more problematic to stay within the regulations during a clinical examination on the order of 5-15 minutes.

### 5.9.1 Perspective

The *in vivo* sequence provided a very high frame rate of 1145 fps and a temporal resolution of 14 ms per independent velocity estimate, offering new opportunities for studying the 3-D blood flow dynamics. Although not investigated, the high temporal resolution should be sufficient to capture the motion of short-lived vortices and rotations in 3-D, that are reported to have a lifetime of approximately 100-200 ms (Evans, J. A. Jensen, and Nielsen 2011). As the flow turbulence in 2-D has been shown to correlate with the degree of stenosis in the aortic heart valve (K. Hansen et al. 2016), what extra information could 3-D flow provide? With access to turbulence estimates in 3-D, new pathology screening methods might develop and the impact of an intervention can be monitored non-invasive.

Also, another non-invasive method, currently only available for experimental use, is pressure gradients derived from VFI data. Currently, *in vivo* pressure gradients have been derived from 2-D vector flow obtained with a synthetic aperture technique (Olesen et al. 2015). The method assumes that the out-of-plane velocity component is neglectable; this is only valid to a certain degree. With 3-D vector flow present, this assumption can be

excluded, and an improved basis for non-invasive pressure gradient estimation may be achievable.

The presented method still needs to overcome some challenges before a real-time 3-D TO vector flow with a matrix array can be implemented on a commercial scanner. For instance, the large number of elements and connections results in a large and heavy cable and is a computational expensive task. The next chapter presents a study, which tries to address some of these issue through introducing a 2-D row-column addressed array with only  $62+62$  elements.



# CHAPTER 6

## Row-Column 3-D Vector Flow

---

**Summary** *The previous chapter demonstrated, that 3-D vector flow could be achieved with a 2-D matrix array containing 1024 active channels. In this chapter, a similar 3-D TO method is implemented on a 2-D row-column (RC) addressed prototype array containing only 124 elements. It is investigated both through simulations and via experimental setups in various flow conditions, if this significant reduction in the element count can still provide precise and robust 3-D vector flow estimates in a plane. The chapter explores and discusses the gained advantages compared with the 2-D matrix array as well as the inherent challenges that come with the RC addressed arrays.*

### 6.1 Purpose

Since the idea of row-column (RC) addressed arrays was introduced, the main focus has been on its imaging properties (Chee et al. 2014; Sampaleanu et al. 2014; Christiansen et al. 2015) without exploring the potential of estimating blood flow. However, if the RC array technology it to be a valid candidate for clinical usage in the future, a complete solution with both B-mode imaging and flow estimation should be fully implemented. The purpose of this chapter is therefore to demonstrate the feasibility of implementing 3-D vector flow on an RC array using a modified version of the 3-D TO method. Furthermore, the purpose of this chapter is to identify the limitations of the RC array and discuss possible solutions. Lastly, the presented work should demonstrate that precise velocity estimates can be obtained with only 62+62 active elements, which is a significant reduction compared with a fully populated matrix array. The chapter is based on Paper A, I, V, VI, and VII.

### 6.2 Background

Previous literature on flow estimation using an RC array is very sparse, and only one other approach by Flesch *et al.* 2015 (unpublished) presented at the IEEE symposium has been reported. In their work, a  $32 \times 32$  matrix array was emulated to effectively work as a  $32+32$  RC addressing array and used to estimate volumetric Doppler images *in vivo*.

Implementation of the 3-D vector flow estimator on an RC array is a further development of the original TO method proposed by J. A. Jensen and Munk (Jensen and Munk 1998; Jensen 2001) and described in Chapter 3, as well as the experimental implementation demonstrated in the previous Chapter 5.

Two RC arrays with similar technological properties and geometries were applied throughout this study: A piezo version and a CMUT. As default, the piezo transducer was used for the measurements if nothing else is stated.

### 6.3 TO on an RC array

The basic principles of 3-D TO method, as described in Chapter 3 and applied in Chapter 5, can be implemented on an RC array with some modifications. As previously mentioned, a total of five beamformed lines are needed to estimate 3-D vector flow along a line with TO. With a 2-D matrix probe, all five lines can be beamformed from one transmit event, since electrical delays can be applied to generate a focal point and two-way focusing is possible. However, since only focal lines can be generated from focused transmit events with RC arrays and only one-way focusing is possible, two distinct transmit events are necessary for beamforming the required five lines, see Fig. 6.1. From each transmit event three lines are beamformed. Two of the lines,  $TO_{left}$  and  $TO_{right}$ , are used to estimate the velocity component perpendicular to the tallest dimension of the receiving elements using the TO method. The third line,  $r_{center}$ , is used to estimate the axial velocity with the conventional autocorrelation method. By combining the estimated transverse velocity components, one from each transmit event, with one of the two independent axial estimates, a 3-D velocity vector along the direction of the respective beamformed centerline can be achieved.

This interleaved setup was implemented in both the applied M-mode sequence and a steered sequence.

#### 6.3.1 RC beamforming

Conventional delay-and-sum beamforming assumes that the geometry of transmitting and receiving elements are point sources emitting spherical waves. However, the emitted wavefront from a single RC element is shaped as a cylindrical surface, where it can be viewed as a circle arc in a plane orthogonal to the long dimension and as a plane wave in the plane orthogonal to the short dimension. Therefore, the point source approximation breaks down even for small RC arrays and leads to errors in the time-of-flight calculations. A better approximation treats the elements as line segments, which influences the time-of-flight calculations (Rasmussen et al. 2015).

For line segments, the time-of-flight is calculated as the shortest path between the transmitting element, the point  $\mathbf{p}$  and the receiving element divided by the speed of sound  $c$ . The shortest distance between the transmitting element and  $\mathbf{p}$  is the Euclidean distance between  $\mathbf{p}$  and  $\mathbf{t}$ , where  $\mathbf{t}$  is the projection of  $\mathbf{p}$  onto the transmitting line element. The same holds when finding the shortest distance from  $\mathbf{p}$  to the receiving element, where  $\mathbf{r}$  gives the shortest Euclidean distance, see Fig. 6.2.

At a closer examination of Fig. 6.2, it is seen that several points will have the same time-of-flight for the distances  $|\mathbf{p}-\mathbf{r}|$  and  $|\mathbf{p}-\mathbf{t}|$ , when investigating the case with one transmit

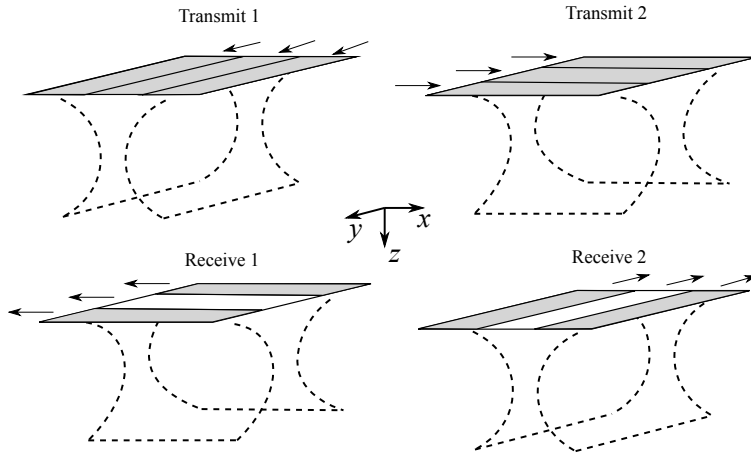


**Figure 6.1:** Illustration showing the transmit and receive principles of 3-D TO velocity estimation with an RC array. In one embodiment, two sequences are used: First, transmit focusing is performed in the  $x$ -dimension, and the transverse oscillation field is synthesized in the  $y$ -direction. This allows estimation of flow in the direction perpendicular to the tall dimension of the elements, i.e. the  $y$ -component of the velocity vector. Afterwards, the transmit/receive-sequence is flipped to allow estimation of the  $x$ -component of the velocity vector. The grey shaded areas are added to conceptually illustrate where a non-zero apodization is present. From Paper **A**.

and one receive element. The beamformed signal at this specific time-of-flight will therefore be the sum of the scattered signal from all of these points. When beamforming the signal for any other receive element  $r_n$ , multiple points will again have the same time-of-flight for the distances  $|\mathbf{p}-\mathbf{r}_n|$  and  $|\mathbf{p}-\mathbf{t}_l|$ . However these sets of points are different for every receive element, except the one located exactly at  $\mathbf{p}$ . When summing the beamformed signal from all of the receiving elements, it is expected that the scattered signal from surrounding unwanted points is suppressed whereas the contributions from  $\mathbf{p}$  are enhanced. In this project, where focused emissions are used, the effect should be enhanced even more.

The RC beamformer applied in this study is based on the reviewed principles and are thoroughly described in (Rasmussen et al. 2015).

## 6.4 Transmission sequence

### 6.4.1 M-mode

The M-mode sequence consisted of the two electronically focused emissions  $R$  and  $C$ . The sequence was used when 3-D vector flow estimates along one line were made. An

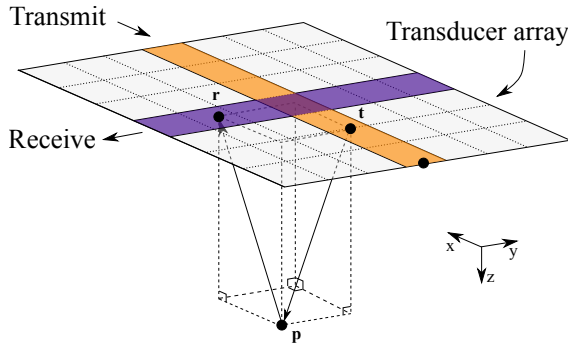


**Figure 6.2:** Estimation of time-of-flight using an RC beamformer. The shortest time-of-flight possible between the transmitting and receiving line elements going through the point  $\mathbf{p}$  originates from the point  $\mathbf{t}$  and ends at  $\mathbf{r}$ . Dividing the shortest path found by the speed of sound gives the time-of-flight used in the delay-and-sum beamformer. Modified from (Rasmussen et al. 2015).

illustration of the M-mode sequence is seen in Fig. 6.3. From the row emissions  $R$ , three of the five needed lines can be beamformed and the two velocity components  $v_x$  and  $v_z$  along the centerline can be derived. In the opposite scenario, with transmit on the columns  $C$  and receive on the rows, the  $v_y$  and  $v_z$  velocity components can be estimated. Thus, the applied emissions sequence is made by first transmitting on the rows and receiving on the columns and afterwards emitting with columns and receiving on the rows. The M-mode sequence was, thus, designed to alternately transmit the two emissions  $R$  and  $C$  in the following way.

$$R \rightarrow C \rightarrow R \rightarrow C \rightarrow R \dots$$

By combining the two transverse estimates found from each transmit event with an axial estimate, the 3-D vector velocities are found.

#### 6.4.2 Steered sequence

With a few modifications of the M-mode sequence in the transmit setup and in the data processing, 3-D vector flow in an entire plane could be obtained. This sequence consisted of one focused emission  $C_1$  using column elements and  $N$  focused emissions  $R_i$  using row elements, where  $i = 1 \dots N$ . Three-dimensional vector flow was, thus, estimated in points along the  $N$  steered directions in the  $zy$ -plane, see Fig. 6.4. From the row transmit event  $R_i$ , the  $v_{x_i}$  and  $v_{z_i}$  velocity components could be estimated in points along the direction of the respective beamformed centerline. However, the  $C_1$  column transmit

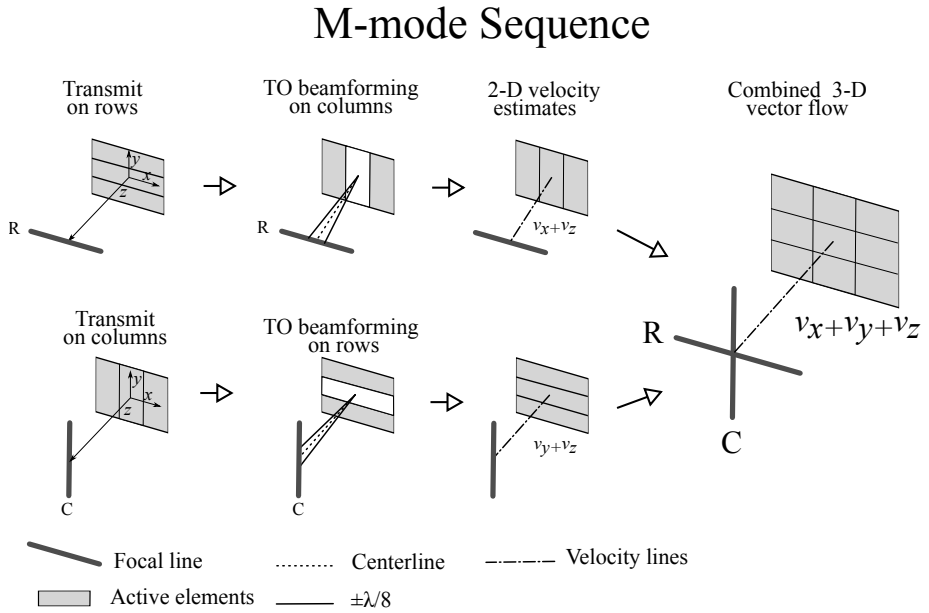


**Figure 6.3:** RC M-mode sequence for estimating 3-D vector flow along the direction where the focal lines are intersecting.

event provided the required data for beamforming the lines needed for estimating all  $v_{y_i}$  and  $v_{z_i}$  velocity components, as this transmit event sonifies the  $zy$ -scan plane. The steered transmit sequence used is schematically written as

$$\begin{array}{ccccccc}
 C_1 & \rightarrow & R_1 & \rightarrow & R_2 & \rightarrow & R_3 & \rightarrow & \dots & R_N \\
 C_1 & \rightarrow & R_1 & \rightarrow & R_2 & \rightarrow & R_3 & \rightarrow & \dots & R_N \\
 \vdots & & & & \vdots & & & & & \vdots
 \end{array}$$

Both the M-mode and the steered flow sequences yield continuous data, which means that the distance between each identical emission type is equally distributed in time for all time.

## Steered Sequence

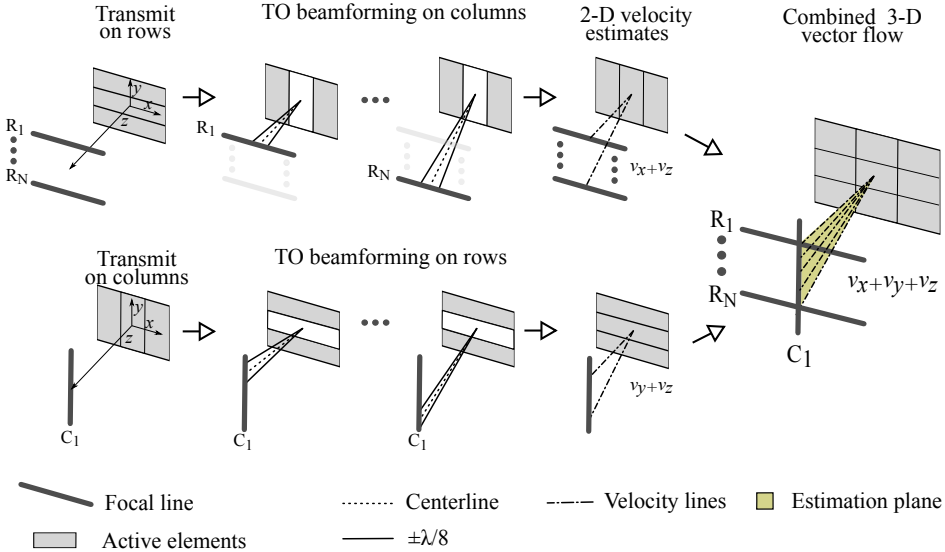


**Figure 6.4:** The steered RC sequence for obtaining 3-D vector flow using TO in a cross sectional plane is designed in the following way: first, after each column emission  $C_1$ , multiple steered row emissions  $R_N$  are emitted. From each row emission three lines are beamformed in accordance with the steering directions and  $v_x$  and  $v_z$  can be estimated along each direction. Second, from a single column emission  $C_1$ , three lines are beamformed along each steering direction yielding  $v_y$  and  $v_z$  velocity estimates along the  $N$  directions. 3-D vector flow is estimated in points along directions originating from the center of the aperture and through the intersection between the focal lines. The estimation plane is obtained when interpolating the combined 3-D vector flow estimates.

## 6.5 Parametric simulation study

A parametric simulation study was commenced to identify the optimal choice of parameters for 3-D vector flow estimation on an RC probe, and, equally important, when the estimator breaks down. Several parameters were varied, including: Flow direction, ensemble length, pulse length, transmit (Tx) and receive (Rx) apodization, steering angles, TO peak apodization spacing and the width of the TO peak. The selected parameters had an influence on the proposed method's angle independence, frame rate, intensity level, field-of-view, velocity range and accuracy. The parametric study was performed with the M-mode sequence and an overview of the parameter space, with the default values can be seen in Table 6.1.

**Table 6.1:** Variables in parameter study

Influencing	Parameter	Values
Angle independence	Beam-to-flow angle $\alpha$ [°]	<b>90</b> , 75, 60, 45
	Flow angle $\beta$ [°]	<b>0</b> , 15, 30, 45
Frame rate	Ensemble length $e$	4, 8, 16, <b>32</b> , 64
Intensity	Pulse length [cycles]	2,4, <b>6</b> ,8
Field-of-view	Steering angle $\theta_{zy}$ [°]	<b>0</b> , 5, ..., 40, 45
Velocity range	TO apo. width [no. of elements]	1, 5, ..., <b>25</b>
	TO apo. peak spacing [no. of elements]	25, 27, ..., <b>35</b>
Intensity	Transmit apo.	<b>Hann</b> , Tukey, Boxcar
Accuracy	Receive apo. (Axial)	<b>Hann</b> , Tukey, Boxcar
Accuracy	Receive apo. (TO)	<b>Hann</b> , Tukey, Boxcar

### 6.5.1 Environment

The ultrasound simulation program Field II (Jensen and Svendsen 1992; Jensen 1996) was used to simulate a 62+62 3 MHz 2-D RC array with  $\lambda/2$  pitch. A  $16 \times \text{pitch}$  roll-off apodization was simulated in continuation of each element to reduce ghost echoes produced from the tall active line elements (Rasmussen et al. 2015). A  $20 \times 20 \times 20 \text{ mm}^3$  cubic phantom containing a cylindrical blood vessel ( $\emptyset = 12 \text{ mm}$ ) located at 3 cm depth was defined for the simulations. Scatterers inside the cylinder were translated in accordance with a circular symmetric parabolic velocity profile. Scatterers outside the cylinder were considered stationary. The magnitude of the scattering amplitude was 40 dB higher for the stationary scatterers than for the moving blood cell mimicking scatterers. In total, 10 000 scatterers were distributed in the phantom to ensure that more than 10 scatterer per resolution cell were present. The peak velocity  $v_0$  in the parabolic flow was  $1 \text{ m s}^{-1}$  and propagation was in the x-direction as default. Rotation of the scatter phantom could be made around two axes; around the  $y$ -axis, denoted the beam-to-flow angle  $\alpha$  and rotation around the  $z$ -axis denoted  $\beta$  (see Fig. 6.5). In the default setup, no rotation was applied and a  $90^\circ$  beam-to-flow angle was present.

### 6.5.2 Performance evaluation

A statistical approach was used to quantify and compare the performance when estimating the 3-D vector flow for different settings. At each sample point  $z$  inside the vessel, the mean velocity  $\bar{v}(z)$  and the standard deviation  $\sigma(z)$  averaged over  $N$  frames for each

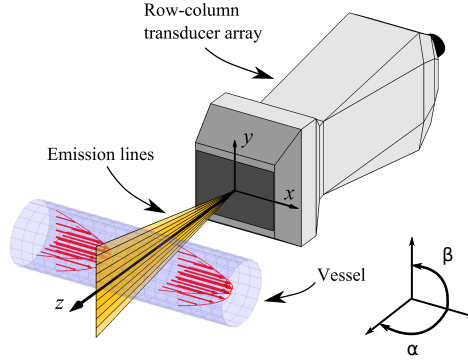


**Figure 6.5:** Simulation setup, where 3-D vector flow estimates can be obtained in an M-mode (along the  $z$ -direction) or along steered directions. The flow could be rotated around the  $y$ -axis and the  $z$ -axis, denoted  $\alpha$  and  $\beta$ , respectively.

velocity component, was found as

$$\bar{v}(z) = \frac{1}{N} \sum_{i=1}^N v_i(z) \quad (6.1)$$

$$\sigma(z) = \sqrt{\frac{1}{N-1} \sum_{i=1}^N (v_i(z) - \bar{v}(z))^2}. \quad (6.2)$$

The mean relative bias  $\tilde{B}$  between the estimated velocity and the expected velocity  $v_\mu(z)$  at each depth was calculated as

$$\tilde{B} = \frac{1}{v_0 N_z} \sum_{z=1}^{N_z} (\bar{v}(z) - v_\mu(z)), \quad (6.3)$$

with  $v_0$  being the theoretical peak velocity and  $N_z$  all the discrete samples located within 90 % of the vertical vessel radius measured from its center. Boundary effects caused by e.g. echo cancelling may give a wrong impression of the estimator's actual performance, which the 90 % acceptance rule should help prevent. A similar relative mean standard deviation  $\tilde{\sigma}$  was calculated as

$$\tilde{\sigma} = \frac{1}{v_0} \sqrt{\frac{1}{N_z} \sum_{z=1}^{N_z} \sigma(z)^2}. \quad (6.4)$$

The two quantitative performance metrics  $\tilde{B}$  and  $\tilde{\sigma}$  were used in the study for a comparison between different parameter settings.

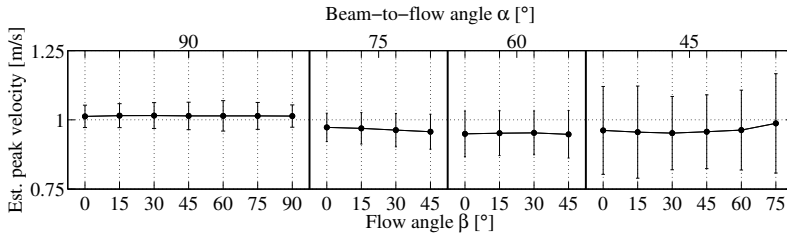


**Figure 6.6:** Estimated mean peak velocity at various angle combinations shown with the standard deviation.

### 6.5.3 M-mode results

For a thorough review of the parametric study, the reader is encouraged to read Paper I, as this section only contains a summary of the results. In general, the results should be seen in light of the flow being constant and unidirectional in all but as few cases.

#### PEAK VELOCITY ESTIMATION

The capability of estimating accurate angle independent peak velocities with the RC array was tested by changing  $\alpha$  and  $\beta$  in various combinations. The peak velocities were estimated from 100 independent and uncorrelated observations by calculating the absolute velocity  $|v| = \sqrt{v_x^2 + v_y^2 + v_z^2}$  at all depths and taking the maximum value from each observation. The mean peak velocity at different vessel orientations is seen in Fig. 6.6.

The decoupled 3-D velocity profile estimates for a selection of flow orientations are presented in Fig. 6.7.

#### FLOW DIRECTION

The best performance is found for the fully transverse flow, where  $\alpha = 90^\circ$ , yielding a bias  $\tilde{B}_{v_x}$ , that stays between 0.2-3.5 %, with  $\tilde{\sigma}_{v_x}$  between 4.6-5.7 %. The worst performance is found at  $\alpha = 45^\circ$ , where  $\tilde{\sigma}_{v_x}$  and  $\tilde{\sigma}_{v_y}$  reaches 20 %, as presented in Fig. 6.8(a).

#### ENSEMBLE LENGTH

The best estimates were found with the largest ensemble length  $e = 64$ , where  $\tilde{B}_{v_x} = 1.8$  % and  $\tilde{\sigma}_{v_x} = 3.8$  % compared with  $\tilde{B}_{v_x} = 7.5$  % and  $\tilde{\sigma}_{v_x} = 8.1$  % for  $e = 8$ . The same pattern was seen for  $\tilde{B}_{v_y}$  and  $\tilde{\sigma}_{v_y}$ , see Fig. 6.8(c).

#### PULSE LENGTH

The transmitted pulse length was changed from 2 to 8 cycles in steps of two cycles.  $\tilde{B}_{v_x}$  increased from  $-2.1$  % at two cycles up to 2.6 % when using 8 cycles. Standard deviation

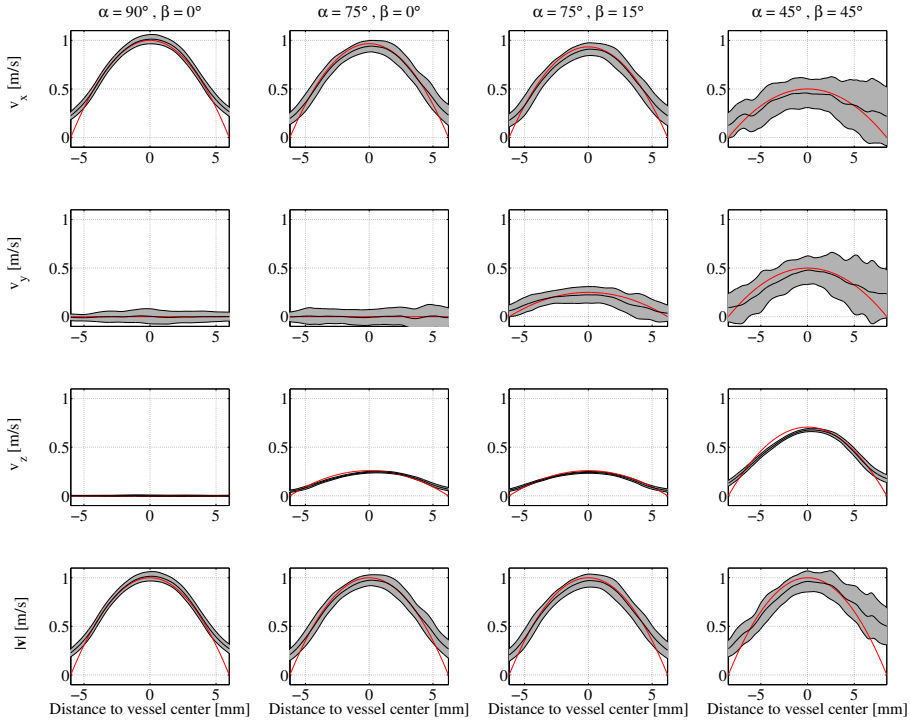


**Figure 6.7:** The decoupled estimated velocity component (black line)  $\pm$  one standard deviation (gray area) at a representative selection of different vessel rotation combinations is presented, along with the theoretical velocity component (red line). The bottom row shows the absolute velocity magnitude combined from the three velocity component estimates.

and bias for the remaining estimates were almost unaffected by changing the pulse length, presumably because no flow was present in these directions. Results are shown in Fig. 6.8(d).

### APODIZATION

Different transmit and receive apodization shapes were investigated, and the findings are presented in Fig. 6.8(e). In the direction of the flow, the lowest bias was found when a Hann window was used in transmit and a boxcar apodization was used in receive, here  $\tilde{B}_{v_x} = -0.1\%$ . The standard deviation increased slightly for this combination, but was relatively unaffected by the transmit and receive apodization, since  $\tilde{\sigma}_{v_x}$  for

all combinations of using a Hann window in transmit was between 4.6 % and 5.5 %. However,  $\tilde{\sigma}_{v_y}$  was highly affected by the transmit apodization and was 5.6 %, 11.7 %, 7.5 %, respectively when receive apodization was fixed to a boxcar, and transmit varied between a Hann, boxcar and a Tukey window.

### STEERING ANGLES

Focused emissions were steered in the  $zy$ -plane spanning from  $0^\circ$  to  $45^\circ$  in steps of  $5^\circ$ . The estimator deteriorates significantly for angles greater than  $20^\circ$ , where  $\tilde{B}_{v_x}$  increases in a negative direction from a stable level around 1-2 % Fig. 6.8(f). The explanation for the breakdown is found in the geometry of the RC array and the position of the integrated apodization. The returning echo from a scatterer placed outside the physical aperture  $|x| > 8.4$  mm or  $|y| > 8.4$  mm will first hit the integrated apodization element, resulting in a damped signal compared with a scatterer that was placed inside the physical aperture. The maximum dampening of the signal is found when the scatterer is placed outside the dimensions of the integrated apodization  $|x| > 12.7$  mm or  $|y| > 12.7$  mm. For a  $15^\circ$  steering angle, the lateral displacement of a scatterer located at 30 mm depth is 8 mm, which is inside the physical aperture. For a  $20^\circ$  steering angle the performance gradually breaks down, since the lateral displacement of the scatterer is 11.9 mm. This effect affects the performance more when increasing the steering angle, since a larger fraction of the scatterers are placed outside the physical aperture.

### TO SPACING

With a default TO peak width of 25 elements, the minimum element spacing between the two peaks was 25 and maximum 37 element before exceeding the aperture. A gradually improved performance was seen when increasing the separation between the two apodization peaks. At a 25 element spacing,  $\tilde{B}_{v_x}$  was 5.0 % and improved to 1.3 % for the 37 element spacing. Similarly,  $\tilde{B}_{v_y}$  improved from  $-0.6$  % to  $-0.1$  %. Likewise,  $\tilde{\sigma}_{v_x}$  and  $\tilde{\sigma}_{v_y}$  decreased from 6.8 % and 8.4 % to 4.8 % and 5.9 %, respectively. Axial estimates were unaffected when changing TO specific parameters, as the estimator is decoupled from the TO method, see Fig. 6.8(g).

### TO WIDTH

The spacing between the TO peaks was kept fixed while changing the apodization width.  $\tilde{B}_{v_y}$  and  $\tilde{\sigma}_{v_y}$  did not change significantly when varying the TO width. This could probably be attributed to the actual vessel orientation where  $v_y = 0$  m/s.  $\tilde{B}_{v_x}$  changed from 2.4 % when two delta functions were used in receive, to 1.3 % for a 25 elements wide Hann apodization. Similarly,  $\tilde{\sigma}_{v_x}$  changed from 17.1 % to 4.8 %, see Fig. 6.8(h).

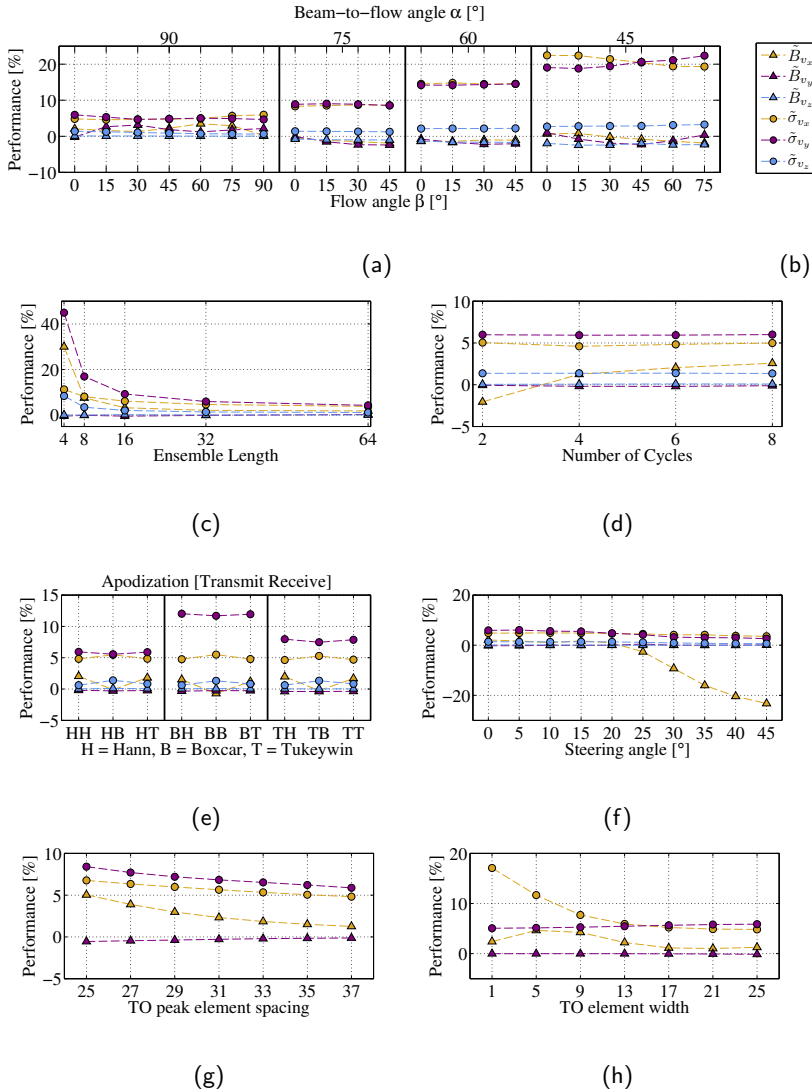


**Figure 6.8:** (a), (c)-(h) Results from the presented parameter study. An explanation to the legends is shown in b). Obtained from (Holbek et al. 2016), which also gives a thorough review of the results.

### 6.5.4 Parametric study conclusion

The result shows, that regardless of the vessel orientation, the expected peak velocity  $v_0$  was always within the standard deviation. However, the best performance was obtained at a  $90^\circ$  beam-to-flow angle. The parametric simulation study, where the entire velocity profile was compared with the reference values, yielded similar conclusion. The best performance was achieved with a  $90^\circ$  beam-to-flow angle and was almost unaffected by the flow angle. The study also concluded that flow estimation was only possible within physical dimensions of the aperture and that the largest apodization spacing with the widest TO peaks would provide the smallest bias and the highest precision.

## 6.6 Experimental setup

The observations made in this parametric simulation study were applied in the experimental setup. The sequence parameters were as default the same as stated in Table 6.1.

### 6.6.1 Materials and equipment

A 62+62 2-D RC piezo prototype probe was used in the experiments with similar properties as the simulated array. Each row/column dimension consisted of 62 elements with the ends being dedicated for integrated apodization. The probe had a center frequency  $f_0$  of 3.0 MHz which was also the transmit center frequency in the experimental setup. The pitch was  $270\ \mu\text{m}$  and the kerf was  $25\ \mu\text{m}$ , yielding an active aperture area of  $1.67 \times 1.67\ \text{cm}^2$ . Four integrated edge apodization elements were used to suppress the expected ghost echoes.

All measurements were conducted with the experimental scanner SARUS, where raw RF data from all 124 channels were stored at a sampling frequency of 35 MHz. The high precession AIMS III Scanning Tank (Onda, Sunnyvale, CA) and a HGL-0400 (Onda, Sunnyvale, CA) hydrophone were used for intensity measurements. Flow was estimated in the in-house built flow-rig ( $\varnothing = 12\ \text{mm}$ ), where blood mimicking fluid was circulating at a constant speed, and in the straight-vessel phantom ( $\varnothing = 8\ \text{mm}$ ), that was connected to the pulsating flow pump.

## 6.7 Measurements

### 6.7.1 Intensity measurements

Intensity measurements were conducted for the M-mode sequence to ensure, that the generated pressure field was as expected and to examine which field-of-view could be expected. Intensity measurements were conducted in a c-plane at the focal depth, following the procedure described in (Jensen, Rasmussen, et al. 2016). An  $f_{prf}$  of 750 Hz was applied.

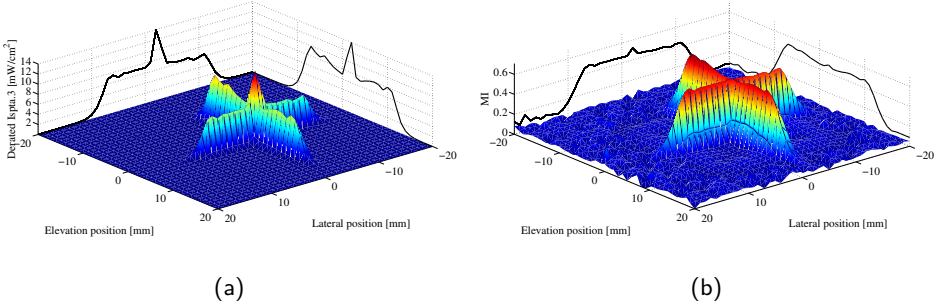


**Figure 6.9:** Intensity measurements for an M-mode sequence with focused emissions in (0, 0, 30 mm) at  $f_{prf} = 750$  Hz. a)  $I_{spta.3}$ , b) MI.

## RESULTS

The measured MI and  $I_{spta.3}$  values are shown in Fig. 6.9. The results confirm, that the transmitted wave generates a focal line, and that the pressure generated from row elements are similar in amplitude to those generated from column elements. Furthermore, the measurements also confirm, that with the current setup, flow can only be estimated in the forward-looking plane of the RC transducer as concluded in the parametric simulation study.

### 6.7.2 Flow-rig M-mode

The M-mode flow sequence was used to estimate 3-D vector flow through the center line of the pipe in the flow-rig. Measurements from four representative combinations of  $\alpha$  and  $\beta$  were conducted. A total of  $2 \times 32 \times 100$  emissions were used for each measurement setup. The peak velocity  $v_0$  was set to  $0.5 \text{ m s}^{-1}$  and the pulse repetition frequencies  $f_{prf}$  were [1500, 2500, 6900] for the respective beam-to-flow-angles  $\alpha = [90^\circ, 75^\circ, 50^\circ]$ , to ensure that the aliasing limit was not exceeded in the limiting velocity component  $v_z$ . The  $f_{prf}$  was halved compared with the simulations to maintain the same ratio between  $v_0$  and  $f_{prf}$ .

## RESULTS

The estimated mean peak velocities calculated as  $|\mathbf{v}|$  for each setup were [48.5, 50.4, 50.6, 58.2]  $\text{cm s}^{-1} \pm [3.0, 5.9, 3.5, 8.7] \text{ cm s}^{-1}$  for the respective flow combinations  $[\alpha; \beta] = [90^\circ; 0^\circ], [75^\circ; 0^\circ], [75^\circ; 15^\circ], [50^\circ; 45^\circ]$ .  $\tilde{B}_{v_x}$  stays between  $-3.1\%$  and  $-4.8\%$  for the four constellations. Similarly,  $\tilde{B}_{v_z}$  stays between  $-3.8\%$  and  $1.5\%$  whereas  $\tilde{B}_{v_y}$  increases from a level between  $-0.9\%$  and  $2.1\%$  in the first three setups to  $-10.9\%$  for  $[50^\circ; 45^\circ]$ . The lowest mean relative standard deviation is found at  $[90^\circ; 0^\circ]$ , where

$(\tilde{\sigma}_x, \tilde{\sigma}_y, \tilde{\sigma}_z) = (8.7\%, 5.1\%, 0.8\%)$ . The maximum standard deviation is found for the angle combination  $[50^\circ; 45^\circ]$ , where  $(\tilde{\sigma}_x, \tilde{\sigma}_y, \tilde{\sigma}_z) = (19.9\%, 21.3\%, 6.5\%)$ . The large deviation in the estimated velocities compared with the expected, are supposed to be due to reverberation artifacts from the pipe.

### 6.7.3 Flow-rig steered

With the same equipment and measurement setup, 3-D vector flow was measured in a cross sectional plane using the steered emission sequence. The sequence consisted of 11 steered row emissions spanning from  $-12^\circ$  to  $12^\circ$  in steps of  $2.4^\circ$  and a single unsteered column emission. The  $f_{prf}$  was 9.0 kHz and a total of  $32 \times 12 \times 100$  emissions were transmitted, corresponding to 100 frames when an ensemble length of 32 was used.

#### RESULTS

Based on the out-of-plane velocity component and the pipe area, the volumetric flow rate for each frame was estimated. The mean volumetric flow rate was  $91.2 \pm 3.1 \text{ L h}^{-1}$  compared with the expected  $102.6 \text{ L h}^{-1}$ , which is a negative bias of 11.1 %.

### 6.7.4 Pulsating flow M-mode

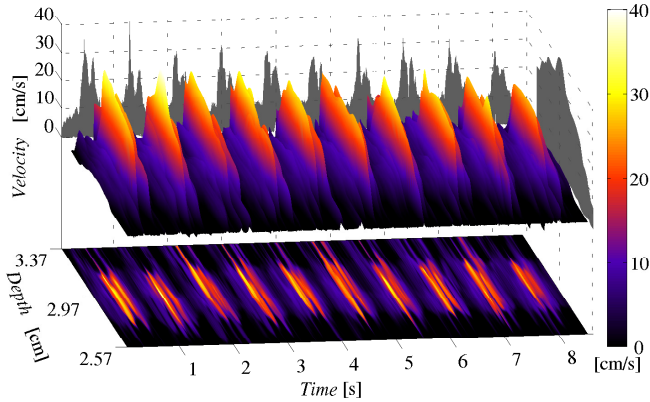
M-mode flow measurements were made using the flow pump and the straight-vessel phantom. A predefined carotid flow profile was chosen with a cycle time of 0.84 s and a flow rate of  $2.54 \text{ mL/stroke} \pm 3\%$ . The transducer was placed 30 mm from the center of the vessel in a  $90^\circ$  beam-to-flow angle. At an  $f_{prf}$  of 750 Hz, a total of 8.5 s of data were recorded by SARUS, corresponding to 10 full cycles. An ensemble length of 32 was applied in the data processing.

#### RESULTS

Since the cycle time was fixed throughout the data acquisition, a time coherent addition of all 10 cycles was made. The predominant out-of-plane  $v_x$  velocity component was investigated further, and the mean velocity in the center of the vessel during each cycle was estimated to be  $11.3 \pm 0.4 \text{ cm s}^{-1}$ . The out-of-plane component as a function of time is presented in Fig. 6.10.

### 6.7.5 Pulsating flow steered

With the steered sequence and the pulsating flow pump, 3-D vector flow was estimated in a cross sectional plane of a straight vessel phantom. The sequence consisted of 11 steered row emissions spanning from  $-8^\circ$  to  $8^\circ$  in steps of  $1.6^\circ$  and a single unsteered column emission. The  $f_{prf}$  was 9.0 kHz, translating to 750 frames per second. The ensemble length was 32.0 and flow rates were estimated based on the cross-sectional area and the velocity component perpendicular to this plane.



(a)

**Figure 6.10:** M-mode illustration of the dominating out-of-plane ( $v_x$ ) velocity component estimated in the pulsating setup.

## RESULTS

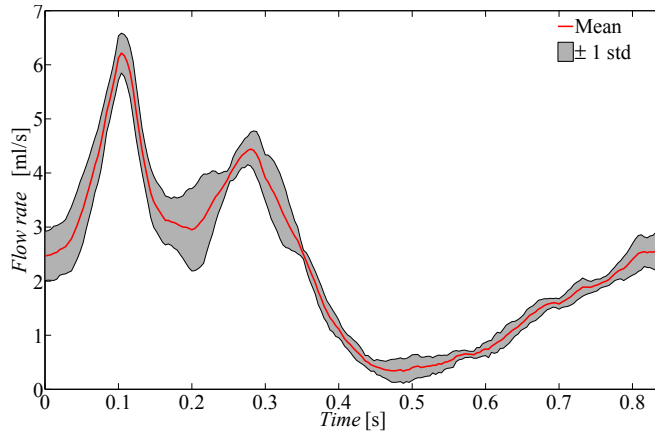
A total of 4.3 s were recorded, corresponding to 5 cycles. The mean flow rate was estimated to be  $2.3 \pm 0.1$  mL/stroke, compared with the expected  $2.54 \pm 0.08$  mL/stroke, see Fig. 6.11. In Fig. 6.12, a 3-D vector representation of the flow during the mimicking peak-systole as well as the end-diastole is seen.

### 6.7.6 CMUT

A CMUT version of the prototype 2-D RC array with similar properties was used to estimate 3-D vector flow in the flow-rig with the M-mode sequence. A DC bias voltage of 180 V was chosen to deflect the top electrode and an sinusoidal AC voltage was applied on top of this to set the electrode into motion and generate the ultrasonic waves. A total of 20 frames were acquired at an  $f_{prf} = 1.4$  kHz and at a  $90^\circ$  beam-to-flow angle.

## RESULTS

The peak transverse velocity was  $0.48 \pm 0.02$  m s $^{-1}$  corresponding to a  $-10.9\%$  bias compared with the expected  $0.54$  m s $^{-1}$ . Estimates in the lateral and axial direction showed negligible flow as expected with a small mean standard deviation of  $\pm 0.02$  m s $^{-1}$  and  $\pm 0.01$  m s $^{-1}$ , respectively (see Fig. 6.13). Along the central 90% of the vessel



(a)

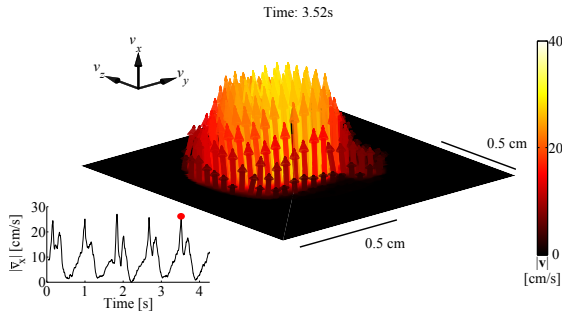
**Figure 6.11:** Estimated flow rate profile averaged from 5 coherently aligned cycles (red curve) with  $\pm$  one standard deviation (gray).

diameter, the relative mean bias was  $(-4.9, -0.4, 0.5) \%$  with a mean relative standard deviation of  $(6.7, 4.9, 2.5) \%$  for  $(v_x, v_y, v_z)$ , respectively.

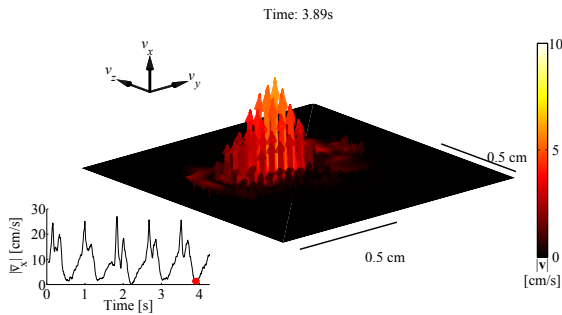
The sensitivity of the CMUT probe highly depends on the DC voltage, which conservatively set to 180 V compared with the theoretical estimated pull-in voltage of 240 V. Increasing the DC voltage pulls the top-electrode closer to the bottom electrode and thereby increases the coupling coefficient describing the relationship between the conversion of electrical power to mechanical energy and vice versa. Increasing the DC voltage is not without risks, since irreversible processes might occur if exceeding the pull-in voltage threshold. Due to the conservative choice of DC voltage, the performance of the CMUT RC probe was expected to be worse than for the piezo version. Therefore, the experimental validation of RC 3-D vector flow was carried out with the piezo probe.

## 6.8 Conclusion and perspective

A parametric simulation study was performed to identify the behaviour of 3-D TO vector flow on an RC array and wherein the limitations existed. The parametric study concluded that the lowest bias and standard deviation were obtained when a fully transverse flow was present, and that wide and distant separated TO peaks were preferred. Furthermore, the study concluded that only flow within the forward looking image plane could be obtained. The observations made in the simulation study were applied in the experimental setup.



(a)



(b)

**Figure 6.12:** Cross sectional 3-D vector flow representation estimated in the pulsating setup during (a) peak-systole and (b) end-diastole. Please note, that the velocity scale during peak-systole is four times larger than for the end-diastole. The lower left figure shows the estimated out-of-plane velocity magnitude in the center of the vessel.

The experimental results were in good agreement with similar simulation setups. For instance, the estimated peak velocity had a mean relative bias of 1.3 % and a relative mean standard deviation of 4 % in the simulations and similar a mean relative bias of  $-3.8\%$  and a relative mean standard deviation of 5.9 % in the measurements for the optimal flow angle constellation  $[\alpha; \beta] = [90^\circ; 0^\circ]$ .

With a steered emissions sequence it was possible to estimate the flow rate in a pulsatile environment with a negative bias of 9.4 % but at a standard deviation of only

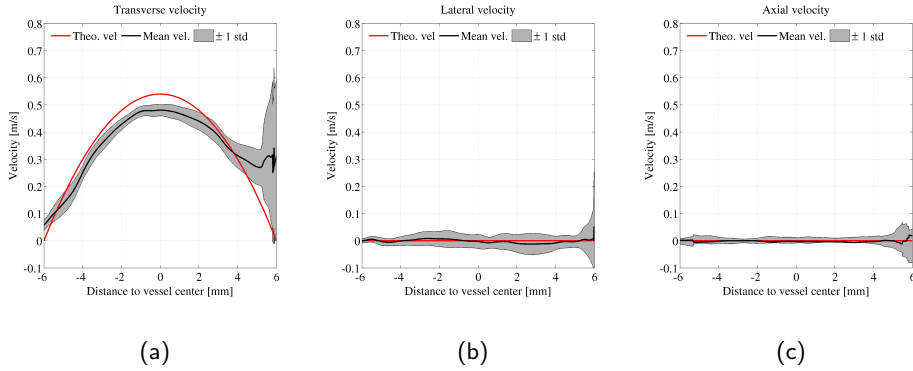


**Figure 6.13:** Measured velocity profiles (solid black line) and  $\pm$  one standard deviation (dotted lines) plotted on top of the theoretical expected velocity profile (red line) in the transverse direction (a), the lateral direction (b) and the axial direction (c). The velocity profiles are displayed across the vessel of diameter 12 mm

4.3 %. The 3-D vector flow estimates were obtained at a very high frame rate of 750 frames per second, which is sufficient for capturing blood movement with high temporal variations.

Based on the overall results, it can be concluded that 3-D TO vector flow can be implemented on a 62+62 2-D prototype piezo RC array. Furthermore, promising preliminary results with a similar CMUT probe indicate, that the method is compatible with this interesting transducer fabrication technique.

For *in vivo* applications, when e.g. measuring in the common carotid artery, several adjustments can be made to the presented steered sequence to cope with velocities on the order of  $1 \text{ m s}^{-1}$ . For instance, the lateral wavelength can be increased to 0.4 cm by shortening the spacing between the TO peaks to 31 elements. Similarly the  $f_{prf}$  can be increased to 15 kHz without exceeding the FDA limits. By applying a  $\frac{\pi}{2}$  phase shift and using 11 steered row emissions and one column emission, the detectable velocity range at 3 cm depth could be calculated using eq. 5.2 to be  $[-63 \text{ cm s}^{-1}; 188 \text{ cm s}^{-1}]$ , which is within the expected *in vivo* velocity range of healthy individuals.

With only 124 elements the RC array has a channel count similar to a conventional commercial linear array. The significant reduction in the total amount of channels paves the way for a real-time implementation of 3-D vector flow using TO, due to the reduced processing time. The large physical aperture furthermore allows for a larger penetration depth, enabling new applications of 3-D vector flow estimation in the clinic.

### 6.8.1 Perspectives

Although row-column addressing of the arrays solves some of the interconnection challenges and reduces the computational load significantly, it introduces some new issues.

One of the main issues is the fact, that imaging can only be achieved in the forward-looking dimension with RC arrays. This is a crucial limitation if the technique should be implemented for clinical use, due to the narrow field-of-view. Fabricating RC arrays with a larger element count and an unchanged pitch maintains the properties of the arrays, while increasing the field-of-view, due to the larger physical aperture. This solution is only feasible to a certain extent, since e.g. cardiac scans requires a small physical aperture that can fit in between the ribs. Yet another approach to extend the field of view, but maintaining the dimensions of the aperture, is by mounting a diverging lens on top of the array or by fabricating curved 2-D RC arrays. Spreading out the energy with a lens is counterintuitive compared with the lenses applied in linear arrays for creating an elevation focus. However, it should be noted that the area of a 2-D RC array typically is larger than for a matrix array (in our case  $2.79 \text{ cm}^2$  for the RC array and  $0.92 \text{ cm}^2$  for the matrix array), allowing for the dispersion of the energy. The idea of diverging the waves and the consequences in the beamforming are described in the patent application in Paper **D**.

With the implementation of 3-D vector flow in a plane on an RC array, the next step seems to explore the feasibility of extending the method to estimate volumetric 3-D vector flow. The next chapter reviews two proposed ideas for estimating 3-D vector flow in either multiple planes or in every point in a full volume.

# CHAPTER 7

## Row-Column 3-D Volumetric Vector Flow

---

**Summary** *The previous chapter presented a method for 3-D vector flow estimation using an RC array. An extension of the method is proposed in this chapter, where volumetric 3-D vector flow estimates from multiple planes via focused emissions are obtained in an experimental setup. Furthermore, a different approach for achieving 3-D vector flow information at any given point in a volume is proposed by combining SA imaging techniques with the directional transverse oscillation method. Preliminary proof-of-concept simulation results are presented for the SA imaging approach.*

### 7.1 Purpose

Currently, experimental work within 3-D and 4-D MRI have shown some promising preliminary application of volumetric 3-D vector flow, including whole heart 4-D flow, arterial and venous hemodynamics in various regions, and stenotic common carotid arteries (Bogren, Buonocore, and Valente 2004; Harloff et al. 2009; Markl et al. 2012; Arvidsson et al. 2016). Although the results are impressive, the limitations of 4-D flow obtained with MRI includes long scan times (up to hours), and limited spatial and temporal resolution. These limitations could be overcome if new methods for volumetric 3-D vector flow imaging could be developed for ultrasound systems, which would be of interest both for the patients wellbeing and from a socio-economic perspective.

The aim of this chapter, is therefore to introduce two approaches for obtaining volumetric 3-D vector flow estimates using an RC array. The basic concept of the proposed methods are based on the ideas described in Patent I and Paper A.

### 7.2 Background

Previous literature on volumetric blood flow estimation from real-time data acquisition is sparse. In fact, the first 1-D volumetric flow estimation was achieved very recently by Provost *et al.* 2014 (Provost, Papadacci, Arango, et al. 2014) and (Provost, Papadacci, Demene, et al. 2015). The field is developing, and new methods for full 3-D volumetric vector flow estimation have just been reported in the literature for vector Doppler (Correia et al. 2016), speckle tracking (Wigen and Løvstakken 2016), and synthetic aperture

directional beamforming (Villagomez-Hoyos et al. 2016). Common for the presented volumetric 3-D vector flow result, are, that they were obtained with 2-D matrix arrays.

### 7.3 Introduction

This chapter presents two approaches for estimating volumetric 3-D vector flow using an RC array with only 124 channels. Three-dimensional vector flow in a volume can be obtained via e.g. focused emissions or by transmitting diverging waves. The focused emission approach is a plane-by-plane method, which usually results in an unsatisfactory volume rate due to the high amount of emissions in many directions and has limited application. Diverging waves, on the other hand, can be used in combination with SA techniques and DTO to obtain very high volume rates at the cost of a reduced SNR, due to the dispersion of the dissipated energy. In the following sections, two approaches for volumetric 3-D vector flow estimation are investigated, both exploiting the advantages that come with the RC array.

### 7.4 Plane-by-plane 3-D volumetric vector flow

The first attempt to produce volumetric 3-D vector flow is by modifying the steered transmission sequence proposed in 6.4.2. As 3-D vector flow can be obtained along points at the intersection between a column and a row transmission, the solution seems to be an increase in the number of column transmission for generating more planes with the desired intersections. With 11 row emissions and one column emission, 3-D vector flow was obtained in a single plane as shown in Fig. 6.12. However, transmitting one additional steered column emission would generate an additional plane with 11 new intersections and thereby an extra plane containing 3-D vector flow. For each additional steered column emission added to the transmit sequence, one extra plane with 3-D vector flow is generated. The idea for obtaining volumetric 3-D vector flow with a plane-by-plane approach is therefore to add the emissions  $C_j$  to the transmit sequence, where  $j$  is an integer that runs from 1 to  $M$ . This will result in multiple planes containing 3-D vector flow, that can be combined to form a volume. An illustration of the volumetric sequence is seen in Fig. 7.1. The repeating volumetric sequence is schematically written as

$$\begin{array}{cccccccc}
 C_1 & \rightarrow & C_2 & \rightarrow & \dots & C_M & \rightarrow & R_1 \rightarrow R_2 \rightarrow R_3 \rightarrow \dots R_N \\
 & & \vdots & & & & & \vdots \\
 & & & & & & & \vdots \\
 C_1 & \rightarrow & C_2 & \rightarrow & \dots & C_M & \rightarrow & R_1 \rightarrow R_2 \rightarrow R_3 \rightarrow \dots R_N,
 \end{array}$$

and is the sequence applied in the experimental validation. Since the detectable velocity range scales with the total number of flow emissions as  $\sim \frac{1}{N_{flow}}$  with TO, where  $N_{flow}$

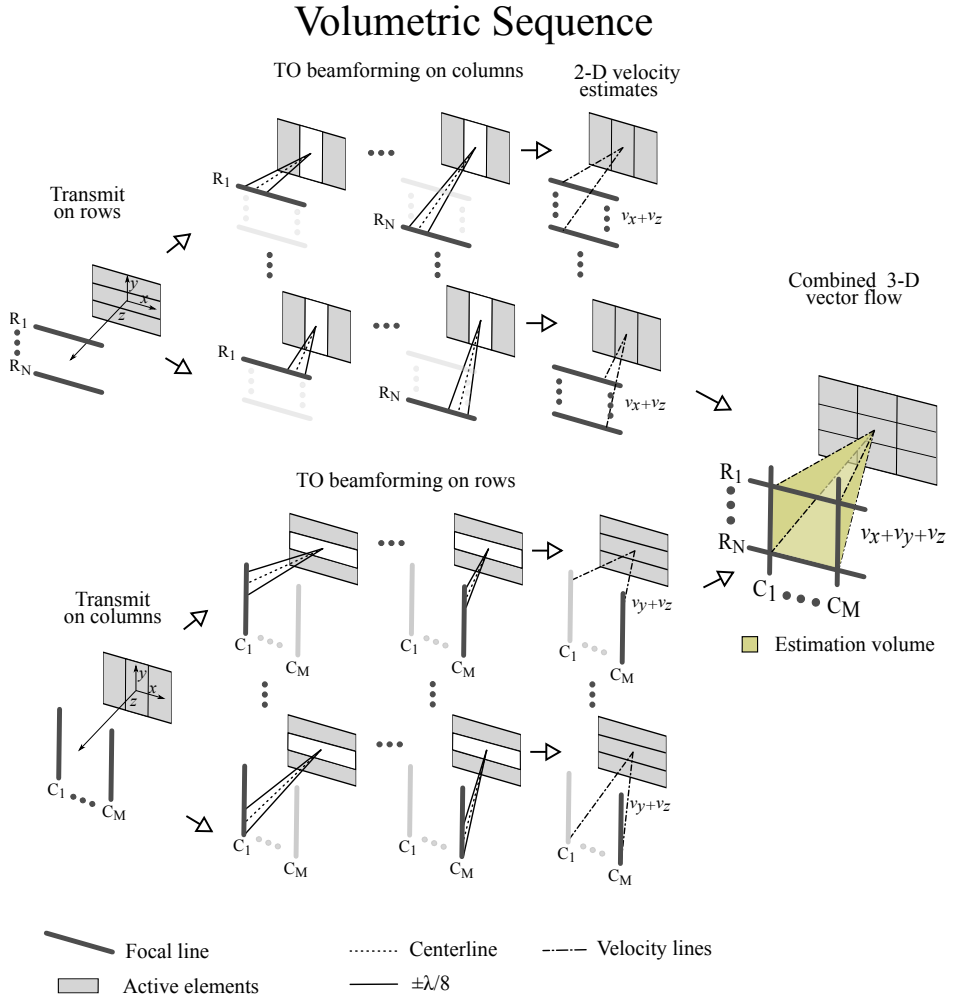


**Figure 7.1:** The volumetric sequence is an extension of the steered sequence, Fig. 6.4. The extension consists of the additional  $M$  column emission, which provides  $M$  new planes with 3-D vector flow. The  $M$  planes can finally be combined to provide volumetric 3-D flow information. From Patent I.

$= M + N$ , it sets some limitation for the number of obtainable planes before reaching the aliasing limit. Thus, the actual sequence design is a tradeoff between having a satisfactory spatial resolution and maintaining a field-of-view that covers the ROI while still being able to estimate velocities in the expected range.

## 7.5 Flow-rig measurements

A single measurement was made in the flow-rig, where the flow rate was  $49.2 \text{ L h}^{-1}$  translating to a peak velocity in the parabolic flow of  $v_0 = 24.1 \text{ cm s}^{-1}$ . The volumetric sequence consisted of 11 row emissions and 9 column emissions and was designed to acquire continuous data. The row emissions were steered from  $-15^\circ$  to  $15^\circ$  in steps of  $3^\circ$  and the column emissions from  $-8^\circ$  to  $8^\circ$  in steps of  $2^\circ$ , effectively resulting in nine cross-sectional scan planes. At 3 cm depth, this corresponded to a c-plane spanning the dimension  $16.1 \text{ mm} \times 8.4 \text{ mm}$ . The  $f_{prf}$  was 10.5 kHz. The center of the vessel was located 2.9 cm from the transducer's surface and data were processed in accordance with the approach proposed in Chapter 6.

### RESULTS

A total of 35 frames, each composed of 64 transmit cycles were acquired, corresponding to 4.3 seconds of data. Each velocity estimate was calculated from 32 beamformed transmit events yielding 70 independent velocity estimates for each plane. A volumetric representation of the angle corrected mean out-of-plane velocity estimates are shown in Fig. 7.2. A better illustration of the present parabolic flow is seen in Fig. 7.3, where the mean out-of-plane velocity component for the nine cross-sectional scan planes are shown. Based on the velocity component perpendicular to the cross-sectional area, the mean flow rate for each plane was calculated, see Fig. 7.4. A positive bias was found for all of the steering angles, with the smallest at  $4^\circ$  (4.8%) and the largest at  $-8^\circ$  (17.4%). Similarly, the smallest standard deviation was found for the plane steered by  $2^\circ$  (13.2%) and the largest standard deviation was at a steering of  $-8^\circ$  (19.3%). The overall mean flow rate, based on the estimated value for each plane was  $53.5 \pm 2.2 \text{ L h}^{-1}$ . The two remaining velocity components for the nine planes are shown in Fig. 7.5 ( $v_z$ ) and in Fig. 7.6 ( $v_y$ ). The estimated axial velocities reflect the steering of the planes. For negative steering angles, a positive magnitude of  $v_z$  is found, indicating that flow is propagating towards the transducer in the given plane, and vice versa for planes with a positive steering angle, where flow is propagating away from the transducer. The results indicate that the beam-to-flow angle was close to  $86^\circ$ , as the smallest axial velocity was estimated in the plane steered  $4^\circ$ . The  $v_y$  velocities similarly indicate that a slight rotation of the flow was present, as a general mean positive velocity component was estimated. However, erroneous velocities are estimated at larger steering angles, which may be due to the chosen lateral wavelength not matching the expected velocity range or that a further optimization of the beamforming for steered directions are required.

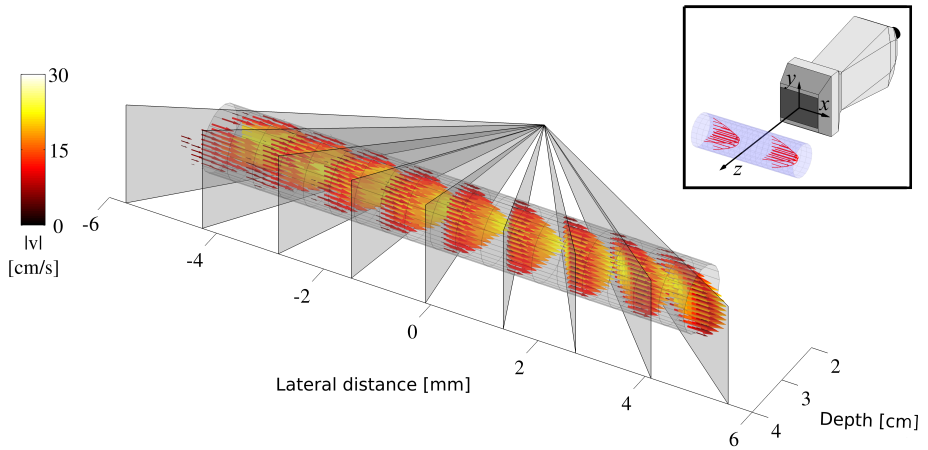


**Figure 7.2:** Experimental volumetric flow results obtained in the flow-rig displayed with the nine steered planes.

## 7.6 Synthetic aperture 3-D volumetric vector flow

### 7.6.1 Basic principles in 2-D

With synthetic aperture imaging techniques it is possible to beamform a low resolution image after each transmit event, and when adding several low resolution images coherently, a high resolution image is obtained (Nikolov and Jensen 2002). By filtering the high resolution image in the Fourier domain with two separated Gaussian functions, as described in Section 3.4, a lateral oscillation with a wavelength desired by the filtering function is induced. An additional image, is an analytical  $90^\circ$  phase-shifted version of the original image, can subsequently be generated by performing a spatial Hilbert transformation on the filtered image. These two images are used as input to the conventional TO estimator, which can provide 2-D in-plane vector flow information in the entire plane, when comparing the phase change across multiple high resolution planes. These principles found the basic idea when expanding the synthetic aperture flow estimation using  $k$ -space filtering and TO from 2-D vector flow in a plane to 3-D vector flow in a volume.

### 7.6.2 Basic principles in 3-D

The SA imaging technique can be expanded to acquire volumetric data if a 2-D array is applied. Considering an RC array, a low resolution volume can be obtained by performing a single-element transmission on e.g. a column element and include all the row elements in the receive beamforming stage. By subsequently transmitting with a different column

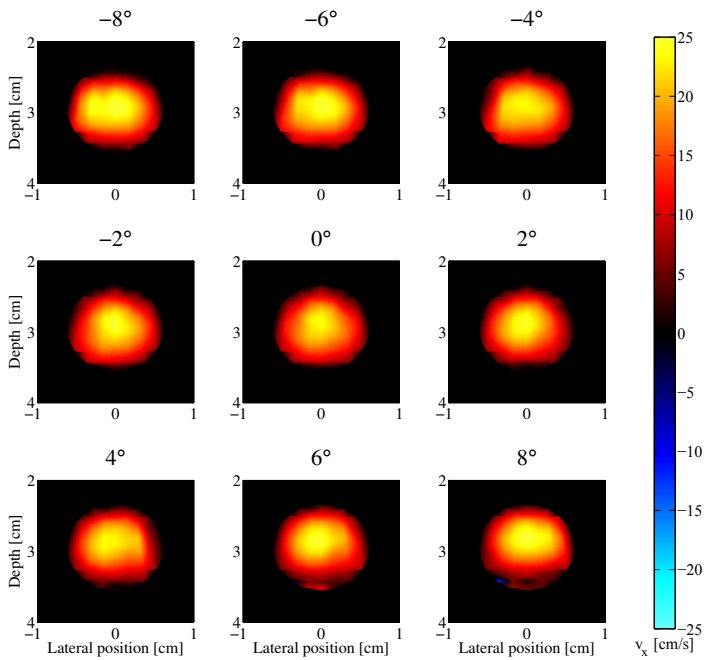


**Figure 7.3:** Mean out-of-plane velocity for the 9 cross-sectional planes steered from  $-8^\circ$  to  $8^\circ$  in steps of  $2^\circ$  averaged from 70 frames.

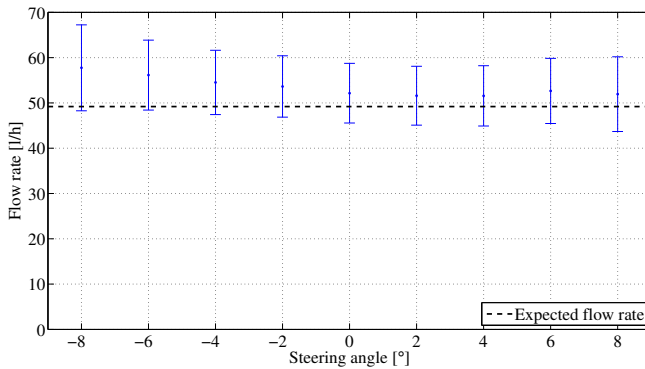


**Figure 7.4:** Estimated flow rate for each plane  $\pm$  one standard deviation (blue bar) and the expected flow rate (dotted black line).

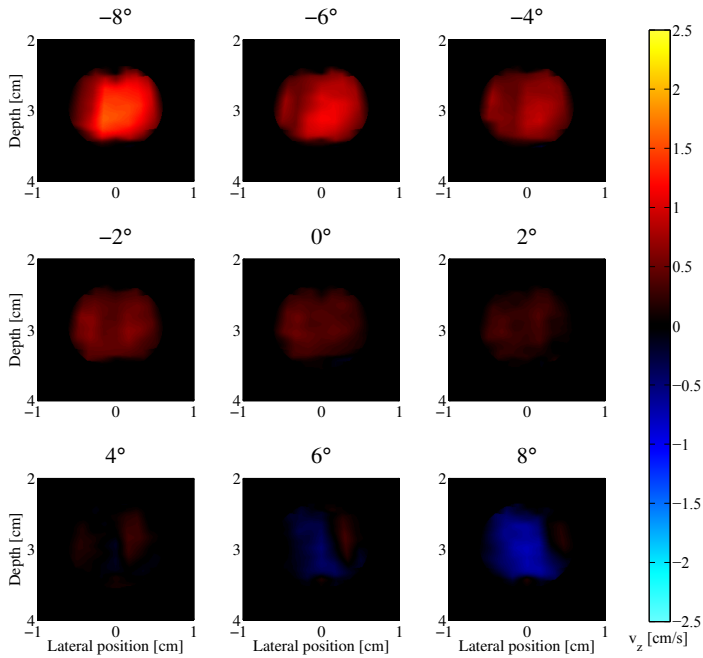


**Figure 7.5:** Mean  $v_z$  velocity for the nine cross-sectional planes steered from  $-8^\circ$  to  $8^\circ$  in steps of  $2^\circ$  averaged from 70 frames. Please note that the displayed velocity range is a tenth of  $v_x$ .

element and beamform with all row elements, a slightly different low resolution image is generated, see Fig. 7.7. Continuing this procedure for  $N$  column elements will result in  $N$  different low resolution volumes. Finally, the low resolution volumes can be added to form a high resolution volume  $HRV_{CR}$ , indicating that Tx is performed with column elements and Rx with row elements. By switching the transmit and receive apertures, a similar high resolution volume can be achieved, when transmitting with rows and receiving with columns ( $HRV_{RC}$ ).

The two distinct high resolution volumes ( $HRV$ ) are subsequently processed after dicing out the  $HRV$ 's into multiple high resolution planes ( $HRP$ ) as seen in Fig.7.8 and processed one plane at a time. The planes were taken out of the volume in the plane parallel to the tallest dimension of the transmitting aperture. This means, that the planes obtained from  $HRV_{CR}$  were orthogonal to the planes obtained from  $HRV_{RC}$ . The reason being, that the best spatial resolution is present in the dimension parallel to the transmitting element, due to the relative larger number of receiving elements in the orthogonal dimension.

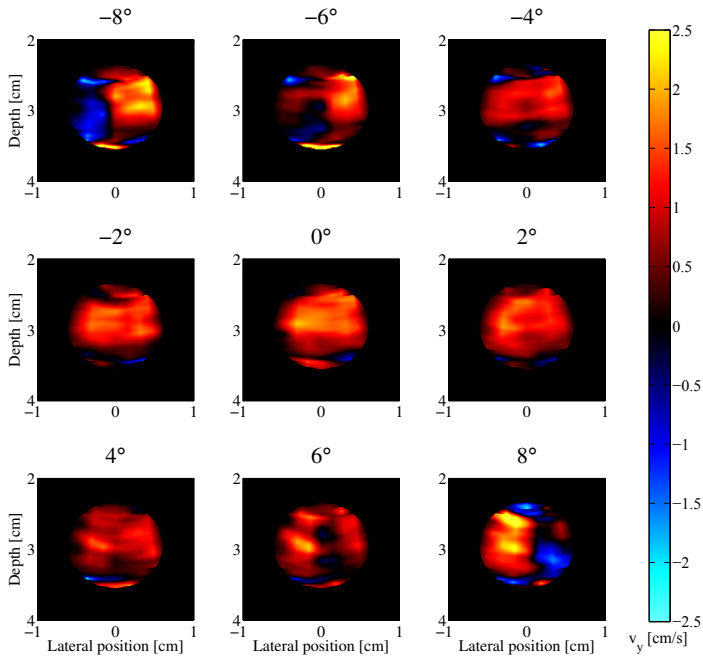


**Figure 7.6:** Mean  $v_y$  velocity for the nine cross-sectional planes steered from  $-8^\circ$  to  $8^\circ$  in steps of  $2^\circ$  averaged from 70 frames. Please note that the displayed velocity range is a tenth of  $v_x$ .

After dividing the volumes into planes, the process chain follows the 2-D case described in Section 7.6.1. Since only the axial oscillation is present in each  $HRP$ , the image is filtered in the 2-D Fourier domain with two separated Gaussian functions centered around the desired frequency, as suggested in the 2-D case (Salles et al. 2015). When returning from the Fourier domain, a transverse oscillation is now synthesized in the image.

IQ data in the lateral direction is obtained by performing a spatial Hilbert transformation on each of the double oscillating high resolution planes. These two signals (the Hilbert transformed and non-Hilbert transformed signal) can now be used as input to the conventional TO velocity estimator. Data from  $HRV_{CR}$  are used to estimate the velocity component in the direction parallel to the tallest dimension of the column elements, and data from  $HRV_{RC}$  are correspondingly used to estimate the velocity component in the orthogonal dimension. Both high resolution volumes ( $HRV_{RC}$  and  $HRV_{CR}$ ) can be used to estimate the axial velocity component. The output of the velocity estimator is the in-plane vector flow information in the entire plane. As the planes derived from

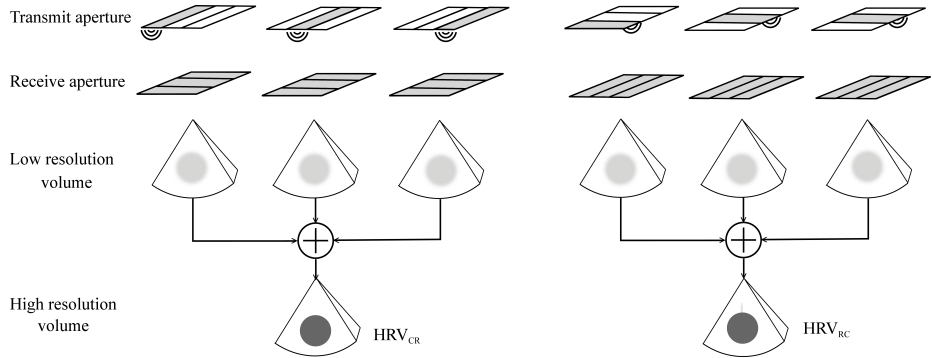


**Figure 7.7:** Illustration of single element transmission synthetic aperture. From each transmit event a low resolution volume is beamformed with all the elements from the orthogonal aperture. By adding up all the low resolution volumes created from similar receive apertures a high resolution volume ( $HRV$ ) can be formed. Two high resolution volumes after each cycle of transmit events are made; one created with Tx on columns and receive on rows ( $HRV_{CR}$ ), and another created with the opposite scenario ( $HRV_{RC}$ ). From Patent I.

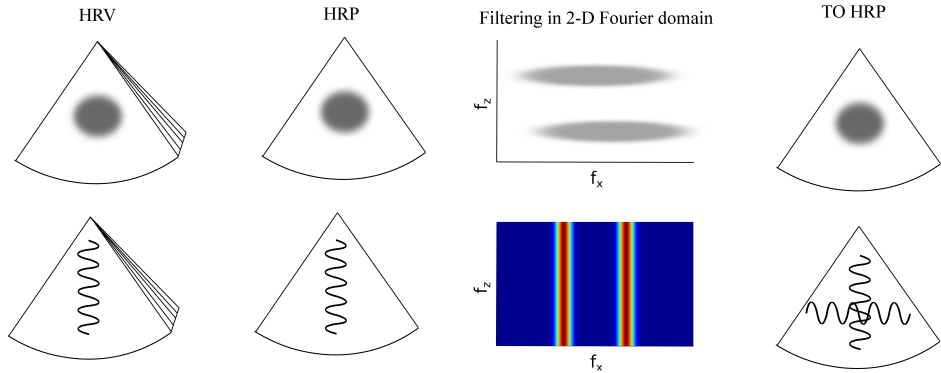


**Figure 7.8:** The  $HRV$  having only axial oscillations is sliced into multiple high resolution planes  $HRP$ . Each of these planes are then filtered in the 2-D Fourier domain to generate a lateral oscillation frequency. The TO  $HRP$  containing both axial and transverse oscillations are formed after taking the inverse 2-D Fourier transformation of the filtered  $HRP$ . From Patent I.

$HRV_{CR}$  are orthogonal to the planes derived from  $HRV_{RC}$ , the respective estimated lateral velocity components will similarly be orthogonal to each other. Thus, volumetric 3-D vector can be obtained by combining the estimated lateral velocity components at each point in the volume along with the axial velocity component estimated from either of the planes.

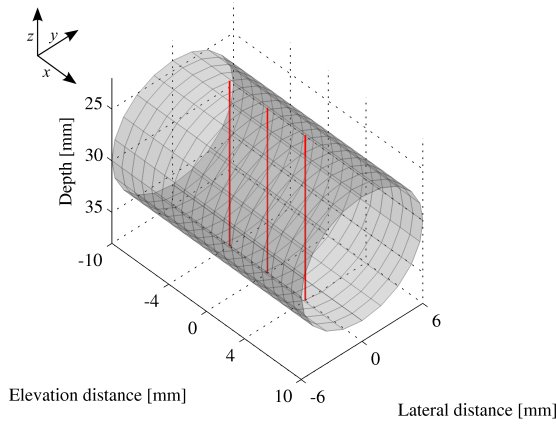


**Figure 7.9:** The simulation setup, where  $v_x$  and  $v_y$  are estimated along the axial direction at three different sites illustrated by the red lines.

### 7.6.3 Simulation setup

The proposed SA method was used to estimate the blood flow in a simulated 2 cm long vessel ( $\varnothing = 12$  mm) located 3 cm from the transducer. No stationary tissue scatterer were added in the simulations. The beam-to-flow-angle was  $90^\circ$  and a parabolic flow profile with a peak velocity of  $v_0 = 0.5$  m s $^{-1}$  was mimicked. Two different flow rotation angles  $\beta$  about the axial direction were simulated ( $0^\circ$  and  $30^\circ$ ). The simulated transducer was a 62+62 RC array which had properties identical to the one applied in Chapter 6. The single element transmit cycle was composed of 12 transmission, 6 row emissions and 6 column emissions fired interleaved from the element indices 9, 18, 27, 36, 45, and 54. The transmitted pulse was a 3.0 MHz single cycle sinusoidal, transmitted at a pulse repetition frequency of 12 kHz. A total of 10 frames were simulated, each consisting of  $32 \times (2 \times 6)$  emissions.

### 7.6.4 Processing

In this proof-of-concept study,  $v_x$  and  $v_y$  were estimated along the axial direction at three sites. The three sites were located at  $x = -4$  mm, 0 mm, and 4 mm, and the  $y$  coordinate was adjusted, depending on the vessel rotation, to achieve estimates through the center of the vessel, see Fig. 7.9. An axial velocity estimator was not implemented.

From each cycle of row emissions, six low resolution images were beamformed and combined to yield one high resolution plane  $HRP_{RC}$ . The same procedure was applied for the column emissions, such that an  $HRP_{CR}$  was generated after each transmit cycle. The spacing between each beamformed point was  $\lambda_z/10$  in both directions. In total, 320  $HRP_{RC}$  and 320  $HRP_{CR}$  were generated at each of the three estimation locations. All

of the  $HRP$  were filtered in the Fourier domain, with two Gaussian windows centered around the frequencies  $\pm 750 \text{ s}^{-1}$ . Subsequently, a spatial Hilbert transformation was performed. Finally, the  $HRP$ 's were fed to the TO estimator, where each velocity estimate was composed of data from 32 transmit cycles. The  $HRP'_{CR}$ s were used for estimating the  $v_x$  velocity component and the  $HRP_{RC}$  were used for estimating the  $v_y$  velocity component.

## 7.7 Results

The smallest relative mean bias ( $\tilde{B}$ ) and lowest relative mean standard deviation ( $\tilde{\sigma}$ ) were found in the  $zy$ -plane at  $x = 0 \text{ mm}$ . Here,  $\tilde{B}_{|v|}$  was 5.8 % and 6.2 % with  $\tilde{\sigma}_{|v|} = 8.5 \%$  and 6.2 % for  $\beta = 0^\circ$  and  $30^\circ$ , respectively (see Fig. 7.10 and 7.11). At  $x = \pm 4 \text{ mm}$ ,  $\tilde{\sigma}_{|v|}$  was less than 10 % for  $\beta = 30^\circ$ , whereas  $\tilde{\sigma}_{|v|}$  was  $\sim 15 \%$  for  $\beta = 0^\circ$ . The highest bias was found at  $x = -4 \text{ mm}$  for  $\beta = 30^\circ$  where  $\tilde{B}_{v_x} = 28.6 \%$  and  $\tilde{B}_{v_y} = 35.6 \%$ .

## 7.8 Conclusion and perspective

Two approaches for volumetric 3-D vector flow estimation were proposed in this chapter. The first, a focused steered emissions sequence combined with the conventional TO estimator showed that 3-D vector flow and flow rates could be estimated in nine planes. The general positive bias was present and the overall flow rate was estimated to be  $53.5 \pm 2.2 \text{ L h}^{-1}$ , which is an 8.7 % bias. An increased bias towards larger steering angles was discovered. It is anticipated, that this effect is due to the rotation of the double oscillating field, which changes with the degree of steering. Future work should focus on optimizing the TO beamforming in accordance with the actual steering angle.

The second proposed method was an SA approach. The proof-of-concept study showed that the best performance of the estimator was achieved along the axial direction originating from the center of the transducer. Here, the absolute velocity magnitude, based on the lateral and elevation components, could be estimated with a relative mean bias of 5.8 % ( $\beta = 0^\circ$ ) and 6.2 % ( $\beta = 30^\circ$ ). Moving away from this position resulted in a significantly increased relative mean bias whereas the mean relative standard deviation actually decreased slightly. This was especially significant for the steered vessel, where  $\tilde{B}_{v_x}$  increased to 28.6 % and  $\tilde{B}_{v_y}$  to 35.6 %. Future work should investigate why a gradually increased bias is seen when moving away from the orego of the transducer and optimize this. A possible explanation could be the degree of rotation of the PSF, when located relatively far away from the center of the transducer.

The approach of separating  $HRV_{RC}$  and  $HRV_{CR}$  for estimating their respective velocity components along the tallest dimension of the transmitting element is not unambiguous. Although this attempt with the applied transmit and processing parameters provided the most robust estimates, other combinations may perform equally or even better. For instance, the high resolution planes could be selected from a high resolution

volume created from the addition of  $HRV_{RC}$  and  $HRV_{CR}$ , or even in a linear combination with  $HRV_{RR}$  and  $HRV_{CC}$ , where the same aperture is used in both Tx and Rx.

The most promising of the two presented methods for volumetric 3-D vector flow imaging using an RC array seems to be the SA approach. Being able to estimate the 3-D velocity vector at every point in the entire volume provides a large flexibility in the analyzing phase. The proposed technique utilizes the large area for each element in the single element transmission sequence, but might be far from an optimal solution. Thus, further optimizing of the transmit stage must be investigated. One of the drawbacks of the single elements transmission sequence, is that the sonified volume for each emission is relatively small compared with e.g. grouping elements in sub-apertures and applying a virtual source either behind or in front of the transducer. The method would presumably benefit from implementing plane waves or diverging waves in the transmit stage compared with single-element emissions. This would sonify a larger region with a higher energy, so that fewer transmit events are needed and the inter frame movement between the added low resolution volumes is reduced as much as possible.

As a final remark, it is very encouraging and promising that volumetric 3-D vector flow techniques could be implemented on a 2-D RC array containing only 124 elements.

### 7.8.1 Perspective

The overall aim of the proposed method is an implementation on a commercial scanner for clinical use. However, even with a fully developed method for off-line volumetric 3-D vector flow estimation, the next step of rendering the data in real-time for an operator requires a solution for two major issues. One major challenge is the computational workload of beamforming a low resolution volume for every transmit event, and furthermore, 3-D volumetric time-varying flow is extremely difficult to visualize and comprehend. The computational load can either be lowered by decreasing the temporal and spatial resolution or by processing the data offline. The second major task requires more collaboration with the operators before a solid solution for rendering volumetric 3-D/4-D vector flow is found. Especially when scanning regions with highly complex flow, e.g. in the heart, an examination in real-time seems overwhelming. A possible future clinical setup could be to pursue the idea of offline data processing, where the flow is investigated after completion of the scan. This is also the standard in 4-D MRI. With this approach the operator could examine the desired transverse, frontal and sagittal plane and, furthermore, move back and forth in time.

Volumetric flow data obtained with ultrasound would also allow for new features in the clinic e.g. pressure gradient estimation. Due to high temporal and spatial resolution required for deriving pressure gradients from velocity fields, ultrasound would be a prime candidate compared with MRI. Yet other applications could be the study of vortices in the heart or volume flow in multiple vessels simultaneously.

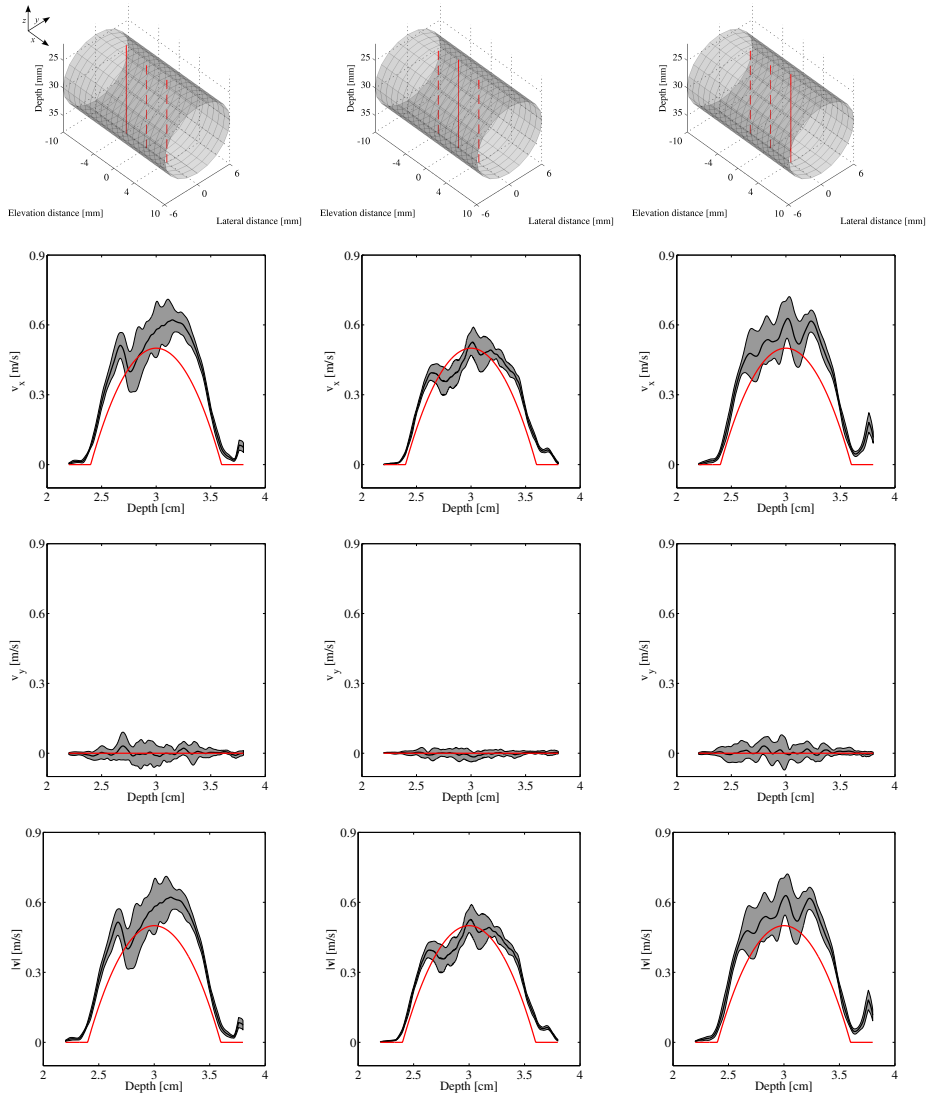


**Figure 7.10:** Upper row: The solid red line illustrates all the points where flow in the corresponding columns is estimated for a straight vessel with no rotation. The subsequent rows show the estimated velocity profile for  $v_x$ ,  $v_y$ , and  $|v|$  (black lines)  $\pm$  one standard deviation (grey area) along with the theoretical profile (red curve) as a function of depth.

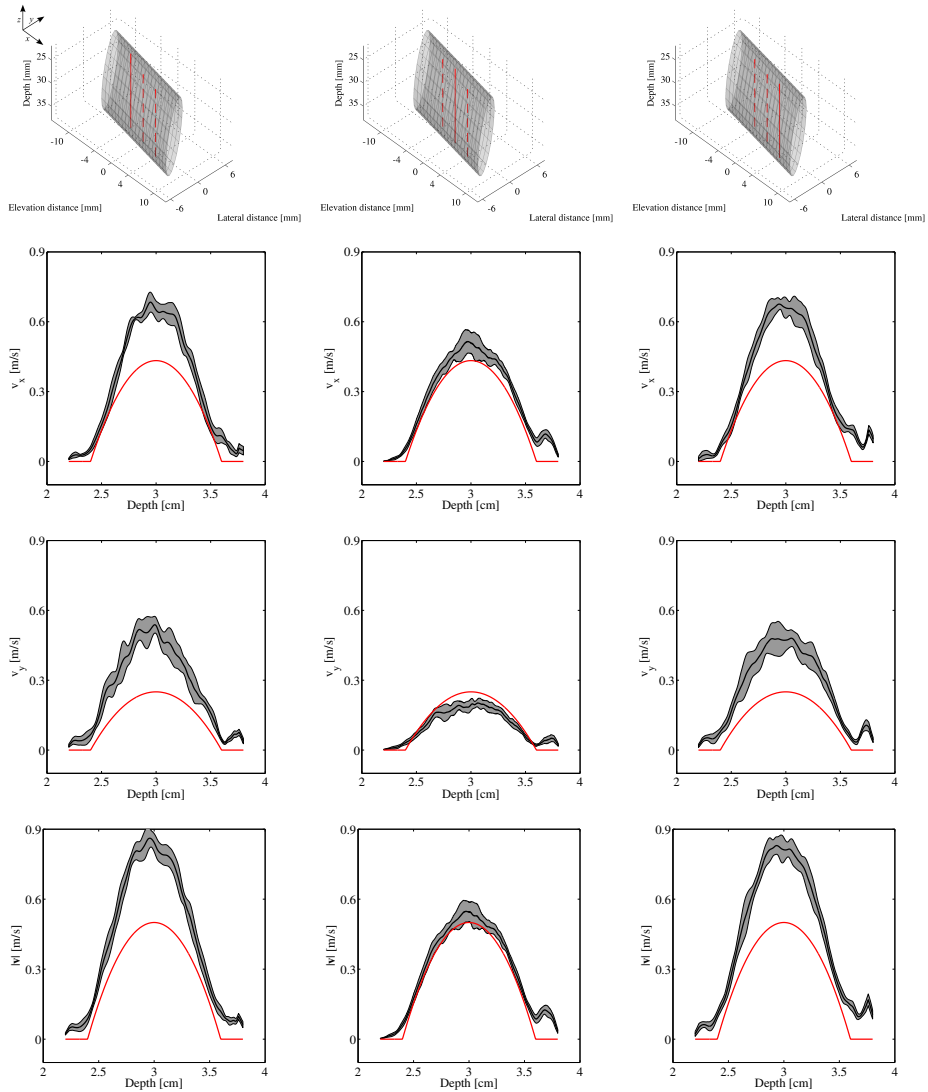


**Figure 7.11:** Upper row: The solid red line illustrates all the points where flow in the corresponding columns is estimated for a vessel rotated  $30^\circ$ . The subsequent rows show the estimated velocity profile for  $v_x$ ,  $v_y$ , and  $|v|$  (black lines)  $\pm$  one standard deviation (grey area) along with the theoretical profile (red curve) as a function of depth.

## CHAPTER 8

# Project Conclusion and Perspectives

---

The main scope of this PhD project titled "3-D Vector Flow Imaging", has been to firmly establish the field of estimating 3-D vector flow using TO.

In chapter 5, a method for estimating 3-D vector flow in a plane at frame rates in the kHz range was proposed. The proposed high frame rate technique relied on the access to continuous data acquisition, which paved the way for new adaptive echo cancelling algorithms. Two measures were validated, the peak velocity and the flow rates. With the 3-D velocity vector, angle-independent peak velocities were estimated and compared against MRI derived through-plane velocities and 1-D spectral Doppler estimates. Flow rates were derived from a manual delineation of the lumen and the velocity component perpendicular to this plane. No assumption about vessel geometry or circular symmetric flow was needed in the calculations. The outcome of the validation study was a negative bias of 3.9% on the flow rate derived from US compared with MRI, whereas estimated peak velocities for 3-D US had a negative bias of 7.5% compared with the reference 1-D spectral Doppler measurement. Here MRI had a negative bias of 23.7% compared with the reference value. The 3-D vector flow method showed promising results, but the dimension and weight of the cables, along with the large computational processing task from the 1024 channel transducer, required a solution to make it feasible for clinical use.

A possible solution was investigated in chapter 6, where 3-D TO vector was implemented on a 62+62 RC addressing prototype probe. A simulation parametric study was performed to optimize the method and identify possible deteriorations of the estimator. The optimized setup was implemented in an experimental setup using a proto-type RC probe. Measurements made with the prototype probe yielded results similar to the simulated ones. A steered sequence, providing 750 frames per second, was used to estimate pulsating flow in a straight vessel phantom. Based on data from 5 pulse cycles, the flow rate was estimated to  $2.3 \pm 0.1$  mL/stroke compared with the expected  $2.54 \pm 0.08$  mL/stroke.

Finally, the 3-D TO vector flow method was expanded from one plane to provide 3-D vector flow information in a full volume. Two approaches were presented; where one was demonstrated in a proof-of-concept experimental setup.

The results presented in this thesis with the 2-D matrix probe demonstrate, that 3-D vector flow can provide angle-independent estimates comparable to MRI. However, the computational load does not currently allow real-time rendering in the clinic. The real-time processing task, on the other hand, could easily be handled by an ultrasound imaging system, if an RC probe was used instead. It is therefore the author's conviction, that RC

arrays possess an unredeemed potential for displaying 3-D vector flow in real-time for clinical use, when some of the teething problems have been solved. Currently, the major drawback with an RC array is the limited field-of-view. However, this can to some degree be solved by expanding the dimensions of the array, or by mounting a diverging lens on the surface of the transducer.

## 8.1 Perspective

As a developer of 3-D vector flow methods, it is tempting to state that these techniques are the future in the clinic. Not only do these angle independent methods reduce operator decisions, they also provide the true velocities, since all velocity components are estimated, which improves the precision and accuracy. However, a great effort still remains before 3-D vector flow is used on a daily basis in the clinics. First of all, it will be difficult to change habits and convince operators to use vector flow technique at first instance, since 1-D CFM or spectral Doppler has been around for so many years. Secondly, an improved visualization tool needs to be developed for the clinicians to comprehend the extra information provided with 3-D vector flow. Even more complicated is the task of visualizing and analysing volumetric 3-D vector flow. Here, a possible solution might be to sacrifice the real-time rendering and instead perform the desired scan and analyse it afterwards. This is currently the case with other imaging modalities, such as MRI and CT, where a volumetric acquisition is analysed offline, so that any scan plane can be examined.

The benefits of having 3-D vector flow estimates are many. 3-D velocity data can be applied directly to estimate volume flow, peak velocities, vortex analysis and diagnosis of cardiovascular diseases, all angle independently and with reduced operator dependency compared with 2-D techniques. Moreover, the 3-D velocity data can be further processed to yield pressure gradient estimates obtained non-invasively. Whether the technique becomes widespread relies greatly on reducing the cost of the technology and making it easily accessible and intuitive to use. Here, RC arrays possess a large potential, especially if fabrication of these array types is performed with the cost efficient CMUT technology. Lastly, future work should investigate the feasibility of implementing the proposed methods for 3-D vector flow estimation on an RC array with a diverging lens, to obtain a complete VFI solution with a satisfactory field-of-view.

# Bibliography

---

## References from Chapter 1

- Hansen, K., H. Møller-Sørensen, J. Kjaergaard, M. Jensen, J. Lund, M. Pedersen, J. Jensen, and M. Nielsen (2016). “Intraoperative vector flow imaging using ultrasound of the ascending aorta among 40 patients with normal, stenotic and replaced aortic valves”. In: *Ultrasound Med. Biol.* Accepted (cit. on pp. 2, 3).
- Jensen, J. A. and P. Munk (1998). “A New Method for Estimation of Velocity Vectors”. In: *IEEE Trans. Ultrason., Ferroelec., Freq. Contr.* 45, pp. 837–851 (cit. on p. 6).
- Jensen, J., M. B. Stuart, and J. A. Jensen (2015). “High Frame Rate Vector Velocity Estimation using Plane Waves and Transverse Oscillation”. In: *Proc. IEEE Ultrason. Symp.* Pp. 1–4. DOI: 10.1109/ultsym.2015.0423 (cit. on p. 2).
- WHO (2011). *Global status report on noncommunicable diseases 2010* (cit. on p. 1).

## References from Chapter 2

- Bae, M. H. and M. K. Jeong (2000). “A study of synthetic-aperture imaging with virtual source elements in B-mode ultrasound imaging systems”. In: *IEEE Trans. Ultrason., Ferroelec., Freq. Contr.* Vol. 47, pp. 1510–1519 (cit. on p. 15).
- Bennett, S., D. K. Peterson, D. Corl, and G. S. Kino (1982). “A real-time synthetic aperture digital acoustic imaging system”. In: *Acoust. Imaging*. Ed. by P. Alais and A. F. Metherell. Vol. 10, pp. 669–692 (cit. on p. 15).
- Bonnefous, O. and P. Pesqué (1986). “Time Domain Formulation of Pulse-Doppler Ultrasound and Blood Velocity Estimation by Cross Correlation”. In: *Ultrason. Imaging* 8, pp. 73–85. DOI: 10.1016/0161-7346(86)90001-5 (cit. on p. 12).
- Capineri, L., M. Scabia, and L. Masotti (2002). “A Doppler system for dynamic vector velocity maps”. In: *Ultrasound Med. Biol.* 28.2, pp. 237–248 (cit. on p. 15).
- Correia, M., J. Provost, M. Tanter, and M. Pernot (2016). “In-vivo 4D Ultrafast Vector Flow Imaging: quantitative assessment of arterial blood flow”. In: *Proc. IEEE Ultrason. Symp.* Pp. 1–4 (cit. on p. 15).
- Dotti, D., E. Gatti, V. Svelto, A. Uggè, and P. Vidali (1976). “Blood flow measurements by ultrasound correlation techniques”. In: *Energia Nucleare* 23.11, pp. 571–575 (cit. on p. 12).

- Ekroll, I. K., A. Swillens, P. Segers, T. Dahl, H. Torp, and L. Løvstakken (2013). “Simultaneous quantification of flow and tissue velocities based on multi-angle plane wave imaging”. In: *IEEE Trans. Ultrason., Ferroelec., Freq. Contr.* 60.4, pp. 727–738 (cit. on p. 15).
- Fadnes, S., I. K. Ekroll, S. A. Nytnes, H. Torp, and L. Løvstakken (2015). “Robust Angle-Independent Blood Velocity Estimation Based on Dual-Angle Plane Wave Imaging”. In: *IEEE Trans. Ultrason., Ferroelec., Freq. Contr.* 62.10, pp. 1757–1767. DOI: 10.1109/tuffc.2015.007108 (cit. on p. 15).
- Fadnes, S., S. A. Nytnes, H. Torp, and L. Lovstakken (2014). “Shunt Flow Evaluation in Congenital Heart Disease Based on Two-Dimensional Speckle Tracking”. In: *Ultrasound Med. Biol.* 40.10, pp. 2379–2391. DOI: 10.1016/j.ultrasmedbio.2014.03.029 (cit. on p. 14).
- Fahrbach, K. (1970). “Ein Beitrag Zur Blutgeschwindigkeitsmessung unter Anwendung des Dopplereffektes”. In: *Elektromedizin* 15.1, pp. 26–36 (cit. on p. 14).
- Flynn, J., R. Daigle, L. Pflugrath, P. Kaczkowski, and K. Linkhart (2011). “Estimation and display for vector Doppler imaging using planewave transmissions”. In: *Proc. IEEE Ultrason. Symp.* Pp. 413–418 (cit. on p. 15).
- Hansen, K. L., J. Udesen, F. Gran, J. A. Jensen, and M. B. Nielsen (2009). “In-vivo examples of flow patterns with the fast vector velocity ultrasound method”. In: *Ultraschall in Med.* 30, pp. 471–476 (cit. on p. 14).
- Hansen, P. L., G. Cross, and L. H. Light (1974). “Beam-angle independent Doppler velocity measurement in superficial vessels”. In: *Clinical Blood Flow Measurement*. London: Sector Publishing (cit. on p. 14).
- Jensen, J. A. (1996). *Estimation of Blood Velocities Using Ultrasound: A Signal Processing Approach*. New York: Cambridge University Press (cit. on p. 10).
- Jensen, J. A. and S. I. Nikolov (2002). “Transverse flow imaging using synthetic aperture directional beamforming”. In: *Proc. IEEE Ultrason. Symp.* Pp. 1488–1492 (cit. on p. 16).
- (2004). “Directional Synthetic Aperture Flow Imaging”. In: *IEEE Trans. Ultrason., Ferroelec., Freq. Contr.* 51, pp. 1107–1118 (cit. on p. 14).
- Jensen, J. A., S. Nikolov, K. L. Gammelmark, and M. H. Pedersen (2006). “Synthetic Aperture Ultrasound Imaging”. In: *Ultrasonics* 44, e5–e15 (cit. on p. 14).
- Jensen, J. A. and N. Oddershede (2006). “Estimation of velocity vectors in synthetic aperture ultrasound imaging”. In: *IEEE Trans. Med. Imag.* 25, pp. 1637–1644 (cit. on p. 14).
- Kasai, C., K. Namekawa, A. Koyano, and R. Omoto (1985). “Real-Time Two-Dimensional Blood Flow Imaging using an Autocorrelation Technique”. In: *IEEE Trans. Son. Ultrason.* 32, pp. 458–463 (cit. on p. 10).
- Kortbek, J. and J. A. Jensen (2006). “Estimation of velocity vector angles using the directional cross-correlation method”. In: *IEEE Trans. Ultrason., Ferroelec., Freq. Contr.* 53, pp. 2036–2049 (cit. on p. 14).

- Namekawa, K., C. Kasai, M. Tsukamoto, and A. Koyano (1982). "Realtime bloodflow imaging system utilizing autocorrelation techniques". In: *Ultrasound '82*. Ed. by R. Lerski and P. Morley. New York: Pergamon Press, pp. 203–208 (cit. on p. 10).
- Nikolov, S. I. (2001). "Synthetic Aperture Tissue and Flow Ultrasound Imaging". PhD thesis. 2800, Lyngby, Denmark: Ørsted•DTU, Technical University of Denmark (cit. on pp. 15, 16).
- Nikolov, S. I. and J. A. Jensen (2001). "Velocity estimation using synthetic aperture imaging". In: *Proc. IEEE Ultrason. Symp.* Pp. 1409–1412 (cit. on p. 14).
- (2002). "Virtual ultrasound sources in high-resolution ultrasound imaging". In: *Proc. SPIE - Progress in biomedical optics and imaging*. Vol. 3, pp. 395–405 (cit. on p. 15).
- Pastorelli, A., G. Torricelli, M. Scabia, E. Biagi, and L. Masotti (2008). "A real-time 2-D vector Doppler system for clinical experimentation". In: *IEEE Trans. Med. Imag.* 27.10, pp. 1515–1524 (cit. on p. 15).
- Peterson, D. K. and G. S. Kino (1984). "Real-Time Digital Image Reconstruction: A Description of Imaging Hardware and an Analysis of Quantization Errors". In: *IEEE Trans. Son. Ultrason.* 31.4, pp. 337–351. DOI: 10.1109/T-SU.1984.31514 (cit. on p. 15).
- Phillips, P. J., A. P. Kadi, and O. T. von Ramm (1995). "Feasibility study for a two-dimensional diagnostic ultrasound velocity mapping system". In: *Ultrasound Med. Biol.* 21.2, pp. 217–229. DOI: [http://dx.doi.org/10.1016/S0301-5629\(94\)00113-8](http://dx.doi.org/10.1016/S0301-5629(94)00113-8) (cit. on p. 14).
- Picot, P. A. and P. M. Embree (1994). "Quantitative volume flow estimation using velocity profiles". In: *IEEE Trans. Ultrason., Ferroelec., Freq. Contr.* 41, pp. 340–345 (cit. on p. 12).
- Provost, J., C. Papadacci, J. E. Arango, M. Imbault, M. Fink, J. L. Gennisson, M. Tanter, and M. Pernot (2014). "3-D ultrafast ultrasound imaging in vivo". In: *Phys. Med. Biol.* 59.19, pp. L1–L13 (cit. on p. 15).
- Ricci, S., L. Bassi, and P. Tortoli (2014). "Real-time vector velocity assessment through multigate Doppler and plane waves". In: *IEEE Trans. Ultrason., Ferroelec., Freq. Contr.* 61.2, pp. 314–324 (cit. on p. 15).
- Scabia, M., M. Calzolari, L. Capineri, L. Masotti, and A. Fort (2000). "A real-time two-dimensional pulsed-wave Doppler system". In: *Ultrasound Med. Biol.* 26.1, pp. 121–131 (cit. on p. 14).
- Sherwin, C. W., J. P. Ruina, and D. Rawcliffe (1962). "Some early developements in synthetic aperture radar systems". In: *IRE Trans. Mil. Elect.* MIL-6.2, pp. 111–115 (cit. on p. 15).
- Tanter, M., J. Bercoff, L. Sandrin, and M. Fink (2002). "Ultrafast compound imaging for 2-D motion vector estimation: application to transient elastography". In: *IEEE Trans. Ultrason., Ferroelec., Freq. Contr.* 49, pp. 1363–1374 (cit. on p. 15).
- Trahey, G. E., J. W. Allison, and O. T. von Ramm (1987). "Angle independent ultrasonic detection of blood flow". In: *IEEE Trans. Biomed. Eng.* BME-34, pp. 965–967 (cit. on p. 13).

- Udesen, J., F. Gran, K. L. Hansen, J. A. Jensen, C. Thomsen, and M. B. Nielsen (2008). “High Frame-Rate Blood Vector Velocity Imaging Using Plane Waves: simulations and preliminary experiments”. In: *IEEE Trans. Ultrason., Ferroelec., Freq. Contr.* 55.8, pp. 1729–1743 (cit. on p. 14).
- Villagomez-Hoyos, C. A., M. B. Stuart, K. L. Hansen, M. B. Nielsen, and J. A. Jensen (2016). “Accurate Angle Estimator for High Frame Rate 2-D Vector Flow Imaging”. In: *IEEE Trans. Ultrason., Ferroelec., Freq. Contr.* 63.6, pp. 842–853 (cit. on p. 14).
- Wigen, M. and L. Løvstakken (2016). “In vivo three-dimensional intra-cardiac vector flow imaging using a 2D matrix array transducer”. In: *Proc. IEEE Ultrason. Symp.* Pp. 1–4 (cit. on p. 14).
- Yiu, B. Y., S. S. Lai, and A. C. Yu (2014). “Vector projectile imaging: time-resolved dynamic visualization of complex flow patterns.” In: *Ultrasound Med. Biol.* 40.9, pp. 2295–2309 (cit. on p. 15).
- Ylitalo, J. T. and H. Ermert (1994). “Ultrasound synthetic aperture imaging: Monostatic approach”. In: *IEEE Trans. Ultrason., Ferroelec., Freq. Contr.* 41, pp. 333–339 (cit. on p. 15).

### References from Chapter 3

- Alessandrini, M., A. Basarab, L. Boussel, X. Guo, A. Serusclat, D. Friboulet, D. Kouamé, O. Bernard, and H. Liebgott (2014). “A New Technique for the Estimation of Cardiac Motion in Echocardiography Based on Transverse Oscillations: A Preliminary Evaluation In Silico and a Feasibility Demonstration In Vivo”. In: *IEEE Trans. Med. Imag.* 33.5, pp. 1148–1162 (cit. on p. 25).
- Anderson, M. E. (1998). “Multi-dimensional velocity estimation with ultrasound using spatial quadrature”. In: *IEEE Trans. Ultrason., Ferroelec., Freq. Contr.* 45, pp. 852–861 (cit. on p. 19).
- Basarab, A., P. Gueth, H. Liebgott, and P. Delachartre (2009). “Phase-based block matching applied to motion estimation with unconventional beamforming strategies”. In: *IEEE Trans. Ultrason., Ferroelec., Freq. Contr.* 56.5, pp. 945–957 (cit. on p. 25).
- Bonnefous, O. (1988). “Measurement of the complete (3D) velocity vector of blood flows”. In: *Proc. IEEE Ultrason. Symp.* Pp. 795–799 (cit. on p. 25).
- Jensen, J. A. (2001). “A New Estimator for Vector Velocity Estimation”. In: *IEEE Trans. Ultrason., Ferroelec., Freq. Contr.* 48.4, pp. 886–894 (cit. on pp. 19, 22).
- (2015). “Improved Vector Velocity Estimation using Directional Transverse Oscillation”. In: *Proc. IEEE Ultrason. Symp.* IEEE, pp. 1–4. DOI: 10.1109/ULTSYM.2015.00111 (cit. on p. 25).
- (2016). “Directional Transverse Oscillation Vector Flow Estimation”. In: *IEEE Trans. Ultrason., Ferroelec., Freq. Contr.* 63, Submitted (cit. on p. 25).
- Jensen, J. A., A. H. Brandt, and M. B. Nielsen (2015). “Convex Array Vector Velocity Imaging Using Transverse Oscillation and Its Optimization”. In: *IEEE Trans. Ultra-*

- son., Ferroelec., Freq. Contr.* 62.12, pp. 2043–2053. DOI: 10.1109/TUFFC.2015.006970 (cit. on p. 23).
- Jensen, J. A. and P. Munk (1998). “A New Method for Estimation of Velocity Vectors”. In: *IEEE Trans. Ultrason., Ferroelec., Freq. Contr.* 45, pp. 837–851 (cit. on p. 19).
- Jensen, J., M. B. Stuart, and J. A. Jensen (2015). “High Frame Rate Vector Velocity Estimation using Plane Waves and Transverse Oscillation”. In: *Proc. IEEE Ultrason. Symp.* Pp. 1–4. DOI: 10.1109/ultsym.2015.0423 (cit. on p. 25).
- Kasai, C., K. Namekawa, A. Koyano, and R. Omoto (1985). “Real-Time Two-Dimensional Blood Flow Imaging using an Autocorrelation Technique”. In: *IEEE Trans. Son. Ultrason.* 32, pp. 458–463 (cit. on p. 23).
- Lenge, M., A. Ramalli, P. Tortoli, C. Cachard, and H. Liebgott (2015). “Plane-Wave Transverse Oscillation for High-Frame-Rate 2-D Vector Flow Imaging”. In: *IEEE Trans. Ultrason., Ferroelec., Freq. Contr.* 62.12, pp. 2126–2137 (cit. on p. 25).
- Liebgott, H. (2010). “Fourier domain beamforming for transverse-oscillations”. In: *Proc. IEEE Ultrason. Symp.* Pp. 1755–1758 (cit. on p. 26).
- Liebgott, H., J. Fromageau, J. E. Wilhjelm, D. Vray, and P. Delachartre (2005). “Beamforming scheme for 2D displacement estimation in ultrasound imaging”. In: *EURASIP J. Adv. Signal Process.* 2005.8, pp. 1212–1220 (cit. on p. 25).
- Liebgott, H., A. B. Salem, A. Basarab, H. Gao, P. Claus, J. D’hooge, P. Delachartre, and D. Friboulet (2009). “Tangential sound field oscillations for 2D motion estimation in echocardiography”. In: *Proc. IEEE Ultrason. Symp.* Pp. 498–501 (cit. on p. 25).
- Liebgott, H., J. Wilhjelm, J. A. Jensen, D. Vray, and P. Delachartre (2007). “PSF dedicated to estimation of displacement vectors for tissue elasticity imaging with ultrasound”. In: *IEEE Trans. Ultrason., Ferroelec., Freq. Contr.* 54.4, pp. 746–756 (cit. on p. 25).
- Pihl, M. J., J. Marcher, and J. A. Jensen (2012). “Phased-Array Vector Velocity Estimation Using Transverse Oscillations”. In: *IEEE Trans. Ultrason., Ferroelec., Freq. Contr.* 59.12, pp. 2662–2675 (cit. on p. 21).
- Salles, S., A. J. Y. Chee, D. Garcia, A. C. H. Yu, D. Vray, and H. Liebgott (2015). “2-D arterial wall motion imaging using ultrafast ultrasound and transverse oscillations”. In: *IEEE Trans. Ultrason., Ferroelec., Freq. Contr.* 62.6, pp. 1047–1058. DOI: 10.1109/TUFFC.2014.006910 (cit. on p. 25).
- Salles, S., H. Liebgott, D. Garcia, and D. Vray (2015). “Full 3-D Transverse Oscillations: A Method for Tissue Motion Estimation”. In: *IEEE Trans. Ultrason., Ferroelec., Freq. Contr.* 62.8, pp. 1473–1485 (cit. on p. 25).
- Shiina, T., K. Kondo, and M. Yamakawa (2009). “Displacement Vector Measurement based on Two-dimensional Modulation Method with Hyperbolic Scanning”. In: *Proc. IEEE Ultrason. Symp.* Pp. 2284–2287 (cit. on p. 25).

## References from Chapter 4

- Austeng, A. and S. Holm (2002). “Sparse 2-D arrays for 3-D phased array imaging - design methods”. In: *IEEE Trans. Ultrason., Ferroelec., Freq. Contr.* 49.8, pp. 1073–1086 (cit. on p. 31).
- Chen, A. I. H., L. L. P. Wong, A. S. Logan, and J. T. W. Yeow (2011). “A CMUT-based real-time volumetric ultrasound imaging system with row-column addressing”. In: *Proc. IEEE Ultrason. Symp.* Pp. 1755–1758 (cit. on p. 32).
- Christiansen, T. L., M. F. Rasmussen, J. P. Bagge, L. N. Moesner, J. A. Jensen, and E. V. Thomsen (2015). “3-D Imaging Using Row–Column–Addressed Arrays With Integrated Apodization — Part II: Transducer Fabrication and Experimental Results”. In: *IEEE Trans. Ultrason., Ferroelec., Freq. Contr.* 62.5, pp. 959–971 (cit. on pp. 28, 32).
- Davidson, R. E., J. A. Jensen, and S. W. Smith (1994). “Two-Dimensional Random Arrays for Real Time Volumetric Imaging”. In: *Ultrason. Imaging* 16.3, pp. 143–163 (cit. on p. 31).
- Démoré, C. E. M., A. Joyce, K. Wall, and G. Lockwood (2009). “Real-time volume imaging using a crossed electrode array”. In: *IEEE Trans. Ultrason., Ferroelec., Freq. Contr.* 56.6, pp. 1252–1261 (cit. on p. 31).
- Halvorsrod, T., W. Luzi, and T. Lande (2005). “A log-domain beamformer for medical ultrasound imaging systems”. In: *IEEE Trans. Circuits Syst. I, Reg. Papers* 52.12, pp. 2563–2575. DOI: 10.1109/TCSI.2005.857544 (cit. on p. 30).
- Holbek, S., T. L. Christiansen, M. Engholm, A. Lei, M. B. Stuart, C. Beers, L. N. Moesner, J. P. Bagge, E. V. Thomsen, and J. A. Jensen (2016). “3-D Vector Flow Using a Row-Column Addressed CMUT Array”. In: *Proc. SPIE Med. Imag.* Vol. 9790, pages (cit. on p. 29).
- Iversen, D., F. Lindseth, G. Unsgaard, H. Torp, and L. Lovstakken (2013). “Model-Based Correction of Velocity Measurements in Navigated 3-D Ultrasound Imaging During Neurosurgical Interventions”. In: *IEEE Trans. Med. Imag.* 32.9, pp. 1622–1631 (cit. on p. 29).
- Jensen, J. A., H. Holtén-Lund, R. T. Nilsson, M. Hansen, U. D. Larsen, R. P. Domsten, B. G. Tomov, M. B. Stuart, S. I. Nikolov, M. J. Pihl, Y. Du, J. H. Rasmussen, and M. F. Rasmussen (2013). “SARUS: A Synthetic Aperture Real-Time Ultrasound System”. In: *IEEE Trans. Ultrason., Ferroelec., Freq. Contr.* 60.9, pp. 1838–1852 (cit. on p. 30).
- Karadayi, K., R. Managuli, and Y. Kim (2009). “Three-Dimensional Ultrasound: From Acquisition to Visualization and From Algorithms to Systems”. In: *IEEE Rev Biomed Eng* 2, pp. 23–39 (cit. on p. 30).
- Lockwood, G. R., P.-C. Li, M. O’Donnell, and F. S. Foster (1996). “Optimizing the Radiation Pattern of Sparse Periodic Linear Arrays”. In: *IEEE Trans. Ultrason., Ferroelec., Freq. Contr.* 43, pp. 7–14 (cit. on p. 31).

- Lockwood, G. R., J. R. Talman, and S. S. Brunke (1998). "Real-time 3-D ultrasound imaging using sparse synthetic aperture beamforming". In: *IEEE Trans. Ultrason., Ferroelec., Freq. Contr.* 45, pp. 980–988 (cit. on p. 29).
- Logan, A. S., L. L. P. Wong, and J. T. W. Yeow (2009). "2-D CMUT wafer bonded imaging arrays with a row-column addressing scheme". In: *Proc. IEEE Ultrason. Symp.* Pp. 984–987 (cit. on p. 28).
- Merz, E., F. Bahlmann, and G. Weber (1995). "Volume scanning in the evaluation of fetal malformations: a new dimension in prenatal diagnosis." In: *Ultrasound Obstet. Gyn.* 5, pp. 222–227 (cit. on p. 29).
- Morton, C. E. and G. R. Lockwood (2003). "Theoretical assessment of a crossed electrode 2-D array for 3-D imaging". In: *Proc. IEEE Ultrason. Symp.* Pp. 968–971 (cit. on p. 31).
- Provost, J., C. Papadacci, J. E. Arango, M. Imbault, M. Fink, J. L. Gennisson, M. Tanter, and M. Pernot (2014). "3-D ultrafast ultrasound imaging in vivo". In: *Phys. Med. Biol.* 59.19, pp. L1–L13 (cit. on p. 30).
- Ramalli, A., E. Boni, A. Savoia, and P. Tortoli (2015). "Density-Tapered Spiral Arrays for Ultrasound 3-D imaging". In: *IEEE Trans. Ultrason., Ferroelec., Freq. Contr.* 62.8, pp. 1580–1588 (cit. on p. 31, 32).
- Rasmussen, M. F., T. L. Christiansen, E. V. Thomsen, and J. A. Jensen (2015). "3-D Imaging Using Row-Column-Addressed Arrays With Integrated Apodization — Part I: Apodization Design and Line Element Beamforming". In: *IEEE Trans. Ultrason., Ferroelec., Freq. Contr.* 62.5, pp. 947–958 (cit. on p. 28).
- Rasmussen, M. F. and J. A. Jensen (2013). "3D ultrasound imaging performance of a row-column addressed 2D array transducer: a simulation study". In: *Proc. SPIE Med. Imag.* 86750C, pp. 1–11 (cit. on p. 33).
- Sampaleanu, A., P. Zhang, A. Kshirsagar, W. Moussa, and R. Zemp (2014). "Top-orthogonal-to-bottom-electrode (TOBE) CMUT arrays for 3-D ultrasound imaging." In: *IEEE Trans. Ultrason., Ferroelec., Freq. Contr.* 61.2, pp. 266–276 (cit. on p. 32).
- Savoia, A. S., G. Caliano, and M. Pappalardo (2012). "A CMUT Probe for Medical Ultrasonography: From Microfabrication to System Integration". In: *IEEE Trans. Ultrason., Ferroelec., Freq. Contr.* 59.6, pp. 1127–1138 (cit. on p. 28).
- Savord, B. and R. Solomon (2003). "Fully sampled matrix transducer for real time 3D ultrasonic imaging". In: *Proc. IEEE Ultrason. Symp.* Vol. 1, pp. 945–953 (cit. on p. 30).
- Seo, C. H. and J. T. Yen (2006). "64 x 64 2-D array transducer with row-column addressing". In: *Proc. IEEE Ultrason. Symp.* Vol. 1, pp. 74–77 (cit. on p. 32).
- (2007). "256x256 2-D array transducer with row-column addressing for 3-D imaging". In: *Proc. IEEE Ultrason. Symp.* Pp. 2381–2384 (cit. on p. 32).
- (2008). "Recent results using a 256 x 256 2-D array transducer for 3-D Rectilinear Imaging". In: *Proc. IEEE Ultrason. Symp.* Vol. 1-4, pp. 1146–1149 (cit. on p. 32).

- Smith, S. W., H. G. Pavy, and O. T. von Ramm (1991). “High speed ultrasound volumetric imaging system – Part I: Transducer design and beam steering”. In: *IEEE Trans. Ultrason., Ferroelec., Freq. Contr.* 38, pp. 100–108 (cit. on p. 30).
- von Ramm, O. T., S. W. Smith, and H. G. Pavy (1991). “High speed ultrasound volumetric imaging system – Part II: Parallel processing and image display”. In: *IEEE Trans. Ultrason., Ferroelec., Freq. Contr.* 38, pp. 109–115 (cit. on p. 30).
- Yen, J. T., C. H. Seo, S. I. Awad, and J. S. Jeong (2009). “A dual-layer transducer array for 3-D rectilinear imaging”. In: *IEEE Trans. Ultrason., Ferroelec., Freq. Contr.* 56.1, pp. 204–212 (cit. on p. 32).

## References from Chapter 5

- Correia, M., J. Provost, M. Tanter, and M. Pernot (2016). “In-vivo 4D Ultrafast Vector Flow Imaging: quantitative assessment of arterial blood flow”. In: *Proc. IEEE Ultrason. Symp.* Pp. 1–4 (cit. on p. 35).
- Evans, D. H., J. A. Jensen, and M. B. Nielsen (2011). “Ultrasonic colour Doppler imaging”. In: *Interface Focus* 1.4, pp. 490–502 (cit. on p. 52).
- FDA (2008). *Information for Manufacturers Seeking Marketing Clearance of Diagnostic Ultrasound Systems and Transducers*. Tech. rep. Center for Devices, Radiological Health, United States Food, and Drug Administration (cit. on p. 46).
- Hansen, K., H. Møller-Sørensen, J. Kjaergaard, M. Jensen, J. Lund, M. Pedersen, J. Jensen, and M. Nielsen (2016). “Intraoperative vector flow imaging using ultrasound of the ascending aorta among 40 patients with normal, stenotic and replaced aortic valves”. In: *Ultrasound Med. Biol.* Accepted (cit. on p. 52).
- Hoeks, A. P. G., J. J. W. van de Vorst, A. Dabekaussen, P. J. Brands, and R. S. Reneman (1991). “An efficient algorithm to remove low frequency Doppler signal in digital Doppler systems”. In: *Ultrason. Imaging* 13, pp. 135–145 (cit. on p. 38).
- Holbek, S., C. Ewertsen, H. Bouzari, M. Pihl, K. Hansen, M. B. Stuart, M. Stuart, M. Nielsen, and J. A. Jensen (2016). “Ultrasonic 3-D vector flow method for quantitative in vivo peak velocity and flow rate estimation”. In: *IEEE Trans. Ultrason., Ferroelec., Freq. Contr.* In press (cit. on pp. 38, 45, 48–50).
- Jensen, J. A. (1996). *Estimation of Blood Velocities Using Ultrasound: A Signal Processing Approach*. New York: Cambridge University Press (cit. on p. 41).
- (2001). “A New Estimator for Vector Velocity Estimation”. In: *IEEE Trans. Ultrason., Ferroelec., Freq. Contr.* 48.4, pp. 886–894 (cit. on p. 35).
- Jensen, J. A., H. Holtén-Lund, R. T. Nilsson, M. Hansen, U. D. Larsen, R. P. Domsten, B. G. Tomov, M. B. Stuart, S. I. Nikolov, M. J. Pihl, Y. Du, J. H. Rasmussen, and M. F. Rasmussen (2013). “SARUS: A Synthetic Aperture Real-Time Ultrasound System”. In: *IEEE Trans. Ultrason., Ferroelec., Freq. Contr.* 60.9, pp. 1838–1852 (cit. on p. 43).
- Jensen, J. A. and P. Munk (1998). “A New Method for Estimation of Velocity Vectors”. In: *IEEE Trans. Ultrason., Ferroelec., Freq. Contr.* 45, pp. 837–851 (cit. on p. 35).

- Jensen, J. A., M. F. Rasmussen, M. J. Pihl, S. Holbek, C. A. Villagomez-Hoyos, D. P. Bradway, M. B. Stuart, and B. G. Tomov (2016). “Safety Assessment of Advanced Imaging Sequences, I: Measurements”. In: *IEEE Trans. Ultrason., Ferroelec., Freq. Contr.* 63.1, pp. 110–119 (cit. on p. 46).
- Jensen, J., J. B. Olesen, M. B. Stuart, P. M. Hansen, M. B. Nielsen, and J. A. Jensen (2016). “Vector velocity volume flow estimation: Sources of error and corrections applied for arteriovenous fistulas”. In: *Ultrasonics* 70, pp. 136–146. DOI: <http://dx.doi.org/10.1016/j.ultras.2016.04.023> (cit. on p. 52).
- Nikolov, S. I. and J. A. Jensen (2001). “Velocity estimation using synthetic aperture imaging”. In: *Proc. IEEE Ultrason. Symp.* Pp. 1409–1412 (cit. on p. 36).
- (2003). “In-vivo Synthetic Aperture Flow Imaging in Medical Ultrasound”. In: *IEEE Trans. Ultrason., Ferroelec., Freq. Contr.* 50.7, pp. 848–856 (cit. on p. 36).
- Olesen, J. B., C. A. Villagomez-Hoyos, M. S. Traberg, and J. A. Jensen (2015). “Non-invasive Estimation of Pressure Changes along a Streamline using Vector Velocity Ultrasound”. In: *Proc. IEEE Ultrason. Symp.* Pp. 1–4 (cit. on p. 52).
- Pihl, M. J. and J. A. Jensen (2014). “A Transverse Oscillation Approach for Estimation of Three-Dimensional Velocity Vectors. Part I: Concept and Simulation Study”. In: *IEEE Trans. Ultrason., Ferroelec., Freq. Contr.* 61, pp. 1599–1607 (cit. on pp. 35, 37).
- Pihl, M. J., M. B. Stuart, B. G. Tomov, P. M. Hansen, M. B. Nielsen, and J. A. Jensen (2013). “In Vivo Three-Dimensional Velocity Vector Imaging and Volumetric Flow Rate Measurements”. In: *Proc. IEEE Ultrason. Symp.* Pp. 72–75 (cit. on p. 36).
- Pihl, M. J., M. B. Stuart, B. G. Tomov, M. F. Rasmussen, and J. A. Jensen (2014). “A Transverse Oscillation Approach for Estimation of Three-Dimensional Velocity Vectors. Part II: Experimental Validation”. In: *IEEE Trans. Ultrason., Ferroelec., Freq. Contr.* 51.10, pp. 1608–1618 (cit. on pp. 35, 37).
- Provost, J., C. Papadacci, J. E. Arango, M. Imbault, M. Fink, J. L. Gennisson, M. Tanter, and M. Pernot (2014). “3-D ultrafast ultrasound imaging in vivo”. In: *Phys. Med. Biol.* 59.19, pp. L1–L13 (cit. on p. 35).
- Villagomez-Hoyos, C. A. (2016). “Synthetic Aperture Vector Flow Imaging”. PhD thesis. Technical University of Denmark. URL: <http://findit.dtu.dk/en/catalog/2347162876> (cit. on p. 40).

## References from Chapter 6

- Chee, R. K. W., A. Sampaleanu, D. Rishi, and R. J. Zemp (2014). “Top Orthogonal to Bottom Electrode (TOBE) 2-D CMUT Arrays for 3-D Photoacoustic Imaging”. In: *IEEE Trans. Ultrason., Ferroelec., Freq. Contr.* 61.8, pp. 1393–1395 (cit. on p. 55).
- Christiansen, T. L., M. F. Rasmussen, J. P. Bagge, L. N. Moesner, J. A. Jensen, and E. V. Thomsen (2015). “3-D Imaging Using Row–Column-Addressed Arrays With Integrated Apodization — Part II: Transducer Fabrication and Experimental Results”. In: *IEEE Trans. Ultrason., Ferroelec., Freq. Contr.* 62.5, pp. 959–971 (cit. on p. 55).

- Holbek, S., T. L. Christiansen, M. B. Stuart, C. Beers, E. V. Thomsen, and J. A. Jensen (2016). “3-D Vector Flow Estimation with Row-Column Addressed Arrays”. In: *IEEE Trans. Ultrason., Ferroelec., Freq. Contr.* Accepted (cit. on p. 66).
- Jensen, J. A. (1996). “Field: A Program for Simulating Ultrasound Systems”. In: *Med. Biol. Eng. Comp.* 10th Nordic-Baltic Conference on Biomedical Imaging, Vol. 4, Supplement 1, Part 1, pp. 351–353 (cit. on p. 61).
- (2001). “A New Estimator for Vector Velocity Estimation”. In: *IEEE Trans. Ultrason., Ferroelec., Freq. Contr.* 48.4, pp. 886–894 (cit. on p. 55).
- Jensen, J. A. and P. Munk (1998). “A New Method for Estimation of Velocity Vectors”. In: *IEEE Trans. Ultrason., Ferroelec., Freq. Contr.* 45, pp. 837–851 (cit. on p. 55).
- Jensen, J. A., M. F. Rasmussen, M. J. Pihl, S. Holbek, C. A. Villagomez-Hoyos, D. P. Bradway, M. B. Stuart, and B. G. Tomov (2016). “Safety Assessment of Advanced Imaging Sequences, I: Measurements”. In: *IEEE Trans. Ultrason., Ferroelec., Freq. Contr.* 63.1, pp. 110–119 (cit. on p. 67).
- Jensen, J. A. and N. B. Svendsen (1992). “Calculation of Pressure Fields from Arbitrarily Shaped, Apodized, and Excited Ultrasound Transducers”. In: *IEEE Trans. Ultrason., Ferroelec., Freq. Contr.* 39, pp. 262–267 (cit. on p. 61).
- Rasmussen, M. F., T. L. Christiansen, E. V. Thomsen, and J. A. Jensen (2015). “3-D Imaging Using Row-Column-Addressed Arrays With Integrated Apodization — Part I: Apodization Design and Line Element Beamforming”. In: *IEEE Trans. Ultrason., Ferroelec., Freq. Contr.* 62.5, pp. 947–958 (cit. on pp. 56–58, 61).
- Sampaleanu, A., P. Zhang, A. Kshirsagar, W. Moussa, and R. Zemp (2014). “Top-orthogonal-to-bottom-electrode (TOBE) CMUT arrays for 3-D ultrasound imaging.” In: *IEEE Trans. Ultrason., Ferroelec., Freq. Contr.* 61.2, pp. 266–276 (cit. on p. 55).

## References from Chapter 7

- Arvidsson, P. M., S. J. Kovacs, J. Töger, R. Borgquist, E. Heiberg, M. Carlsson, and H. Arheden (2016). “Vortex ring behavior provides the epigenetic blueprint for the human heart”. In: *Scientific Reports* 6.22021 (cit. on p. 75).
- Bogren, H. G., M. H. Buonocore, and R. J. Valente (2004). “Four-dimensional magnetic resonance velocity mapping of blood flow patterns in the aorta in patients with atherosclerotic coronary artery disease compared to age-matched normal subjects”. In: *J. Magn. Reson. Imaging* 19.4, pp. 417–427 (cit. on p. 75).
- Correia, M., J. Provost, M. Tanter, and M. Pernot (2016). “In-vivo 4D Ultrafast Vector Flow Imaging: quantitative assessment of arterial blood flow”. In: *Proc. IEEE Ultrason. Symp.* Pp. 1–4 (cit. on p. 75).
- Harloff, A., F. Albrecht, J. Spreer, A. F. Stalder, J. Bock, A. Frydrychowicz, J. Schollhorn, A. Hetzel, M. Schumacher, J. Hennig, and M. Markl (2009). “3D blood flow characteristics in the carotid artery bifurcation assessed by flow-sensitive 4D MRI at 3T”. In: *Magn. Reson. Med.* 61.1, pp. 65–74 (cit. on p. 75).

- Markl, M., A. Frydrychowicz, S. Kozerke, M. Hope, and O. Wieben (2012). “4D flow MRI”. In: *J. Magn. Reson. Imaging* 36.5, pp. 1015–1036 (cit. on p. 75).
- Nikolov, S. I. and J. A. Jensen (2002). “Virtual ultrasound sources in high-resolution ultrasound imaging”. In: *Proc. SPIE - Progress in biomedical optics and imaging*. Vol. 3, pp. 395–405 (cit. on p. 79).
- Provost, J., C. Papadacci, J. E. Arango, M. Imbault, M. Fink, J. L. Gennisson, M. Tanter, and M. Pernot (2014). “3-D ultrafast ultrasound imaging in vivo”. In: *Phys. Med. Biol.* 59.19, pp. L1–L13 (cit. on p. 75).
- Provost, J., C. Papadacci, C. Demene, J.-L. Gennisson, M. Tanter, and M. Pernot (2015). “3-D Ultrafast Doppler Imaging Applied to the Noninvasive Mapping of Blood Vessels In Vivo”. In: *IEEE Trans. Ultrason., Ferroelec., Freq. Contr.* 62.8, pp. 1467–1472 (cit. on p. 75).
- Salles, S., A. J. Y. Chee, D. Garcia, A. C. H. Yu, D. Vray, and H. Liebgott (2015). “2-D arterial wall motion imaging using ultrafast ultrasound and transverse oscillations”. In: *IEEE Trans. Ultrason., Ferroelec., Freq. Contr.* 62.6, pp. 1047–1058. DOI: 10.1109/TUFFC.2014.006910 (cit. on p. 82).
- Villagomez-Hoyos, C. A., S. Holbek, M. B. Stuart, and J. A. Jensen (2016). “High Frame Rate Synthetic Aperture 3D Vector Flow Imaging”. In: *Proc. IEEE Ultrason. Symp.* Pp. 1–4 (cit. on p. 76).
- Wigen, M. and L. Løvstakken (2016). “In vivo three-dimensional intra-cardiac vector flow imaging using a 2D matrix array transducer”. In: *Proc. IEEE Ultrason. Symp.* Pp. 1–4 (cit. on p. 75).



## **3-D Vector Flow Estimation with Row-Column Addressed Arrays**

**Simon Holbek**, Thomas Lehrmann Christiansen, Matthias Bo Stuart,  
Christopher Beers, Erik Vilian Thomasen, and Jørgen Arendt Jensen

*Accepted for publication in IEEE Trans. Ultrason., Ferroelec., Freq. Contr.*



# 3-D Vector Flow Estimation with Row-Column Addressed Arrays

Simon Holbek, Thomas Lehmann Christiansen, Matthias Bo Stuart, Christopher Beers, Erik Vilain Thomsen, and Jørgen Arendt Jensen

**Abstract**—Simulation and experimental results from 3-D vector flow estimations for a 62+62 2-D row-column (RC) array with integrated apodization are presented. A method for implementing a 3-D transverse oscillation (TO) velocity estimator on a 3.0 MHz RC array is developed and validated. First, a parametric simulation study is conducted where flow direction, ensemble length, number of pulse cycles, steering angles, transmit/receive apodization, and TO apodization profiles and spacing are varied, to find the optimal parameter configuration. The performance of the estimator is evaluated with respect to relative mean bias  $\bar{B}$  and mean standard deviation  $\bar{\sigma}$ . Second, the optimal parameter configuration is implemented on the prototype RC probe connected to the experimental ultrasound scanner SARUS. Results from measurements conducted in a flow-rig system containing a constant laminar flow and a straight-vessel phantom with a pulsating flow are presented. Both an M-mode and a steered transmit sequence are applied. Three-dimensional vector flow is estimated in the flow-rig for four representative flow directions. In the setup with 90° beam-to-flow angle, the relative mean bias across the entire velocity profile is (-4.7, -0.9, 0.4)% with a relative standard deviation of (8.7, 5.1, 0.8)% for ( $v_x, v_y, v_z$ ). The estimated peak velocity is 48.5 cm/s  $\pm$  3.0 cm/s giving a -3% bias. The out-of-plane velocity component perpendicular to the cross section is used to estimate volumetric flow rates in the flow-rig at a 90° beam-to-flow angle. The estimated mean flow rate in this setup is 91.2 L/h  $\pm$  3.1 L/h corresponding to a bias of -11.1%. In a pulsating flow setup, flow rate measured during five cycles is 2.3 mL/stroke  $\pm$  0.1 mL/stroke giving a negative 9.7% bias. It is concluded that accurate 3-D vector flow estimation can be obtained using a 2-D RC addressed array.

## I. INTRODUCTION

Real-time estimation of blood velocities is a valuable tool for diagnosing cardiovascular diseases [1]. Currently, most commercial scanners are only able to estimate the axial velocity component, which is used for diagnosing the degree of stenosis and for volume flow estimation [1]–[4]. The technique is subject to the angle-dependency problem, which leads to inaccuracies in the estimates [5], [6]. This problem was solved with 2-D vector flow techniques as speckle tracking [7], [8], directional beamforming [9], [10], vector Doppler techniques [8], [11]–[14] and the transverse oscillation (TO) method [15]–[17]. However, since blood propagates in all three dimensions, the true dynamics are only revealed with 3-D vector flow.

This work was financially supported by grants 82-2012-4 from the Danish National Advanced Technology Foundation and from BK Ultrasound ApS (Helve, Denmark).

S. Holbek, M.B. Stuart and J.A. Jensen are with the Center for Fast Ultrasound Imaging, Department of Electrical Engineering, Technical University of Denmark, Kgs. Lyngby, Denmark.

T.L. Christiansen and E.V. Thomsen are with the Department of Micro- and Nanotechnology, Technical University of Denmark, Kgs. Lyngby, Denmark. C. Beers is with Sound Technology, Inc., State College, Pennsylvania, USA

Several techniques have been proposed for 3-D velocity estimation using either a 1-D transducer [18], [19] or a 2-D matrix array [20]–[22]. The drawback of the proposed methods with a 1-D transducer is that they often are not providing real-time estimates or the setup and calibration scheme are very cumbersome. Although good results have been presented in the literature with a 2-D matrix array, this type of probe faces various fabrication issues and processing limitations. One major drawback with the matrix probe is that the total number of interconnections in a  $N \times N$  element transducer, scales with  $N^2$ , which causes connection issues. Moreover, the generated amount of channel data complicates the task of real-time processing. Thus, solutions for 3-D imaging with low channel count 2-D transducers have been investigated in the literature.

One of the ideas that has emerged, is to create a 2-D row-column (RC) addressed array [23], [24]. A RC addressed array can be viewed as two orthogonally oriented quadratic 1-D arrays with tall elements, mounted on top of each other. Compared to an  $N \times N$  matrix array, the total number of interconnections in an  $N + N$  RC array is reduced by a factor of  $N/2$ , which eases the interconnect and opens up for transducers with both a large footprint and a small pitch.

Several versions and layouts of 2-D RC arrays have been presented for imaging purposes, for both piezoelectric arrays [25], [26] and Capacitive Micromachined Ultrasonic Transducers (CMUTs) [27]–[29]. However, the potential of estimating blood flow with RC arrays has only recently been reported in the literature [30]. Due to the low channel count on such an array, a realtime implementation of 3-D vector flow estimation in the clinic seems highly feasible.

This work develops a technique for 3-D vector flow estimation on a 2-D 62+62 piezo RC prototype probe with integrated element apodization, using the TO method. The RC probe was made in collaboration with Sound Technology, Inc. (State College, PA, USA) and has similar parameters as the 62+62 RC CMUT probe presented in previous work for experimental use [29]. The feasibility of the technique is explored in a simulation study, where several parameters are varied, including beam steering angle, flow angle, ensemble lengths and apodization profiles, to optimize the setup. The conclusions drawn from the parametric study are used to optimize the experimental setup using the prototype probe. Experiments with the RC probe were used to demonstrate the feasibility of estimating 3-D vector flow both in a flow-rig, containing a laminar parabolic flow profile, and in a vessel where a flow pump was driving a pulsatile carotid waveform.

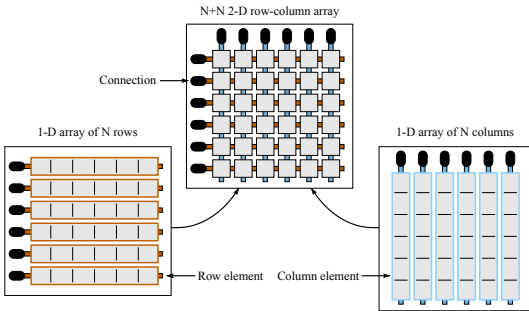


Figure 1: Two  $1 \times N$  and  $N \times 1$  1-D one-way focused linear arrays are mounted orthogonally on top of each other to form the 2-D row-column addressed  $N + N$  array. Modified from [31].

The paper expands on previous work [30]. Specifically, the simulations part has been extended from one single parameter setup to cover a full parametric study, and the experimental setup has been expanded to cover intensity measurements, different flow directions, a steered transmit sequence, and measurements on pulsatile flow.

## II. 2-D ROW-COLUMN ADDRESSED ARRAYS

When describing a 2-D RC addressed array as two orthogonally oriented quadratic 1-D arrays on top of each other, it seems valid to apply current theories and techniques on these transducer arrays. However, when working with 2-D RC arrays, several precautions are necessary regarding e.g. conventional approximations about transducer geometry as well as some restrictions that are present in both transmit and receive. This section covers the most common precautions and how they were resolved in this work.

### A. The concept of RC

The concept of a 2-D RC addressed array is easiest described as a  $1 \times N$  and a  $N \times 1$  1-D array merged together to form a  $N + N$  array, which can be accessed from either its row index or column index as seen in Fig. 1. In transmit, any number or combination of elements can be excited at a time, as long as they are oriented in the same direction. In receive, however, data from all  $2N$  elements can be accessed simultaneously [29]. Focusing is performed in one lateral dimension by electronically applying a time delay to each element, as described in Section II-D.

A 2-D RC array can be viewed as a special case of a 2-D matrix array, where whole lines of elements are connected to work as a unit. The reduced flexibility in transmit, and the lack of access to element data from  $N^2$  channels with a RC array, translates to reduced fabrication complexity and data processing requirements, which eases a real-time implementation.

### B. Integrated apodization

Despite the advantages that follows with the RC arrays, one inherent drawback comes from its tall elements, which

produces several ghost echoes emerging from the element edges [24], [31]. The largest amplitude of the ghost echo is approximately 40 dB lower than the amplitude of the main echo. The scattered signal from a blood cell is typical -40 dB less than the echo from the surrounding vessel wall, which stresses the importance of suppressing these artifacts for accurate velocity estimation. It was shown that edge waves could be reduced without affecting the main echo by implementing a roll-off apodization at the end of each line element [32]. Based on these suggestions, each end of the line elements include a Hann shaped roll-off apodization of length  $16 \times \text{pitch}$ .

### C. Beamforming RC data

Conventional delay-and-sum beamforming assumes that the geometry of transmitting and receiving elements are point sources emitting spherical waves. The emitted wavefront from a single RC element is, however, shaped as a cylindrical surface, where it can be viewed as a circle arc in a plane orthogonal to the long dimension and as a plane wave in the plane orthogonal to the short dimension. Therefore, the point source approximation breaks down even for small RC arrays and leads to errors in the time-of-flight calculations. A better approximation treats the elements as line segments, which influences the time-of-flight calculations used in the delay-and-sum beamformer [32].

The applied beamformer [32] takes the position of the emitting element (source), the time of emission, and the position of the receiving elements (drains) as input. When beamforming data from focused emissions, where multiple elements are emitting according to a specified delay curve the same approach as for single element emissions was used. Thus, the element with the smallest delay time was chosen as the source, and all elements in the orthogonal dimensions were used as drains in the beamformer.

### D. Focusing with RC arrays

As previously stated, the wavefront from a single RC element can be viewed as a plane wave in one plane and a circle arc in the orthogonal plane. Therefore, when multiple line elements are excited according to a specified delay curve, the wavefronts will add up to form a focal line rather than a focal point. Steered electronically focused emissions are possible, but only in the direction orthogonal to the transmitting line elements. The focal line spans the dimension of the excited elements as seen in Fig. 2, where the maximum pressure for a focused emission at the focal depth is simulated.

If the same elements are used for both transmitting and receiving, the beamformed data will correspond to the averaged received echo along the focal line, since focused emissions generate a line shaped pressure field. Due to this, beamforming was made with elements oriented orthogonally to the emitting elements. These issues with RC arrays have to be taken into consideration when designing the emission sequence.

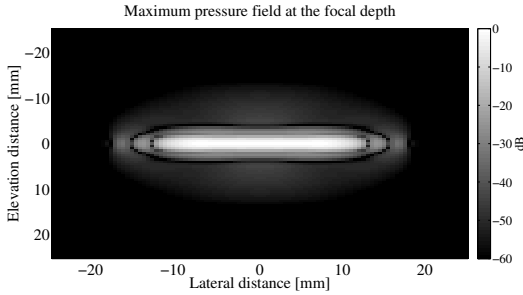


Figure 2: Pressure field generated with focused emissions. A focal line rather than a focal point is made with a RC array. The simulation parameters were the default values described in Table I.

### III. THE TRANSVERSE OSCILLATION METHOD

Several approaches and applications of TO have been reported in the literature, for instance for tissue displacement estimation [33]–[35] and for vector flow estimation [15]–[17], [20]. This work explores a TO method for estimating vector flow by generating two decoupled double-oscillating fields in receive. The received signals are affected by axial or transverse blood flow motion, which propagates through the double-oscillating fields. By using a phase-shift estimator, the axial and transverse motion can be detected. The basic steps of the applied TO method are described in the following section. A more thorough explanation of the theory is given in [15], [16], [20].

#### A. Basic concept

The idea of the TO method is to develop an angle-independent 2-D velocity estimator by generating two double oscillating fields (left and right) in receive. Ideally, the right field should be a spatially Hilbert transformed version of the left one. Spatial quadrature sampling is needed to estimate the axial and transverse velocity components and their direction.

The two  $90^\circ$  shifted double-oscillating fields are made by a spatial transverse separation of  $\lambda_x/4$  in the beamforming, where  $\lambda_x$  is the transverse oscillation period. The oscillation period is controllable and determined by the receive apodization profile. The apodization should contain two symmetrically placed peaks separated by the distance  $d_x$ . At a certain axial depth  $z$ ,  $\lambda_x$  is calculated as

$$\lambda_x(z) = 2\lambda_z \frac{z}{d_x}, \quad (1)$$

where  $\lambda_z$  is the wavelength of the emitted pulse in the medium. Being able to control the transverse wavelength by changing the distance between the two apodization peaks is one of the advantages of the method. As the maximum detectable velocity scales with  $\lambda_x$ , it provides a flexible tool for estimating both low and high velocities.

#### B. Beamforming

With the applied TO method, it is possible to estimate two velocity components, if a 1-D array is used; one component perpendicular to the element orientation in addition to the axial component. Three beamformed lines are needed for this; one center line for the axial estimator and two steered lines for the transverse estimate. The center line  $r_{center}$  is beamformed along the direction  $(0, 0, z)$ , using delay-and-sum and a traditional apodization profile. For the two steered lines, a traditional TO apodization profile with two separated peaks is applied and beamforming is performed along the lines  $(x, y, z) = (\pm\lambda_x(z)/8, 0, z)$  to create the  $\lambda_x/4$  spatial separation.

The method can be expanded to estimate 3-D velocities, if a 2-D array is used. The third velocity component can be obtained by applying the same procedure as for the transverse component, but this time by beamforming the two steered lines at  $\pm\lambda_y/8$  in the orthogonal direction. All five lines can either be beamformed in parallel from the same transmission or be combined from multiple consecutive transmission. For RC TO, the last approach was used, for reasons explained in Section IV. The five beamformed signals are subsequently used as input to the estimator.

#### C. The estimator

The axial velocity  $v_z$  estimates are based on the auto-correlation approach [36], and the two transverse velocity components are found by using the TO method [15] [16]. Since the applied array is geometrically identical in the transverse and lateral direction, the same apodization profile was applied for both cases, implying that  $d_x = d_y$ , which yields similar transverse wavelengths  $\lambda_x = \lambda_y$ . The estimator for calculating  $v_x$  is therefore also valid for  $v_y$ , when beamforming in the orthogonal directions. The aliasing limit for this estimator is

$$v_{x_{max}} = \frac{\lambda_x}{4k} f_{prf}, \quad (2)$$

where  $f_{prf}$  is the pulse repetition frequency,  $\lambda_x$  the transverse wavelength and  $k$  the lag used in the autocorrelation.

The described TO method was used for velocity estimation in the simulation study and in the experimental setup.

### IV. TRANSVERSE OSCILLATION ON A RC ARRAY

Implementing TO on a RC array requires a few modifications compared to a fully addressed 2-D array, and this section explains how it was done.

#### A. Transmission Sequences

In this study, 3-D vector flow was estimated either in points along the axial  $(0, 0, z)$  direction (M-mode) or in points along several lines in the  $zy$ -plane (Steered). A total of 5 beamformed lines are needed to estimate 3-D vector flow along a line with TO. But since it is not possible to generate a focal point with a RC array, from which all 5 lines could be beamformed simultaneously the transmit sequences have to be interleaved. Two different flow transmit sequences were thus designed and used:

1) *M-mode*: The M-mode sequence consisted of the two electronically focused emissions  $R$  and  $C$ . The sequence was used, when 3-D vector flow estimates along one line was made. An illustration of the M-mode sequence is seen in Fig. 3. From the row emissions  $R$ , three of the five needed lines can be beamformed and the two velocity components  $v_x$  and  $v_z$  along the centerline can be derived. In the opposite scenario with transmit on the columns  $C$  and receive on the rows, the  $v_y$  and  $v_z$  velocity components can be estimated. The applied emissions sequence is, thus, made by first transmitting on the rows and receiving on the columns and afterwards emitting with columns and receiving on the rows. The M-mode sequence was, thus, designed to alternately transmit the two emissions  $R$  and  $C$  in the following way.

$$R \rightarrow C \rightarrow R \rightarrow C \rightarrow R \dots$$

This sequence is repeated  $N_e$  times for each frame. By combining the two transverse estimates found from each transmit event with an axial estimate, the 3-D vector velocities are found.

2) *Steered*: The steered transmit sequence was used to estimate 3-D vector flow in the cross-sectional plane in a vessel. This sequence consisted of one focused emission  $C_1$  using column elements and  $N$  focused emissions  $R_i$  using row elements, where  $i = 1 \dots N$ . 3-D vector flow was, thus, estimated in points along the  $N$  steered directions in the  $zy$ -plane. The column emission generated a plane wave within the cross sectional  $zy$ -scan plane, whereas plane waves perpendicular to the scan plane were steered in the  $zy$ -plane when using the row elements, see Fig. 4. From the row transmit event  $R_i$ , the  $v_{x_i}$  and  $v_{z_i}$  velocity components could be estimated in points along the direction of the respective beamformed centerline. However, the  $C_1$  column transmit event provided the required data for beamforming the lines needed for estimating all  $v_{y_i}$  and  $v_{z_i}$  velocity components, as this transmit event sonifies the  $zy$ -scan plane. The steered transmit sequence used is schematically written as

$$\begin{aligned} C_1 \rightarrow R_1 \rightarrow R_2 \rightarrow R_3 \rightarrow \dots R_N \\ C_1 \rightarrow R_1 \rightarrow R_2 \rightarrow R_3 \rightarrow \dots R_N \end{aligned}$$

Both sequences yields continuous data, which means that the distance between each identical emission type is equally distributed in time for all time. The advantages of continuous data are that very high frames rate can be obtained, and that dynamic ensemble lengths and echo canceling filters can be applied. The higher obtainable frame rate with continuous data occurs, since a sliding window can be applied on the beamformed data to generate one velocity estimate. The velocity estimate can be updated from each new similar emissions, since the new data can replace the oldest data in the estimator.

## B. Generating the transverse oscillation

The TO method depends on generating two double-oscillating fields, where one of the fields is a  $90^\circ$  phase shifted version of the second one. If this is not the case, the velocity estimates will be biased [37]. In theory, the two fields should always be  $90^\circ$  degree phase-shifted when  $\lambda_x$  is calculated according to (1). However, (1) is only a mathematical approximation which leads to a deviation from the true  $\lambda_x$  needed for a correct beamforming. The task is therefore to estimate  $\lambda_x$  as precisely as possible to beamform the two  $90^\circ$  phase-shifted double-oscillating fields.

This work uses the theoretical  $\lambda_x$  to simulate two beamformed pulse-echo (PE) fields at the focal depth. A Hilbert transformation  $\mathcal{H}\{\cdot\}$  of the left TO beamformed line  $r_{left}$  was plotted along with the corresponding right TO line  $r_{right}$ , see Fig. 5. If the two signals were  $90^\circ$  phase shifted, the two lines would lay on top of each other. An optimization routine was run to find the  $\lambda_x$  which minimized the lateral distance between the absolute values of the two peak amplitudes. This wavelength was considered the true  $\lambda_x$  and was used in the beamformation.

A second transverse wavelength,  $\bar{\lambda}_x$ , was calculated from the 2-D spatio-temporal frequency spectrum [37].  $\bar{\lambda}_x$  was used as the transverse wavelength in the velocity estimator to reduce the bias [37]. The same transverse wavelengths were applied for beamforming and estimating  $v_y$  due to transducer symmetry.

## C. Data Processing

The raw RF data were processed on a Linux cluster. The same procedure was applied for all conducted measurements. Matched filtering was applied to the individual channel data by convolving it with the time-reversed emitted pulse to increase SNR. From each transmit event three lines were beamformed. Two of the lines,  $r_{left}$  and  $r_{right}$ , were used to estimate the velocity component perpendicular to the tallest dimension of the receiving elements using the TO method, and the third line,  $r_{center}$ , was used to estimate the axial velocity with an autocorrelation approach [36]. Stationary echo canceling was performed by subtracting the mean value from the  $N_e$  emissions in each frame for each beamformed line. After echo cancelling, the data were fed to the respective velocity estimator. By combining the estimated transverse velocity components, one from each transmit event, with one of the two independent axial estimates, a 3-D velocity vector along the direction of the respective beamformed centerline was obtained. An estimation plane was obtained by scan converting and interpolating the estimates.

## V. SIMULATION ENVIRONMENT

The simulations in this study were performed with the ultrasound simulation program Field II [38] [39]. This section describes how the simulations were carried out, and which parameters were used.

Several parameters were used in the simulation environment. Some were kept fixed and others were varied in the

## M-mode Sequence

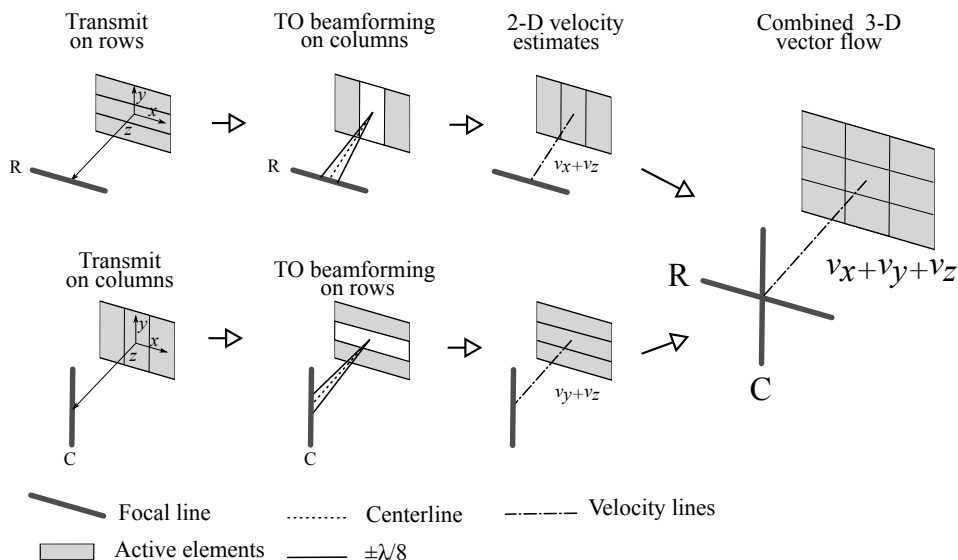


Figure 3: RC M-mode sequence for 3-D vector flow obtained along the center line with TO. The  $R$  emission is made using row elements and generates a focal line in the  $zx$ -plane. Three lines are beamformed along the directions;  $(\pm\lambda_x(z)/8, 0, z)$  and  $(0, 0, z)$  used for estimating  $v_x$  and  $v_z$ . Subsequently a focal line in the orthogonal  $zy$ -plane is generated using the column elements  $C$ . By beamforming the lines  $(0, \pm\lambda_y(z)/8, z)$  and  $(0, 0, z)$ ,  $v_y$  and  $v_z$  can be estimated. Finally, 3-D vector flow along the overlapping line is formed by combining the three estimated velocity components.

parameter study. The chosen parameters were varied to investigate the performance of the method. Parameters influencing the proposed method's angle independence, frame rate, intensity level, field-of-view, velocity range and accuracy were varied. The parameters with their default values (written in bold) are found in Table I.

A 2-D row-column array with integrated apodization was simulated with a center frequency,  $f_0 = 3.0$  MHz similar to the one described in [29], [32]. Each dimension consisted of 62 elements with a pitch of  $270 \mu\text{m} \approx \lambda/2$ , where  $\lambda$  is the wavelength in water with the given  $f_0$ . The kerf was set to  $25 \mu\text{m}$  or  $\approx \lambda/20$ . At the end of each line element, a Hann roll-off element apodization of size  $16 \times \text{pitch}$  was simulated.

A 6-cycles sinusoidal pulse was transmitted at  $f_0$  from either all row or all column elements. As default, the emitted ultrasound was focused at  $(x, y, z) = (0, 0, 30)$  mm. In the study where the steering angle  $\theta_{zy}$  was varied in the  $zy$ -plane, the axial focus was always in 30 mm depth. The pulse repetition frequency  $f_{prf}$  was 3.0 kHz as default.

A fixed symmetric Hann window spanning 62 elements was applied as apodization when transmitting the pulse from either all row or column elements. In receive, a symmetric Hann window apodization across all elements orthogonal to the transmitting aperture was applied for the axial velocity estimator. A similar procedure was followed when beamforming

the two lines needed for estimating the transverse velocities, where only the apodization profile was changed to contain two symmetric Hann windowed apodization peaks of width  $w = 25 \times \text{pitch}$  spaced by a distance  $d$ , of  $35 \times \text{pitch}$ .

A  $20 \times 20 \times 20$  mm<sup>3</sup> cubic phantom containing a cylindrical blood vessel ( $\varnothing = 12$  mm) located at 3 cm depth was defined for the simulations. Scatterers inside the cylinder were translated according to a circular symmetric parabolic velocity profile, and scatterers outside the cylinder were considered stationary. The magnitude of the scattering amplitude was 40 dB higher for the stationary scatterers than for the moving blood cell mimicking scatterers. In total, 10000 scatterers were distributed in the phantom to ensure that more than 10 scatterer per resolution cell was present [40]. The peak velocity  $v_0$  in the parabolic flow was 1 m/s and propagation was in the  $x$ -direction as default. Rotation of the scatter phantom could be made around two axes; around the  $y$ -axis, denoted the beam-to-flow angle  $\alpha$  and rotation around the  $z$ -axis denoted  $\beta$ . In the default setup, no rotation was applied and a 90 degree beam-to-flow angle was present. An illustration of the similar experimental setup is seen in Fig. 6.

A total of 100 frames for each parameter configuration were simulated. With an ensemble length,  $N_e$ , of 32, a total of  $2 \times 32 \times 100$  emissions were used for each parameter setup. 100 velocity profiles were estimated in both the lateral and

## Steered Sequence

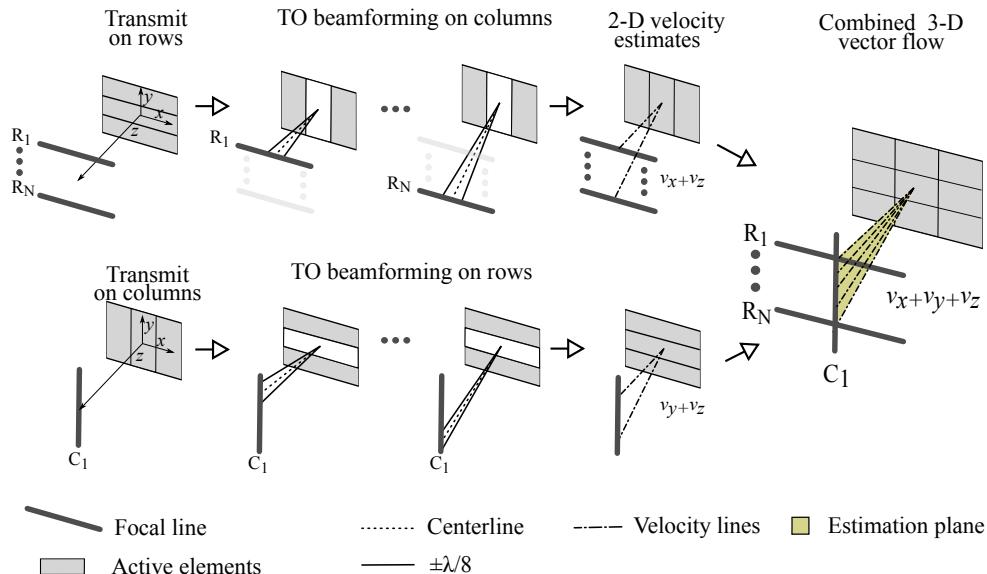


Figure 4: RC steered sequence for 3-D vector flow obtained in a cross sectional plane with TO. Compared to the M-mode sequence, the steered sequence differs in two ways; first, after each column emission  $C_1$ , multiple steered row emissions  $R_N$  are emitted. From each row emission three lines are beamformed according to the steering directions and  $v_x$  and  $v_z$  can be estimated along each direction. Second, from a single column emission  $C_1$ , three lines are beamformed along each steering direction yielding  $v_y$  and  $v_z$  velocity estimates along the  $N$  directions. 3-D vector flow is estimated in points along directions originating from the center of the aperture and through the intersection between the focal lines. The estimation plane is obtained when interpolating the combined 3-D vector flow estimates.

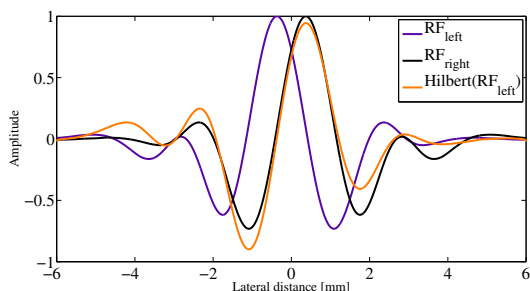
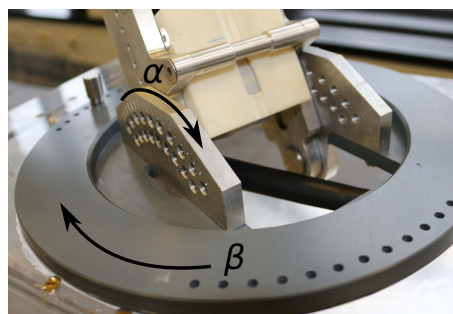


Figure 5: Beamformed  $r_{left}$  and  $r_{right}$  shown together with  $\mathcal{H}\{r_{left}\}$  at 3 cm depth. A  $90^\circ$  phase-shift is present, as  $r_{right}$  and  $\mathcal{H}\{r_{left}\}$  are on top of each other.



(a)

Figure 6: Illustration of the setup where a row-column transducer array is located 3 cm from the center of the vessel. In the default setup, the vessel is perpendicular to the transducer and the focal point is located in the center of the vessel. Two rotations of the 2-D prototype RC probe are applied;  $\alpha$ , which changes the beam-to-flow angle and  $\beta$  which changes the flow rotation angle.

transverse direction and 200 velocity profiles in the axial directions due to the alternating between row and column emissions. All velocity profiles were independent as a random reposition of the scatterer was used after each frame.

Table I: Variables in Parameter Study

Influencing	Parameter	Values
Angle independence	Beam-to-flow angle $\alpha$ [°]	90, 75, 60, 45
	Flow angle $\beta$ [°]	0, 15, 30, 45
Frame rate	Ensemble length $N_e$	4, 8, 16, <b>32</b> , 64
Intensity	Pulse length [cycles]	2,4,6,8
Field-of-view	Steering angle $\theta_{zy}$ [°]	0, 5, ..., 40, 45
Velocity range	TO apo. width [pitch]	1, 5, ..., <b>25</b>
	TO apo. peak spacing [pitch]	25, 27, ..., <b>35</b>
Intensity Accuracy	Transmit apo.	<b>Hann</b> , Tukey, Boxcar
Accuracy	Receive apo. (Axial)	<b>Hann</b> , Tukey, Boxcar
	Receive apo. (TO)	<b>Hann</b> , Tukey, Boxcar

## VI. EQUIPMENT & MATERIALS

This section gives an introduction to all the equipment and materials used in the experimental setup. The 2-D RC prototype probe and the experimental ultrasound scanner SARUS [41] were used in all experiments in combination with one or more pieces of the described equipment.

### A. The 2-D RC prototype probe

A 62+62 2-D piezo RC prototype probe was used in the experiments with similar properties as the simulated array. Each row/column dimension consisted of 62 elements with the ends being dedicated for integrated apodization. Hence, the probe is denoted a 62+62 RC probe. The probe had a center frequency  $f_0$  of 3.0 MHz which was also the transmit center frequency in the experimental setup. The pitch was 270  $\mu\text{m}$  and the kerf was 25  $\mu\text{m}$  yielding an active aperture area of  $1.67 \times 1.67 \text{ cm}^2$ . Four integrated edge apodization elements were used to reduce ghost echoes produced from the tall active line elements [32].

### B. SARUS

All measurements were conducted with the experimental ultrasound scanner SARUS. Raw RF data from all 124 channels were stored with a sampling frequency of 35 MHz. The excitation voltage was 75 V.

### C. Onda system

The ONDA system consisted of a high precession AIMS III Scanning Tank (Onda, Sunnyvale, CA), a HGL-0400 (Onda, Sunnyvale, CA) hydrophone, an ATH-2000 attenuator, and a AH-2010 preamplifier. The equipment was assembled in the order with the hydrophone first, followed by the attenuator and the preamplifier, which was connected through a cable to SARUS. The assembled equipment was mounted in the scanning tank and was remotely controlled through a MATLAB interface and could move freely in all three spatial directions. The ONDA system was used to conduct the intensity measurements, as described in [42].

### D. Flow-rig

An in-house built flow-rig system was used to validate the measured flow profile. The flow-rig contained a long inlet of 1.2 m, which ensured that a steady laminar parabolic flow profile was present at the measuring site. Blood mimicking fluid was driven inside the system by a centrifugal pump in a closed loop circuit. At the measuring site, a straight rubber pipe ( $\varnothing = 12 \text{ mm}$ ) was immersed into a water tank containing demineralized water. The volume flow  $Q$ , was measured with a MAG 1100 flow meter (Danfoss, Hasselager, Denmark). Peak velocity  $v_0$  was estimated as  $v_0 = Q/(\pi R^2)$ . The expected velocity profile could then be calculated as  $v(r) = (1 - \frac{r^2}{R^2})v_0$ , where  $r$  is the distance from the center of the pipe. The transducer was placed in a fixture, where beam-to-flow angle  $\alpha$ , the flow rotation angle  $\beta$  and the distance to the pipe were adjustable variables, see Fig. 6. The fixture was then placed in the water tank and aligned to the center of the pipe. Several measurements with different combinations of  $\alpha$  and  $\beta$  where made.

### E. Pulsatile flow pump

A second flow system (CompuFlow 1000, Shelley Medical Imaging Technologies, Toronto, Canada) was used to generate a pre-defined time-varying carotid flow waveform, where the pulse duration and flow rate of the waveform was adjustable. The manufacturer specified flow rate accuracy of the system was  $\pm 3\%$ . The flow pump was connected to the straight-vessel phantom described in the following section.

### F. Straight-vessel phantom

A customized tissue mimicking phantom (Dansk Fantom Service, Frederiksund, Denmark) containing a straight-vessel ( $\varnothing = 8 \text{ mm}$ ) was used in combination with the flow pump. This phantom was only used when measuring pulsatile flow.

## VII. SIMULATION PARAMETER STUDY

To quantify and compare the performance when estimating the 3-D vector flow for different settings a statistical approach was used. All 100 estimated velocity profiles for a given setting were independent and comparable across parameter choice, as the same random number initialization seed was used for scatter distribution. At each sample point  $z$  inside the vessel, the mean velocity  $\bar{v}(z)$  and the standard deviation  $\sigma(z)$  averaged over  $N$  frames for each velocity component, was found as

$$\bar{v}(z) = \frac{1}{N} \sum_{i=1}^N v_i(z) \quad (3)$$

$$\sigma(z) = \sqrt{\frac{1}{N-1} \sum_{i=1}^N (v_i(z) - \bar{v}(z))^2} \quad (4)$$

The mean relative bias  $\tilde{B}$  between the estimated velocity and the expected velocity  $v_\mu(z)$  at each depth was calculated as

$$\tilde{B} = \frac{1}{v_0 N_z} \sum_{z=1}^{N_z} (\tilde{v}(z) - v_\mu(z)), \quad (5)$$

with  $v_0$  being the theoretical peak velocity and where  $N_z$  were all discrete samples located within 90% of the vertical vessel radius measured from its center. Boundary effects caused by e.g. echo canceling might give a wrong impression of the estimator's actual performance, which the 90% acceptance rule should help prevent. A similar relative mean standard deviation  $\tilde{\sigma}$  was calculated as

$$\tilde{\sigma} = \frac{1}{v_0} \sqrt{\frac{1}{N_z} \sum_{z=1}^{N_z} \sigma(z)^2}. \quad (6)$$

The two quantitative performance metrics  $\tilde{B}$  and  $\tilde{\sigma}$  were used in the study for a comparison between different parameter settings.

#### A. Pulse repetition frequency

Although (2) states that the detectable velocity range scales with  $f_{prf}$ , the applied values should be adjusted according to the expected velocities to reduce the standard deviation [21], [43]. In this simulation study,  $f_{prf}$  was scaled such that the expected peak velocity was 80% of the maximum detectable velocity. However, since three velocity components were estimated coherently from the same transmissions, individual maximum velocities could be detected, depending on the actual orientation of the vessel. As a consequence of this,  $f_{prf}$  was set to [3000 5000 9700 13800] Hz for  $\alpha = [90^\circ \ 75^\circ \ 60^\circ \ 45^\circ]$  respectively, to ensure that the aliasing limit was not exceeded for any of the three velocity components.

#### B. Flow direction

With the default parameter values listed in Table I, the flow phantom was rotated in different angle combinations. A total of 100 frames were recorded for each angle combination and data were processed as described in Section II. The ability to estimate angle-independent peak velocities from the 3-D velocity vector is shown in Fig. 7. For a  $90^\circ$  beam-to-flow, the estimated peak velocity is found to be within 1.3-1.6% of  $v_0$  for any investigated  $\beta$  rotation. Decreasing  $\alpha$  in general leads to a  $\sigma$ , which increases from 4.6% for  $\alpha = 90^\circ$ , to 5.8%, 8.2% and 15.2% for  $\alpha = 75^\circ$ ,  $60^\circ$ , and  $45^\circ$  respectively. Results for the performance metrics are shown in Fig. 8a. For  $\alpha = 90^\circ$ ,  $\tilde{B}_{v_x}$  stays between 0.2-3.5% with  $\tilde{\sigma}_{v_x}$  between 4.6-5.7%. As  $\alpha$  increases,  $\tilde{\sigma}_{v_x}$  and  $\tilde{\sigma}_{v_y}$  increases to 9% for  $\beta = 15^\circ$ , 15% for  $\beta = 30^\circ$  and up to 20% when  $\beta = 45^\circ$  for both  $\tilde{\sigma}_{v_y}$  and  $\tilde{\sigma}_{v_x}$ . The bias  $\tilde{B}_{v_y}$  and  $\tilde{B}_{v_x}$ , however, only changes slightly from  $\approx 0.1\%$  and down to  $-2.6\%$  when  $[\alpha; \beta] = [45^\circ; 45^\circ]$ . A representative selection of velocity profiles from different rotation combinations are shown in Fig. 9. The figure shows how the standard deviation gradually increases for  $v_x$  and  $v_y$ , which affects the final absolute velocity magnitude profile.

#### C. Ensemble length

The effect of the ensemble length  $N_e$  was investigated in Fig. 8c. All estimates were derived from the same simulation, containing 100 frames each made from 2x64 emissions. The best estimates were found with the largest ensemble length  $N_e = 64$ , where  $\tilde{B}_{v_x} = 1.8\%$  and  $\tilde{\sigma}_{v_x} = 3.8\%$  compared to  $\tilde{B}_{v_x} = 7.5\%$  and  $\tilde{\sigma}_{v_x} = 8.1\%$  for  $N_e = 8$ . The same pattern was seen for  $\tilde{B}_{v_y}$  and  $\tilde{\sigma}_{v_y}$ . A rapid increase in the standard deviation was seen when the ensemble length was lowered. This was expected, as the standard deviation is proportional to the included statistics and scales with  $1/\sqrt{N_e}$ . However, a surprisingly high bias was found. A short ensemble length can increase the temporal resolution, but lowers the robustness of the estimator. This can especially be exploited when continuous data is present, such that the ensemble length is variable and adapts to the initial temporal variation of the flow.

#### D. Pulse length

The transmitted pulse length was varied from 2 to 8 cycles in steps of two cycles.  $\tilde{B}_{v_x}$  increased from  $-2.1\%$  at two cycles and up to  $2.6\%$  when using 8 cycles. Standard deviation and bias for the remaining estimates were almost unaffected by changing the pulse length, presumably because no flow was present in these directions. Results are shown in Fig. 8d.

#### E. Apodization

Different transmit and receive apodization shapes were investigated, and the findings are presented in Fig. 8e. In the direction of the flow, the lowest bias was found when a Hann window was used in transmit and a boxcar apodization was used in receive, here  $\tilde{B}_{v_x} = -0.1\%$ . The standard deviation increased slightly for this combination, but was relatively unaffected of the transmit and receive apodization, since  $\tilde{\sigma}_{v_x}$  for all combinations of using a Hann window in transmit was between 4.6% and 5.5%. However,  $\tilde{\sigma}_{v_y}$  was highly affected by the transmit apodization and was 5.6%, 11.7%, 7.5% when receive apodization was fixed to a boxcar, and transmit varied between a Hann, boxcar and a Tukey window, respectively.

#### F. Steering angles

Focused emissions were steered in the  $zy$ -plane spanning from  $0^\circ$  to  $45^\circ$  in steps of  $5^\circ$ . To make a fair comparison, the simulated phantom was shifted a certain distance in the  $y$ -direction to ensure that the focal line was always placed in the center of the vessel. Velocity profiles were derived from each steering angle and compared to the expected value. The resulting performance metrics are shown in Fig. 8f. The estimator deteriorates significantly for angles  $> 20^\circ$ , where  $\tilde{B}_{v_x}$  increases in a negative direction from a stable level around 1-2%. The explanation to the breakdown is found in the geometry of the RC array and the position of the integrated apodization. The returning echo from a scatterer placed outside the physical aperture  $|x| > 8.4$  mm or  $|y| > 8.4$  mm will first hit the integrated apodization element, which results in a damped

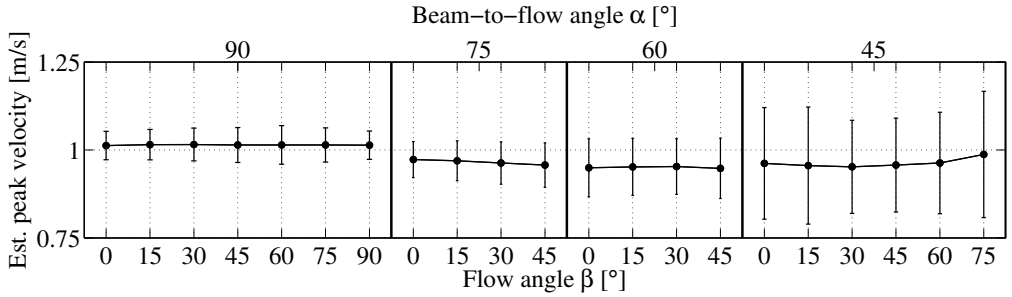


Figure 7: Peak velocities derived from the estimated 3-D vector velocities as a function of vessel orientation.

signal compared to a scatterer that was placed inside the physical aperture. The maximum dampening of the signal is found when the scatterer is placed outside the dimensions of the integrated apodization  $|x| > 12.7$  mm or  $|y| > 12.7$  mm. For a  $15^\circ$  steering angle, the center of the vessel was placed in (8, 0, 30) mm, inside the physical aperture. For a  $20^\circ$  steering angle the performance gradually breaks down, since the center of the vessel now is placed at (11.9, 0, 30) mm, beneath the integrated roll-off apodization. This effect affects the performance more when increasing the steering angle, since a larger fraction of the scatterers are placed outside the physical aperture.

### G. TO spacing

With a default TO peak width of 25 elements, the minimum element spacing between the two peaks was 25 and maximum 37 element before exceeding the aperture. The  $\lambda_x$  used in the beamformation was found for each setup along with the optimized  $\tilde{\lambda}_x$  used in the velocity estimator as described in Section IV-B. A gradually improved performance was seen when increasing the separation between the two apodization peaks, see Fig. 8g. At a 25 element spacing,  $\tilde{B}_{v_x}$  was 5.0% and improved to 1.3% for the 37 element spacing. Similarly,  $\tilde{B}_{v_y}$  improved from  $-0.6\%$  to  $-0.1\%$ . Likewise,  $\tilde{\sigma}_{v_x}$  and  $\tilde{\sigma}_{v_y}$  decreased from 6.8% and 8.4% to 4.8% and 5.9% respectively. Axial estimates were unaffected when varying TO specific parameters, as the estimator is decoupled from the TO method.

### H. TO width

Varying the apodization width, while keeping the spacing between the peaks fixed, changes the transverse wavelength slightly. As the width decreases,  $\lambda_x$  increases slightly. To make a fair comparison, both  $\lambda_x$  and  $\tilde{\lambda}_x$  were estimated for each investigated width as described in Section IV-B.  $\tilde{B}_{v_y}$  and  $\tilde{\sigma}_{v_y}$  did not change significantly when varying the TO width, which probably should be attributed to the actual vessel orientation where  $v_y = 0$  m/s, see Fig. 8h.  $\tilde{B}_{v_x}$  changed from 2.4%, when two delta functions were used in receive to 1.3% for a 25 elements wide Hann apodization.  $\tilde{\sigma}_{v_x}$  changed similarly from 17.1% to 4.8%.

Table II: Experimental parameter choice

Parameter	Value
Ensemble length $N_e$	32
Pulse length	8
TO apo. width [pitch]	25
TO apo. peak spacing [pitch]	35
Transmit apo.	Hann
Receive apo. Axial/TO	Hann

### I. Parameter study summary

The effect on the velocity estimation performance was investigated when varying several parameters. Based on the presented findings, the following conclusions can be drawn: The best measuring position for the TO method on a 2-D RC array is found when a beam-to-flow angle of  $90^\circ$  can be obtained, which is common *in-vivo*. The performance is decreasing as  $\alpha$  is lowered, since the increase in  $f_{prf}$  (to avoid the aliasing limit) increases the standard deviation for an autocorrelation estimator [43]. A Hann apodization is preferred in transmit, whereas the shape of the receive apodization has less impact on the performance. The transmitted pulse length should be between 4 and 8 cycles and preferably to the lower end, when intensity levels are of concern. An optimal TO peak apodization should be as wide as possible and separated as much as possible. However, the actual shape needs to be optimized depending on the size of the applied array. Also, the expected velocity range needs to be taken into account when designing the apodization profiles. The number of emissions averaged over,  $N_e$ , should be 16 or above to ensure robust estimates. Accurate velocity estimates can be obtained for steered beams at angles  $\leq 20^\circ$  where the absolute biases are  $< 3\%$  and  $\tilde{\sigma}$  does not exceed 6%. The estimator gradually breaks down when flow outside the physical aperture is examined.

Based on the simulation study, the suggested choice of parameters listed in Table II were fixed and used in the experimental validation described in the following sections.

## VIII. INTENSITY MEASUREMENTS

Prior to the experimental validation, intensity measurements with the optimized parameter configuration were made to



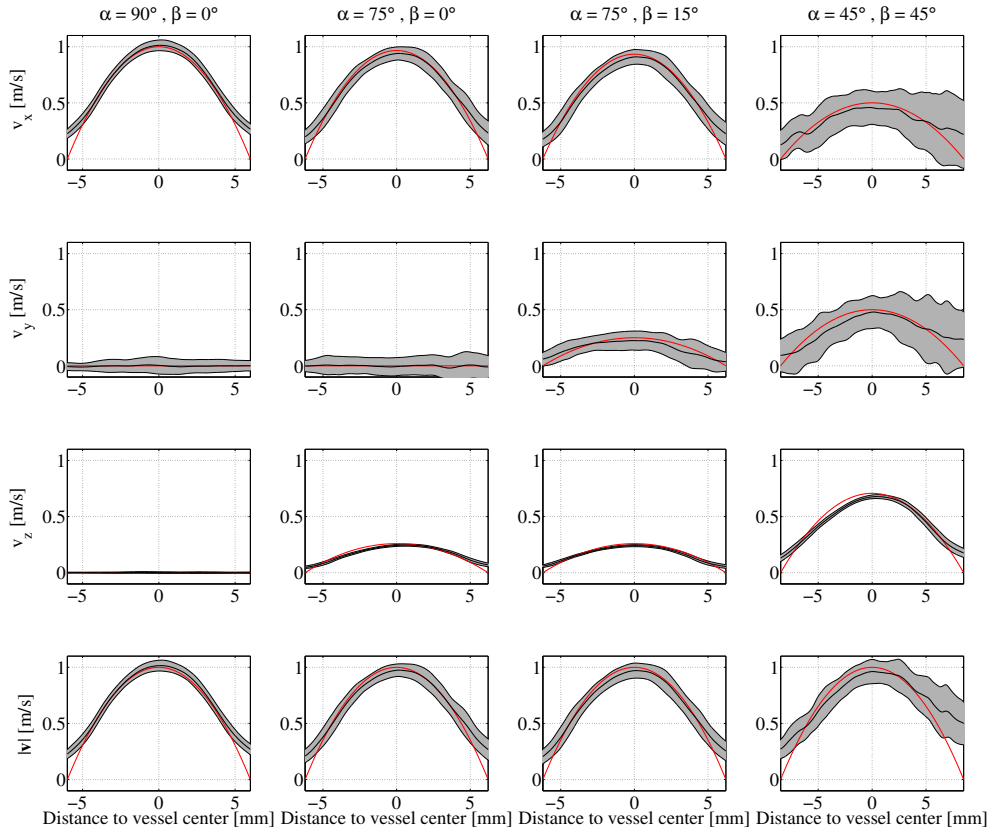


Figure 9: The decoupled estimated velocity component (black line)  $\pm$  one standard deviation (gray area) at a representative selection of different vessel rotation combinations are presented, along with the theoretical velocity component (red line). The bottom row shows the absolute velocity magnitude combined from the three velocity component estimates.

to be symmetric around both focal lines for  $I_{spta.3}$ . However, since  $I_{spta.3}$  is composed by adding up the contribution from each emission, a peak in the intensity is expected in (0, 0, 30 mm) where the two focal lines are crossing. The peak intensity is supposed to be twice the value measured at the focal lines close to the end of the physical aperture, since both transmit events contribute equally to  $I_{spta.3}$  in (0, 0, 30 mm). The derated  $I_{spta.3}$  values are shown in Fig. 10b. A symmetric  $I_{spta.3}$  field is seen around the two focal lines with a peak centered in (0, 0, 30 mm). The peak  $I_{spta.3}$  is 14.0 mW/cm<sup>2</sup> and is reduced to 6.9 mW/cm<sup>2</sup> and 7.0 mW/cm<sup>2</sup> at  $\pm$  2 mm from the peak value in the elevation direction. Intensity measurements were performed at a  $f_{prf} = 750$  Hz.

## IX. EXPERIMENTAL RESULTS

This section describes the experimental measurements conducted. The presented measurements and results are presented in gradually increasing complexity.

### A. Flow-rig measurements

1) *M-mode*: The M-mode flow sequence was used to estimate 3-D vector flow through the center line of the pipe in the flow-rig. Measurements from four representative combinations of  $\alpha$  and  $\beta$  were conducted. A total of  $2 \times 32 \times 100$  emissions were used for each measurement setup. The peak velocity  $v_0$  was set to 0.5 m/s and the pulse repetition frequencies  $f_{prf}$  were [1500, 2500, 6900] for the respective beam-to-flow-angles  $\alpha = [90^\circ, 75^\circ, 50^\circ]$ , to ensure that the aliasing limit was not exceeded in the limiting velocity component  $v_z$ . The  $f_{prf}$  was halved compared to the simulations to maintain the same ratio between  $v_0$  and  $f_{prf}$ .

Results from the four measurements are shown in Fig. 11, where the individual velocity components are shown along with their respective mean standard deviation and the true profile. The estimated mean peak velocities calculated as  $|v|$  for each setup were [48.5, 50.4, 50.6, 58.2] cm/s  $\pm$  [3.0, 5.9, 3.5, 8.7] cm/s for the respective flow combinations  $[\alpha; \beta] = [90^\circ; 0^\circ], [75^\circ; 0^\circ], [75^\circ; 15^\circ], [50^\circ; 45^\circ]$ .  $\hat{B}_{v_x}$  stays between

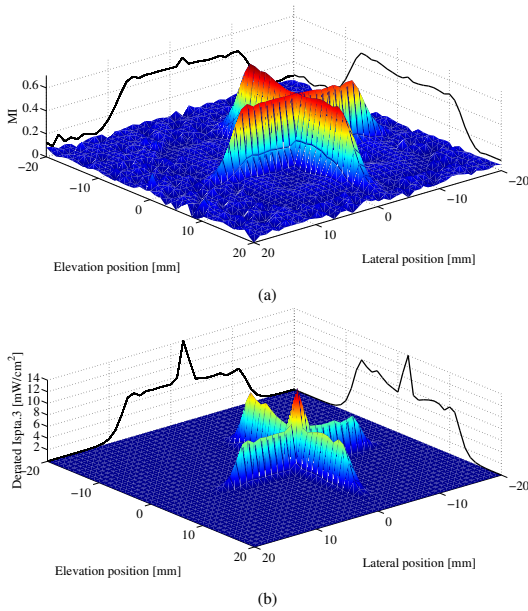


Figure 10: Intensity measurements of the M-mode flow sequence performed in the  $yx$ -plane at the depth of 30 mm at a  $f_{prf} = 750$  Hz. a) Estimated MI. b) Estimated  $I_{spta,3}$ .

−3.1% and −4.8% for the four constellations. Similarly  $\tilde{B}_{v_z}$  stays between −3.8% and 1.5% whereas  $\tilde{B}_{v_y}$  increases from a level between −0.9% and 2.1% in the first three setups to −10.9% for  $[50^\circ; 45^\circ]$ . The lowest mean relative standard deviation is found at  $[90^\circ; 0^\circ]$ , where  $(\tilde{\sigma}_x, \tilde{\sigma}_y, \tilde{\sigma}_z) = (8.7\%, 5.1\%, 0.8\%)$ . The maximum standard deviation is found for the angle combination  $[50^\circ; 45^\circ]$ , where  $(\tilde{\sigma}_x, \tilde{\sigma}_y, \tilde{\sigma}_z) = (19.9\%, 21.3\%, 6.5\%)$ . The large deviation in the estimated velocities compared to the expected, are supposed to be due to reverberation artifacts from the pipe.

2) *Steered*: With the same equipment and measurement setup, 3-D vector flow was measured in a cross sectional plane using the steered emission sequence. The sequence consisted of 11 steered row emissions spanning from  $-12^\circ$  to  $12^\circ$  in steps of  $2.4^\circ$  and a single unsteered column emission. The  $f_{prf}$  was 9.0 kHz and a total of  $32 \times 12 \times 100$  emissions were transmitted, corresponding to 100 frames when an ensemble length of 32 was used. A vector representation of the mean cross sectional 3-D vector flow averaged over all frames is seen in Fig. 12a. Based on the out-of-plane velocity component and the pipe area, the volumetric flow rate for each frame was estimated. The mean volumetric flow rate was  $91.2 \text{ L/h} \pm 3.1 \text{ L/h}$  compared to the expected  $102.6 \text{ L/h}$ .

### B. Pulsating flow measurements

1) *M-mode*: M-mode flow measurements were made using the flow pump and the straight-vessel phantom. A predefined

carotid flow profile was chosen with a cycle time of 0.84 s and a flow rate of  $2.54 \text{ mL/stroke} \pm 3\%$ . The transducer was placed 30 mm from the center of the vessel in a  $90^\circ$  beam-to-flow angle. At an  $f_{prf}$  of 750 Hz a total of 8.5 s were recorded by SARUS, corresponding to 10 full cycles. The sliding window was set to move in steps of 3 data points and an ensemble length of 32 was applied in the data processing. The predominant out-of-plane  $v_x$  velocity component is shown as a function of time in Fig. 12b. Since the cycle time was fixed through the data acquisition, a time coherent addition of all 10 cycles was made. The mean velocity in the center of the vessel during each cycle was  $11.3 \text{ cm/s} \pm 0.4 \text{ cm/s}$  and is seen in Fig. 12c.

2) *Steered*: With the same equipment and measurement setup, 3-D vector flow was measured in a cross sectional plane using the steered emission sequence. The sequence consisted of 11 steered row emissions spanning from  $-8^\circ$  to  $8^\circ$  in steps of  $1.6^\circ$  and a single unsteered column emission. The  $f_{prf}$  was 9.0 kHz, which translates to 750 frames per second. A total of 4.3 s were recorded, corresponding to 5 cycles. The sliding window and ensemble length used in the processing was 3 and 32, respectively. The flow rate, based on the cross sectional vessel area and the out-of-plane velocity component averaged over 5 cycles was  $2.3 \text{ mL/stroke} \pm 0.1 \text{ mL/stroke}$ , compared to the expected  $2.54 \text{ mL/stroke}$ . The high frame rate captures the repeating pulsating behavior and the high velocities during peak-systole were  $25.6 \text{ cm/s} \pm 0.9 \text{ cm/s}$  and the lower velocities during end-diastole were  $1.1 \text{ cm/s} \pm 0.7 \text{ cm/s}$ . A 3-D vector representation of the flow both during the peak-systole and end-diastole is seen in Fig. 13

## X. DISCUSSION & CONCLUSION

The feasibility of implementing 3-D vector flow using the TO method on a prototype 62+62 RC probe was demonstrated through various simulation setups and experimental measurements.

The experimental results were in good agreement with similar simulation setups. For instance, the estimated peak velocity had a mean relative bias of 1.3% and a relative mean standard deviation of 4% in the simulations and similar a mean relative bias of −3.8% and a relative mean standard deviation of 5.9% in the measurements for the flow angle constellation  $[\alpha; \beta] = [90^\circ; 0^\circ]$ .

A cross sectional view of the 3-D vector flow in the flow-ring was estimated with a steered emissions sequence. Based on the cross sectional area and the out-of-plane velocity component, the flow rate was found to be  $91.2 \text{ L/h} \pm 3.1 \text{ L/h}$  compared to the expected  $102.6 \text{ L/h}$ .

Evaluation of the performance, when estimating velocities in time-varying complex flow, was made with the flow pump. The results showed the pulsating flow pattern, and the estimated mean velocity in the center of the vessel during one period was  $11.3 \text{ cm/s} \pm 0.4 \text{ cm/s}$ , when averaging over 10 periods. Furthermore, both the slow and fast flow could be estimated in a cross-sectional scan plane and the mean flow rate from 5 cycles was found to be  $2.3 \text{ mL/stroke} \pm 0.1 \text{ mL/stroke}$  with a negative bias of 9.7%. Both pulsating

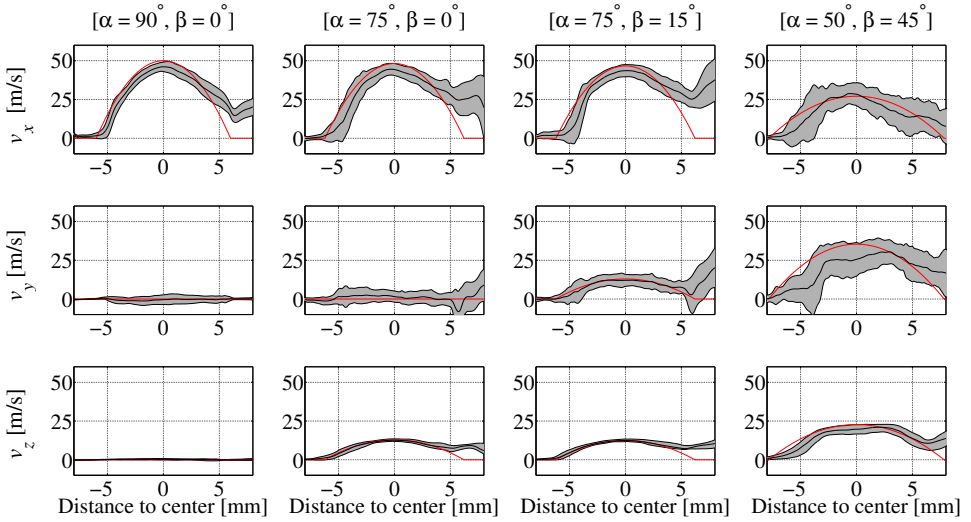


Figure 11: Individual mean estimated velocity components (black line)  $\pm$  one standard deviation (gray area) at a representative selection of different flow rotation combinations are presented with the expected profiles (red line).

flow results had a standard deviation below 5%, which shows that the estimates are consistent and reproducible. In general a negative bias was found both in the simulations and in the experimental exploration. Further investigation of this behavior is needed to determine whether it is related to the estimation of the transverse wavelength or influenced by other effects.

The relatively low experimental peak velocities ( $\sim 25$ - $30$  cm/s) compared to the peak-systole in the common carotid artery ( $\sim 1$  m/s) were chosen to avoid the production and circulation of air bubbles in the system, which might corrupt the estimates. The presented method is not limited to slow flow, hence realistic peak velocities *in vivo* of 1 m/s can be obtained by adjusting  $f_{prf}$ , the number of steering angles, and the transverse wavelengths to match the flow conditions.

Intensity measurements with the RC probe showed that focused emissions generated plane waves, which sonified lines spanning the tall dimension of an element. The results of the intensity measurements forms the basis of the attainable field-of-view for vector flow imaging using the applied prototype RC probe. With the current probe design, vector flow can be obtained in an area limited to a box of approximately  $20$  mm  $\times$   $20$  mm and the  $z$ -axis.

The presented results demonstrate that 3-D vector flow can be obtained with only 124 active elements, if they are positioned in a row-column wise scenario. Since most scanners on the market can sample at least 128 channels simultaneously, real time 3-D vector flow estimation no longer requires a customized research ultrasound scanner and a fully addressed matrix probe, but only a commercial scanner with access to raw channel data and a RC probe.

For *in vivo* applications, when e.g. measuring in the common carotid artery, several adjustments can be made to the presented steered sequence to cope with velocities on the order of 1 m/s. For instance, the TO peak element spacing can be shortened (as described in Section VII-G) to yield a larger

lateral wavelength which translates to a higher detectable  $v_{max}$  according to 2. Furthermore, since the proposed method uses a phase estimator which ranges from  $[-\pi : \pi]$  which translates to a velocity range of  $[-v_{max} : v_{max}]$ , a phase shift of e.g.  $\frac{\pi}{2}$  can be applied such that the phase range changes to  $[-\frac{\pi}{2} : \frac{\pi}{2}]$ , which shifts the detectable velocity range to  $[-\frac{1}{2}v_{max} : \frac{1}{2}v_{max}]$  for better estimation of larger positive velocities. A feasible sequence for estimating realistic *in vivo* velocities could contain  $N = 11$  steered row emissions and one column emission, have a TO peak spacing of 31 elements and be emitted at a  $f_{prf} = 15$  kHz. At 3 cm the detectable positive velocity  $v_{max}$  would then be

$$v_{x_{max}} = \frac{\lambda_x f_{prf}}{4k N + 1} = \frac{0.40 \text{ cm } 15 \text{ kHz}}{4 * 1 \cdot 11 + 1} = 125 \text{ cm/s}, \quad (7)$$

which could be increased to 188 cm/s by applying a  $\frac{\pi}{2}$  phase shift. The presented sequence would produce ultra fast vector flow estimates of 1250 frames per second.

Future work is planned to validate the clinical application of 3-D vector flow on the RC probe, when a permission by the science ethics board has been granted for *in vivo* usage.

#### ACKNOWLEDGMENT

This work was supported by grant 82-2012-4 from the Danish National Advanced Technology Foundation and by BK Ultrasound Aps. The authors would also like to thank BK Ultrasound Aps. and Sound Technology Inc., for development of the RC probe.

#### REFERENCES

- [1] G. M. von Reutern, M. W. Goertler, N. M. Bornstein, M. D. Sette, D. H. Evans, A. Hetzel, M. Kaps, F. Perren, and et al., "Grading carotid stenosis using ultrasonic methods," *Stroke*, vol. 43, no. 3, pp. 916-921, 2012.

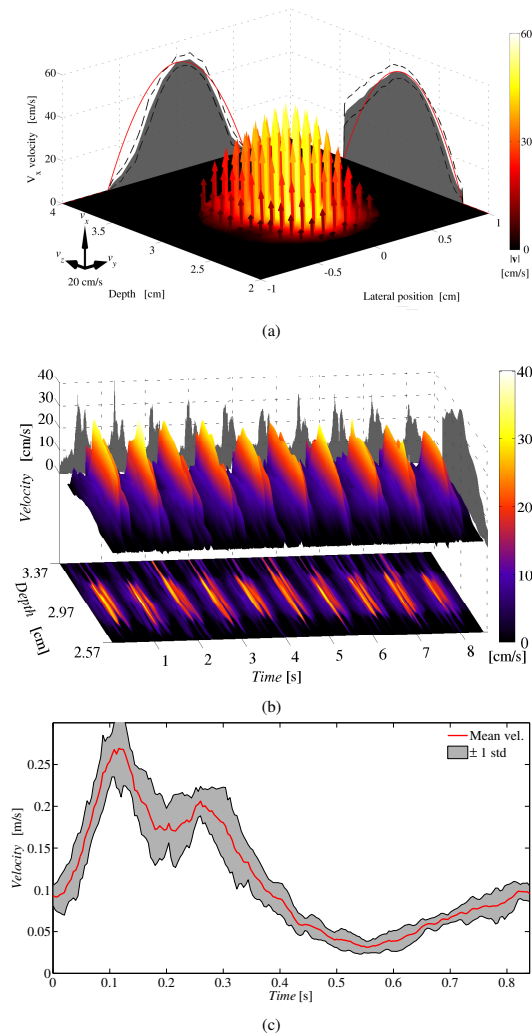


Figure 12: Cross sectional mean 3-D vector flow averaged over 100 frames. The magnitude and direction of the flow (at a certain position) is depicted by the length and the color of the arrows. The shaded gray areas represents the projection of the flow in the respective direction with its standard deviation (dotted line). The theoretical flow profiles are illustrated by the red lines. b) M-mode of the out-of-plane  $v_x$  velocity component measured in a pulsating carotid flow waveform. c) Mean  $v_x$  velocity in the center of the vessel throughout a period averaged over 10 cycles.

[2] K. L. Gould, "Quantification of coronary artery stenosis in vivo," *Circ Res.*, vol. 57, no. 3, pp. 341–353, 1985.  
 [3] P. A. Picot and P. M. Embree, "Quantitative volume flow estimation using velocity profiles," *IEEE Trans. Ultrason., Ferroelec., Freq. Contr.*

vol. 41, pp. 340–345, 1994.  
 [4] E. G. Grant, C. B. Benson, G. L. Moneta, A. V. Alexandrov, J. D. Baker, E. I. Bluth, B. A. Carroll, and et al., "Carotid artery stenosis: gray-scale and doppler us diagnosis - society of radiologists in ultrasound consensus conference," *Radiology*, vol. 229, no. 2, pp. 340–346, 2003, m. Eliasziw and J. Gocke and B. S. Hertzberg.  
 [5] R. W. Gill, "Measurement of blood flow by ultrasound: Accuracy and sources of error," *Ultrasound Med. Biol.*, vol. 11, pp. 625–641, 1985.  
 [6] J. Jensen, J. B. Olesen, M. B. Stuart, P. M. Hansen, M. B. Nielsen, and J. A. Jensen, "Vector velocity volume flow estimation: Sources of error and corrections applied for arteriovenous fistulas," *Ultrasonics*, vol. 70, pp. 136–146, 2016.  
 [7] G. E. Trahey, J. W. Allison, and O. T. von Ramm, "Angle independent ultrasonic detection of blood flow," *IEEE Trans. Biomed. Eng.*, vol. BME-34, pp. 965–967, 1987.  
 [8] S. Fadnes, I. K. Ekroll, S. A. Nyrmes, H. Torp, and L. Løvstakken, "Robust angle-independent blood velocity estimation based on dual-angle plane wave imaging," *IEEE Trans. Ultrason., Ferroelec., Freq. Contr.*, vol. 62, no. 10, pp. 1757–1767, October 2015.  
 [9] J. A. Jensen, "Directional velocity estimation using focusing along the flow direction: I: Theory and simulation," *IEEE Trans. Ultrason., Ferroelec., Freq. Contr.*, vol. 50, pp. 857–872, 2003.  
 [10] J. A. Jensen and R. Bjerngaard, "Directional velocity estimation using focusing along the flow direction: II: Experimental investigation," *IEEE Trans. Ultrason., Ferroelec., Freq. Contr.*, vol. 50, pp. 873–880, 2003.  
 [11] B. Dunmire, K. W. Beach, K.-H. Labs, M. Plett, and D. E. Strandness, "Cross-beam vector Doppler ultrasound for angle independent velocity measurements," *Ultrasound Med. Biol.*, vol. 26, pp. 1213–1235, 2000.  
 [12] M. Tanter, J. Bercoff, L. Sandrin, and M. Fink, "Ultrafast compound imaging for 2-D motion vector estimation: application to transient elastography," *IEEE Trans. Ultrason., Ferroelec., Freq. Contr.*, vol. 49, pp. 1363–1374, 2002.  
 [13] D. Garcia, J. C. del Alamo, D. Tanne, R. Yotti, C. Cortina, E. Bertrand, J. C. Antoranz, E. Perez-David, R. Rieu, F. Fernandez-Aviles, and J. Bermejo, "Two-dimensional intraventricular flow mapping by digital processing conventional color-doppler echocardiography images," *IEEE Trans. Med. Imag.*, vol. 29, no. 10, pp. 1701–1713, 2010.  
 [14] S. Ricci, L. Bassi, and P. Tortoli, "Real-time vector velocity assessment through multigate Doppler and plane waves," *IEEE Trans. Ultrason., Ferroelec., Freq. Contr.*, vol. 61, no. 2, pp. 314–324, 2014.  
 [15] J. A. Jensen and P. Munk, "A new method for estimation of velocity vectors," *IEEE Trans. Ultrason., Ferroelec., Freq. Contr.*, vol. 45, pp. 837–851, 1998.  
 [16] J. A. Jensen, "A new estimator for vector velocity estimation," *IEEE Trans. Ultrason., Ferroelec., Freq. Contr.*, vol. 48, no. 4, pp. 886–894, 2001.  
 [17] M. Lenge, A. Ramalli, P. Tortoli, C. Cachard, and H. Liebgott, "Plane-wave transverse oscillation for high-frame-rate 2-D vector flow imaging," *IEEE Trans. Ultrason., Ferroelec., Freq. Contr.*, vol. 62, no. 12, pp. 2126–2137, December 2015.  
 [18] I. A. Hein, "3-D flow velocity vector estimation with a triple-beam lens transducer — experimental results," *IEEE Trans. Ultrason., Ferroelec., Freq. Contr.*, vol. 44, pp. 85–95, 1997.  
 [19] S. Berg, H. Torp, B. O. Haugen, and S. Samstad, "Volumetric blood flow measurement with the use of dynamic 3-dimensional ultrasound color flow imaging," *J. Am. Soc. Echocardiogr.*, vol. 13, no. 5, pp. 393–402, 2000.  
 [20] M. J. Pihl and J. A. Jensen, "A transverse oscillation approach for estimation of three-dimensional velocity vectors. Part I: Concept and simulation study," *IEEE Trans. Ultrason., Ferroelec., Freq. Contr.*, vol. 61, pp. 1599–1607, 2014.  
 [21] M. J. Pihl, M. B. Stuart, B. G. Tomov, M. F. Rasmussen, and J. A. Jensen, "A transverse oscillation approach for estimation of three-dimensional velocity vectors. Part II: Experimental validation," *IEEE Trans. Ultrason., Ferroelec., Freq. Contr.*, vol. 51, no. 10, pp. 1608–1618, 2014.  
 [22] J. Provost, C. Papadacci, J. E. Arango, M. Imbault, M. Fink, J. L. Gennisson, M. Tanter, and M. Pernot, "3-D ultrafast ultrasound imaging in vivo," *Phys. Med. Biol.*, vol. 59, no. 19, pp. L1–L13, 2014.  
 [23] C. E. Morton and G. R. Lockwood, "Theoretical assessment of a crossed electrode 2-D array for 3-D imaging," in *Proc. IEEE Ultrason. Symp.*, 2003, pp. 968–971.  
 [24] C. E. M. Démoré, A. Joyce, K. Wall, and G. Lockwood, "Real-time volume imaging using a crossed electrode array," *IEEE Trans. Ultrason., Ferroelec., Freq. Contr.*, vol. 56, no. 6, pp. 1252–1261, 2009.  
 [25] C. H. Seo and J. T. Yen, "64 x 64 2-D array transducer with row-column addressing," in *Proc. IEEE Ultrason. Symp.*, vol. 1, 2006, pp. 74–77.

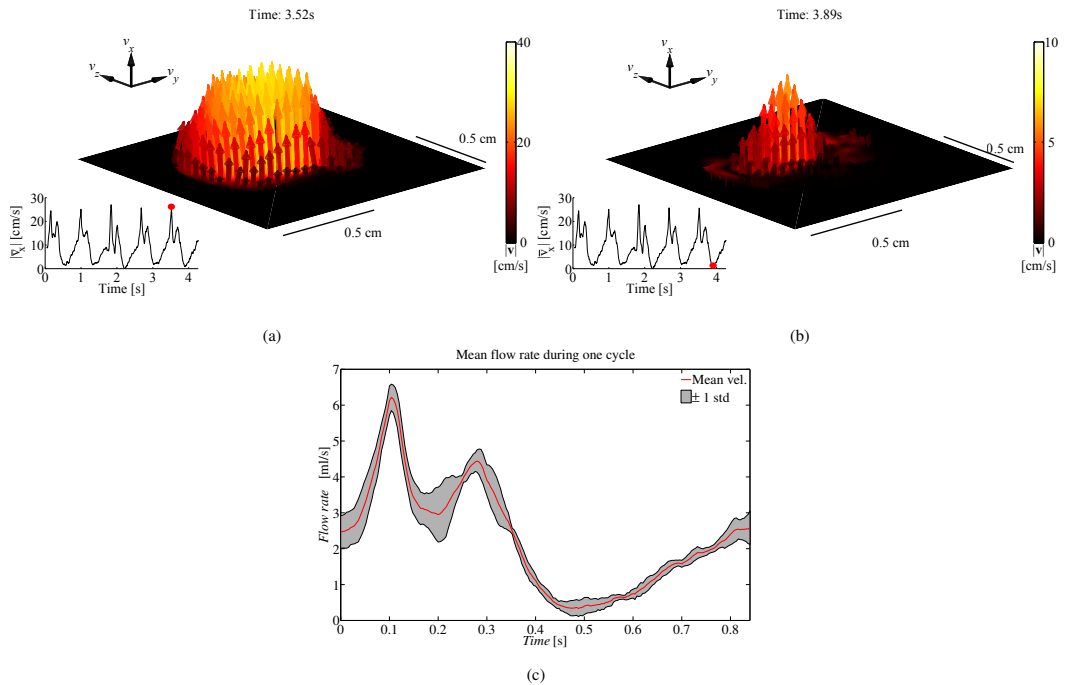


Figure 13: Cross sectional 3-D vector flow representation estimated in the pulsating setup during (a) peak-systole and (b) end-diastole. Please note that the velocity scale during peak-systole is four times larger than for the end-diastole. c) mean flow rate with std averaged across 5 cycles. A video of the complete flow is show in video 1.

[26] J. T. Yen, C. H. Seo, S. I. Awad, and J. S. Jeong, "A dual-layer transducer array for 3-D rectilinear imaging," *IEEE Trans. Ultrason., Ferroelec., Freq. Contr.*, vol. 56, no. 1, pp. 204–212, 2009.

[27] A. I. H. Chen, L. L. P. Wong, A. S. Logan, and J. T. W. Yeow, "A CMUT-based real-time volumetric ultrasound imaging system with row-column addressing," in *Proc. IEEE Ultrason. Symp.*, oct 2011, pp. 1755–1758.

[28] A. Sampaleanu, P. Zhang, A. Kshirsagar, W. Moussa, and R. Zemp, "Top-orthogonal-to-bottom-electrode (TOBE) CMUT arrays for 3-D ultrasound imaging," *IEEE Trans. Ultrason., Ferroelec., Freq. Contr.*, vol. 61, no. 2, pp. 266–276, 2014.

[29] T. L. Christiansen, M. F. Rasmussen, J. P. Bagge, L. N. Moesner, J. A. Jensen, and E. V. Thomsen, "3-D imaging using row-column-addressed arrays with integrated apodization — part II: Transducer fabrication and experimental results," *IEEE Trans. Ultrason., Ferroelec., Freq. Contr.*, vol. 62, no. 5, pp. 959–971, 2015.

[30] S. Holbek, T. L. Christiansen, M. F. Rasmussen, M. B. Stuart, E. V. Thomsen, and J. A. Jensen, "3-D vector velocity estimation with row-column addressed arrays," in *Proc. IEEE Ultrason. Symp.*, 2015, pp. 1–4.

[31] M. F. Rasmussen and J. A. Jensen, "3D ultrasound imaging performance of a row-column addressed 2D array transducer: a simulation study," in *Proc. SPIE Med. Imag.*, 2013, pp. 1–11, 86750C.

[32] M. F. Rasmussen, T. L. Christiansen, E. V. Thomsen, and J. A. Jensen, "3-D imaging using row-column-addressed arrays with integrated apodization — Part I: Apodization design and line element beamforming," *IEEE Trans. Ultrason., Ferroelec., Freq. Contr.*, vol. 62, no. 5, pp. 947–958, 2015.

[33] H. Liebgott, A. Basarab, P. Gueth, D. Friboulet, and P. Delachartre, "Transverse oscillations for tissue motion estimation," *Ultrasonics*, vol. 50, no. 6, pp. 548–555, 2010.

[34] H. Liebgott, J. Fromageau, J. E. Wilhjelm, D. Vray, and P. Delachartre, "Beamforming scheme for 2D displacement estimation in ultrasound imaging," *EURASIP J. Adv. Signal Process.*, vol. 2005, no. 8, pp. 1212–1220, 2005.

[35] S. Salles, H. Liebgott, D. Garcia, and D. Vray, "Full 3-D transverse oscillations: A method for tissue motion estimation," *IEEE Trans. Ultrason., Ferroelec., Freq. Contr.*, vol. 62, no. 8, pp. 1473–1485, 2015.

[36] C. Kasai, K. Namekawa, A. Koyano, and R. Omoto, "Real-Time Two-Dimensional Blood Flow Imaging using an Autocorrelation Technique," *IEEE Trans. Son. Ultrason.*, vol. 32, pp. 458–463, 1985.

[37] J. A. Jensen, A. H. Brandt, and M. B. Nielsen, "Convex array vector velocity imaging using transverse oscillation and its optimization," *IEEE Trans. Ultrason., Ferroelec., Freq. Contr.*, vol. 62, no. 12, pp. 2043–2053, 2015.

[38] J. A. Jensen, "Field: A program for simulating ultrasound systems," *Med. Biol. Eng. Comp.*, vol. 10th Nordic-Baltic Conference on Biomedical Imaging, Vol. 4, Supplement 1, Part 1, pp. 351–353, 1996.

[39] J. A. Jensen and N. B. Svendsen, "Calculation of pressure fields from arbitrarily shaped, apodized, and excited ultrasound transducers," *IEEE Trans. Ultrason., Ferroelec., Freq. Contr.*, vol. 39, pp. 262–267, 1992.

[40] B. J. Oosterveld, J. M. Thijssen, and W. A. Verhoef, "Texture of B-mode echograms: 3-D Simulations and experiments of the effects of diffraction and scatterer density," *Ultrason. Imaging*, vol. 7, no. 2, pp. 142–160, Apr. 1985.

[41] J. A. Jensen, H. Holten-Lund, R. T. Nilsson, M. Hansen, U. D. Larsen, R. P. Domsten, B. G. Tomov, M. B. Stuart, S. I. Nikolov, M. J. Pihl, Y. Du, J. H. Rasmussen, and M. F. Rasmussen, "SARUS: A synthetic aperture real-time ultrasound system," *IEEE Trans. Ultrason., Ferroelec., Freq. Contr.*, vol. 60, no. 9, pp. 1838–1852, 2013.

[42] J. A. Jensen, M. F. Rasmussen, M. J. Pihl, S. Holbek, C. A. Villagomez-Hoyos, D. P. Bradway, M. B. Stuart, and B. G. Tomov, "Safety assessment of advanced imaging sequences, I: Measurements," *IEEE Trans. Ultrason., Ferroelec., Freq. Contr.*, vol. 63, no. 1, pp. 110–119, 2016.

[43] J. A. Jensen, *Estimation of Blood Velocities Using Ultrasound: A Signal Processing Approach*. New York: Cambridge University Press, 1996.



## **Ultrasonic 3-D Vector Flow Method for Quantitative *in vivo* Peak Velocity and Flow Rate Estimation**

**Simon Holbek**, Caroline Ewertsen, Hamed Bouzari, Michael Johannes Pihl,  
Kristoffer Lindskov Hansen, Matthias Bo Stuart, Carsten Thomsen,  
Michael Bachmann Nielsen, and Jørgen Arendt Jensen

*Under review for IEEE Trans. Ultrason., Ferroelec., Freq. Contr*



# Ultrasonic 3-D vector flow method for quantitative *in vivo* peak velocity and flow rate estimation

Simon Holbek, Caroline Ewertsen, Hamed Bouzari, Michael Johannes Pihl, Kristoffer Lindskov Hansen, Matthias Bo Stuart, Carsten Thomsen, Michael Bachmann Nielsen, and Jørgen Arendt Jensen

**Abstract**—Current clinical ultrasound systems are limited to show blood flow movement in either 1-D or 2-D. In this paper, a method for estimating 3-D vector velocities in a plane using the Transverse Oscillation (TO) method and the experimental ultrasound scanner SARUS is presented. The aim of this paper is to exploit the advantages of 3-D vector flow information obtained with a proposed ultrasound method, to reduce manual intervention and thereby increase precision and consistency in peak velocity and flow rate measurements. The emission sequence provides 3-D vector flow estimates at 1145 frames per second in a plane. It is demonstrated, that 3-D vector flow in a cross sectional image plane, can be used to estimate accurate angle-independent flow rates both in a phantom study and *in vivo*. The method is first validated in two phantom studies, where flow rates are measured in a flow-rig, providing a constant parabolic flow, and in a straight-vessel phantom ( $\varnothing = 8$  mm) connected to a flow pump capable of generating time varying waveforms. Flow rates are estimated to be  $82.1 \pm 2.8$  L/min in the flow-rig compared with the expected 79.8 L/min, and to  $2.68 \pm 0.04$  mL/stroke in the pulsating environment compared with the expected  $2.57 \pm 0.08$  mL/stroke. Secondly, flow rates estimated with the presented method in the common carotid artery of a healthy volunteer are compared with similar measurements derived in an MRI scanner using a 1-D through-plane velocity sequence. Mean flow rates were  $6.5 \pm 0.6$  mL/stroke for the presented method and  $7.44 \pm 0.04$  mL/stroke for the MRI measurements. The results show that the estimated flow rates with the 3-D vector flow method have a high precision and are comparable to similar results obtained with MRI.

## I. INTRODUCTION

CARDIOVASCULAR diseases account for 30% of global deaths [1]. A better understanding of the true blood flow dynamics would increase the chances of diagnosing critical diseases at an earlier stage, thereby improving treatment success rates. Since vascular flow can propagate in all three dimensions, 3-D vector flow imaging at a very high frame rate is a necessity for providing operators with additional information about pathology.

Currently, velocity estimation in most commercial scanners is limited to estimating only the axial velocity using, e.g., spectral Doppler, which requires manual angle correction by the operator to obtain the true velocity magnitude. Despite

this manoeuvre being subject to critical errors in the velocity estimation, due to the correctness of the angle correction [2], [3], it is a widely used tool for peak velocity and flow rate estimation. However, angle correction schemes are not required for 2-D or 3-D vector flow techniques. Various methods for estimating 2-D vector flow or 2-D flow dynamics have been proposed by using speckle tracking [4], synthetic aperture flow [5], [6], [7], plane waves [8], [9], [10], Doppler vortography [11], and Transverse Oscillation (TO) [12], [13]. 2-D vector flow gives a more realistic estimation of the actual flow, but does not provide information about the out-of-plane velocity component.

Some of the methods proposed for vector flow estimation can also be extended to 3-D, but all of them require data sampled in two dimensions to estimate all three velocity components. Several 2-D sampling techniques have been proposed, for instance triple-beam lens transducers [14], row-column addressed 2-D arrays [15][16], and a 2-D piezoelectric matrix array [17].

A 2-D piezoelectric transducer was used in previous work, which showed that all three velocity components can be obtained for two crossing planes [18] using a 3-D implementation of the TO method [19] [20], and Provost *et al.* estimated the axial velocities in a full volume using Doppler techniques with a similar transducer [21]. The true 3-D velocity vector provides the physician with valuable information of the complex flow, without relying on transducer orientation.

Currently, state of the art magnetic resonance imaging (MRI) can provide 4-D blood flow velocity estimates for large volumes [22] and is often referred to as the gold standard for accurate non-invasive blood velocity estimation. Several studies have compared blood flow estimated from an ultrasound (US) scanning with similar observations obtained in MRI [23], [24]. They showed that US estimates are comparable to MRI, although having a positive bias. One of the drawbacks of MRI is the long acquisition time, where data are averaged over 10-15min [22][25], which makes it less suitable for estimation of peak velocities, and furthermore, the cost of the scan is significantly higher than a US scan.

In this work, the precision of 3-D US vector flow estimation is validated, first in two phantom measurements, and second, when compared against MRI by measuring the flow rates in the common carotid artery in a healthy volunteer.

Previous work with the 2-D matrix probe by our group has covered a parametric study of an M-mode sequence using the 3-D TO method for both a simulation setup, and in an experimental setup, where the blood flow estimation performance

This work was financially supported by grants 82-2012-4 from the Danish National Advanced Technology Foundation and from BK Ultrasound ApS (Herlev, Denmark).

S. Holbek, Hamed, Bouzari, M.J. Pihl, M. B. Stuart and J.A. Jensen are with the Center for Fast Ultrasound Imaging, Department of Electrical Engineering, Technical University of Denmark, Kgs. Lyngby, Denmark.

C. Ewertsen, K.L. Hansen, C. Thomsen and M.B. Nielsen are with Department of Radiology, Copenhagen University Hospital, Rigshospitalet, Copenhagen E, Denmark

on a laminar parabolic flow was investigated. [19], [20]. This paper is based on the conference proceedings [26] and expands on previous work by introducing an emissions sequence with twice the amount of flow lines, twice the acquisition time, and provides B-mode volumes obtained with synthetic aperture techniques. This was achieved primarily by adjusting the phase shift estimator to lie within the expected velocity range and by sampling data from a shorter range than previous. The revised approach was therefore obtained without sacrificing frame rate, resolution etc. It is the first peer-reviewed paper to present *in vivo* 3-D vector flow imaging (VFI) using TO. Validation of the derived angle independent 3-D vector flow estimates are compared with a gold standard MRI through-plane measurement.

## II. MATERIALS & METHODS

This Section introduces the equipment and methods used for the experimental US measurements, in terms of emission sequence, data processing and theoretical properties of the TO velocity estimator. The study was performed after approval by the Danish National Committee on Biomedical Research Ethics (H-1-2014-FSP-072).

### A. Scanner setup

The experimental ultrasound scanner SARUS [27] with 1024 channels in receive and transmit was used along with a 3.5 MHz, 0.3 mm pitch, 0.278 mm height 32x32 element 2-D phased array transducer (Vermon S.A., Tours, France) for data acquisition. See Table I for transducer specifications. The emitted frequency was 3.0 MHz. Data were sampled from all 1024 channels and stored for offline processing on a Linux cluster.

### B. Flow-rig

An in-house built flow-rig system was used to validate flow rate estimates in a steady flow. The flow-rig contained a long inlet of 1.2 m, which ensured that a steady laminar parabolic flow profile was present at the measuring site. Blood mimicking fluid was driven inside the vessel by a centrifugal pump in a closed loop circuit. At the measuring site, the rubber vessel ( $\varnothing = 12$  mm) was immersed into a water tank containing demineralized water. The volume flow  $Q$ , was measured with a MAG 1100 flow meter (Danfoss, Hasselager, Denmark). The transducer was placed in a fixture at a  $90^\circ$  beam-to-flow angle and the fixture was then placed in the water tank and aligned to the center of the vessel. A flow rate of 79.80 mL/min translating to a peak velocity of 39 cm/s was chosen.

### C. Pulsatile flow pump

For the phantom measurements a predefined pulsatile carotid flow profile was generated with a flow pump (CompuFlow 1000 System, Shelley Medical Imaging Technologies, Ontario, Canada) circulating blood mimicking fluid with a backscattering coefficient equivalent to blood cells into a straight-vessel phantom ( $\varnothing = 8$  mm and 0.8 mm thick), which

was surrounded by a tissue mimicking material. The attenuation of the tissue mimicking material was 0.5 dB/cm-MHz and the speed of sound was 1540 m/s which complies with previous reported properties [28]. With the included software CompuFlow 1000 System, a carotid flow profile was generated with a cycle time of 0.84 s and a flow rate of 2.57 mL/stroke  $\pm 3\%$  as specified by the manufacturer.

### D. Emission sequence

Considering a conventional transmit sequence composed of the unique flow lines  $F_i$ ,  $i = 1, 2, \dots, N$ , and the unique B-mode emissions  $B_j$ ,  $j = 1, 2, \dots, M$  (see Fig. 1), a schematic representation of one full transmit cycle would be written as

$$\begin{array}{c} \overbrace{F_1 \rightarrow F_1 \cdots \rightarrow F_1}^{\text{Ensemble length, } e} \\ F_2 \rightarrow F_2 \cdots \rightarrow F_2 \\ \vdots \\ F_N \rightarrow F_N \cdots \rightarrow F_N \\ B_1 \rightarrow B_2 \cdots \rightarrow B_M \end{array}$$

where the ensemble length  $e$ , is the number of emissions used for each estimate (Flow or B-mode). Each unique flow line  $F_i$  is emitted sequentially a pre-defined amount of times until the next round of a different flow line is emitted. This continues until all  $F_N$  transmit events are completed. The flow transmissions are followed by emitting one of all the  $M$  B-mode emissions. After each cycle of a unique flow emissions e.g.  $F_1$ , velocity estimates along this direction can be obtained. The same argument holds for the remaining  $N$  flow lines. After the  $M$  B-mode emissions, one B-mode image or volume can be achieved. Finally, the velocity information along all the estimated directions are assembled and can be combined with the B-mode image. Such a sequence has a high detectable velocity range but comes at the cost of a low frame rate, since estimates are made line-by-line.

An alternative emissions sequence exists, where all identical transmit events are spaced equally in time. This type of sequence is considered a continuous data scheme [5], [29]. Continuous data can be obtained through synthetic aperture imaging, for plane waves, when focused emissions are chosen, or for any other setup, as long as the transmit sequence is designed according to the aforementioned requirements.

One of the advantages of continuous data are that very high frame rates in the kHz range can be obtained [5], [7], [13], [29], [30]. The high frame rate is achievable as a sliding window can be moved along the processed data, in such a way, that whenever a new acquisition has been made, it replaces the oldest sample within the ensemble length in the velocity estimator. Furthermore, several adaptive algorithms can be applied to improve the estimates. For instance, when continuous data are available, the number of emissions needed in the respective estimator may vary or more advanced echo canceling filters may be used.

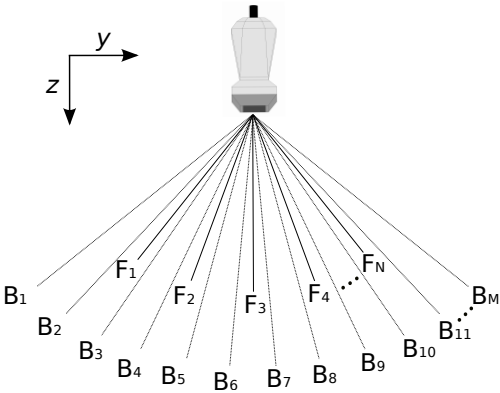


Fig. 1: Illustration of how an emission sequence for continuous data acquisition could be constructed. First, the flow lines  $F_{1 \rightarrow N}$  are emitted followed by the diverging B-mode emission  $B_1$ . The next cycle contains the flow lines  $F_{1 \rightarrow N}$  and ends with the B-mode emission  $B_2$ . This continues until  $B_N$  is reached, and the sequence can be repeated. The angles spanned are only for illustrative purpose and not to scale.

The idea is, that the duration between emissions of two identical flow lines  $F_i$ , or two identical B-mode emissions  $B_j$ , should be the same at all times. This is achieved by emitting the flow lines  $F_{1 \rightarrow N}$  consecutively, followed by emitting the B-mode emission  $B_1$ . Next, the flow lines  $F_{1 \rightarrow N}$  are emitted, followed by the B-mode emission  $B_2$  etc. When the last unique B-mode emissions  $B_M$  has been transmitted, the sequence repeats itself from the beginning. A schematic representation of the emission sequence would be

$$\begin{array}{l}
 F_1 \rightarrow F_2 \rightarrow F_3 \rightarrow F_4 \cdots \rightarrow F_N \rightarrow B_1 \rightarrow \\
 F_1 \rightarrow F_2 \rightarrow F_3 \rightarrow F_4 \cdots \rightarrow F_N \rightarrow B_2 \rightarrow \\
 \vdots \quad \quad \quad \vdots \quad \quad \quad \vdots \quad \quad \quad \vdots \\
 F_1 \rightarrow F_2 \rightarrow F_3 \rightarrow F_4 \cdots \rightarrow F_N \rightarrow B_M \rightarrow
 \end{array}$$

The presented emission sequence fulfills the requirement of having the same time span between two similar transmit events, and can acquire continuous data. Based on the above mentioned principles an interleaved emissions sequence with  $M = 36$  and  $N = 10$  was designed. The flow lines were steered from  $-15^\circ$  to  $15^\circ$  in steps of  $3.3^\circ$ . Electronic delay profiles were applied on all 1024 elements in transmit to generate a focal point at 35 mm depth for the flow sequence. The 36 B-mode emissions with virtual point sources placed 15 mm behind the transducer at different locations, were applied to generate a  $60^\circ \times 60^\circ$  field-of-view volume using synthetic aperture imaging techniques, see Fig. 2. From each B-mode emission, a low resolution volume was beamformed. After a full transmit cycle, 36 low resolution volumes were coherently added to form the final high resolution volume. After each  $B_M$

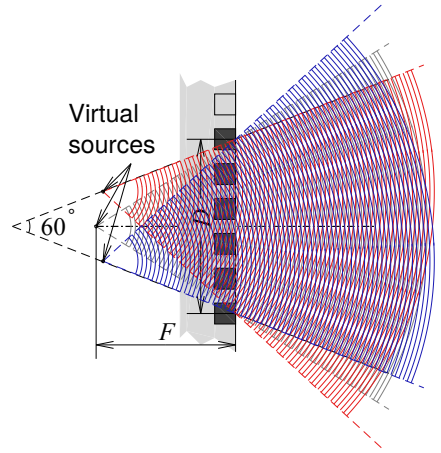


Fig. 2: Synthetic aperture B-mode imaging beam steering and no translation. The concept is here illustrated in a plane parallel to the 2-D transducer and is not to scale. The virtual sources are located behind the aperture.  $D$  is the active aperture dimension, and  $F$  denotes the focal point distance of the middle emission to the center of the active aperture. The final high resolution B-mode volume is the overlapping region with a  $60^\circ$  field of view.

emission, a full volume with a  $60^\circ \times 60^\circ$  field-of-view could be beamformed. An 8 cycle Hanning-weighted pulse was used for flow emissions and a 2 cycle excitation was used for B-mode emissions. A summary of the variables used for the flow and B-mode sequence is seen in Table I.

#### E. FDA limits

Intensity measurements were performed to ensure compliance with current FDA intensity regulations [31]. A setup with an Onda HGL-0400 hydrophone (Onda Corp., Sunnyvale, CA) connected to an Onda ATH-2000 attenuator connected to an Onda AH-2000 pre-amplifier was placed in a water tank to measure the pressure field, generated in the plane where the highest intensities were expected, i.e the  $zy$ -plane where flow emissions were transmitted [32]. At every specified point in the  $zy$ -plane, the pressure field was recorded for one complete cycle of the transmit sequence (B-mode and flow) as applied in the measurements. The derated mechanical index (MI) was 1.14 and the system pulse repetition frequency  $f_{prf}$  was scaled to 12.6 kHz for the *in vivo* measurements to obtain  $I_{spta.3} = 439 \text{ mW/cm}^2$  in accordance with FDA limits.

#### F. Data processing

The stored data were processed offline. The raw RF data were matched filtered by convolving the signal with the time-reversed excitation pulse and Hilbert transformed, before the IQ data were beamformed with the Beamformation Toolbox 3 [33]. In this part, the three velocity components were decoupled, such that one line was beamformed for the axial

velocity estimation and two dedicated lines were beamformed for each of the two transverse velocity estimates. In total five unique beamformed lines were used to estimate the 3-D velocity vector for each flow line. For a more extensive description of the employed 3-D TO method, see previous work [19], [20], [34]. Echo cancellation of the beamformed data were performed with two different approaches, depending on the expected tissue motion; in the flow-rig measurement, where no tissue movement was expected, echo canceling was performed by subtracting the mean value from 16 samples from the signal. In cases where pulsating flow was resulting in tissue movement, a frequency energy cut-off based algorithm [35], where an ensemble length of 256 was used to filter out frequency contents from tissue movement in the Fourier domain.

### G. Velocity estimators

The axial velocity  $v_z$  estimates were based on the autocorrelation approach [36], and the two transverse velocity components were found by using the TO phase shift estimator and the beamforming procedure described in [12][37].

For each transverse velocity estimate, two TO beams were beamformed along the lines separated spatially by their respective transverse wavelengths  $\lambda_x/4$  or  $\lambda_y/4$ , thereby generating two fields phase-shifted by  $90^\circ$ . The two transverse wavelengths are theoretically given by

$$\begin{aligned}\lambda_x(z) &= 2\lambda_z \frac{z}{d_x} \\ \lambda_y(z) &= 2\lambda_z \frac{z}{d_y},\end{aligned}\quad (1)$$

where  $\lambda_z$  is the wavelength of the emitted pulse,  $z$  is the axial depth of the beamformed RF-line and  $d_x, d_y$  the distance between the center of the two peaks in the receive apodization in the  $x$ - and  $y$ -directions. The receive apodization profile consists of two rect profiles spanning respective 8 and 10 elements, with a spacing of 24 elements for  $d_y$  and 22 elements for  $d_x$ . From [37], the maximum detectable transverse velocities that can be estimated before reaching the aliasing limit are

$$\begin{aligned}v_{x_{max}} &= \frac{\lambda_x}{4k} \frac{f_{prf}}{N+1} \\ v_{y_{max}} &= \frac{\lambda_y}{4k} \frac{f_{prf}}{N+1},\end{aligned}\quad (2)$$

where  $k$  is the lag used in the autocorrelation and  $f_{prf}$ , is the effective pulse repetition frequency between two identical transmit events.

The applied 2-D array transducer contains three inactive rows in the  $x$ -direction due to construction issues. The dimensions of the actual transducer is therefore  $35 \times 32$  with the active aperture being  $32 \times 32$ . Due to the asymmetric geometry of the transducer and different spacing between the TO apodization profiles, two distinct transverse wavelengths must be found and used for velocity estimation in 3-D.

The transverse wavelengths  $\lambda_x$  and  $\lambda_y$  were 3.21 mm and 2.55 mm, respectively, at the depth of 2 cm. The wavelengths

were estimated from the TO spatio-temporal frequency spectrum to lower the bias on the estimated velocities [38], and were simulated in Field II [39], [40]. The transverse wavelengths were used to calculate the respective TO beamforming angles as they were approximately scalable through a linear fit.

The robustness of the velocity estimate is improved by averaging the estimated velocities over the pulse length [37]. The number of emissions per estimate was 16.

### H. Phase shifting

The TO method is a phase shift estimator where a four-quadrant inverse tangent operation is used in the calculations. Thus, there exist a limitation on the maximum detectable velocity, since the phase range spans from  $[-\pi : \pi]$ , which translates to  $[-v_{max} : v_{max}]$ . This phase range can be shifted a maximum of  $\pi$  in either direction where it is most useful to increase the maximally detectable velocity without reaching the aliasing limit [41]. In this study the phase range was placed at  $[-\frac{\pi}{2}, \frac{3\pi}{2}]$ , which translates to a detectable velocity range of  $[-\frac{1}{2}v_{max} : \frac{3}{2}v_{max}]$  to match the expected velocities.

### I. Sliding window

A sliding window in the temporal direction, containing 16 samples, was applied in the off-line processing such that data from the oldest transmit event were replaced by data from the newest transmit event. With this setup, the obtainable frame rate was  $1145$  frames per second ( $f_{prf}/(N+1)$ ) at  $f_{prf} = 12.6$  kHz, which translates to fully independent estimates every 14 ms.

### J. Interpolation

Since velocity estimation is only performed along the direction of the flow lines, interpolation was performed to produce a color flow map (CFM). Interpolation was done by first scan converting the velocities according to their steering angle and then by performing a spline interpolation with boundary conditions outside the drawn mask set to zero velocity. At 20 mm depth, this corresponded to a lateral spacing between the flow lines of 1.2 mm. The final image had the dimensions of  $512 \times 512$  pixels ( $30 \times 30$  mm<sup>2</sup>). A manual segmentation mask  $M$  of the lumen was made based on the B-mode images to determine the flow regions.

### K. Flow rate estimation

The instantaneous volumetric flow rate  $Q(t)$  is defined as

$$Q(t) = \sum_i A_i v_i(t), \quad (3)$$

where the cross-section of the blood vessel is divided into small areas of size  $A_i$  each with a velocity component  $v_i(t)$ , propagating perpendicularly to  $A_i$ . In this paper, the index value  $i$  for the velocity component was replaced by the pixel values in  $(x_j, y_k)$  and the cross-sectional area  $A$  was the metric area of a pixel size which was constant. The flow rates at each

pixel were calculated by multiplying the scan converted out-of-plane velocity component  $v_x(x_j, y_k)$  with the corresponding pixel value for the drawn mask  $M(x_j, y_k)$  and the cross-sectional area  $A$ . Mask values were either 0 or 1 and constant in time. The flow rate at time  $t$  was then

$$Q(t) = \sum_j \sum_k A v_x(x_j, y_k, t) M(x_j, y_k), \quad (4)$$

where the summation ran over all the  $j \times k$  pixels in the image.

In the experimental setup, flow rates were estimated based on a beamformed B-mode volume where the plane parallel to the flow transmissions was taken out for further processing. The B-mode image was used for manually delineating a mask of the cross sectional vessel. Only flow within this mask was examined in the further processing. After the delineation mask was drawn, the flow was processed, scan converted, interpolated and the mask was multiplied onto the final estimates. Within this mask, the flow rates, based on the velocity component perpendicular to the plane was calculated as a function of time.

#### L. Angle Estimation

The processed data provide the velocity components  $v_x, v_y$  and  $v_z$  along each steered direction, hence the direction of the flow, given by the angles  $\alpha$  and  $\beta$  can be determined as

$$\alpha = \sin^{-1} \frac{v_z}{|\mathbf{v}|} \quad (5)$$

$$\beta = \arctan \frac{v_y/|\mathbf{v}|}{v_x/|\mathbf{v}|} = \arctan \frac{v_y}{v_x}, \quad (6)$$

where  $|\mathbf{v}|$  is the magnitude of the velocity,  $\alpha$  is the rotation around the  $y$ -axis and  $\beta$  the rotation around the  $z$ -axis. The estimated angles were used to estimate the direction of the flow in the *in vivo* setup.

### III. US MEASUREMENT SETUP

The following section describes the different parameters used for the phantom and *in vivo* measurements. Transducer properties and flow estimation parameters are listed in Table I. An illustration of the experimental setup and its coordinate system is seen in Fig. 3. The only difference between phantom and *in vivo* measurements was the  $f_{prf}$ , which was set to match the actual flow velocities.

#### A. Flow-rig measurements

The transducer was oriented to acquire 3-D vector flow in a cross sectional scan plane and fixated in a  $90^\circ$  beam-to-flow angle with a distance of 2.6 cm from transducer surface to the vessel center.  $f_{prf}$  was scaled to 5 kHz to match with the expected velocity range. The maximum detectable out-of-plane velocity component  $v_x$ , which was expected to have the largest magnitude, was at 2 cm depth

$$v_{x,max} = \frac{\lambda_x f_{prf}}{4 N + 1} = \frac{0.32 \text{ cm } 5000 \text{ s}^{-1}}{4 \cdot 10 + 1} = 36 \text{ cm/s}. \quad (7)$$

With the  $\pi/2$  phase shift, this translates to a detectable velocity range of [-18; 55] cm/s.

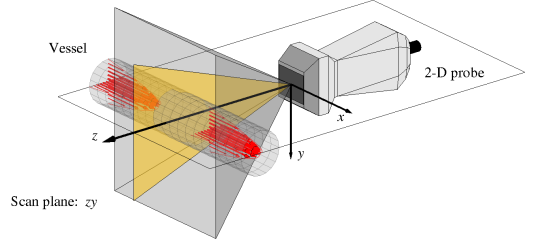


Fig. 3: A 2-D matrix probe was oriented at a  $90^\circ$  degree beam-to-flow angle with the flow moving in the  $x$ -direction. Flow data (yellow plane) are only obtained for the  $zy$ -plane, whereas B-mode (gray box) is present in a symmetric volume. The angles spanned are only for illustrative purpose and not to scale.

#### B. Flow pump measurements

The transducer was oriented to acquire 3-D vector flow in a cross sectional scan plane and fixated in a  $90^\circ$  beam-to-flow angle with a distance of 1.9 cm from transducer surface to the vessel center.  $f_{prf}$  was 5 kHz and a  $\pi/2$  phase shift was applied to comply with the expected velocity range.

#### C. Clinical setup for *in vivo* measurements

The *in vivo* measurement was performed on a healthy 27-year old male, who had been resting for 15 min before measurements were conducted to ensure steady state flow. The scans were performed by an experienced radiologist (CE). Prior to the experimental scans, a 1-D spectral Doppler reference measurement was made for comparison with the similar measurement made prior to the MRI scans. The reference measurements were made with a linear 5.2 MHz probe (9032, BK Ultrasound, Herlev, Denmark) on a commercial scanner (BK 5000, BK Ultrasound, Herlev, Denmark). Properties for the *in vivo* sequence are summarised in Table I.

The system pulse repetition frequency  $f_{prf}$  was 12.6 kHz in the *in vivo* study to yield a higher detectable velocity range, especially for the  $v_x$ -component, which was [-45 ; 137] cm/s at 2 cm depth. Cross sectional measurements were conducted 2-3 cm before the bifurcation in the common carotid artery.

### IV. MRI SCANS

#### A. MRI experimental setup

A 1.5 T whole body scanner (Avanti, Siemens, Erlangen, Germany) was used for estimation of through-plane velocities in a cross sectional view of the right common carotid artery. A retrospective electrocardiography (ECG) gated phase contrast sequence in combination with a head and a neck matrix coil were used to estimate through-plane velocities in a plane. The sequence had a repetition time of 42 ms, echo time 3 ms, flip angle  $20^\circ$ , pixel resolution of  $1.1 \times 1.1$  mm in an image of size  $216 \times 256$  pixels, slice thickness 5 mm, and a maximum velocity encoding of  $\pm 1.0$  m/s. Estimates were retrieved from 210 heartbeats. An anatomical image

TABLE I: Transducer and Emissions Sequence Setup

Transducer		Flow Parameters		B-mode	
Parameter	Value	Parameter	Phantom <i>In vivo</i>	Parameter	Value
Transducer type	2-D phased array	Excitation signal	8 cycled sin. Hanning weighted	Excitation signal	2 cycled sin.
No. of elements in x	35 ( 3 inactive rows)	Frequency	3 MHz	Frequency	3 MHz
No. of elements in y	32	Flow lines $N$	10	B-mode emissions $M$	$6 \times 6$
Pitch in x & y	0.3 mm	$f_{prf}$	5 kHz 12.6 kHz	Virtual source	-1.5 cm
Height	0.278 mm	Steering angles	$[-15^\circ; 15^\circ]$	Field-of-view	$60^\circ \times 60^\circ$
Kerf	0.022 mm	Emissions per estimate	16	Emissions per volume	36
Sampling frequency	17.5 MHz	$\lambda_x$ & $\lambda_y$	3.21 mm & 2.55 mm	Tx apodization	Hann
Center frequency	3.5 MHz	Focal depth	35 mm	Rx apodization	Hann.

with similar resolution was acquired parallel to the applied flow sequence. Three similar measurements were performed such that a standard deviation on MRI results could be estimated. The measurements were conducted 2-3 cm before the bifurcation in the common carotid artery to comply with the *in vivo* 3-D ultrasound measurement. The volunteer had been resting 10 min before the MRI scans. Prior to the MRI scans, a spectral Doppler measurement with similar equipment as described in III-C was performed for reference.

### B. MRI processing

A total of three velocity data sets were acquired and processed offline. Each data set contained anatomical and through-plane velocity information in an entire plane from 50 different time instances in the cardiac cycle. A data set was processed by reading the stored DICOM files into MATLAB and adding up all the 50 temporal frames to create a combined anatomical intensity map, (see Fig. 4a), to suppress noise and enhance vessel regions. Based on the intensity map, a binary image was created with a threshold of 35% of the maximum intensity to segment out vessel regions (Fig. 4b). A morphological opening operation was used to remove objects less than  $20 \text{ mm}^2$  from the binary image. A boundary detection algorithm was run on the binary image, to identify the perimeter of the remaining object. Based on the identified regions of interest (ROI), a manually selection of the region, where the cross sectional common carotid artery was expected to be was performed (Fig. 4c), which created a binary ROI mask. Since anatomical data and flow data were acquired in parallel, the selected mask was applied on the flow data (Fig. 4d), such that all pixels inside the ROI were used to estimate peak velocities and temporal flow rates as stated in(4). The described procedure was applied on all three acquisitions.

## V. RESULTS

### A. Flow-rig measurements

A total of 15.8 s of data were acquired. Due to an ensemble length of 16, the temporal flow rate estimates were divided into sections of similar size, and the mean from each section was calculated. The standard deviation was calculated from the mean of all the sections. This gave an estimated flow rate of  $82.1 \pm 2.8 \text{ L/min}$  compared with the expected  $79.80 \text{ L/min}$ . The delineated area was  $114 \text{ mm}^2$  compared with the theoretical  $113 \text{ mm}^2$ .

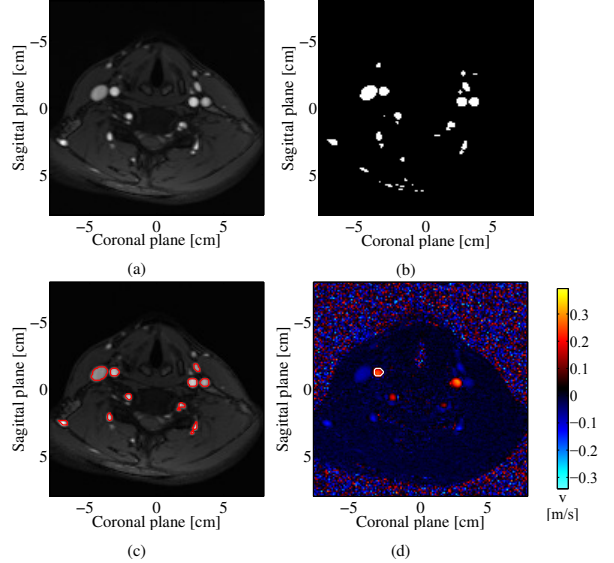


Fig. 4: a) Summed anatomical intensity map. b) Binary anatomical image based on a 35% threshold of the maximum intensity c) Identified ROI after morphological opening and boundary detection, which was presented for the radiologist for identification of the right common carotid artery. d) Mean velocity image with the identified ROI superimposed on top (white ring). Pixels inside this ROI were used for flow rate and peak velocity estimation.

### B. Flow pump measurements

A total of 18.9 s of data were acquired and data processing was made similar to the flow-rig measurement. The delineated mask of the cross sectional vessel is shown in Fig. 5.

The estimated temporal flow rates were used to automatically estimate the average time between each cycle with an autocorrelation routine. A cycle time of 838 ms, which translates to 382 velocity estimates per cycle and 22 cycles in total, was observed. This was in agreement with the software specified 840 ms.

The data set was divided into 22 cycles, which could be coherently aligned. The temporal volumetric flow rates with the cycle division is shown for the first 10 s of acquisition,

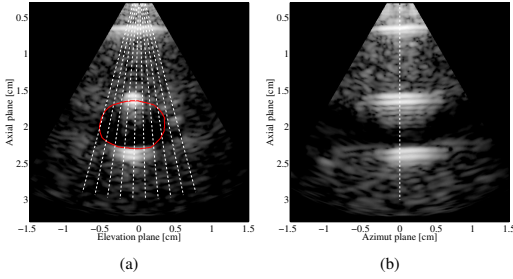


Fig. 5: a) Cross sectional image plane of the straight-vessel phantom with the drawn mask (red curve) and the flow emissions (dotted lines). b) Longitudinal scan plane orthogonal to a). The images are planes taken out from the beamed volume and are shown at 50 dB dynamic range.

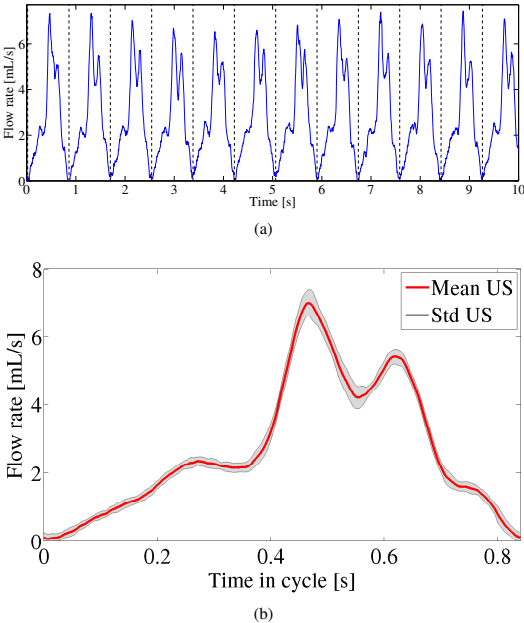


Fig. 6: a) Temporal volumetric flow rate based on the delineated cross sectional vessel area and the velocity component perpendicular to the plane. The dotted lines illustrate the start and end of the estimated cycle. b) Mean cycle flow rate (red curve)  $\pm$  one standard deviation (grey area) estimated from 22 coherently aligned flow rate estimates.

see Fig. 6a. A flow rate of  $2.68 \pm 0.04$  mL/stroke was found from the coherently aligned 22 cycles (see Fig. 6b) compared with the  $2.57 \pm 0.08$  mL/stroke specified by the manufacturer. The delineated vessel area was  $48.4 \text{ mm}^2$  compared with the expected area of  $50.3 \text{ mm}^2$  calculated from the specified vessel radius.

### C. *In vivo* US measurements

For the *in vivo* measurements, 7.5 s of data were recorded. Data were processed as described in Section V-B. A heart cycle time of 1.17 s gave an estimated heart rate of 51 beats/min, which translates to 1345 velocity estimates per cycle. In total 6 complete heart cycles were identified, and the vessel center was located at a depth of 1.5 cm.

Thus, the temporal flow rates could be divided into 6 complete heart cycles as shown in Fig. 7a. Due to the short acquisition time, it was expected that the temporal flow rates during each cycle could be coherently aligned. Alignment of the flow rates are shown in Fig. 7b.

Fig. 7c, shows the aligned mean flow rate. A flow rate of  $6.5 \pm 0.6$  mL/stroke, translating to 333 mL/min, was seen for the 6 cycles and the vessel area was estimated to  $62 \text{ mm}^2$ . The maximum peak systolic velocity magnitude for each cycle was  $99 \pm 3$  cm/s compared with a value of  $107 \pm 2$  cm/s obtained with spectral Doppler techniques and the commercial scanner prior to the measurements (Fig. 7d).

Since 3-D vector flow data were present, the beam-to-flow angle  $\alpha$  and the flow rotation angle  $\beta$  was calculated throughout the coherently added cycles. The angles were calculated from the similar ROI as used for estimating peak velocities. A flow entirely perpendicular to the scan plane (i.e. a  $90^\circ$  beam-to-flow angle) would result in  $\alpha = 0^\circ$  and  $\beta = 0^\circ$ . The temporal flow directions are seen in Fig. 8 with the mean precession values  $\alpha = 2.4^\circ \pm 0.9^\circ$  and  $\beta = -29.1^\circ \pm 0.8^\circ$ . The angulation of the transducer is also illustrated in a 3-D vector flow map during the end-diastole (Fig. 9a) but mostly during the peak-systole (Fig. 9).

### D. MRI measurements

Data from the three MRI measurement were processed off-line as described IV-B. The mean vessel area of the right common carotid artery was found to be  $41.7 \text{ mm}^2$  and temporal flow rates and peak velocities are shown in respective Fig. 7c and 7d. The mean flow rate was  $7.44 \text{ mL/stroke} \pm 0.04$  mL/stroke and the peak velocity was  $77 \pm 1$  cm/s compared with  $101 \pm 1$  cm/s obtained with spectral Doppler before the measurements. The heart cycle lasted 1.29 s, which translates to a flow rate of 346 mL/min.

## VI. DISCUSSION

Both phantom measurements showed that the proposed method for flow rate estimation provided a high precision of 3.4% and 1.5% for constant and pulsatile flow, respectively. Furthermore a small bias was seen of 2.9% for the flow-rig measurement and 4.3% for the pulsating flow pump measurement.

For the estimated peak velocities using 3-D vector flow and MRI, an offset of  $\approx 0.2$  m/s throughout the heart cycle was seen for the US measurements. There may be several explanations for this bias. The peak velocities estimated with US were angle independent and derived from the 3-D velocity vector, whereas MRI peak velocities were entirely based on the through plane component. With MRI the highest peak velocities are therefore expected to be obtained, if the common

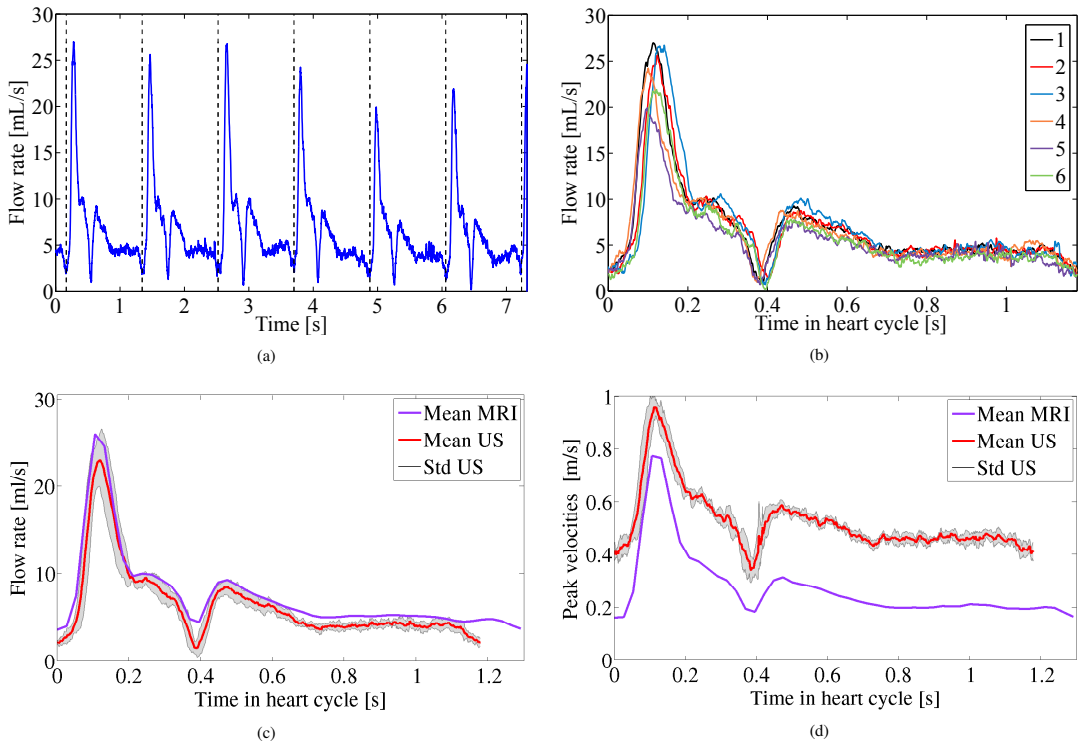


Fig. 7: a) Estimated flow rates (blue curve) with the applied heart cycle division (dotted lines). b) Estimated flow rates of the 6 coherently aligned heart cycles. c) Mean volumetric flow rate throughout a heart cycle seen with MRI (purple curve) and US (red curve  $\pm$  one standard deviation). d) Peak through plane velocities seen with MRI (purple curve) and US (red curve  $\pm$  one standard deviation).

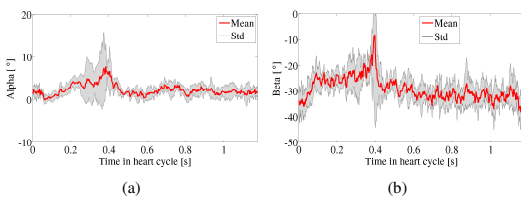


Fig. 8: a) Estimated *in vivo* beam-to-flow angle  $\alpha$ . b) Estimated *in vivo* flow direction  $\beta$ .

carotid artery was aligned to be perpendicular to the imaging scan plane. This could not be assured, which can explain the underestimation. The underestimation of peak velocities with MRI, can also be due to the spatial and temporal resolution. The spatial resolution of  $1.2 \text{ mm}^2/\text{pixel}$  results in velocity estimates averaged within a relatively large area compared with both 3-D VFI and spectral Doppler estimates. This smoothing effect is further enhanced by the long acquisition of 210 heart beats, where very small patient movements of

only 0.5 mm will result in a shift in the velocity estimates by one pixel.

A fair comparison between MRI and the 3-D vector flow method is by estimating flow rates. This measure is angle independent, as long as the cross sectional vessel area is present and the velocities perpendicular to this plane are estimated, which was the case for both MRI and the US measurements.

A high precision was found for the US estimated flow rates of 9.1% even though data from only 6 completed cycles were present. MRI had a much higher precision of only 0.5%, which comes from 3 acquisitions each containing the mean from 210 heart beats. The actual estimated mean flow rates with US and MRI did deviate by 15% when measuring in mL/stroke, but only by 3.9% when using mL/min. However, the results were obtained based on two different cross-sectional vessel areas of  $62 \text{ mm}^2$  for US and  $42 \text{ mm}^2$  for MRI. It is difficult to tell, if the vessel was delineated correctly in both modalities, since a ground-truth could not be obtained, and also, since the vessel could intersect with the respective scan-plane at different angles. Future work should investigate the effect of using a time-varying vessel mask, which both tracks

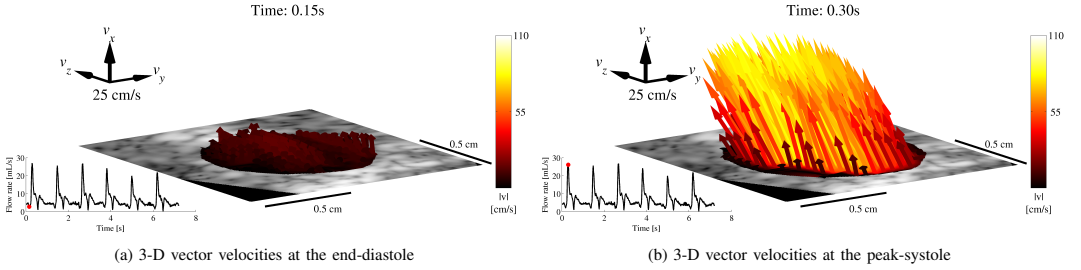


Fig. 9: 3-D vector flow from the common carotid artery during the end-diastole a) and during peak-systole b). The coloured arrows depicts the direction of the flow and its magnitude. The velocity arrows are plotted on top of a B-mode image and only values within the delineated mask are shown. The scan was not conducted exactly cross-sectional to the vessel, which is revealed in b) where a significant  $v_y$  velocity component is present. The bottom-left graph shows the flow rate at the time instance in the heart cycle indicated by the the red dot.

the displacement and the expansion/contraction of the vessel.

Even though the volunteer had undergone the same resting procedure prior to both MRI and US measurements, the flow dynamics were expected to fluctuate. However, the spectral Doppler results obtained prior to both measurements showed consistency ( $PS = 101.3 \pm 1.2$  cm/s before MRI and  $106.8 \pm 1.7$  cm/s before US) and the heart cycle time was 1.29 s during MRI measurements and 1.17 s while obtaining the US data. The fluctuation in flow dynamics between the two measurements was therefore expected to be small.

Sampling data from a total of 1024 channels can seem somewhat impractical, but currently, these are the order of 2-D fully populated matrix probes. Even significantly larger matrix array are currently available for commercial use, as the 9.212 element fully sampled phased matrix array X6-1 PureWave xMATRIX probe from Phillips (Eindhoven, Netherlands). The high channel count results both in complex interconnection processes and in an increased computational load. Due to this, the idea of row-column addressing the elements evolved [42], [43]. A row-column addressed array reduces the number of elements from  $N \times N$  in a matrix array to  $N + N$ . Despite the significant reduction of channels, these arrays have a great potential and thus, 3-D VFI using TO has been implemented using a  $62 + 62$  element row-column array [44].

In this study focused emission were used for vector flow estimation, although a 2-D array was used. The reason being, that focused emissions provides a higher signal-to-noise ratio (SNR) compared to plane waves or diverging waves at the focal point. Future work should explore the potential for combining TO with plane waves or diverging wave transmission, which can be used to estimate 3-D vector flow in a plane or in the entire volume. Recent work has been reported in the literature for estimating volumetric 3-D flow using a 2-D matrix probe for plane waves combined with vector Doppler [45], and synthetic aperture directional beamforming combined with diverging waves [46]. For these kind of transmissions, the transmitted energy will be distributed into a larger region compared with focused emissions. This results in a poorer SNR but might be compensated by the several transmit events overlapping each other.

Vector Doppler techniques exploits that the triangulation of individual axial velocity estimates achieved from plane waves steered in different directions, can provide 2-D or 3-D VFI. The methods uses a phase shift estimator, where the aliasing limit is proportional to the axial wavelength. As a consequence of this, transmit sequences used for vector Doppler methods are restricted to only contain few unique flow emissions to avoid reaching the aliasing limit, compared with a sequence used for TO. However, this can be counterbalanced by the axial estimator usually being more robust and subject to fewer optimization routines than the TO estimator. The similar is present when comparing a transmit sequence used for a directional beamforming approach with a sequence used for TO. To maintain a high degree of correlation between consecutive high resolution images, used in the directional beamforming approach, the time between similar transmit events must be kept at a minimum. If this can be achieved, the directional beamforming method can produce very convincing results of complex flow *in vivo* [7], although accompanied by a very high computational load compared with TO.

The real advantage of 3-D VFI US as a tool for flow rate or peak velocity estimation, lies in its mobility, where it can be applied directly at the patient bedside at a fraction of the cost of a similar MRI measurement. If a high precision and consistency can be provided, the presented method has several potential clinical applications as e.g. blood flow surveillance of dialysis patients, peak velocity estimation in stenotic regions, monitoring of patients during surgery etc. The 3-D vector flow information provides an additional potential diagnostic tool since blood dynamics can be explored in all its three propagation directions. A recent study interoperative, using 2-D vector flow techniques, found a correlation between the degree of blood turbulence in the systolic flow and whether patients had a normal aortic valve or an aortic valve stenosis. Furthermore, the turbulence measure was applied to evaluate the improvement before and after valve replacement. [47]. With access to 3-D VFI, diagnostics using blood turbulence measures might be even further improved.



## **3-D Velocity Estimation for Two Planes *in vivo***

**Simon Holbek**, Michael Johannes Pihl, Caroline Ewertsen,  
Michael Bachmann Nielsen, and Jørgen Arendt Jensen

*Proceeding of IEEE International Ultrasonics Symposium., p. 1706-1709, 2014*

*Accepted for poster presentation in Chicago, Illinois, United States, 2014.*



# 3-D Velocity Estimation for Two Planes *in vivo*

Simon Holbek\*, Michael Johannes Pihl\*, Caroline Ewertsen†, Michael Bachmann Nielsen† and Jørgen Arendt Jensen\*

\* Center for Fast Ultrasound Imaging, Dept. of Elec. Eng., Bldg. 349, Technical University of Denmark, 2800 Kgs. Lyngby, Denmark

† Department of Radiology, Copenhagen University Hospital, 2100 Copenhagen, Denmark

**Abstract**—3-D velocity vectors can provide additional flow information applicable for diagnosing cardiovascular diseases e.g. by estimating the out-of-plane velocity component. A 3-D version of the Transverse Oscillation (TO) method has previously been used to obtain this information in a carotid flow phantom with constant flow. This paper presents the first *in vivo* measurements of the 3-D velocity vector, which were obtained over 3 cardiac cycles in the common carotid artery of a 32-year-old healthy male volunteer. Data were acquired using a Vermon 3.5 MHz 32x32 element 2-D phased array transducer and stored on the experimental scanner SARUS. The full 3-D velocity profile can be created and examined at peak-systole and end-diastole without ECG gating in two planes. Maximum out-of-plane velocities for the three peak-systoles and end-diastoles were  $68.5 \pm 5.1$  cm/s and  $26.3 \pm 3.3$  cm/s, respectively. In the longitudinal plane, average maximum peak velocity in flow direction was  $65.2 \pm 14.0$  cm/s at peak-systole and  $33.6 \pm 4.3$  cm/s at end-diastole. A commercial BK Medical ProFocus UltraView scanner using a spectral estimator gave 79.3 cm/s and 14.6 cm/s for the same volunteer. This demonstrates that real-time 3-D vector velocity imaging without ECG gating yields quantitative *in vivo* estimations on flow direction and magnitude.

## I. INTRODUCTION

Ultrasound (US) is a commonly used approach for estimating blood velocities. The information about the direction and magnitude of the blood flow is of great importance in the clinic for diagnosing various cardiovascular diseases [1] [2]. The possibility of estimating the full 3-D velocity vector in any given plane would provide valuable additional information for the medical doctors. Currently 3-D vector velocity can be acquired with MRI, but this image modality can only show a flow cycle that is averaged from 10-15 minutes of data acquisition [3][4]. Therefore the flow in real-time is not shown. Furthermore, MRI also has the disadvantage compared to ultrasound that the cost is much higher and that it can be more uncomfortable to the patients.

The 3-D Transverse Oscillation (TO) method has previously shown good results for out-of-plane flow rate estimation in a phantom with constant flow, as well as in *in vivo* M-mode measurements of the 3-D velocity vector at the center of a carotid artery [5]. These values are currently estimated clinically from spectral Doppler velocities. A correct velocity value is obtained when: The vessel has circular symmetry, the US beam penetrates the middle of the vessel, and when the angle correction is done correctly [6]. By implementing the 3-D TO technique to obtain the full 3-D velocity vector *in vivo* for the out-of-plane components, the accuracy of the measured flow rates and peak velocities in the vessel could be improved, as this approach is unaffected by vessel geometry.

More flexibility in probe placement is also obtained as results are angle independent.

This paper shows that the 3-D TO method can be used to estimate the full 3-D velocity vector *in vivo* for two crossing scan planes in the common carotid artery for a 32-year-old healthy male volunteer.

## II. METHODS

### A. Scanner setup

An experimental ultrasound scanner SARUS [7] with 1024 channels in receive and transmit was used along with a Vermon 3.5 MHz 32x32 element 2-D phased array transducer (Vermon S.A., Tours, France) for data acquisition. Data were sampled from all 1024 channels and stored for offline processing on a Linux cluster. An illustration of the experimental setup is given in previous work [5].

### B. Emissions sequence

At 13 Hz, 45 frames consisting of two crossing planes were acquired with a complex interleaved sequence composed of 768 emissions. The emission sequence for each plane was as follows (see illustration on Fig. 1): First the left half-plane was created by emitting 5 unique flow emissions running from  $F_1$  to  $F_5$  consecutively. After the emission of  $F_5$  the first B-mode  $B_1$  shot is emitted. This is followed by the emissions  $F_{1-5}$  with  $B_2$  emitted after the last flow line,  $F_5$ . This pattern continues for 32 cycles and the full sequence for the left half-plane can schematically be written as:

$$\begin{array}{cccccccc} F_1 & \rightarrow & F_2 & \rightarrow & F_3 & \rightarrow & F_4 & \rightarrow & F_5 & \rightarrow & B_1 & \rightarrow \\ F_1 & \rightarrow & F_2 & \rightarrow & F_3 & \rightarrow & F_4 & \rightarrow & F_5 & \rightarrow & B_2 & \rightarrow \\ \vdots & & \vdots & \\ F_1 & \rightarrow & F_2 & \rightarrow & F_3 & \rightarrow & F_4 & \rightarrow & F_5 & \rightarrow & B_{32} & \rightarrow \end{array}$$

The right half-plane is created in a similar way such that the flow emissions  $F_{5-9}$  are followed by the B-mode line  $B_{33}$  etc. where the flow line  $F_5$  is the only unique emission that is present in both half-planes. The second plane is created immediately after emission  $B_{64}$  and contains additionally 64 unique B-mode lines and 9 unique flow lines since  $F_5$  also is present in this plane. The repetition of  $F_5$  in all 4 half-planes allows for velocity estimation of continuous data in the center shot. Each plane consisted of 64 B-mode emissions spanning the angles from  $-31.5^\circ$  to  $31.5^\circ$  in steps of  $1^\circ$  and  $32 \times 10$  flow emissions covering the angle span from  $-12^\circ$  to  $12^\circ$  in steps of

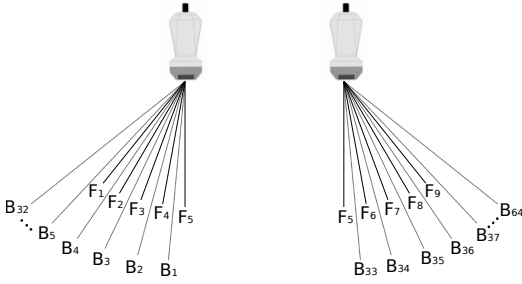


Fig. 1. *Left*: The emissions sequence for the left half-plane. First the unique flow lines  $F_{1-5}$  are emitted and are followed by the unique B-mode line  $B_1$ . The emission of  $B_1$  if followed by the emissions  $F_{1-5}$  that are followed by  $B_2$  and so on. This continues 32 times until  $B_{32}$  is emitted. *Right*: The emissions sequence for the right half-plane. The emission procedure is the same as for the left half-plane but with new unique flow and B-mode lines. Only  $F_5$  is emitted again which ensures that continuous data in the center can be obtained. Note that angles between lines are not representative for the used sequence but serves as an illustration of the principles.

$3^\circ$ . With a pulse repetition frequency (PRF) of 9.9 kHz and by creating one half-plane at a time, the effective PRF for each flow line was 1.65 kHz. With this experimental setup, sequence and sampling depth, a total duration of 3.5 s of continuous data could be stored.

The reason for constructing such a complex sequence was to increase the number of flow lines used in each plane to cover the region of interest without lowering frame rates to inadequate levels. Also, the effective PRF for each flow line was taken into account in the sequence design, since this, together with the transverse wavelength at a specific depth, determines the maximum velocity that can be estimated without aliasing. The maximum velocities that could be estimated in 2 cm depth with the auto-correlation method were in our case:

$$\max V_x = \frac{\lambda_x}{4} \cdot PRF = \frac{0.228 \text{ cm}}{4} \cdot 1650 \text{ s}^{-1} = 94 \text{ cm/s}$$

$$\max V_y = \frac{\lambda_y}{4} \cdot PRF = \frac{0.257 \text{ cm}}{4} \cdot 1650 \text{ s}^{-1} = 106 \text{ cm/s}$$

Where  $\lambda_x$  and  $\lambda_y$  were the transverse wavelengths. These value were calculated beforehand to ensure that the maximum velocities in the carotid could be estimated.

### C. FDA limits

Intensity measurements of the complex emission sequence used for the *in-vivo* measurements were conducted with an acoustic intensity measurement system, AIMS III (Onda, Sunnyvale, California, USA). The derated value for MI was 1.50, and the pulse repetition frequency was scaled to 9.9 kHz to obtain  $I_{spta,3} = 720 \text{ mW/cm}^2$  in compliance with the FDA limits [8]. Thermal measurements were also conducted for the sequence by measuring the temperature on the surface of the transducer for 30 minutes at continuous emission. The measurements showed a temperature rise of  $7.3^\circ \text{ C}$  in air and a rise in temperature in a tissue mimicking phantom (Danish Phantom Design, Frederikssund, Denmark) of  $2.7^\circ \text{ C}$ . Both in compliance with the IEC limits of a maximum temperature rise of  $27^\circ \text{ C}$  in air and  $10^\circ \text{ C}$  for tissue at 30 minutes consecutive emission [9].

### D. Clinical setup

To ensure a steady flow, the volunteer had been resting for 15 minutes before the measurements were conducted. A spectrogram of the volunteer's common carotid artery was acquired using a BK8670 linear transducer and a BK Medical ProFocus scanner. Since the spectrogram and the vector flow imaging (VFI) data could not be obtained simultaneously, due to use of different scanners and transducers, the VFI data were obtained immediately after the collection of the spectrogram data.

### E. Data processing

The stored data were processed offline, where the raw RF data were match filtered and Hilbert transformed before the IQ data were beamformed with the Beamformation Toolbox 3 [10]. In this part, the three velocity components were decoupled, such that one line was beamformed for the axial velocity estimation and two dedicated lines were beamformed for each of the transverse and elevation velocity estimates. In total 5 unique beamformed lines were used to estimate the 3-D velocity vector for each flow line. For a more extensive description of the 3-D transverse oscillation method used, see previous work [11]. Echo cancellation of the beamformed data was subsequently done with a low frequency Doppler filter algorithm [12] due to the rapidly moving vessel walls in the peak-systole.

The axial velocity estimates were based on the autocorrelation approach [13] whereas the transverse and elevation estimates relied on the TO method [14][15]. Due to the geometry and the asymmetry of the transducer, two distinct and simulated transverse wavelength were used;  $\lambda_x = 2.28 \text{ mm}$  and  $\lambda_y = 2.57 \text{ mm}$ . The estimated velocities were finally rotated according to their steering angle and linearly interpolated. Each velocity estimate was based on a packet size of 32 emissions. The discrimination used to select between flow and B-mode image in the vessel was drawn manually by an experienced radiologist based on one B-mode image.

## III. RESULTS

Forty-five cross-sectional frames were acquired in which three cardiac cycles could be identified. Figure 2 shows the three velocity components in the transverse out-of-plane for two consecutive frames. The left column shows the velocities at the end-diastole, where the maximum velocities are (30.1, 8.4, 1.0) cm/s in the  $(v_x, v_y, v_z)$  directions respectively. The column to the right are the three velocity components at one of the identified peak-systoles with maximum velocities of (74.3, 28.4, 2.5) cm/s.

Figure 3 shows the three velocity components in the longitudinal ZX-plane for two consecutive frames. The left column shows the velocities at the end-diastole, where the maximum velocities are (35.4, 12.5, 4.9) cm/s in the  $(v_x, v_y, v_z)$  directions respectively. The column to the right are the three velocity components at one of the identified peak-systoles with maximum velocities of (75.0, 74.9, 20.7) cm/s.

For comparison the similar angle corrected  $v_x$  velocities estimated with spectral Doppler on a commercial scanner in the middle of the vessel and along the direction of flow were

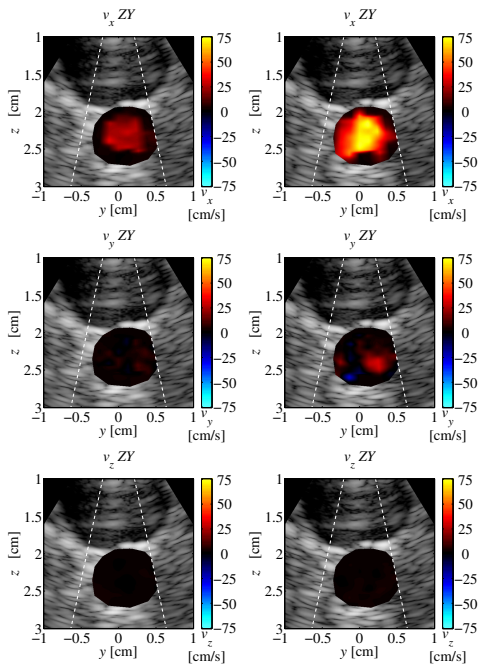


Fig. 2. Magnitude of each velocity component in the ZY-plane for two consecutive frames in the dataset: frame 1 (left) and frame 2 (right). Frame 1 is identified as the end-diastole and frame 2 is identified as peak-systole with maximum out-of-plane  $v_x$  velocity of 74.3 cm/s. The two dotted white lines on each image illustrate the span of the flow emissions.

14.6 m/s at end-diastole and 79.3 m/s at peak systole (data not shown).

The maximum out-of-plane velocities for the three identified end-diastoles and peak-systoles were  $68.5 \pm 5.1$  cm/s and  $26.3 \pm 3.3$  cm/s, respectively. For the longitudinal ZX-plane the three identified end-diastoles and peak-systoles were  $65.2 \pm 14.0$  cm/s and  $33.6 \pm 4.3$  cm/s, respectively

Since each velocity estimate is averaged from 32 emissions that are acquired in the time it takes to produce one half plane ( $32 \times (5+1)$  emissions), the estimated velocities will always have lower maximum velocities and higher minimum velocities compared to what can be obtained on a commercial scanners with spectral Doppler. This is due to a longer acquisition time that results in a velocity estimate that is averaged over a longer time interval than spectral Doppler.

In Fig. 4, velocity profiles of the out-of-plane  $v_x$  component can be seen for the two centerlines in frames 1 and 2. The profiles illustrate the out-of-plane velocity at the end-diastole (red curve) and during peak-systole (blue curve). The velocity profile at end-diastole exhibits a more plug flow curve than at the peak-systole. For a 3-D vector velocity representation of the peak-systole flow in the ZY-plane see Fig. 5.

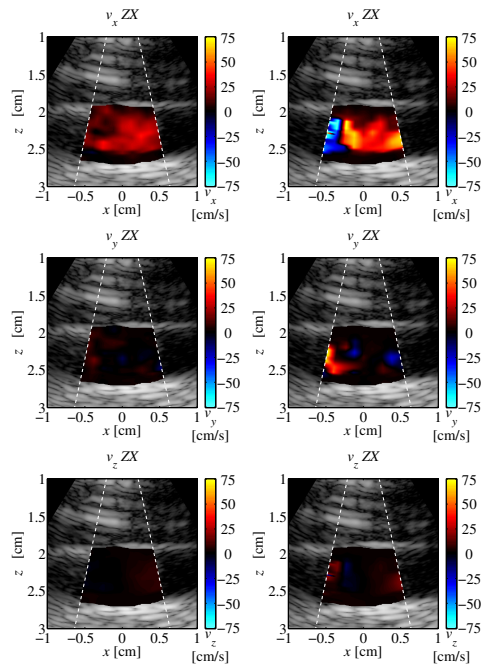


Fig. 3. Magnitude of each velocity component in the ZX-plane for two consecutive frames in the dataset: frame 1 (left) and frame 2 (right). Frame 1 is identified as the end-diastole and frame 2 is identified as peak-systole with maximum  $v_x$  velocity of 74.9 cm/s. The two dotted white lines on each image illustrate the span of the flow emissions. The erroneous velocity estimates in the left half plane at the peak-systole might be due to the rapid wall-movement that weakens the effect of the echo canceling filter.

#### IV. DISCUSSION

The small active aperture in the 2-D transducer used results in a relatively long lateral wavelength that complicates the estimation of slow flow. Furthermore, the small aperture also complicates the construction of an accurate echo-canceling filter, which is designed to suppress the RF-signal from slowly moving tissue. This is especially seen during peak-systole where the echo-canceling filter has some difficulties to suppress the strong signal from the rapid wall-movement, which can lead to biased velocity estimation. The rapid wall-movement can be an explanation to why erroneous velocity estimates occur during peak-systole in Fig. 3. The velocity estimates in the right half-plane at peak systole in the ZX-plane are as expected and are quantitative comparable with the velocities obtained during peak-systole in the ZY-plane (see Fig. 2). Since the emissions sequence obtains data for one half-plane at a time a short time difference is present between the estimates which can explain why erroneous velocity estimates only are present in one plane and that peak and mean velocities differs from the two crossing planes.

Some disadvantages of the sequence used, are that the packet size and the PRF have to be predefined before the measurements, as is normally adjusted in commercial scanners

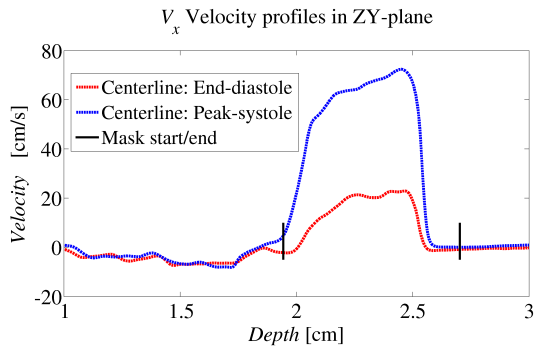


Fig. 4. Velocity profiles for the centerline estimate of the out-of-plane components in the ZY-plane. The red curve shows the  $V_x$  as a function of depth just before peak systole and the blue curve shows it at the identified peak-systole. The two black lines mark the end and beginning of the discriminator for that line.

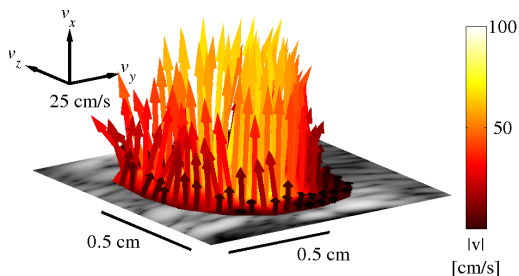


Fig. 5. 3-D vector velocity representation of the blood flow at peak-systole in the ZY-plane.

by the user. For estimating slow flow a low PRF and a large packet size is preferable, whereas for fast flow the opposite is needed for the best velocity estimation.

The TO method can gain from the large transverse wavelength, which makes it possible to estimate large velocities in the lateral and elevation direction. The larger wavelength makes it possible to either lower the PRF or to redesign the sequence and emit more unique flow lines and still be able to estimate all present velocities.

## V. CONCLUSION

This paper demonstrates for the first time, real-time *in vivo* 3-D vector velocities measured with US. The obtained  $V_x$  velocities averaged over three peak-systoles were 15.8% lower for the ZY-plane and 21.6% lower for the ZX-plane, than velocities estimated with spectral Doppler using a commercial scanner. Intensity and heat measurements were conducted, both in compliance with the FDA limits. The results show that 3-D VFI can be obtained *in vivo* with a 2-D transducer using

the TO method. It is a step towards estimating flow rates for diagnosing cardiovascular diseases without making any assumptions about vessel geometry or angle correction.

## ACKNOWLEDGMENT

This work was supported by grant 82-2012-4 from the Danish Advanced Technology Foundation and by BK Medical Aps.

## REFERENCES

- [1] G. M. von Reutern and M. W. Goertler and N. M. Bornstein and M. D. Sette and D. H. Evans and A. Hetzel and M. Kaps and F. Perren and A. Razumovky and et al., title = "Grading Carotid Stenosis Using Ultrasonic Methods, *Stroke*, vol. 43, no. 3, pp. 916–921, 2012.
- [2] G. R. Hong, M. Kim, G. Pedrizzetti, and M. A. Vannan, "Current clinical application of intracardiac flow analysis using echocardiography," *Journal of Cardiovasc Ultrasound*, vol. 21, no. 4, pp. 155–162, 2013.
- [3] M. Markl, A. Harloff, T. A. Bley, M. Zaitsev, B. Jung, E. Weigang, M. Langer, J. Hennig, and A. Frydrychowicz, "Time-resolved 3D MR velocity mapping at 3T: improved navigator-gated assessment of vascular anatomy and blood flow," *Journal of magnetic resonance imaging*, vol. 25, no. 4, pp. 824–831, 2007.
- [4] J. Eriksson, C. Carlhall, P. Dyverfeldt, J. Engvall, A. Bolger, and T. Ebbers, "Semi-automatic quantification of 4D left ventricular blood flow," *Journal of Cardiovascular Magnetic Resonance*, vol. 12, no. 1, p. 9, 2010.
- [5] M. J. Pihl, M. B. Stuart, B. G. Tomov, P. M. Hansen, M. B. Nielsen, and J. A. Jensen, "In vivo three-dimensional velocity vector imaging and volumetric flow rate measurements," in *Proc. IEEE Ultrason. Symp.*, July 2013, pp. 72–75.
- [6] R. W. Gill, "Measurement of blood flow by ultrasound: Accuracy and sources of error," *Ultrasound Med. Biol.*, vol. 11, pp. 625–641, 1985.
- [7] J. A. Jensen, H. Holten-Lund, R. T. Nilsson, M. Hansen, U. D. Larsen, R. P. Domsten, B. G. Tomov, M. B. Stuart, S. I. Nikolov, M. J. Pihl, Y. Du, J. H. Rasmussen, and M. F. Rasmussen, "SARUS: A synthetic aperture real-time ultrasound system," *IEEE Trans. Ultrason., Ferroelec., Freq. Contr.*, vol. 60, no. 9, pp. 1838–1852, 2013.
- [8] FDA, "Information for manufacturers seeking marketing clearance of diagnostic ultrasound systems and transducers," Center for Devices and Radiological Health, United States Food and Drug Administration, Tech. Rep., 2008.
- [9] IEC, "Medical electrical equipment - part 2-37: Particular requirements for the safety of ultrasonic medical diagnostic and monitoring equipment," International Electrotechnical Commission, Tech. Rep., 2004.
- [10] J. M. Hansen, M. C. Hemmsen, and J. A. Jensen, "An object-oriented multi-threaded software beamformation toolbox," in *Proc. SPIE Med. Imag.*, vol. 7968, March 2011, pp. 79680Y 1–9. [Online]. Available: <http://dx.doi.org/10.1117/12.878178>
- [11] M. J. Pihl and J. A. Jensen, "3D velocity estimation using a 2D phased array," in *Proc. IEEE Ultrason. Symp.*, 2011, pp. 430–433.
- [12] A. P. G. Hoeks, J. J. W. van de Vorst, A. Dabekausen, P. J. Brands, and R. S. Reneman, "An efficient algorithm to remove low frequency Doppler signal in digital Doppler systems," *Ultrason. Imaging*, vol. 13, pp. 135–145, 1991.
- [13] C. Kasai, K. Namekawa, A. Koyano, and R. Omoto, "Real-Time Two-Dimensional Blood Flow Imaging using an Autocorrelation Technique," *IEEE Trans. Son. Ultrason.*, vol. 32, pp. 458–463, 1985.
- [14] J. A. Jensen and P. Munk, "A New Method for Estimation of Velocity Vectors," *IEEE Trans. Ultrason., Ferroelec., Freq. Contr.*, vol. 45, pp. 837–851, 1998.
- [15] J. A. Jensen, "A New Estimator for Vector Velocity Estimation," *IEEE Trans. Ultrason., Ferroelec., Freq. Contr.*, vol. 48, no. 4, pp. 886–894, 2001.

# Paper IV

---

## ***In vivo* 3-D Vector Velocity Estimation with Continuous Data**

**Simon Holbek**, Michael Johannes Pihl, Caroline Ewertsen, Michael Bachmann Nielsen,  
and Jørgen Arendt Jensen

*Proceeding of IEEE International Ultrasonics Symposium., p. 1-4, 2015*

*Accepted for oral presentation in Taipei, Taiwan, 2015.*



# In Vivo 3-D Vector Velocity Estimation with Continuous Data

Simon Holbek\*, Michael Johannes Pihl\*, Caroline Ewertsen†, Michael Bachmann Nielsen† and Jørgen Arendt Jensen\*

\* Center for Fast Ultrasound Imaging, Dept. of Elec. Eng., Bldg. 349, Technical University of Denmark, 2800 Kgs. Lyngby, Denmark

† Department of Radiology, Copenhagen University Hospital, 2100 Copenhagen, Denmark

**Abstract**—In this study, a method for estimating 3-D vector velocities at very high frame rate using continuous data acquisition is presented. An emission sequence was designed to acquire real-time continuous data in one plane. The transverse oscillation (TO) method was used to estimate 3-D vector flow in a carotid flow phantom and *in vivo* in the common carotid artery of a healthy 27-year old female. Based on the out-of-plane velocity component during four periodic cycles, estimated flow rates in an experimental setup was  $2.96 \text{ ml/s} \pm 0.35 \text{ ml/s}$  compared to the expected  $3.06 \text{ ml/s} \pm 0.09 \text{ ml/s}$ . In the *in vivo* measurements, three heart cycles acquired at 2.1 kHz showed peak out-of-plane velocities of 83 cm/s, 87 cm/s and 90 cm/s in agreement with the 92 cm/s found with spectral Doppler. Mean flow rate was estimated to 257 ml/min. The results demonstrate that accurate real-time 3-D vector velocities can be obtained using the TO method, which can be used to improve operator-independence when examining blood flow *in vivo*, thereby increasing accuracy and consistency.

## I. INTRODUCTION

The cardiovascular blood flow is very complex as it propagates in all three dimension, where short lived vortices can arise and vanish within 100-200 ms [1]. So, to provide the true dynamics of the blood flow, 3-D vector velocities at a high frame rate is therefore necessary. However, current methods for velocity estimations are mainly restricted to 1-D or 2-D methods.

For estimating 2-D vector flow various methods have been proposed, e.g., speckle tracking [2], directional beamforming [3], plane wave emissions as suggested in [4] and transverse oscillation (TO) [5]. 2-D vector flow gives a more realistic picture of the actual flow, but does not provide information about the out-of-plane velocity component.

For realtime out-of-plane velocity estimation, a 2-D transducer is needed. A 2-D piezoelectric transducer was used in previous work, which showed that all three velocity components can be obtained for two crossing planes [6] using a 3-D implementation of the TO method [7] [8] and Provost *et al* with a similar transducer, estimated the axial velocities in a full volume using Doppler techniques [9].

One method to increase the frame rate significant, is by designing an emission sequence for continuous data acquisition. Continuous data acquisition offers several interesting options; for instance, the frame rates for velocity estimates can be increased to the kHz range, which helps to capture complex flow patterns. Second, adaptive velocity estimation algorithms can be applied to create a more complex and dynamic echo

cancelling or increase the detectable velocity range under the rapid changing conditions during a cardiac cycle.

This paper presents the results from 3-D vector velocity estimation using continuous data in both an experimental setup and for an *in vivo* measurement. The out-of-plane velocity components is in both cases used to derive the flow rates. With the applied emissions sequence, ultrafast frame rates up to 2.1 kHz was obtained. In combination with the TO method, both slow flow in the end-diastole and fast flow in the peak-systole could be detected.

## II. MATERIALS & METHODS

This section describes the continuous 3-D method. It introduces the equipment, emission sequence, data processing, and theoretical properties of the TO velocity estimator. The basic principles of the TO method is described in [5][10].

### A. Emission sequence

In Fig. 1 an illustration is seen of how the applied sequence was designed to yield continuous data. The idea is that the duration between emissions of two identical flow lines  $F_i$  should be the same at all times. This could for instance be achieved by emitting the flow lines  $F_1$ - $F_5$  consecutively, followed by emitting the B-mode line  $B_1$ . Next, the flow lines  $F_{1-5}$  would be emitted again, followed by the B-mode line  $B_2$  etc. When the desired amount of B-mode lines  $B_n$  has been reached, the sequence repeats itself from the beginning. The number of unique B-mode emission  $B_N$  was set to 64 in all measurements. A schematic representation of an emission sequence is

$$\begin{array}{cccccccc} F_1 \rightarrow F_2 \rightarrow F_3 \rightarrow F_4 \rightarrow F_5 \rightarrow B_1 \rightarrow & & & & & & & \\ F_1 \rightarrow F_2 \rightarrow F_3 \rightarrow F_4 \rightarrow F_5 \rightarrow B_2 \rightarrow & & & & & & & \\ & \vdots & \vdots & \vdots & \vdots & \vdots & \vdots & \\ F_1 \rightarrow F_2 \rightarrow F_3 \rightarrow F_4 \rightarrow F_5 \rightarrow B_N \rightarrow & & & & & & & \end{array}$$

This would produce continuous flow data and one or multiple continuous B-modes images if desired.

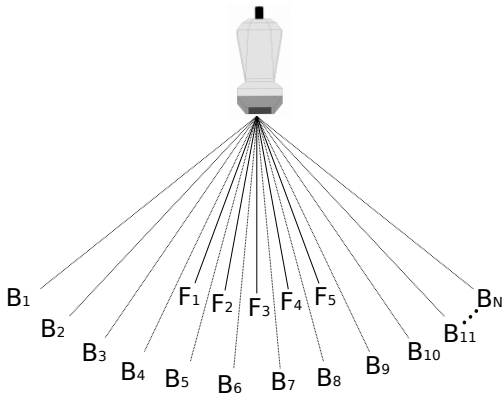


Fig. 1. Illustration of how an emission sequence for continuous data acquisition could be constructed. First, the flow lines from  $F_1$  to  $F_5$  are emitted followed by a B-mode line  $B_1$ . The next cycle contains again all the flow lines from  $F_1$  to  $F_5$  and is ended with the B-mode line  $B_2$ . This continues until  $B_N$  is reached, and the first cycle can be repeated again. The angles spanned are only for illustrative purpose and not to scale.

### B. Velocity estimators

The axial velocity estimates were based on the autocorrelation approach [15], and the two transverse velocity components were found by using the TO method [5][10].

For each transverse velocity estimate two TO beams were beamformed along the lines separated spatially by their respective transverse wavelengths  $\lambda_x/4$  or  $\lambda_y/4$ , thereby generating two fields phase-shifted by  $90^\circ$ . The two transverse wavelengths are theoretically given by

$$\begin{aligned}\lambda_x(z) &= 2\lambda_z \frac{z}{d_x} \\ \lambda_y(z) &= 2\lambda_z \frac{z}{d_y},\end{aligned}\quad (1)$$

where  $\lambda_z$  is the wavelength of the emitted pulse,  $z$  is the axial depth of the beamformed RF-line and  $d_x$ ,  $d_y$  are the distances between the two peaks in the receive apodization in the  $x$ - and  $y$ -direction. The apodization used in receive was in both directions two rect profiles spanning 8 elements with a spacing of 16 elements between. From [10], the maximum transverse velocities that could be estimated without reaching the aliasing limit were

$$\begin{aligned}v_{x_{max}} &= \frac{\lambda_x}{4k} f_{prf} \\ v_{y_{max}} &= \frac{\lambda_y}{4k} f_{prf},\end{aligned}\quad (2)$$

where  $k$  is the lag used in the autocorrelation and  $f_{prf}$  is the effective pulse repetition frequency between two emissions of the same flow line.

### C. Measurement setup

The experimental ultrasound scanner SARUS [11] with 1024 channels in receive and transmit was used along with a Vermon 3.5 MHz, 0.3 mm pitch, 0.278 mm height  $32 \times 32$  element 2-D phased array transducer (Vermon S.A., Tours, France) for data acquisition. See Table I for transducer specifications. The emitted frequency was 3.0 MHz, to avoid grating-lobes and reduce transducer heating. Data was sampled from all 1024 channels and stored for offline processing on a Linux cluster.

The employed 2-D matrix probe contains, due to construction issues, three inactive rows in the  $x$ -direction. The dimensions of the actual transducer is therefore  $35 \times 32$  with the active aperture being  $32 \times 32$ .

### D. Setup for flow pump measurements

For the phantom measurements a predefined pulsating carotid flow profile was generated with a flow pump (CompuFlow 1000 System, Shelley Medical Imaging Technologies, Ontario, Canada) containing blood mimicking fluid with backscattering coefficient equivalent to blood cells. With the included software CompuFlow 1000 System, a carotid flow profile was generated with a cycle time of 0.84 s and a flow rate of  $3.06 \text{ ml/s} \pm 0.09 \text{ ml/s}$ . A blood mimicking fluid was pumped through a carotid phantom (Danish Phantom Design, Frederikssund, Denmark) with a diameter of 0.8 cm located at a depth of 2.7 cm. Properties for the sequence used for the experimental setup can be seen in Table I.

### E. Clinical setup

Intensity measurements to ensure compliance with the FDA limits, were performed for the *in vivo* sequence. The derated mechanical index (MI) was 1.29 and the pulse repetition frequency  $f_{prf}$  was scaled to 12.6 kHz to obtain  $I_{spta.3} = 720 \text{ mW/cm}^2$  in accordance with FDA limits. The *in vivo* measurement was performed on a healthy 27-year old female who had been resting for 15 minutes before measurements were conducted to ensure a steady flow. The scans were performed by an experienced radiologist. Properties for the *in vivo* sequence are summarized in Table I as well.

## III. DATA PROCESSING

The stored data was processed offline. The raw IQ data was match filtered and Hilbert transformed before the IQ data was beamformed with the Beamformation Toolbox 3 [12]. In this part, the three velocity components were decoupled, such that one line was beamformed for the axial velocity estimation and two dedicated lines were beamformed for each of the two transverse velocity estimates. In total five unique beamformed lines were used to estimate the 3-D velocity vector for each flow line. Due to the asymmetric geometry of the transducer, two different transverse wavelengths  $\lambda_x$  and  $\lambda_y$  where used for the velocity estimator. The applied transverse wavelengths were  $\lambda_x = 3.42 \text{ mm}$  and  $\lambda_y = 3.90 \text{ mm}$  for the experimental setup and  $\lambda_x = 1.98 \text{ mm}$  and  $\lambda_y = 2.18 \text{ mm}$  for the *in vivo* measurements at the depth of 2.7 cm and 1.5 cm respective. For a more extensive description of the employed 3-D TO method, see previous work [13],[7],[8]. Echo cancellation of the beamformed data was subsequently performed with a low frequency Doppler filter algorithm [14].

TABLE I. TRANSDUCER AND EMISSIONS SEQUENCE SETUP

Transducer		Flow Parameters	
Parameter	Value	Parameter	Phantom <i>In vivo</i>
Transducer type	2-D phased array	Excitation signal	8 cycles Hanning weighted
No. of elements in x	35 (3 inactive rows)	Frequency	3.0 MHz 3.0 MHz
No. of elements in y	32	Number of flow lines $F_N$	11 5
Pitch in x and y	0.3 mm	$f_{prf}$	7.5 kHz 12.6 kHz
Height	0.278 mm	Steering angles	$[-12^\circ; 12^\circ]$ $[-10^\circ; 10^\circ]$
Kerf	0.022 mm	$\Delta$ line separation	2.4° 5°
Sampling frequency	70 MHz	Receive apodization	Rect Rect
Decimation factor	2	No. of elements between TO apodization peaks	24 24
Center frequency	3.5 MHz	No. of elements in TO apodization	8 8

#### IV. RESULTS

In this section, results from the two conducted experiments are presented. First, results from the flow pump experiment are presented, and thereafter results from the *in vivo* experiment.

##### A. Flow pump measurements

From the experimental setup with the flow pump, four seconds of continuous data at 625 Hz was acquired corresponding to 4.8 cycles. Based on a B-mode image showing the cross-sectional view of the vessel, a mask was manually drawn to segment out an area used for velocity estimates. Out-of-plane velocities were calculated in the selected area and the flow rate through it was estimated. The calculated flow rates are seen in Fig. 2. From the known cycle time of 0.84 s, the data set was divided into four phase coherent cycles, and the mean and standard deviation (SD) were calculated. The average flow rate of the profile in Fig. 3 was  $2.96 \pm 0.35$  ml/s compared with the theoretical average flow rate of  $3.06 \text{ ml/s} \pm 0.09 \text{ ml/s}$ .

##### B. In vivo measurements

From the 3.07 seconds of continuous data obtained at 2.1 kHz, three complete heart cycles could be identified. As expected the highest peak velocities were found for the center flow line, which propagated closest to the center of the vessel. Peak out-of-plane velocities in each cycle were 83 cm/s ( $t = 0.69$  s), 87 cm/s and 90 cm/s ( $t = 2.55$  s) based on an M-mode view. Based on the average time between these peak velocities, a heart cycle time of 0.93 s giving a heart rate of 64 beats/min was found. This heart cycle time was used in future calculations.

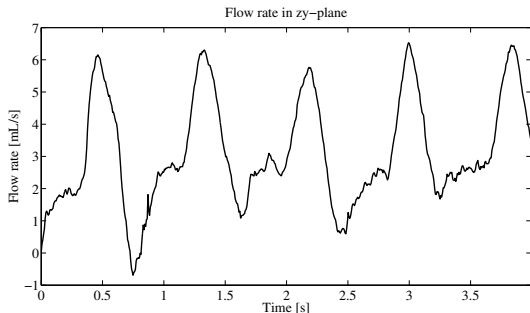


Fig. 2. Flow rates estimated from the out-of-plane velocity component in the experimental setup.

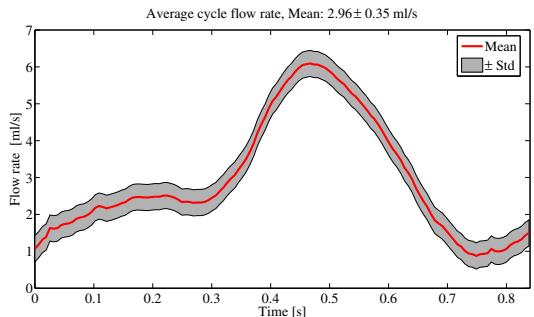


Fig. 3. Mean flow rate averaged over four complete cycles (red line) and one standard deviation (grey area). Mean average flow rate obtained in the phantom experiment was  $2.96 \pm 0.35$  ml/s.

The discriminated velocity estimates for all three components were then scan converted and interpolated yielding a complete 3-D vector velocity map at each time instance. The data set was divided into three subsets each of length 0.93 s. The mean 3-D vector velocities during one cycle was then found by calculating the average velocity estimate for all three velocity components across the three sub-samples. In Fig. 4 3-D vector velocities averaged over three heart cycles at the identified end-diastole are presented. The magnitude of the velocity vector  $|\mathbf{v}| = \sqrt{v_x^2 + v_y^2 + v_z^2}$  was found to be 17.0 cm/s in the center of the vessel. The highest center velocity for  $|\mathbf{v}| = 81.6$  cm/s was identified as the peak-systole. Spatial variance in peak velocity between each heart cycle and a slightly variance in the heart cycle time results in an average  $|\mathbf{v}|$  during peak systole that is lower than the peak  $v_z$  velocities during each of the three heart cycles. The 3-D vector velocity map is seen in Fig. 4. Based on the cross-sectional area and the out-of-plane velocity component, the estimated mean average flow rate was 257 ml/min. In the literature the corresponding flow rate from the carotid artery found with spectral Doppler for a healthy person is 334 ml/min [16].

#### V. DISCUSSION & CONCLUSION

The presented results showed that 3-D vector velocities at very high frame could be obtained when acquiring continuous data. In combination with the TO method, both the slow and fast flow could be detected in pulsating flow setups. The TO method was applicable for estimating accurate flow rates in an experimental setup with a flow pump generating a carotid flow profile.

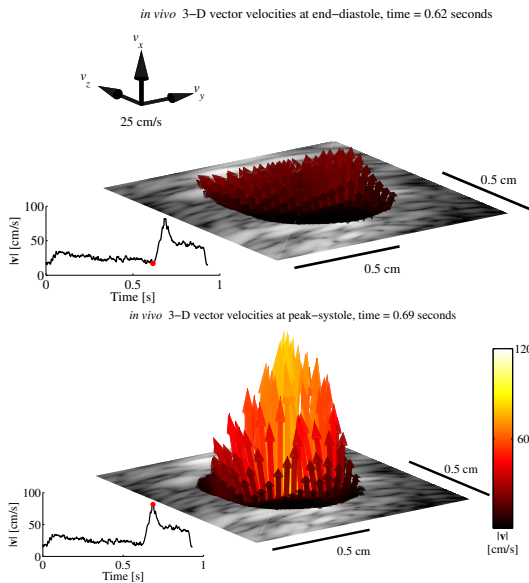


Fig. 4. 3-D vector velocities at the end-diastole,  $|v| = 17.0$  cm/s. 3-D vector velocities at the peak-systole,  $|v| = 81.6$  cm/s. 3-D vector velocities averaged over three complete and consecutive heart cycles. The bottom-left graph shows the magnitude of  $v$  in the center of the vessel at the time instance of the cycle indicated by the red dot. The colored arrows depicts the direction of the flow and its magnitude. The velocity arrows are plotted on top of a B-mode image and only values within the discriminator are shown. Mean flow rate over the averaged cycle was 257 ml/min.

The presented method offers a unique possibility to study complex flow pattern in 3-D, even when slow and fast flow is present. Furthermore, accurate angle-independent flow rates and peak velocity estimates can be derived from the 3-D vector flow. However, further validation of the method against e.g. similar MRI estimates are needed to clarify the accuracy and potential for clinical use.

#### ACKNOWLEDGMENT

This work was supported by grant 82-2012-4 from the Danish National Advanced Technology Foundation and by BK Ultrasound Aps.

#### REFERENCES

[1] D. H. Evans, J. A. Jensen, and M. B. Nielsen, "Ultrasonic colour Doppler imaging," *Interface Focus*, vol. 1, no. 4, pp. 490–502, 2011.

[2] L. N. Bohs and G. E. Trahey, "A novel method for angle independent ultrasonic imaging of blood flow and tissue motion," *IEEE Trans. Biomed. Eng.*, vol. 38, pp. 280–286, 1991.

[3] J. A. Jensen and S. I. Nikolov, "Directional synthetic aperture flow imaging," *IEEE Trans. Ultrason., Ferroelec., Freq. Contr.*, vol. 51, pp. 1107–1118, 2004.

[4] M. Tanter, J. Bercoff, L. Sandrin, and M. Fink, "Ultrafast compound imaging for 2-D motion vector estimation: application to transient elastography," *IEEE Trans. Ultrason., Ferroelec., Freq. Contr.*, vol. 49, pp. 1363–1374, 2002.

[5] J. A. Jensen and P. Munk, "A new method for estimation of velocity vectors," *IEEE Trans. Ultrason., Ferroelec., Freq. Contr.*, vol. 45, pp. 837–851, 1998.

[6] S. Holbek, M. Pihl, C. Ewertsen, M. Nielsen, and J. A. Jensen, "3-D velocity estimation for two planes in vivo," in *Proc. IEEE Ultrason. Symp.*, 2014, pp. 1706–1709.

[7] M. J. Pihl and J. A. Jensen, "A transverse oscillation approach for estimation of three-dimensional velocity vectors. Part I: Concept and simulation study," *IEEE Trans. Ultrason., Ferroelec., Freq. Contr.*, vol. 61, pp. 1599–1607, 2014.

[8] M. J. Pihl, M. B. Stuart, B. G. Tomov, M. F. Rasmussen, and J. A. Jensen, "A transverse oscillation approach for estimation of three-dimensional velocity vectors. Part II: Experimental validation," *IEEE Trans. Ultrason., Ferroelec., Freq. Contr.*, vol. 51, no. 10, pp. 1608–1618, 2014.

[9] J. Provost, C. Papadacci, J. E. Arango, M. Imbault, M. Fink, J. L. Gennisson, M. Tanter, and M. Pernot, "3-D ultrafast ultrasound imaging in vivo," *Physics in Medicine and Biology*, vol. 59, no. 19, pp. L1–L13, 2014.

[10] J. A. Jensen, "A new estimator for vector velocity estimation," *IEEE Trans. Ultrason., Ferroelec., Freq. Contr.*, vol. 48, no. 4, pp. 886–894, 2001.

[11] J. A. Jensen, H. Holten-Lund, R. T. Nilsson, M. Hansen, U. D. Larsen, R. P. Domsten, B. G. Tomov, M. B. Stuart, S. I. Nikolov, M. J. Pihl, Y. Du, J. H. Rasmussen, and M. F. Rasmussen, "SARUS: A synthetic aperture real-time ultrasound system," *IEEE Trans. Ultrason., Ferroelec., Freq. Contr.*, vol. 60, no. 9, pp. 1838–1852, 2013.

[12] J. M. Hansen, M. C. Hemmsen, and J. A. Jensen, "An object-oriented multi-threaded software beamformation toolbox," in *Proc. SPIE Med. Imag.*, vol. 7968, March 2011, pp. 79 680Y 1–9.

[13] M. J. Pihl and J. A. Jensen, "3D velocity estimation using a 2D phased array," in *Proc. IEEE Ultrason. Symp.*, 2011, pp. 430–433.

[14] A. P. G. Hoeks, J. J. W. van de Vorst, A. Dabekaussen, P. J. Brands, and R. S. Reneman, "An efficient algorithm to remove low frequency Doppler signal in digital Doppler systems," *Ultrason. Imaging*, vol. 13, pp. 135–145, 1991.

[15] C. Kasai, K. Namekawa, A. Koyano, and R. Omoto, "Real-Time Two-Dimensional Blood Flow Imaging using an Autocorrelation Technique," *IEEE Trans. Son. Ultrason.*, vol. 32, pp. 458–463, 1985.

[16] P. Likittanasombut, P. Reynolds, D. Meads, and C. Tegeler, "Volume flow rate of common carotid artery measured by Doppler method and color velocity imaging quantification (CVI-Q)," *Journal of Neuroimaging*, vol. 16, no. 1, pp. 34–38, 2006.

## **3-D Vector Velocity Estimation with Row-Column Addressed Arrays**

**Simon Holbek**, Thomas Lehrmann Christiansen, Morten Fischer Rasmussen,  
Matthias Bo Stuart, Erik Vilian Thomasen, and Jørgen Arendt Jensen

*Proceeding of IEEE International Ultrasonics Symposium., p. 1-4, 2015*

*Accepted for poster presentation in Taipei, Taiwan, 2015.*



# 3-D Vector Velocity Estimation with Row-Column Addressed Arrays

Simon Holbek\*, Thomas Lehrmann Christiansen†, Morten Fischer Rasmussen\*,  
Matthias Bo Stuart\*, Erik Vilain Thomasen† and Jørgen Arendt Jensen\*

\* Center for Fast Ultrasound Imaging, Dept. of Elec. Eng., Bldg. 349, Technical University of Denmark,  
2800 Kgs. Lyngby, Denmark

† Department of Micro- and Nanotechnology,  
Technical University of Denmark, 2800 Kgs. Lyngby, Denmark

**Abstract**—The concept of 2-D row-column (RC) addressed arrays for 3-D imaging have shown to be an interesting alternative to 2-D matrix array, due to the reduced channel count. However, the properties for RC arrays to estimate blood velocities have never been reported, which is of great importance for a clinical implementation of this type of array. The aim of this study is, thus, to develop a technique for estimating 3-D vector flow with a RC array using the transverse oscillation (TO) method. The properties are explored both in a simulation study and with a prototype probe for experimental use. In both setups, a 124 channel 2-D RC array with integrated apodization, pitch = 270  $\mu\text{m}$  and a center frequency of 3.0 MHz was used. The performance of the estimator was tested on a simulated vessel ( $\text{Ø} = 12 \text{ mm}$ ) with a parabolic flow profile and a peak velocity of 1 m/s. Measurements were made in a flowrig ( $\text{Ø} = 12 \text{ mm}$ ) containing a laminar parabolic flow and a peak velocity of 0.54 m/s. Data was sampled and stored on the experimental ultrasound scanner SARUS. Simulations yields relative mean biases at (-1.1%, -1.5%, -1.0%) with mean standard deviations of  $\bar{\sigma}$  were (8.5%, 9.0%, 1.4%) % for  $(v_x, v_y, v_z)$  from a 3-D velocity vector in a 15° rotated vessel with a 75° beam-to-flow angle. In the experimental setup with a 90° beam-to-flow angle, the relative mean biases were (-2.6%, -1.3%, 1.4%) with a relative standard deviation of (5.0%, 5.2%, 1.0%) for the respective transverse, lateral and axial velocity component.

## I. INTRODUCTION

Blood velocity estimation with ultrasound has become a commonly used tool for diagnosing cardiovascular diseases [1]. However, even though blood propagates in all three directions, commercial scanners are only capable of estimating 1-D or 2-D blood velocities. To obtain the last velocity component for estimating the true blood flow, a 2-D transducer can be used. A 32x32 element 2-D matrix array (Vermon S.A., Tours, France) was previously used to estimate 3-D vector flow in combination with the transverse oscillation method (TO) [2] [3] and a similar probe was used to estimate axial velocities in a volume using Doppler techniques [4]. One major drawback with the matrix probe is that the total number of interconnections in a  $N \times N$  element transducer, scales with  $N^2$ , which causes fabrication issues. Thus, solutions for 3-D imaging with a sparse 2-D transducer have been investigated in the literature.

One of the ideas that have emerged, was a to create a 2-D row-column (RC) addressed array [5], [6]. A RC addressed array can be viewed as two orthogonally oriented 1-D arrays mounted on top of each other. In a 2-D RC addressed array the

total number of elements is reduced to  $N + N$ , which allows for 2-D arrays with a large footprint at a sparse channel count. This work develops a method for 3-D vector flow estimation using a 2-D RC addressed array. The applied velocity estimator is a modified 3-D version of the transverse oscillation method [7], [8], [9]. 3-D vector flow estimates are shown for both Field II [10] [11] simulations and an experimental setup using a 2-D RC prototype probe with similar properties and transducer specifications.

## II. 2-D ROW-COLUMN ADDRESSED ARRAYS

The concept of a 2-D RC addressed array is easiest described as a  $1 \times N$  and a  $N \times 1$  1-D linear array merged together to form a  $N + N$  array which can be accessed from either its row indices or column indices as seen in Fig. 1. In transmit, any number or combination of elements can be excited at the same time as long as they are oriented in the same direction. In receive, however, data from all  $2N$  elements can be accessed simultaneously. Focusing can be performed in one lateral dimension by electronically applying a time delay to each element.

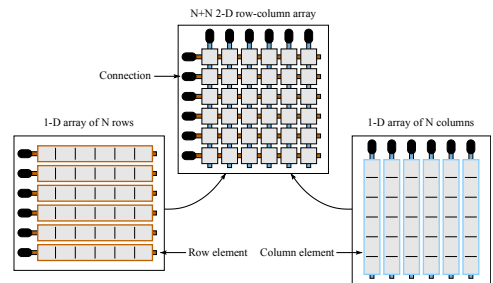


Fig. 1. Two  $1 \times N$  and  $N \times 1$  1-D one-way focused linear array are mounted orthogonal on top of each other to form the 2-D row-column addressed  $N + N$  array.

To some extent, a 2-D RC array is a special case of a 2-D matrix array, where whole lines of elements are locked together to work as a unit. The reduced flexibility in transmit and the lack of access to element data from  $N^2$  channels with a RC array translates to reduced fabrication complexity and data processing requirements. It is a very costly and complicated task to dice out a  $N \times N$  piezo ceramic and to provide electrical

connections to each element, if a large value is chosen for  $N$ . The amount of data to be processed is also reduced with a factor of  $N/2$  for a  $N+N$  RC array with same aperture size as a  $N \times N$  matrix array, which eases a real-time implementation.

The drawback of using RC arrays are their long element, which produce several ghost echoes emerging from the element edges [6],[12]. The amplitude of the most powerful ghost echo is approximately 40 dB lower than the amplitude of the main echo. It was shown that edge waves could be reduced, without affecting the main echo, by implementing a roll-off apodization at the end of each line element [13]. Based on these suggestions, each end of the line elements included a Hann windowed roll-off apodization of length  $16 \times \text{pitch}$ . Integrated apodization was applied in both the simulations and in the 2-D RC prototype probe used for the experimental setup.

### III. MATERIALS & METHODS

The section describes the developed technique for 3-D vector flow estimation using a 2-D RC array. It introduces the velocity estimator, the emission sequence, the applied RC array and the simulation and measurement environment. The description of the method was applied in both cases unless otherwise stated.

#### A. The transverse oscillation method

The TO estimator is a method for estimating 2-D vector flow by generating two decoupled double-oscillating fields in receive. The received signals are affected by axial or transverse blood flow motion which propagates through the double-oscillating fields. By using a phase-shift estimator, the axial and transverse motion can be detected. For a more thorough explanation of the theory, please consider [7], [14], [2] for further reading.

In general, three beamformed lines are needed for estimating 2-D vector flow with TO. One is needed as input for the conventional axial estimator [15] and two lines are needed for the transverse velocity component. The two lines used for transverse estimates are beamformed along the directions  $(\pm\lambda_x(z), 0, z)$ , where  $\lambda_x(z)$  is given by

$$\lambda_x(z) = 2\lambda_z \frac{z}{d_x}, \quad (1)$$

where  $\lambda_z$  is the wavelength of the emitted pulse in the medium. The wavelength is controllable and determined by the receive apodization profile. The apodization should contain two symmetrically placed peaks separated by a distance  $d_x$ . At a certain axial depth  $z$ ,  $\lambda_x$ . The maximum transverse velocity one can estimate without reaching the aliasing limit is then

$$v_{x_{max}} = \frac{\lambda_x}{4k} f_{prf}, \quad (2)$$

where  $k$  is the lag used in the autocorrelation and  $f_{prf}$  is the pulse repetition frequency between two similar emissions. To estimate the third velocity component  $v_y$  two additional lines have to be beamformed along the directions  $(0, \pm\lambda_y(z), z)$ . A total of five beamformed lines are therefore required to estimate 3-D vector flow with the TO method.

#### B. Emissions sequence

A total of 5 beamformed lines are needed to estimate 3-D vector flow along a line with TO. But since it is not possible to generate a focal point with a RC array, from which all 5 lines could be beamformed simultaneously an interleaved sequence was designed. The principle is illustrated in Fig. 2. One focused transmission (transmit 1) is made on the row elements and received on column elements (receive 1). From this, three of the five needed lines can be beamformed and the two velocity components  $v_z$  and  $v_y$  along the centerline can be derived. In the opposite scenario with transmit 2 on the columns (transmit 2) and receive on the rows (receive 2), the  $v_z$  and  $v_x$  velocity components can be found. The applied emissions sequence is, thus, made by first transmitting on the row and receiving on the columns and afterwards emit with columns and receive on the rows. By combining the two transverse estimates found from each transmit event with an axial estimate, the 3-D vector velocities are found. The described sequence was repeated 32 times for each frame. A total of 100 frames, each containing  $2 \times 32$  emissions was obtained in the simulation study and 20 frames were acquired in the experiments. The focal line were in both cases at 3 cm depth.

#### C. The 2-D RC array

A  $62+62$  element 2-D RC array was used in this study. The simulated RC array and the prototype RC probe had same properties, resulting in a pitch = 0.27 mm, kerf = 0.025 mm, sampling frequency = 70 MHz, center frequency  $f_0 = 3.0$  MHz and a footprint length in each dimension of 1.73 cm, see Table I. A 6 cycle sinusoidal pulse was used in transmit.

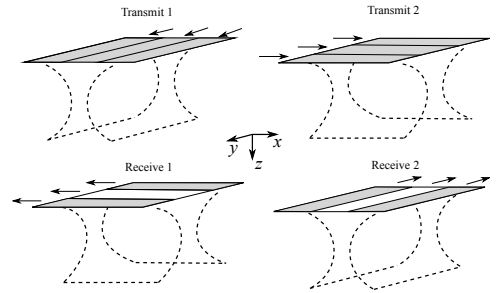


Fig. 2. Illustration of the transmit and receive scenario. First, focused ultrasound is emitted on the rows (transmit 1) and receive on the columns (receive 1). Secondly, the scenario is flipped, and the focused ultrasound is emitted on the columns (transmit 2) and received on the rows (receive 2). The axial velocity can be estimated in both cases. But with the TO approach only the velocity component perpendicular to the receive elements can be estimated. Gray elements are active ones, whereas white elements are inactive according to the required TO apodization profiles (conceptually illustrated by the gray areas).

#### D. Simulation Setup

A  $20 \times 20 \times 20$  mm cubic phantom containing a cylindrical blood vessel ( $\emptyset = 12$  mm) located at 3 cm depth was defined for the simulations. Scatterers inside the cylinder were translated according to a circular symmetric parabolic velocity profile, and scatterers outside the cylinder were considered

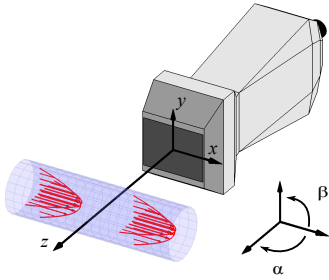


Fig. 3. illustration of the simulation setup and the two rotation angles  $\alpha$  and  $\beta$ , where a row-columns transducer array is located 3 cm from the center of the emulated blood vessel.

stationary. The peak velocity  $v_0$  in the parabolic flow was 1 m/s and propagating in the  $x$ -direction as default. Rotation of the scatter phantom could be made around two axes; around the  $y$ -axis, denoted the beam-to-flow angle  $\alpha$  and rotation around the  $z$ -axis denoted  $\beta$ . An illustration of the setup is seen in Fig. 3. Different combinations of  $\alpha$  and  $\beta$  were investigated and the  $f_{prf}$  was set to [3000 5000 9700 13800] Hz for  $\alpha = [90^\circ 75^\circ 60^\circ 45^\circ]$  respectively, to ensure that the aliasing limit was not exceeded for any of the three velocity components.

#### E. Experimental Setup

The 2-D RC prototype probe was connected to the experimental ultrasound scanner, SARUS [16] from which raw RF data was sampled for all active channels. The probe was fixated above a rubber tube ( $\varnothing = 12$  mm) submerged in water at a distance of 3 cm from the center of the vessel. An illustration of the setup is seen in Fig. 3. The beam-to-flow angle  $\alpha$  was  $90^\circ$  and  $\beta = 0^\circ$ . A centrifugal pump circulated a blood-mimicking fluid (Danish Phantom Design, Frederikssund, Denmark) which ensured a fully developed laminar flow with a parabolic profile. The peak velocity was estimated to be 0.54 m/s based on the vessel diameter and the flow rate measured with a magnetic MAG1100 (Danfoss, Nordborg, Denmark) flowmeter. A lower velocity magnitude, compared to the simulation setup was chosen in the flow rig to avoid intake of air bubbles in the system. The  $f_{prf}$  was therefore scaled accordingly to 1.4 kHz to match the expected velocity range.

#### IV. DATA PROCESSING

The stored data was processed offline. Due to the one-way focusing with a 2-D RC array, only sampled data from row elements were processed, when column elements were used as transmitters and vice versa, as illustrated in Fig. 2. The raw RF data was match filtered and beamformed with a dedicated RC beamformer [13]. For each transmit event, one line was beamformed for the axial velocity estimator and two separated lines were beamformed and used for estimating the velocity component orthogonal to the receiving elements. For the axial estimates, a Hann apodization was applied in receive, and for the transverse estimates two separated Hann peaks as sketched

TABLE I. TRANSDUCER AND EMISSIONS SEQUENCE SETUP

Transducer	
Parameter	Value
Transducer type	2-D Row-Column
No. of elements in x	62
No. of elements in y	62
Pitch in x	0.27 mm
Pitch in y	0.27 mm
Height	0.245 mm
Kerf	0.025 mm
Sampling frequency	70 MHz
Center frequency	3.0 MHz
Footprint size	1.73 cm

in Fig. 2 were used. The two TO apodization peaks were spaced a distance of  $35 \times \text{pitch}$  and had a width of  $25 \times \text{pitch}$ . An autocorrelation approach was used for the axial velocity estimate [15] and the transverse oscillation (TO) method [7][8] was applied for velocity estimates in the transverse and elevation direction. A more extensive description of the 3-D TO method is described in previous works [2], [3].

#### V. RESULTS

The simulated flow phantom was rotated in different angle combinations of  $\alpha$  and  $\beta$ . A total of 100 frames were simulated for each constellation and processed. The ability to estimate angle-independent peak velocities from the 3-D velocity vector is shown in Fig. 4. For a  $90^\circ$  beam-to-flow, the estimated peak velocity is found to be within 1.3-1.6% of  $v_0$  for any investigated  $\beta$  rotation. Decreasing  $\alpha$  in general leads to a higher standard deviation, which increases from a mean value of 4.6% for  $\alpha = 90^\circ$ , to 5.8%, 8.2% and 15.2% for  $\alpha = 75^\circ$ ,  $60^\circ$  and  $45^\circ$  respectively.

A representative selection of three estimated velocity components is seen in Fig. 5. The three velocity components were estimated from a simulated setup where the vessel was rotated in a beam-to-flow angle  $\alpha = 75^\circ$  and  $\beta = 15^\circ$ . The mean relative bias  $\bar{B}$  was (-1.1, -1.5, -1.0) % for the velocity components ( $v_x, v_y, v_z$ ). The corresponding mean standard deviation  $\bar{\sigma}$  were (8.5, 9.0, 1.4) %. The peak velocity was 0.97 m/s compared to the expected 1 m/s.

A total of 20 frames were recorded for the experimental setup and processed offline. The beam-to-flow angle  $\alpha = 90^\circ$  and  $\beta = 0^\circ$ . The experimental results gave  $\bar{B} = (-2.6, -1.3, 1.4)$  % for the velocity components ( $v_x, v_y, v_z$ ) with  $\bar{\sigma} = (5.0, 5.2, 1.0)$  %, see Fig. 6.

#### VI. CONCLUSION

The presented results demonstrate that a developed technique for 3-D vector flow estimation could be implemented

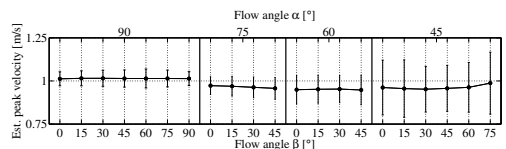


Fig. 4. Peak velocities derived from the estimated 3-D vector velocities as a function of vessel orientation.

### Simulated 3-D Vector Flow

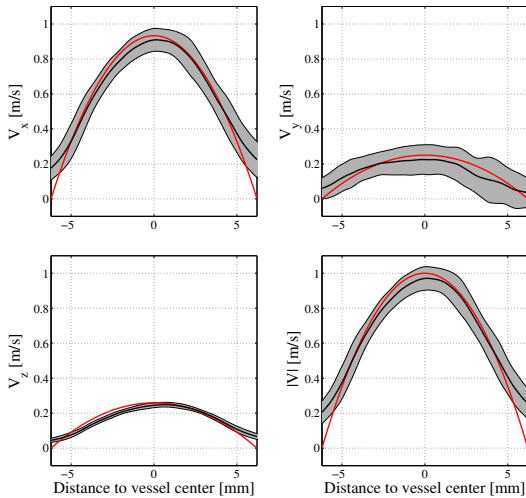


Fig. 5. Simulated 3-D vector flow estimation decomposed into the three velocity components and the absolute velocities. The red line indicates the theoretical velocity profile along with the estimated profile (black) and  $\pm$  one standard deviation (gray area).

### Measured 3-D Vector Flow

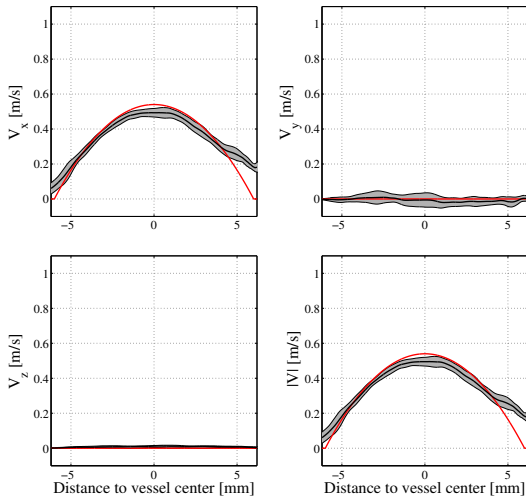


Fig. 6. Measured 3-D vector flow estimation decomposed into the three velocity components and the absolute velocities. The red line indicates the theoretical velocity profile along with the estimated profile (black) and  $\pm$  one standard deviation (gray area).

on a 2-D RC addressed arrays using the TO method. The simulated results were in good agreement with the expected velocities. Although slightly underestimating the velocities in the experimental setup, the expected parabolic velocity profile

could be estimated. However, the results are very promising and demonstrates the potential of RC addressed arrays for velocity estimation.

### ACKNOWLEDGMENT

This work was supported by grant 82-2012-4 from the Danish National Advanced Technology Foundation and by BK Ultrasound Aps.

### REFERENCES

- [1] G. M. von Reutern, M. W. Goertler, N. M. Bornstein, M. D. Sette, D. H. Evans, A. Hetzel, M. Kaps, F. Perren, A. Razumovsky, and et al., "Grading carotid stenosis using ultrasonic methods," *Stroke*, vol. 43, no. 3, pp. 916–921, 2012.
- [2] M. J. Pihl and J. A. Jensen, "A transverse oscillation approach for estimation of three-dimensional velocity vectors. Part I: Concept and simulation study," *IEEE Trans. Ultrason., Ferroelec., Freq. Contr.*, vol. 61, pp. 1599–1607, 2014.
- [3] M. J. Pihl, M. B. Stuart, B. G. Tomov, M. F. Rasmussen, and J. A. Jensen, "A transverse oscillation approach for estimation of three-dimensional velocity vectors. Part II: Experimental validation," *IEEE Trans. Ultrason., Ferroelec., Freq. Contr.*, vol. 51, no. 10, pp. 1608–1618, 2014.
- [4] J. Provost, C. Papadacci, J. E. Arango, M. Imbault, M. Fink, J. L. Gennisson, M. Tanter, and M. Pernot, "3-D ultrafast ultrasound imaging in vivo," *Physics in Medicine and Biology*, vol. 59, no. 19, pp. L1–L13, 2014.
- [5] C. E. Morton and G. R. Lockwood, "Theoretical assessment of a crossed electrode 2-D array for 3-D imaging," in *Proc. IEEE Ultrason. Symp.*, 2003, pp. 968–971.
- [6] C. E. M. Démoré, A. Joyce, K. Wall, and G. Lockwood, "Real-time volume imaging using a crossed electrode array," *IEEE Trans. Ultrason., Ferroelec., Freq. Contr.*, vol. 56, no. 6, pp. 1252–1261, 2009.
- [7] J. A. Jensen and P. Munk, "A new method for estimation of velocity vectors," *IEEE Trans. Ultrason., Ferroelec., Freq. Contr.*, vol. 45, pp. 837–851, 1998.
- [8] J. A. Jensen, "A new estimator for vector velocity estimation," *IEEE Trans. Ultrason., Ferroelec., Freq. Contr.*, vol. 48, no. 4, pp. 886–894, 2001.
- [9] T. L. Christiansen, S. Holbek, M. F. Rasmussen, E. V. Thomsen, and J. A. Jensen, "3-D flow estimation using row-column addressed transducer arrays," US application number: 14/599,857, January 2015.
- [10] J. A. Jensen, "Field: A program for simulating ultrasound systems," *Med. Biol. Eng. Comp.*, vol. 10th Nordic-Baltic Conference on Biomedical Imaging, Vol. 4, Supplement 1, Part 1, pp. 351–353, 1996.
- [11] J. A. Jensen and N. B. Svendsen, "Calculation of pressure fields from arbitrarily shaped, apodized, and excited ultrasound transducers," *IEEE Trans. Ultrason., Ferroelec., Freq. Contr.*, vol. 39, pp. 262–267, 1992.
- [12] M. F. Rasmussen and J. A. Jensen, "3D ultrasound imaging performance of a row-column addressed 2D array transducer: a simulation study," in *Proc. SPIE Med. Imag.*, 2013, pp. 1–11, 86750C.
- [13] M. F. Rasmussen, T. L. Christiansen, E. V. Thomsen, and J. A. Jensen, "3-D imaging using row-column-addressed arrays with integrated apodization — Part I: Apodization design and line element beamforming," *IEEE Trans. Ultrason., Ferroelec., Freq. Contr.*, vol. 62, no. 5, pp. 947–958, 2015.
- [14] J. Udesen and J. A. Jensen, "Investigation of Transverse Oscillation Method," *IEEE Trans. Ultrason., Ferroelec., Freq. Contr.*, vol. 53, pp. 959–971, 2006.
- [15] C. Kasai, K. Namekawa, A. Koyano, and R. Omoto, "Real-Time Two-Dimensional Blood Flow Imaging using an Autocorrelation Technique," *IEEE Trans. Son. Ultrason.*, vol. 32, pp. 458–463, 1985.
- [16] J. A. Jensen, H. Holten-Lund, R. T. Nilsson, M. Hansen, U. D. Larsen, R. P. Domsten, B. G. Tomov, M. B. Stuart, S. I. Nikolov, M. J. Pihl, Y. Du, J. H. Rasmussen, and M. F. Rasmussen, "SARUS: A synthetic aperture real-time ultrasound system," *IEEE Trans. Ultrason., Ferroelec., Freq. Contr.*, vol. 60, no. 9, pp. 1838–1852, 2013.

## **3-D Vector Flow Using a Row-Column Addressed CMUT Array**

**Simon Holbek**, Thomas Lehrmann Christiansen, Mathias Engholm, Anders Lei, Matthias Bo Stuart, Christopher Beers, Lars Nordahl Moesner, Jan Peter Bagge, Erik Vilian Thomasen, and Jørgen Arendt Jensen

*Proceeding of SPIE Ultrasound Imaging. Symp., Vol 9790, p. 979005-979005-8, 2016*

*Accepted for oral presentation in San Diego, California, United States, 2016.*



# *3-D Vector Flow Using a Row-Column Addressed CMUT Array*

Simon Holbek<sup>a</sup>, Thomas Lehrmann Christiansen<sup>b</sup>, Mathias Engholm<sup>b</sup>, Anders Lei<sup>b</sup>, Matthias Bo Stuart<sup>a</sup>, Christopher Beers<sup>c</sup>, Lars Nordahl Moesner<sup>d</sup>, Jan Peter Bagge<sup>d</sup>, Erik Vilain Thomsen<sup>b</sup> and Jørgen Arendt Jensen<sup>a</sup>

<sup>a</sup>Center for Fast Ultrasound Imaging, Department of Electrical Engineering, Technical University of Denmark, Lyngby, Denmark

<sup>b</sup>Department of Micro- and Nanotechnology, Technical University of Denmark, Lyngby, Denmark

<sup>c</sup>Sound Technology, Inc., State College, Pennsylvania, USA

<sup>d</sup>BK Ultrasound, Herlev, Denmark

## ABSTRACT

This paper presents an in-house developed 2-D capacitive micromachined ultrasonic transducer (CMUT) applied for 3-D blood flow estimation. The probe breaks with conventional transducers in two ways; first, the ultrasonic pressure field is generated from thousands of small vibrating micromachined cells, and second, elements are accessed by row and/or column indices. The 62+62 2-D row-column addressed prototype CMUT probe was used for vector flow estimation by transmitting focused ultrasound into a flow-rig with a fully developed parabolic flow. The beam-to-flow angle was 90°. The received data was beamformed and processed offline. A transverse oscillation (TO) velocity estimator was used to estimate the 3-D vector flow along a line originating from the center of the transducer. The estimated velocities in the lateral and axial direction were close to zero as expected. In the transverse direction a characteristic parabolic velocity profile was estimated with a peak velocity of 0.48 m/s ± 0.02 m/s in reference to the expected 0.54 m/s. The results presented are the first 3-D vector flow estimates obtained with a row-column CMUT probe, which demonstrates that the CMUT technology is feasible for 3-D flow estimation.

**Keywords:** 3-D Vector Flow, Row-Column Array, CMUT, Medical Ultrasound

## 1. INTRODUCTION

Blood flow velocity estimation is a widely used diagnostic tool in the clinic.<sup>1</sup> With spectral Doppler or color Doppler techniques, it is possible to estimate blood flow movement towards or away from the transducer. This technique is valuable when peak velocities in a vessel are needed or when an orientation of where blood flow is present. The drawbacks of these techniques are that they are limited to 1-D flow. Newer approaches as speckle tracking,<sup>2</sup> directional beamforming<sup>3</sup> and transverse oscillation (TO)<sup>4</sup> solved this limitation and were able to estimate 2-D in-plane velocities, thereby providing a more realistic representation of the blood flow movement. However, 2-D vector flow does not reveal the true dynamics of the blood flow, since it propagates in all three directions.<sup>5</sup> Getting a better understanding of the dynamics of a complex flow pattern, would probably help diagnosing critical diseases at an earlier stage, thereby improving treatment success rates. Therefore, 3-D ultrasound velocity estimation attracts increasingly more attention, as it provides additional diagnostic tools for clinical purposes in real-time.

To estimate real-time vector flow in 3-D, a 2-D transducer array is required. A 32x32 element fully addressed 2-D matrix array (Vernon S.A., Tours, France) was recently used to estimate 3-D Doppler in the heart<sup>6</sup> and has also been used for 3-D vector flow imaging.<sup>7,8</sup>

However, fully addressed matrix arrays face issues. Consider a fully addressed matrix array with  $N \times N$  elements. The total number of interconnections in these arrays scale with  $N^2$ , which even for only a 32x32 array causes

---

Send correspondence to S. Holbek, E-mail: sholbek@elektro.dtu.dk

extensive fabrication challenges. Moreover, since a pitch of  $\lambda/2$ , where  $\lambda$  is the wavelength of the transmitted wave, is preferable to suppress grating lobes, the physical footprint of such a transducer is relatively small when the total number of interconnections is kept at a reasonable level.

To overcome the challenges with 2-D matrix probes, the idea of row-column (RC) addressed arrays emerged.<sup>9,10</sup> They work as two  $N \times 1$  and  $1 \times N$  wide linear transducers mounted orthogonally to each other to jointly form a 2-D array (see Fig. 1). In transmit, only row-elements or column-elements can be excited, whereas channel data in receive can be acquired for both rows and columns simultaneously. The benefits of RC arrays are that a large footprint can be obtained while maintaining a pitch of  $\lambda/2$  and further having the number of elements reduced. In this study, we show that 3-D realtime vector flow using TO can be obtained using an in-house-developed RC addressed  $62 + 62$  element prototype CMUT (capacitive micromachined ultrasonic transducer) probe,<sup>11,12</sup> assembled by Sound Technology, Inc. (State College, PA,USA).

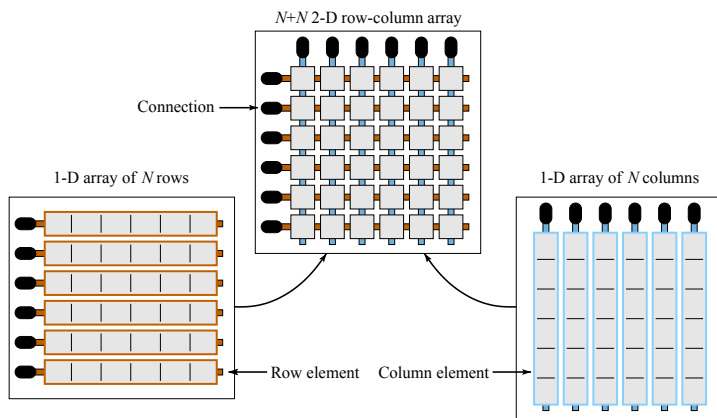


Figure 1: In a RC addressed array, two  $1 \times N$  and  $N \times 1$  arrays are mounted orthogonally on each other, thereby jointly forming a 2-D array of  $N + N$  elements. The row elements and the column elements can be viewed as two wide 1-D linear arrays without elevation focus. In a RC array, the number of interconnections is reduced to  $2N$ . Modified from<sup>13</sup>

## 2. CMUT TECHNOLOGY

Currently, the vast majority of commercial ultrasound transducers are made by dicing the individual elements from a piezoelectric material. When a voltage is applied across them, a deformation will occur and a pressure field is generated. Conversely, a deformation of the piezoelectric material from an external pressure will generate a voltage difference across the crystal. Another technique with similar properties are the CMUTs. Unlike piezoelectric ultrasound transducers that are fabricated with mechanical processes, CMUTs are lead free and fabricated using microelectromechanical systems (MEMS) technology, where structures in the order of microns can be manufactured. This technology offers the possibility of developing nerly kerf-less transducers with almost any choice of pitch, customized geometries, broadbanded transducers with high sensitivity, and at much lower fabrication cost.

The pressure field generated with a CMUT originates from small vibrating CMUT cells. A cross section of such a single CMUT cell is seen on Fig. 2. The task is to generate a CMUT cell, which can vibrate such that ultrasonic waves can be transmitted and received. The CMUT technology works as following; At rest, no voltage is applied to the electrodes and the top plate is unbent. Applying a DC-voltage across the top and bottom electrode, "pulls in" the top electrode and works as the new starting point for the cell. The closer the top electrode can be pulled in, the higher is the obtained sensitivity (unless a complete pull in is made, which collapses the cell). An ultrasound pressure field is generated by applying a sinusoidal AC-voltage across the cell,

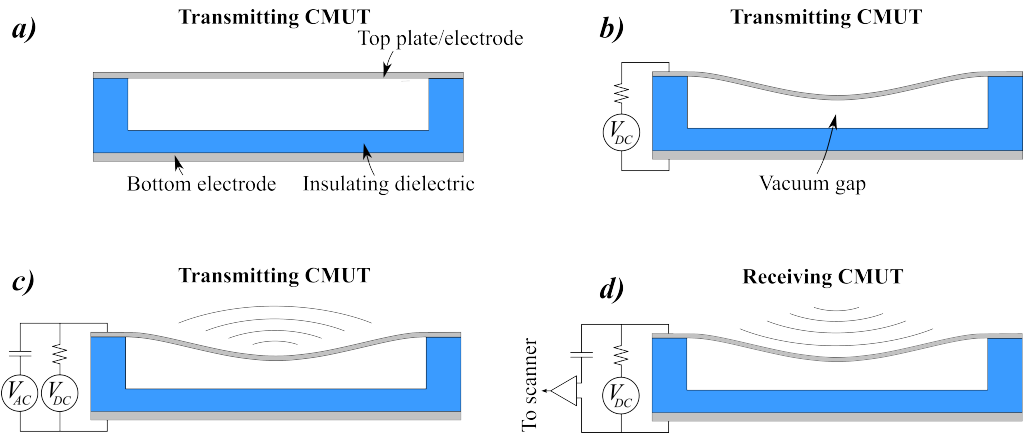


Figure 2: The illustration shows the cross section of a single circular CMUT cell. In a) the initial cell is shown. A DC voltage is applied in b) to pull the top electrode closer to the bottom electrode. The same DC voltage remains throughout both transmit and receive. When the AC voltage is applied the top electrode starts to vibrate around the starting point in c) and ultrasound is transmitted. In receive d), the returned pressure echo will result in a vibrating top electrode which induces a current which is sampled in the ultrasound scanner.

which induces a vibration on the top electrode. In receive the AC-voltage is disabled and the returning echo causes the top electrode to vibrate which generates a signal which is sampled using the connected ultrasound scanner. Each element in a CMUT consists of several CMUT cells that can vibrate in phase to increase the transmitted pressure field. 1-D prototype CMUTs have been manufactured with success,<sup>14</sup> whereas 2-D CMUTs have until now, only been reported for experimental use.<sup>11,12,15</sup> The presented prototype 2-D RC CMUT probe relies on the described CMUT technology.

### 3. METHOD

The following section briefly describes how an M-mode sequence for 3-D vector flow estimation was designed, and how data was sampled and processed.

#### 3.1 Transmit sequence

An interleaved M-mode sequence where focused emissions alternately were emitted from either row elements or column elements was designed, see Fig. 3. The focal depth was 3 cm, which was also the distance to the center of the vessel. A total of 20 frames, each consisting of  $2 \times 32$  emissions were recorded and stored for offline processing.

#### 3.2 The transverse oscillation estimator

A 3-D version of the transverse oscillation (TO) method was used as the velocity estimator in this study.<sup>4,16</sup> The basic principles of TO is to generate a double oscillating field in receive by applying two symmetric apodization peaks spaced by a distance  $d$ . Two lines are then beamformed separated by a distance of  $\lambda_x/4$  within the double oscillating field, where the depth dependent transverse wavelength is given by

$$\lambda_x(z) = 2\lambda_z \frac{z}{d}, \quad (1)$$

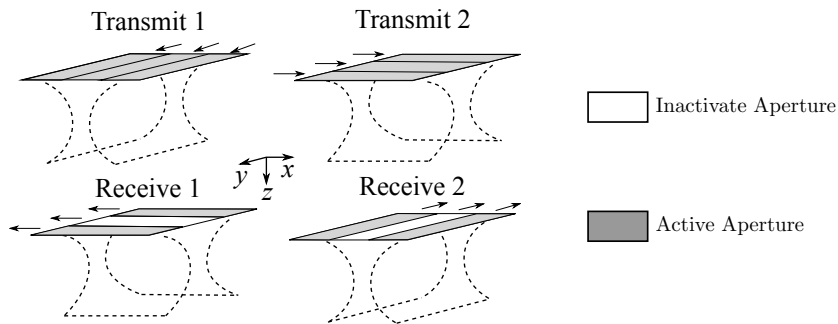


Figure 3: Illustration of the interleaved transmit and receive setup. In the first transmit event, electronically focused ultrasound is emitted with all row elements (transmit 1) and received on the column elements (receive 1). In the second transmit event, the orthogonal scenario is applied, such that focused ultrasound is emitted with all column elements (transmit 2) and received with row elements (receive 2). The inactive aperture is illustrated as white elements, whereas gray elements depicts the active aperture according to the required TO apodization profiles.

with  $z$  being the depth and  $\lambda_z$  the wavelength of the emitted signal. The two beamformed lines can be combined to estimate the velocity component  $v_x$ , transverse to the receiving elements. The same procedure is used for estimating the lateral velocity component  $v_y$ , but this time, the transmit/receive elements are flipped i.e., for  $v_x$  transmit is made on row elements and receive on column elements, and for  $v_y$ , transmit is made with column elements and received with row elements. Due to the symmetry of the RC probe, it is anticipated that the lateral wavelengths  $\lambda_y$  and  $\lambda_x$  are equal. The last velocity component  $v_z$  is calculated using a traditional autocorrelation approach<sup>17</sup> from either of the transmit events. Note here that the three velocity components are obtained simultaneously due to the inter spacing of the emissions. The three estimated velocities  $v_x$ ,  $v_y$  and  $v_z$  are subsequently combined to yield 3-D vector flow along one line.

### 3.3 Data processing

Although RF data was accessible from both row and column elements, only data from the non-transmitting elements was processed i.e. when transmitting with rows, data from columns was processed and vice versa. An in-house developed beamformer was used to beamform the data.<sup>12</sup> A traditional TO apodization profile was used in the beamforming, where two peaks each spanning 25 elements were separated by 37 elements. The TO estimator was used for 3-D vector flow estimation as has been shown in previous work.<sup>16</sup> Specifications for the TO apodization in receive are seen in Table 1. Stationary echo canceling was performed by subtracting the mean values from each pair of 32 emissions from each beamformed line.

## 4. MATERIALS & EQUIPMENT

### 4.1 The 62+62 prototype CMUT probe

A prototype 2-D RC CMUT was used for conducting the measurements. Each side of the RC transducer contained 64 elements, 128 elements in total, where 4 elements were used for integrated apodization purposes.<sup>11,12</sup> The center frequency was 3.0 MHz, the pitch was  $270 \mu\text{m}$  which approximately corresponds to a  $\lambda/2$ . Each element consisted of 1210 small CMUT cells that could be excited simultaneously and vibrate in phase. The length of each CMUT cell was  $56 \mu\text{m}$  and the top plate thickness was  $1.85 \mu\text{m}$ , see Table 1. An image of the disassembled CMUT probe is seen in Fig 4.

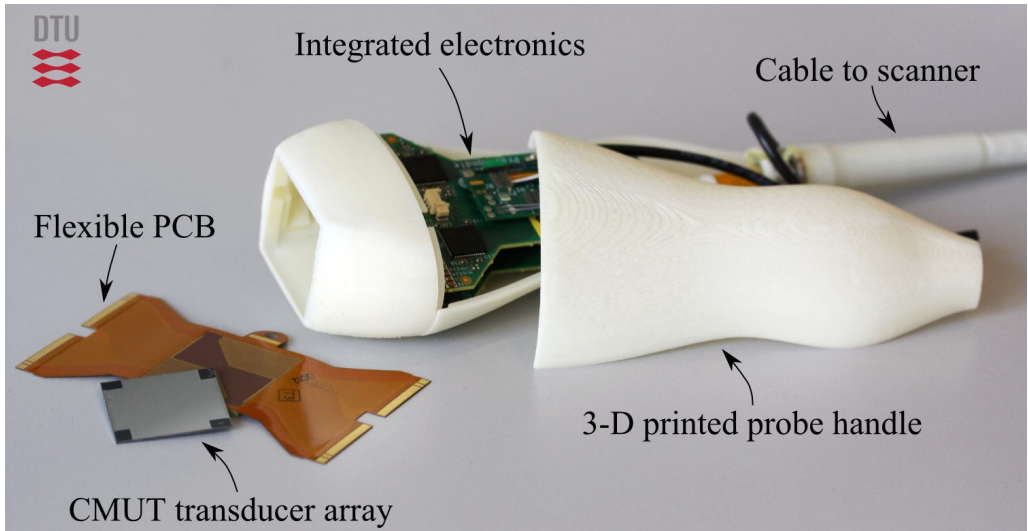


Figure 4: Image showing the disassembled probe with its main components: The CMUT array, which is mounted and wire-bonded on the flexible printed circuit board (PCB), the 3-D printed probe handle and the integrated electronics. From.<sup>18</sup>

#### 4.2 Experimental scanner

The RC CMUT was connected to the experimental ultrasound scanner, SARUS<sup>19</sup> from which raw RF data was acquired for all 128 channels. The applied DC bias voltage was 190 V and the transmit voltage used was 75 V. Data were acquired at a sampling frequency of 70 MHz. The data was stored and processed offline.

#### 4.3 Flow-rig

An in-house built flow-rig system was used for validation of the estimated 3-D vector flow. A centrifugal pump circulated a blood-mimicking fluid (Danish Phantom Design, Frederikssund, Denmark) in the system and a 1.2 m long inlet ensured that a fully developed laminar flow with a parabolic profile was present at the measurement site. The transducer was fixated above a rubber tube ( $\varnothing = 12$  mm) at a distance of 3 cm from the center of the vessel. Based on the volume flow measured with a MAG 1100 flow meter (Danfoss, Hasselager, Denmark), the expected peak velocity  $v_0$  was calculated and compared to the estimated profiles. An illustration of the expected velocity given the actual scan plane is seen in Fig. 5. Transducer specifications, transmit properties and other applied variables are listed in Table 1.

### 5. RESULTS

In Fig. 6 all three velocity components for a line perpendicular to the transducer surface are shown. The estimated velocity profile averaged over 20 frames are illustrated with the solid black line  $\pm$  one standard deviation (dotted lines). The red lines depict the expected velocity profile at a certain depth. Only motion in the transverse direction was expected, where a parabolic profile was seen (see Fig. 6a). The peak transverse velocity was  $0.48$  m/s  $\pm$   $0.02$  m/s corresponding to a -10.9% bias compared to the expected 0.54 m/s. Estimates in the lateral (Fig. 6b) and axial (Fig. 6c) direction showed negligible flow as expected with a small mean standard deviation of  $\pm 0.02$  m/s and  $\pm 0.01$  m/s respective. Along the central 90% of the vessel diameter, the relative

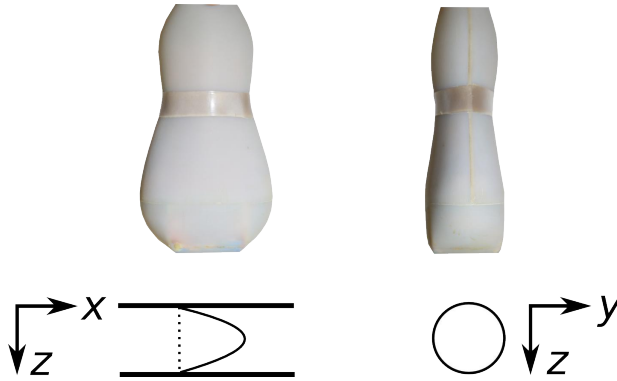


Figure 5: Illustration of the theoretical flow-rig measurement setup, where a parabolic flow profile is present in the  $xz$ -plane and no in-plane velocity is present in the  $zy$ -plane.

Table 1

Transducer & emissions sequence setup		Phantom & processing parameters		
Pitch row/column	270 $\mu\text{m}$	Focus in transmit	3	cm
Kerf row/column	2.5 $\mu\text{m}$	Vessel diameter	12	mm
Row/column elements	64	Peak velocity $v_0$	0.54	m/s
Active elements	124	Emissions per estimate	32	-
Sampling frequency	70 MHz	Apodization in transmit	Hanning	-
Transmit voltage	75 V	TO apodization	Hanning	-
Frames	20	TO peak element distance	37	-
Pulse repetition frequency	3.2 kHz	TO peak element width	25	-

mean bias was  $(-4.9, -0.4, 0.5)\%$  with a mean relative standard deviation of  $(6.7, 4.9, 2.5)\%$  for  $(v_x, v_y, v_z)$  respectively.

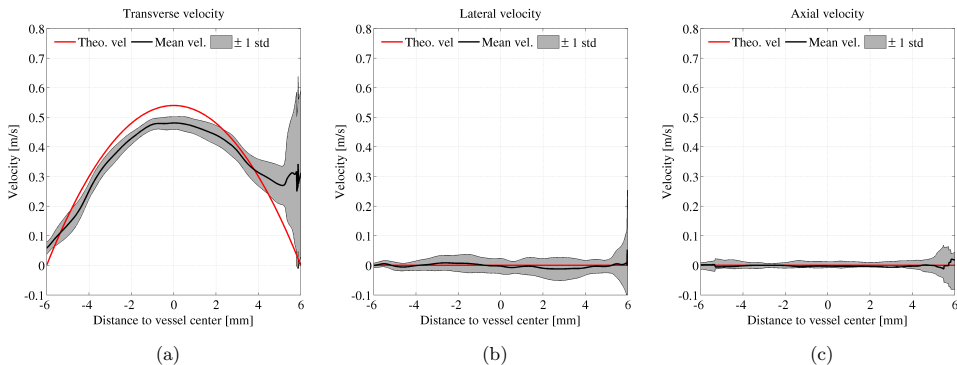


Figure 6: Measured velocity profiles (solid black line) and  $\pm$  one standard deviation (dotted lines) plotted on top of the theoretical expected velocity profile (red line) in the transverse direction (a), the lateral direction (b) and the axial direction (c). The velocity profiles are displayed across the vessel of diameter 12 mm.

## 6. CONCLUSION

The results show that 3-D vector flow can be obtained with a prototype 62+62 2-D RC CMUT probe in an experimental setup. A low relative standard deviation  $<4\%$  was obtained for the estimated peak velocity, which translates to a high consistency in the velocity estimates. Additional measurements will explore the potential of 2-D CMUT's and clarify the compatibility with traditional piezoelectric transducers.

## ACKNOWLEDGMENTS

This work was financially supported by grant 82-2012-4 from the Danish National Advanced Technology Foundation and by BK Ultrasound ApS, Herlev, Denmark.

## REFERENCES

- [1] von Reutern, G. M., Goertler, M. W., Bornstein, N. M., Sette, M. D., Evans, D. H., Hetzel, A., Kaps, M., Perren, F., and et al., A. R., "Grading carotid stenosis using ultrasonic methods," *Stroke* **43**(3), 916–921 (2012).
- [2] Trahey, G. E., Allison, J. W., and von Ramm, O. T., "Angle independent ultrasonic detection of blood flow," *IEEE Trans. Biomed. Eng.* **BME-34**, 965–967 (1987).
- [3] Jensen, J. A., "Directional velocity estimation using focusing along the flow direction: I: Theory and simulation," *IEEE Trans. Ultrason., Ferroelec., Freq. Contr.* **50**, 857–872 (2003).
- [4] Jensen, J. A. and Munk, P., "A new method for estimation of velocity vectors," *IEEE Trans. Ultrason., Ferroelec., Freq. Contr.* **45**, 837–851 (1998).
- [5] Markl, M., Frydrychowicz, A., Kozerke, S., Hope, M., and Wieben, O., "4D flow MRI," *J. Magn. Reson. Imaging* **36**(5), 1015–1036 (2012).
- [6] Provost, J., Papadacci, C., Arango, J. E., Imbault, M., Fink, M., Gennisson, J. L., Tanter, M., and Pernot, M., "3-D ultrafast ultrasound imaging in vivo," *Phys. Med. Biol.* **59**(19), L1–L13 (2014).
- [7] Pihl, M. J., Stuart, M. B., Tomov, B. G., Rasmussen, M. F., and Jensen, J. A., "A transverse oscillation approach for estimation of three-dimensional velocity vectors. Part II: Experimental validation," *IEEE Trans. Ultrason., Ferroelec., Freq. Contr.* **51**(10), 1608–1618 (2014).
- [8] Holbek, S., Pihl, M., Ewertsen, C., Nielsen, M., and Jensen, J. A., "3-D velocity estimation for two planes in vivo," in [*Proc. IEEE Ultrason. Symp.*], 1706–1709 (2014).
- [9] Morton, C. E. and Lockwood, G. R., "Theoretical assessment of a crossed electrode 2-D array for 3-D imaging," in [*Proc. IEEE Ultrason. Symp.*], 968–971 (2003).
- [10] Démoré, C. E. M., Joyce, A., Wall, K., and Lockwood, G., "Real-time volume imaging using a crossed electrode array," *IEEE Trans. Ultrason., Ferroelec., Freq. Contr.* **56**(6), 1252–1261 (2009).
- [11] Christiansen, T. L., Rasmussen, M. F., Bagge, J. P., Moesner, L. N., Jensen, J. A., and Thomsen, E. V., "3-D imaging using row–column-addressed arrays with integrated apodization — part II: Transducer fabrication and experimental results," *IEEE Trans. Ultrason., Ferroelec., Freq. Contr.* **62**(5), 959–971 (2015).
- [12] Rasmussen, M. F., Christiansen, T. L., Thomsen, E. V., and Jensen, J. A., "3-D imaging using row–column-addressed arrays with integrated apodization — Part I: Apodization design and line element beamforming," *IEEE Trans. Ultrason., Ferroelec., Freq. Contr.* **62**(5), 947–958 (2015).
- [13] Rasmussen, M. F. and Jensen, J. A., "3D ultrasound imaging performance of a row-column addressed 2D array transducer: a simulation study," in [*Proc. SPIE Med. Imag.*], 1–11 (2013). 86750C.
- [14] Savoia, A. S., Caliano, G., and Pappalardo, M., "A CMUT probe for medical ultrasonography: From microfabrication to system integration," *IEEE Trans. Ultrason., Ferroelec., Freq. Contr.* **59**(6), 1127–1138 (2012).
- [15] Logan, A. S., Wong, L. L. P., and Yeow, J. T. W., "2-D CMUT wafer bonded imaging arrays with a row-column addressing scheme," in [*Proc. IEEE Ultrason. Symp.*], 984–987 (sep 2009).
- [16] Pihl, M. J. and Jensen, J. A., "A transverse oscillation approach for estimation of three-dimensional velocity vectors. Part I: Concept and simulation study," *IEEE Trans. Ultrason., Ferroelec., Freq. Contr.* **61**, 1599–1607 (2014).

- [17] Kasai, C., Namekawa, K., Koyano, A., and Omoto, R., "Real-Time Two-Dimensional Blood Flow Imaging using an Autocorrelation Technique," *IEEE Trans. Son. Ultrason.* **32**, 458–463 (1985).
- [18] Engholm, M., Christiansen, T. L., Beers, C., Bagge, J. P., Moesner, L. N., Bouzari, H., Lei, A., Berkheimer, M., Stuart, M. B., Jensen, J. A., and Thomsen, E. V., "A hand-held row-column addressed CMUT probe with integrated electronics for volumetric imaging," *Proc. IEEE Ultrason. Symp.*, 1–4 (2015).
- [19] Jensen, J. A., Holten-Lund, H., Nilsson, R. T., Hansen, M., Larsen, U. D., Domsten, R. P., Tomov, B. G., Stuart, M. B., Nikolov, S. I., Pihl, M. J., Du, Y., Rasmussen, J. H., and Rasmussen, M. F., "SARUS: A synthetic aperture real-time ultrasound system," *IEEE Trans. Ultrason., Ferroelec., Freq. Contr.* **60**(9), 1838–1852 (2013).

## **Experimental 3-D Vector Flow Estimation with Row-Column Addressed Arrays**

**Simon Holbek**, Matthias Bo Stuart, and Jørgen Arendt Jensen

*Proceeding of IEEE International Ultrasonics Symposium., p. 1-4, 2016*

*Accepted for oral presentation in Tours, France, 2016.*



# Experimental 3-D Vector Velocity Estimation with Row-Column Addressed Arrays

Simon Holbek, Matthias Bo Stuart, and Jørgen Arendt Jensen

Center for Fast Ultrasound Imaging, Dept. of Elec. Eng., Bldg. 349, Technical University of Denmark, 2800 Kgs. Lyngby, Denmark

**Abstract**—Experimental 3-D vector flow estimates obtained with a 62+62 2-D row-column (RC) array with integrated apodization are presented. A transverse oscillation (TO) velocity estimator is implemented on a 3.0 MHz RC array, to yield real-time 3-D vector flow in a cross-sectional scan plane at 750 frames per second. The method is validated in a straight-vessel phantom ( $\varnothing = 8$  mm) connected to a flow pump capable of generating time-varying carotid waveforms. The out-of-plane velocity component perpendicular to the cross section of the vessel and the cross-sectional area is used to estimate volumetric flow rates. The flow rate measured from five cycles is 2.3 mL/stroke  $\pm$  0.1 mL/stroke giving a negative 9.7% bias compared to the pump settings. It is concluded that 124 elements are sufficient to estimate 3-D vector flow, if they are positioned in a row-column wise manner.

## I. INTRODUCTION

Row-column (RC) addressed 2-D arrays have been suggested as an alternative to the fully populated matrix array for volumetric imaging at a low channel cost [1], [2]. Compared to a  $N \times N$  matrix array, the total number of interconnections in a  $N + N$  RC array is reduced by a factor of  $N/2$ , which eases the interconnect and opens up for transducers with both a large footprint and a small pitch. For instance, a 62 + 62 array uses 124 connections instead of 3844 for the matrix array.

Established and fully tested methods implemented on conventional fully populated matrix arrays, are not directly transferable to RC arrays. For instance, the tall elements produce several ghost echoes emanating from the element edges, which degrades the image quality [2], [3]. A suggested solution to reduce the ghost echoes without affecting the main echo, was to implement a hardware roll-off apodization at the end of each element [3]. Furthermore, the approximation of the elements being small point-sources breaks down, due to the dimensions of the tall elements. A better approximation is therefore to view the elements as line segments, which influences the time-of-flight calculations used in the delay-and-sum beamformer [3].

All these precautions were implemented in previous work, which in a simulation study showed that 3-D vector flow could be estimated in a plane by using a 62+62 3.0 MHz 2-D RC array in combination with a dedicated 3-D RC transverse oscillation (TO) method [4]. Preliminary experimental results with a similar capacitive micromachined ultrasonic transducer (CMUT) demonstrated that 3-D vector flow in an M-mode setup could be obtained for a constant laminar flow [5].

This paper presents a selection of the work presented in the journal article [6] using a piezo RC prototype probe. It is

here demonstrated, that similar results can be obtained in an experimental setup, where 3-D vector flow is estimated in a plane in a pulsatile environment.

## II. MATERIALS & METHOD

### A. Experimental setup

A 62+62 3.0 MHz 2-D piezo RC prototype probe, made in collaboration with Sound Technology, Inc. (State College, PA, USA) [7], was used in the experiments with properties as described in Table I. Integrated hardware roll-off apodization was applied at the end of each element. The RC array was connected to the experimental ultrasound scanner SARUS [8], which stored raw RF from all 124 channels at a sampling frequency of 35 MHz and at an excitation voltage of 75 V.

### B. Flow pump

A flow system (CompuFlow 1000, Shelley Medical Imaging Technologies, Toronto, Canada) was used to generate a pre-defined time-varying carotid flow waveform, with user defined waveform, pulse duration, and flow rate. The manufacturer specified flow rate accuracy of the system is  $\pm 3$ . The flow pump was connected to a customized tissue mimicking phantom (Dansk Fantom Service, Frederiksund, Denmark), containing a straight-vessel ( $\varnothing = 8$  mm).

### C. Focusing with RC arrays

Focusing with RC arrays can be done conventionally, by applying an electronically specified delay curve on an individual channel basis. By varying the delay curve, focused steered emissions can be achieved. Where focusing with RC arrays differs from focusing with a 2-D matrix array, is that a focal line, rather than a focal point is obtained, due to the tall dimensions of the elements.

When examining the wave front created from exciting a single RC element, it can be viewed as a circle arc in one plane, and a plane wave in the orthogonal plane. When multiple transducer elements are excited according to a specified delay curve, the wave fronts will add up to form a focal line.

Since only one-way transmit focusing can be achieved, the transmit and receive aperture must be distinct. Thus, when transmitting with row elements, beamforming was performed with column elements and vice versa, when the orthogonal aperture is used in transmit.

#### D. Beamforming

Conventional delay-and-sum beamforming was performed with a dedicated RC beamformer [3], which takes the position of the emitting element (source), the time of emission, and the position of the receiving elements (drains) as input for calculating the shortest time-of-flight between the transmit element, the beamformed point, and the receiving element.

#### E. Emission sequence

Three-dimensional vector flow in a cross-sectional plane was obtained with a steered transmit sequence as shown in Fig. 1. The sequence consisted of  $N$  focused emissions  $R_i$  using row elements, where  $i = 1 \dots N$ , and one focused emission  $C_1$  using the column elements. For  $N = 1$ , the emission sequence is denoted an M-mode sequence. Three-dimensional vector flow was, thus, estimated in points along the  $N$  steered directions in the  $zy$ -plane. The column emission generated a plane wave within the cross sectional  $zy$ -scan plane, whereas plane waves perpendicular to the scan plane were steered in the  $zy$ -plane when using the row elements. From the row transmit event  $R_i$ , the  $v_{x_i}$  and  $v_{z_i}$  velocity components could be estimated in points along the direction of the respective beamformed centerline. However, the  $C_1$  column transmit event provided the required data for beamforming the lines needed for estimating all  $v_{y_i}$  and  $v_{z_i}$  velocity components, as this transmit event insonifies the  $zy$ -scan plane. The steered transmit sequence used is schematically written as

$$\begin{array}{ccccccc} C_1 & \rightarrow & R_1 & \rightarrow & R_2 & \rightarrow & R_3 & \rightarrow & \dots & R_N \\ C_1 & \rightarrow & R_1 & \rightarrow & R_2 & \rightarrow & R_3 & \rightarrow & \dots & R_N \\ \vdots & & & & \vdots & & & & & \vdots \end{array}$$

This sequence provided continuous data, which means that the distance between each identical emission type is equally distributed in time for all time [9]. The advantages of continuous data are, that very high frames rate can be obtained, and that dynamic ensemble lengths and echo canceling filters can be applied. The higher obtainable frame rate with continuous data occurs, since a sliding window can be applied on the beamformed data to generate one velocity estimate. The velocity estimate can be updated from each new similar emissions, since the new data can replace the oldest data in the estimator.

#### F. The transverse oscillation method

Transverse oscillation (TO) methods [10], [11] allows for estimating both the axial and lateral velocity components, if a 1-D array is used; one component perpendicular to the element orientation in addition to the axial component. Three beamformed lines are needed for this; one center line for the axial estimator and two steered lines for the transverse estimate. The center line  $r_{center}$  is beamformed along the direction  $(0, 0, z)$ , using delay-and-sum and a traditional apodization profile. For the two steered lines, a traditional TO apodization profile with two separated peaks is applied

TABLE I  
TRANSDUCER AND EMISSIONS SEQUENCE SETUP

Parameter	Transducer	
	Value	
Transducer type	2-D Row-Column	
No. of elements in $x$ and $y$	62	
Pitch in $x$ and $y$	0.27 mm	
Width	0.245 mm	
Kerf	0.025 mm	
Sampling frequency	35 MHz	
Center frequency	3.0 MHz	
Footprint size	$1.67 \times 1.67 \text{ cm}^2$	

and beamforming is performed along the lines  $(x, y, z) = (\pm \lambda_x(z)/8, 0, z)$  to create the  $\lambda_x/4$  spatial separation. With a 2-D matrix array, all 5 lines required for 3-D TO can be beamformed from one transmit event [12], [13]

If an interleaved transmit/receive sequence contains both events with transmit on rows and receiving with column elements and vice versa, all three velocity components can be estimated with a 2-D RC array.

### III. DATA PROCESSING

A Linux cluster was used to process the raw RF data off line. Matched filtering was applied on the individual channel data by convolving with the time-reversed emitted pulse to increase SNR. From each transmit event three lines were beamformed. Two of the lines,  $r_{left}$  and  $r_{right}$ , were used to estimate the velocity component perpendicular to the tallest dimension of the receiving elements using the TO method, and the third line,  $r_{center}$ , was used to estimate the axial velocity with an autocorrelation approach [14]. Echo cancellation of the beamformed data were subsequently performed with a low frequency Doppler filter algorithm [15]. The data were subsequently fed to their respective velocity estimators to yield 2-D vector flow estimates. Finally, by combining the estimated transverse velocity components, one from each transmit event, with one of the two independent axial estimates, 3-D velocity vector along the direction of the respective beamformed centerline was obtained. The estimation plane was obtained by scan converting and interpolating the estimates.

### IV. EXPERIMENTAL SETUP

With the described material two measurements were performed with an M-mode and a steered emission sequence. Both measurements used an ensemble length of 32 emissions per velocity estimate. The M-mode had a pulse repetition frequency  $f_{prf}$  of 750 Hz. The steered sequence consisted of 11 row emissions spanning from  $-8^\circ$  to  $8^\circ$  in steps of  $1.6^\circ$  and a single unsteered column emission, from which 3-D vector flow was obtained in a cross-sectional scan plane.  $f_{prf}$  was 9.0 kHz, which translates to 750 frames per second.

### V. RESULTS

Results from the M-mode measurements are shown in Fig. 2, where the time-varying velocity component in the flow direction is illustrated. The results shows the pulsating flow

# Steered Sequence

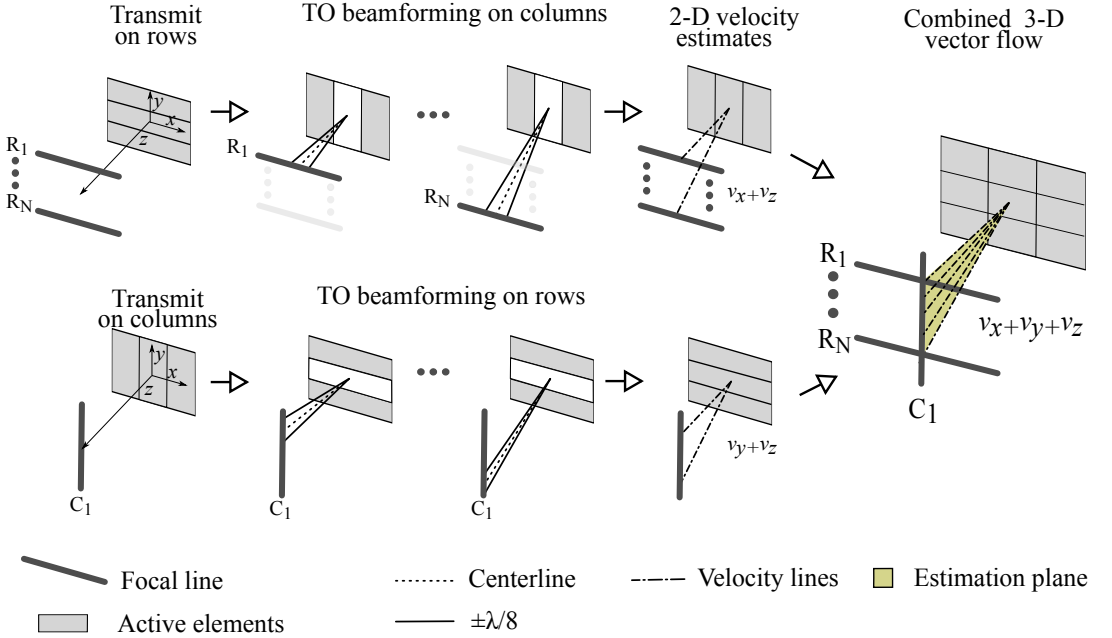


Fig. 1. A steered RC sequence for obtaining 3-D vector flow using TO in a cross sectional plane is designed in the following way; first, after each column emission  $C_1$ , multiple steered row emissions  $R_N$  are emitted. From each row emission three lines are beamformed according to the steering directions and  $v_x$  and  $v_z$  can be estimated along each direction. Second, from a single column emission  $C_1$ , three lines are beamformed along each steering direction yielding  $v_y$  and  $v_z$  velocity estimates along the  $N$  directions. 3-D vector flow is estimated in points along directions originating from the center of the aperture and through the intersection between the focal lines. The estimation plane is obtained when interpolating the combined 3-D vector flow estimates.

pattern, and the estimated mean velocity at the vessel center during one period was  $11.3 \text{ cm/s} \pm 0.4 \text{ cm/s}$ , when averaging over 10 periods.

With the steered sequence 4.3 s of data were recorded, corresponding to 5 cycles. Based on the manufacturer specified cycle time, the estimates were divided into 5 sub samples, which could be coherently aligned. Based on the cross sectional vessel area and the out-of-plane velocity component averaged over 5 cycles, the flow rate was estimated to  $2.3 \text{ mL/stroke} \pm 0.1 \text{ mL/stroke}$ , compared to the expected  $2.54 \text{ mL/stroke}$ , which is a negative bias of 9.7%. Due to the continuous data acquisition a high frame rate with a high temporal resolution can be achieved. The high frame rate captures the repeating pulsating behaviour and the higher velocities during peak-systole were  $25.6 \text{ cm/s} \pm 0.9 \text{ cm/s}$  and the lowest velocities during end-diastole were  $1.1 \text{ cm/s} \pm 0.7 \text{ cm/s}$ . A 3-D vector representation of the flow both during end-diastole and the peak-systole is presented in Fig. 3.

## VI. CONCLUSION

The performance of the presented method, showed that in a pulsatile setup, both the slow and fast flow could be estimated,

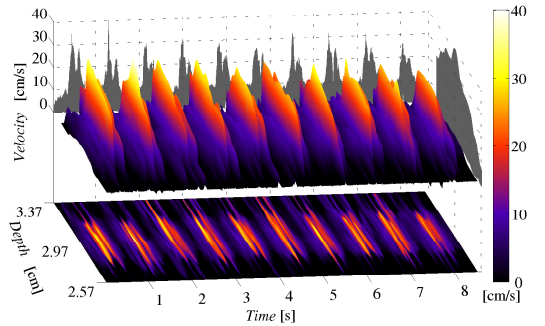


Fig. 2. M-mode of the velocity component in the flow direction measured in a pulsating carotid flow setup.

and that the estimated flow rates from 5 cycles gave a negative bias of 9.7%. The standard deviation on the flow rates was less than 5%, which shows that the estimates are consistent and

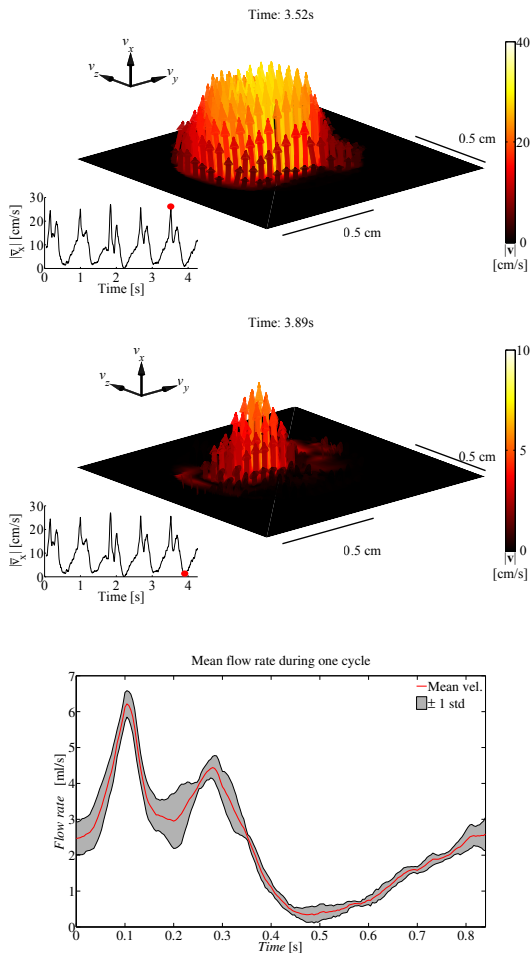


Fig. 3. Cross sectional 3-D vector flow representation estimated in the pulsating setup during (a) peak-systole and (b) end-diastole. Please note that the velocity scale during peak-systole is four times larger than for the end-diastole. c) mean flow rate with one standard deviation averaged across 5 cycles.

reproducible. The negative bias is expected to be due to the degree of beam-steering, which changes the double oscillating TO field and requires further optimization.

However, the presented results demonstrate that a setup with only 124 elements is sufficient to estimate 3-D vector flow. This channel count is similar to that of conventional probes, making realtime implementation on standard commercial plat-

forms possible.

#### ACKNOWLEDGMENT

This work was supported by grant 82-2012-4 from the Danish National Advanced Technology Foundation and by BK Ultrasound Aps.

#### REFERENCES

- [1] C. E. Morton and G. R. Lockwood, "Theoretical assessment of a crossed electrode 2-D array for 3-D imaging," in *Proc. IEEE Ultrason. Symp.*, 2003, pp. 968–971.
- [2] C. E. M. Démoré, A. Joyce, K. Wall, and G. Lockwood, "Real-time volume imaging using a crossed electrode array," *IEEE Trans. Ultrason., Ferroelec., Freq. Contr.*, vol. 56, no. 6, pp. 1252–1261, 2009.
- [3] M. F. Rasmussen, T. L. Christiansen, E. V. Thomsen, and J. A. Jensen, "3-D imaging using row-column-addressed arrays with integrated apodization — Part I: Apodization design and line element beamforming," *IEEE Trans. Ultrason., Ferroelec., Freq. Contr.*, vol. 62, no. 5, pp. 947–958, 2015.
- [4] S. Holbek, T. L. Christiansen, M. F. Rasmussen, M. B. Stuart, E. V. Thomsen, and J. A. Jensen, "3-D vector velocity estimation with row-column addressed arrays," in *Proc. IEEE Ultrason. Symp.*, 2015, pp. 1–4.
- [5] S. Holbek, T. L. Christiansen, M. Engholm, A. Lei, M. B. Stuart, C. Beers, L. N. Moesner, J. P. Bagge, E. V. Thomsen, and J. A. Jensen, "3-D vector flow using a row-column addressed CMUT array," in *Proc. SPIE Med. Imag.*, vol. 9790, 2016, pp. 979005–979005–8.
- [6] S. Holbek, T. L. Christiansen, M. B. Stuart, C. Beers, E. V. Thomsen, and J. A. Jensen, "3-D vector flow estimation with row-column addressed arrays," *IEEE Trans. Ultrason., Ferroelec., Freq. Contr.*, p. Accepted, 2016.
- [7] M. Engholm, T. L. Christiansen, C. Beers, J. P. Bagge, L. N. Moesner, H. Bouzari, A. Lei, M. Berkheimer, M. B. Stuart, J. A. Jensen, and E. V. Thomsen, "A hand-held row-column addressed CMUT probe with integrated electronics for volumetric imaging," in *Proc. IEEE Ultrason. Symp.*, 2015, pp. 1–4.
- [8] J. A. Jensen, H. Holten-Lund, R. T. Nilsson, M. Hansen, U. D. Larsen, R. P. Domsten, B. G. Tomov, M. B. Stuart, S. I. Nikolov, M. J. Pihl, Y. Du, J. H. Rasmussen, and M. F. Rasmussen, "SARUS: A synthetic aperture real-time ultrasound system," *IEEE Trans. Ultrason., Ferroelec., Freq. Contr.*, vol. 60, no. 9, pp. 1838–1852, 2013.
- [9] S. I. Nikolov and J. A. Jensen, "In-vivo Synthetic Aperture Flow Imaging in Medical Ultrasound," *IEEE Trans. Ultrason., Ferroelec., Freq. Contr.*, vol. 50, no. 7, pp. 848–856, 2003.
- [10] J. A. Jensen and P. Munk, "A new method for estimation of velocity vectors," *IEEE Trans. Ultrason., Ferroelec., Freq. Contr.*, vol. 45, pp. 837–851, 1998.
- [11] J. A. Jensen, "A new estimator for vector velocity estimation," *IEEE Trans. Ultrason., Ferroelec., Freq. Contr.*, vol. 48, no. 4, pp. 886–894, 2001.
- [12] M. J. Pihl and J. A. Jensen, "A transverse oscillation approach for estimation of three-dimensional velocity vectors. Part I: Concept and simulation study," *IEEE Trans. Ultrason., Ferroelec., Freq. Contr.*, vol. 61, pp. 1599–1607, 2014.
- [13] M. J. Pihl, M. B. Stuart, B. G. Tomov, M. F. Rasmussen, and J. A. Jensen, "A transverse oscillation approach for estimation of three-dimensional velocity vectors. Part II: Experimental validation," *IEEE Trans. Ultrason., Ferroelec., Freq. Contr.*, vol. 51, no. 10, pp. 1608–1618, 2014.
- [14] C. Kasai, K. Namekawa, A. Koyano, and R. Omoto, "Real-Time Two-Dimensional Blood Flow Imaging using an Autocorrelation Technique," *IEEE Trans. Son. Ultrason.*, vol. 32, pp. 458–463, 1985.
- [15] A. P. G. Hoeks, J. J. W. van de Vorst, A. Dabekausen, P. J. Brands, and R. S. Reneman, "An efficient algorithm to remove low frequency Doppler signal in digital Doppler systems," *Ultrason. Imaging*, vol. 13, pp. 135–145, 1991.

## **3-D Imaging Using RC-Addressed Transducer Arrays: Two-Way Focusing and 3-D VFI**

**Simon Holbek**, Hamed Bouzari, Mathias Engholm, Jonas Jensen  
Matthias Bo Stuart, Erik Vilian Thomasen, and Jørgen Arendt Jensen

*Patent proposal in preparation. Expected to be filed ultimo 2016*

## TECHNICAL FIELD

The following generally relates to ultrasound imaging and more particularly to three-dimensional (3-D) imaging with a row-column addressed transducer array and/or flow estimation with a row-column addressed transducer array.

## BACKGROUND

For 3-D imaging with a two-dimensional (2-D) array of transducing elements, the elements can be individually addressed or group-wise addressed, e.g., using row-column addressing, where groups of elements are accessed either by a row index or a column index such that each row and column is utilized as a single larger element. With traditional row-column addressing, the row and column arrays each steer the transmit beam in one direction. However, the transmit and receive directions are orthogonal to each other. For example, when the row array is used as a transmit array, it can steer the transmit angle in the z-x plane while at the same time the column array receives in the z-y plane. When the sequence is complete, the two arrays switch function, and now the column array is used as a transmit array and the row array as a receive array. This leads to two identical volumes; however, at each point only one-way focusing in transmit and receive is achievable. Three-dimensional vector flow has been implemented with a row and column array in a single plane as described in Christiansen et al., serial number 14/599,857, filed January 2015, and entitled "3-D flow estimation using row-column addressed transducer arrays," which is incorporated herein by references in its entirety. Unfortunately, the lack of two-way focusing and limitations with only 3-D vector flow in a plane render traditional row-column addressing not well-suited for real-time volumetric 3-D vector flow imaging. In view of at least the above, there is an unresolved need for another approach for 3-D imaging with a row-column addressed transducer array and/or flow estimation with a row-column addressed transducer array.

## SUMMARY

Aspects of the application address the above matters, and others. In one aspect, an ultrasound imaging system includes a 2-D transducer array with a first 1-D array of one or more rows of transducing elements configured to produce first ultrasound data and a second 1-D array of one or more columns of transducing elements

configured to produce second ultrasound data. The first and second 1-D arrays are configured for row-column addressing. The ultrasound imaging system further includes a controller configured to control transmission and reception of the first and second 1-D arrays, and a beamformer configured to beamform the received first and second echoes to produce ultrasound data, and an image processor configured to process the ultrasound data to generate an image, which is displayed via a display. In another aspect, a method includes controlling transmission and reception of first and second 1-D arrays of a 2-D transducer array, wherein the first 1-D array includes one or more rows of transducing elements configured to produce first ultrasound data, and the second 1-D array includes one or more columns of transducing elements configured to produce second ultrasound data, wherein the first and second 1-D arrays are configured for row-column addressing, beamforming the received first and second echoes to produce ultrasound data, and processing the ultrasound data to generate an image, which is displayed via a display. In another aspect, a computer readable medium is encoded with non-transitory computer executable instructions which when executed by a processor causes the processor to: control transmission and reception of first and second 1-D arrays of a 2-D transducer array, wherein the first 1-D array includes one or more rows of transducing elements configured to produce first ultrasound data, and the second 1-D array includes one or more columns of transducing elements configured to produce second ultrasound data, wherein the first and second 1-D arrays are configured for row-column addressing, and at least one of beamform the received first and second echoes to produce ultrasound data with two-way focusing in elevation or process the received first and second echoes to estimate volumetric 3-D vector flow information. Those skilled in the art will recognize still other aspects of the present application upon reading and understanding the attached description.

## **BRIEF DESCRIPTION OF THE DRAWINGS**

The application is illustrated by way of example and not limited by the figures of the accompanying drawings, in which like references indicate similar elements and in which: FIGURE 1 schematically illustrates an example imaging system with a 2-D row-column addressed array; FIGURE 2 schematically illustrates an example of the 2-D row-column addressed array; FIGURE 3 schematically illustrates an example of an effective 1-D column array resulting from the row-column addressing with the 2-D row-column addressed array; FIGURE 4 schematically

illustrates an example of an effective 1-D row array resulting from the row-column addressing with the 2-D row-column addressed array; FIGURE 5 depicts a point spread function for the azimuth direction in accordance with an embodiment herein; FIGURE 6 depicts a point spread function for the elevation direction in accordance with an embodiment herein; FIGURE 7 depicts a point spread function for elevation versus azimuth in accordance with an embodiment herein; FIGURE 8 depicts a point spread function for the azimuth direction for traditional row-column addressing; FIGURE 9 depicts a point spread functions for the elevation direction for traditional row-column addressing; FIGURE 10 depicts a point spread functions for elevation versus azimuth for traditional row-column addressing; FIGURE 11 schematically illustrates single element transmission synthetic aperture imaging; FIGURE 12 schematically illustrates processing of the output of the single element transmission synthetic aperture imaging of FIGURE 11; FIGURE 13 schematically illustrates row-column steered sequence for 3-D vector flow obtained in a cross sectional plane with TO; and FIGURE 14 schematically illustrates row-column steered sequence for volumetric 3-D vector flow with TO.

## DETAILED DESCRIPTION

The following describes an approach to achieve two-way focusing in elevation with data acquired with a 2-D row-column addressed array and/or estimate vector flow information with data acquired with the 2-D row-column addressed array. Figure 1 schematically illustrates an example ultrasound imaging system 100. The ultrasound imaging system 100 includes a 2-D transducer array 102 with at least two one-dimensional (1-D) arrays 104 of transducing elements 106 where the 1-D arrays 104 are arranged orthogonal with respect to each other. The 2-D transducer array 102 includes N rows (or columns) and M columns (or rows) of the transducing elements 106, where N and M are positive integers and  $N = M$  or  $N \neq M$ . The 2-D transducer array 102 may include a 16x16, 32x32, 64x64, 128x128, 512x512 larger or smaller array, a non-square/rectangular array, a circular array, and/or another 2-D transducer array. Figure 2 illustrates an example of the 2-D transducer array 102. In Figure 2, the 2-D transducer array 102 is 6x6 array (N=M=6). The 2-D array 102 includes a plurality of rows 2041, 2042, 2043, 2044, 2045, and 2046, collectively referred to herein as rows 204. The 2-D array 102 also includes a plurality of columns 2061, 2062, 2063, 2064, 2065, and 2066, collectively referred to herein as columns 206. The rows 204

and columns 206 include individual elements 208<sub>1,1</sub>, . . . , 208<sub>1,6</sub>, . . . 208<sub>6,1</sub>, . . . 208<sub>6,6</sub>, collectively referred to herein as elements 208. The individual rows 204 and columns 206 are addressable (individually or in groups) respectively through contacts 210<sub>1</sub>, 210<sub>2</sub>, 210<sub>3</sub>, 210<sub>4</sub>, 210<sub>5</sub>, and 210<sub>6</sub>, and 212<sub>1</sub>, 212<sub>2</sub>, 212<sub>3</sub>, 212<sub>4</sub>, 212<sub>5</sub>, and 212<sub>6</sub>, collectively referred to as row contacts 210 and column contacts 212. Row-column addressing effectively transforms the 36-element 2-D array 102 into a six-element, 1-D column array (FIGURE 3) and a six-element, 1-D row array (FIGURE 4). The axial direction is along the beam direction, the azimuth direction is orthogonal to the axial direction and along the transmitting elements, and the elevation direction is orthogonal to the azimuth and axial directions. Returning to FIGURE 1, the transducing elements 106 may include piezoelectric, capacitive micromachined ultrasonic transducer (CMUT), and/or other elements. Furthermore, the transducing elements 106 may include integrated apodization, which may be identical or different for the individual elements. An example is described in patent application PCT/IB2013/002838, filed December 19, 2013, and entitled “Ultrasound Imaging Transducer Array with Integrated Apodization,” the entirety of which is incorporated herein by reference. Furthermore, the 2-D array 102 may have flat 1-D arrays, one curved 1-D array, two curved 1-D arrays, a single curved lens in front of or behind one of the 1-D arrays, a double curved lens in front of or behind the 1-D arrays, a combination of at least one curved 1-D array and at least one curved lens, etc. An example is described in patent application PCT/IB2016/053367, filed June 8, 2016, and entitled “Row-Column Addressed 2-D array with a Double Curved Surface,” the entirety of which is incorporated herein by reference. Transmit circuitry 108 generates pulses that excite a predetermined set of addressed 1-D arrays of the 2-D array 102 to emit one or more ultrasound beams or waves, e.g., into a scan field of view. Receive circuitry 110 receives echoes or reflected waves, which are generated in response to the transmitted ultrasound beam or wave interacting with (stationary and/or flowing) structure in the scan field of view, from a predetermined set of addressed arrays of the 2-D array 102. A controller 112 controls the transmit circuitry 106 and/or the receive circuitry 108. Examples of control include: 1) transmitting and receiving with row elements, 2) transmitting and receiving with column elements, 3) transmitting with row elements and receiving with column elements, 4) transmitting with column elements and receiving with row elements, 5) transmitting with row elements and receiving with row and column elements, 6) transmitting with column elements and receiving with row and column elements, 7) transmitting with row elements and receiving with row and column elements and transmitting with column ele-

ments and receiving with row and column elements, etc. As described in greater detail below, the controller 110 can control the transmit and receive circuitries 106 and 108 to acquire data to create a two-way focusing profile in elevation in the transmit direction. This can be achieved, for example, by controlling the transmit and receive circuitries 106 and 108 to transmit and receive with both rows and columns (example 7 above). This approach improves spatial resolution relative to traditional row-column addressing. As a result, relative to traditional row-column addressing, the number of transmissions can be maintained to yield the full spatial resolution improvement, the number of transmissions can be reduced while still yielding improved spatial resolution, and/or the number of transmissions can be reduced to maintain a particular resolution. For example, to maintain a particular resolution, the number of transmissions in each dimension can be reduced by a factor of 2, 4, etc., relative to traditional row-column addressing. A beamformer 114 processes the echoes, for example, by applying time delays, weighting on the channels, summing, and/or otherwise beamforming received echoes, producing data for generating images in A-mode, B-mode, Doppler, and/or other ultrasound imaging modes. An image processor 116 processes the beamformed data. For B-mode, this may include generating a sequence of focused, coherent echo samples along focused scanlines of a scanplane. The image processor 116 may also be configured to process the scanlines to lower speckle and/or improve specular reflector delineation via spatial compounding, apply filtering such as FIR and/or IIR, etc. A scan converter 118 scan converts the output of the image processor 118 and generates data for display, for example, by converting the data to the coordinate system of the display. The scan converter 118 can be configured to employ analog and/or digital scan converting techniques. The illustrated embodiment further includes a velocity processor 120. In a variation, the velocity processor 120 is omitted and/or is located remote from the imaging system 100, such as in a computing device such as a computer or the like, which is remote from and not part of the imaging system 100. The illustrated velocity processor 120 is configured to process the beamformed row-column addressed data to determine 3-D velocity components. As described in greater detail below, this may include estimating 3-D velocity components from unfocussed diverging waves in combination with synthetic aperture (SA) and direct transverse oscillation (DTO), which yields higher volume rates, estimating 3-D velocity components from focused emissions and TO, and/or estimating 2-D and/or 3-D velocity components using DTO, which yields higher spatial resolution. A rendering engine 122 visually presents one or more of the images and/or the velocity information via a display

monitor 124. In one instance, the data is visually displayed in an interactive graphical user interface (GUI), which allows the user to selectively rotate, scale, and/or manipulate the displayed data through a mouse, a keyboard, touch-screen controls, etc. A user interface 126 includes one or more input devices (e.g., a button, a knob, a slider, a touch pad, etc.) and/or one or more output devices (e.g., a display screen, lights, a speaker, etc.). The user interface 126 can be used to select an imaging mode such as row-column addressing with two-way focusing in elevation and/or 3-D velocity component estimation, e.g., using one or more of the 3-D velocity component estimation approaches described herein. In one instance, the transducer array 102 is part of a probe and the transmit circuitry 108, the receive circuitry 110, the controller 112, the beamformer 114, the image processor 116, the scan converter 118, the velocity processor 120, the rendering engine 122, the display 124, and the user interface 126 are part of a separate console such as a computing system. Communication there between can be through a wired (e.g., a cable and electro-mechanical interfaces) and/or wireless communication channel. In this instance, the console can be similar to a portable computer such as a laptop, a notebook, etc., with additional hardware and/or software for ultrasound imaging. The console can be docked to a docking station and used. Alternatively, the console can be part (fixed or removable) of a mobile or portable cart system with wheels, casters, rollers, or the like, which can be moved around. In this instance, the display 124 may be separate from the console and connected thereto through a wired and/or wireless communication channel. Where the cart includes a docking interface, the laptop or notebook computer type console can be interfaced with the cart and used. An example of a cart system where the console can be selectively installed and removed is described in US publication 2011/0118562 A1, entitled "Portable ultrasound scanner," and filed on November 17, 2009, which is incorporated herein in its entirety by reference. Alternatively, the transducer array 102, the transmit circuitry 108, the receive circuitry 110, the controller 112, the beamformer 114, the image processor 116, the scan converter 118, the velocity processor 120, the rendering engine 122, the display 124, and the user interface 126 are housed within a hand-held ultrasound apparatus, where the housing mechanically supports and/or encloses the components therein. In this instance, the transducer array 102 and/or the display 124 can be part of the housing, being structurally integrated or part of a surface or end of the hand-held ultrasound apparatus. An example of a hand-held device is in US 7,699,776, entitled "Intuitive Ultrasonic Imaging System and Related Method Thereof," and filed on March 6, 2003, which is incorporated herein in its entirety by reference. As

briefly discussed above, in one non-limiting instance, the controller 112 controls the transmit circuitry 108 and the receive circuitry 110 to acquire data to create a two-way focusing profile in elevation in the transmit direction. For this, the controller 112 controls the transmit circuitry 108 and the receive circuitry 110 to transmit with row elements and receive with both row and column elements and then transmit with column elements and receive with both row and column elements, or vice versa, i.e. transmit with column elements and receive with both row and column elements and then transmit with row elements and receive with both row and column elements. Where the transmit and receive elements are the same (i.e. both rows, or both columns), the acquired data is used for two-way focusing in elevation, e.g., at least because the transmit and receive focus lines are both in the same plane. Where the transmit and receive elements are perpendicular to each other (i.e. rows and columns, or columns and rows), the acquired data is used to focus along each transmit focus line with only one-way focusing in elevation. The beamformer 114 beamforms the received echo signals, producing two volumes, a one for transmitting with row elements and receiving the echoes with both row and column elements, and another for transmitting with column elements and receiving the echoes with both row and column elements, both with a two-way focusing profile in elevation in transmit and a one-way profile in receive. These two volumes are combined to produce a volume with a two-way focusing profile in elevation in the transmit direction. In one instance, the two volumes are combined by multiplying them and taking the square root. In general, this approach is well suited for static or moving tissue, e.g. at least because it is not very sensitive to movement. In another instance, the two volumes are combined by summing phase coherent signals. This approach is also well suited for static or moving tissue, although it may be more sensitive to movement. In another instance, the two volumes are combined by taking a minimum value of an absolute value of the two volumes at each point in space. These approaches create a two-way focusing profile in elevation in the transmit direction, which increases spatial resolution in both dimensions, relative to traditional row-column addressing where orthogonal arrays (row and column, or column and row) are used to transmit and receive. In general, the spatial resolution in the perpendicular dimension is improved by using the two-way focusing profile for each point along the transmit focus-line instead of the one-way beam profile. FIGURES 5, 6, and 7 show point spread functions (PSF's) respectively for the azimuth direction, the elevation direction, and elevation versus azimuth. In FIGURE 5, a first or y-axis represents range in units of millimeters (mm) and a second or x-axis represents azimuth in the same

units. In FIGURE 6, a first or y-axis represent the range similar to FIGURE 5, and a second or x-axis represents elevation in the same units. In FIGURE 7, a first or y-axis represents elevation range and a second or x-axis represents azimuth, both in the units of millimeters. For comparative purposes, FIGURES 8, 9, and 10 show PSF's for traditional row-column addressing. In FIGURE 8, a first or y-axis represents range in units of millimeters and a second or x-axis represents azimuth in the same units. In FIGURE 9, a first or y-axis represent the range similar to FIGURE 8, and a second or x-axis represents elevation in the same units. In FIGURE 10, a first or y-axis represents elevation range and a second or x-axis represents azimuth, both in the units of millimeters. FIGURES 7 and 10 show improved spatial resolution with the approached described herein (FIGURE 7) relative to traditional row-column addressing (FIGURE 10). Again, as a result of the improved resolution, the number of transmissions can be maintained to yield the full spatial resolution improvement, the number of transmissions can be reduced while still yielding improved spatial resolution, and/or the number of transmissions can be reduced to maintain a particular resolution, relative to traditional row-column addressing. To have a same lateral resolution for both fully addressed and row-column addressed 2-D arrays, the number of row or column elements on a row-column addressed array is increased. Changing the aperture size will not change the normalized amplitudes, and the side-lobe levels relative to the main lobe level. By squaring the Fourier transform of the apertures, the amplitudes of the side-lobes are halved by a factor of two in decibels (dB) when two-way focusing is performed. A measure of contrast is the side-lobe level. Therefore, the approached described herein will have superior contrast performance relative to the traditional row-column addressed 2-D array one-way focusing. As briefly discussed above, in one non-limiting instance, the velocity processor 120 processes the beamformed row-column addressed echoes to estimate 3-D velocity components from unfocussed diverging waves in combination with synthetic aperture (SA) and direct transverse oscillation (DTO). An example of this described next in connection with FIGURES 11 and 12. In traditional synthetic aperture imaging with a 1-D array, the transmit sequence consists of several unfocused emissions, which can be either single element transmissions or multiple element transmission using virtual sources. After each transmit event, a low resolution image is beamformed by using all elements in receive. When all transmit events have been executed, the low resolution images are added together to form a high resolution image. The high resolution image is equally focused everywhere in the plane. The high resolution image can be processed to render

a B-mode image, but can also be used for vector flow estimation. Patent application PCT/IB2015/051526, filed March 2, 2015, and entitled “Vector velocity estimation with directional transverse oscillation,” which is incorporated herein by reference in its entirety, describes an approach in which a high resolution image is obtained with synthetic aperture (SA) techniques and used to obtain the lateral velocity component in the entire plane, when directed transverse-oscillation (DTO) is applied. The approach described herein expands this to 3-D vector flow for the 2-D row-column addressed transducer array 102, which results in high resolution volumes (HRV’s). FIGURE 11 shows an example data acquisition sequence for obtaining high resolution volumes with the row-column addressed array 102, which are processed by the velocity processor 120 to produce 3-D vector flow estimation in a volume. Due to the large area of each element in a row-column addressed array, enough energy from a single element emission is generated to beamform a low resolution volume. When an emission is made with a column element, all row elements are used in receive to beamform a low resolution volume, and when a row emission is made, all column elements are used in receive to beamform yet another low resolution volume. The interleaved transmit sequence consists of  $N$  emissions distributed between  $N/2$  row emissions and  $N/2$  column emissions. Adding all the  $N/2$  low resolution images beamformed with the aperture containing the row elements yields the high resolution volume HRVCR., and adding all the  $N/2$  low resolution images beamformed with the aperture containing the column elements yields the high resolution volume HRVCR. As shown in FIGURE 12, each of the HRV’s is separated into multiple high resolution planes (HRP’s), and processed by a transverse oscillation (TO) estimator to yield the lateral velocity component. An example of a suitable TO estimator is described in US 6,148,224 A, filed December 30, 2016, and entitled “Apparatus and method for determining movements and velocities of moving objects,” which is incorporated herein by reference in its entirety. The TO estimator requires two TO signals as input, which need to be phase shifted by a quarter of the lateral wavelength. The TO signals can be created in the receive beamforming by changing the apodization function to contain two separated peaks. However, a lateral oscillation can also be generated in the Fourier domain, known as  $k$ -space, to provide better control over the lateral oscillation wavelength. This is accomplished by using a filter in the Fourier domain, which filters a beamformed plane in the lateral dimension to only select  $k$ -space components around a desired lateral oscillation frequency. Example approaches are described in Jensen et al., “High frame rate vector velocity estimation using plane waves and transverse

oscillation,” in Proc. IEEE Ultrason. Symp., 2015, pp. 1–4, and Salles et al., “2-D arterial wall motion imaging using ultrafast ultrasound and transverse oscillations,” IEEE Trans. Ultrason., Ferroelec., Freq. Contr., vol. 62, no. 6, pp. 1047–1058, 2015. FIGURE 12 shows multiplication of the filter and the Fourier transformed plane yields a TO HRP. The plane is filtered in the lateral dimension, while the axial dimension is not filtered, or untouched. The directional information of the flow is preserved by applying a Hilbert transform on the filtered plane (spatial domain) for each of the lines in the lateral direction. These two signals (the Hilbert transformed and non-Hilbert transformed signal) are now used as input to the velocity processor 120. The output of the velocity processor 120 is the 2-D vector flow information for the axial and the lateral velocity components in the entire plane. This routine is then performed on all the planes that makes up for the HRV to yield 2-D vector flow in a volume. The HRVCR is used to estimate the magnitude of the velocity component in the direction parallel to the row elements, and the HRVRC is used to estimate the axial velocity and the velocity component. The axial velocity component can be found the direction parallel to the column elements with a conventional autocorrelation approach or by cross correlation techniques. A suitable conventional autocorrelation approach is described in Kasai et al. Real-Time Two-Dimensional Blood Flow Imaging using an Autocorrelation Technique,” IEEE Trans. Son. Ultrason., vol. 32, pp. 458–463, 1985. A suitable cross correlation technique is described in US 6,725,076 B1, filed May 10 2000, and entitled “Vector velocity estimation using directional beamforming and cross-correlation,” which is incorporated herein by reference in its entirety. Other suitable correlation techniques are described in Jensen, “Directional velocity estimation using focusing along the flow direction: I: Theory and simulation,” IEEE Trans. Ultrason., Ferroelec., Freq. Contr., vol. 50, pp. 857–872, 2003, and Jensen et al., “Directional velocity estimation using focusing along the flow direction: II: Experimental investigation,” IEEE Trans. Ultrason., Ferroelec., Freq. Contr., vol. 50, pp. 873–880, 2003. Combining the estimated axial velocity component with the lateral velocity component found from HRVCR and with the respective lateral velocity component found from HRVRC yields the 3-D vector flow information for the entire volume. As briefly discussed above, in one non-limiting instance, the velocity processor 120 processes the beamformed row-column addressed echoes to estimate 3-D velocity components from focused emissions in a plane and TO. An example of this described next in connection with FIGURE 13. A traditional TO velocity estimator can estimate two velocity components with data acquired with a 1-D array. Examples of such an estimator is described in

Jensen et al., "A new method for estimation of velocity vectors," *IEEE Trans. Ultrason., Ferroelec., Freq. Contr.*, vol. 45, pp. 837–851, 1998, Jensen et al., "A new estimator for vector velocity estimation," *IEEE Trans. Ultrason., Ferroelec., Freq. Contr.*, vol. 48, no. 4, pp. 886–894, 2001, and Pihl et al., "A transverse oscillation approach for estimation of three-dimensional velocity vectors. Part I: Concept and simulation study," *IEEE Trans. Ultrason., Ferroelec., Freq. Contr.*, vol. 61, pp. 1599–1607, 2014. The result is one component perpendicular to the element orientation in addition to an axial component. Three beamformed lines are needed, including one center line for the axial estimator and two steered lines for the transverse estimate. The center line *rcenter* is beamformed along the direction  $(0, 0, z)$ , using delay-and-sum and a traditional apodization profile. For the two steered lines, a traditional TO apodization profile with two separated peaks is applied and beamforming is performed along the lines  $(x, y, z) = (\lambda_x(z)/8, 0, z)$  to create the  $\lambda_x/4$  spatial separation. This approach can be expanded to estimate 3-D velocities with the 2-D row-column addressed transducer array 102. The third velocity component can be obtained by applying the same procedure as for the transverse component, but this time by beamforming the two steered lines at  $\pm\lambda_y/8$  in the orthogonal direction. All five lines are beamformed from two transmit events and combined afterwards. The five beamformed signals are subsequently used as input to the TO velocity estimator. From each transmit event three lines are beamformed at multiple direction. Two of the lines, *rleft* and *rright*, are used to estimate the velocity component perpendicular to the tallest dimension of the receiving elements using the TO method, and the third line, *rcenter*, is used to estimate the axial velocity with an autocorrelation approach, such as that describe in Kasai et al., "Real-Time Two-Dimensional Blood Flow Imaging using an Autocorrelation Technique," *IEEE Trans. Son. Ultrason.*, vol. 32, pp. 458–463, 1985. By combining the estimated transverse velocity components, one from each transmit event, with one of the two independent axial estimates, a 3-D velocity vector along the direction of the respective beamformed centerline is obtained. The transmit sequence can either be designed to yield M-mode data, where 3-D vector flow is estimated in points along the axial  $(0,0,z)$  direction, or it can be expanded to contain 3-D vector flow in a plane, when several steered emissions in one plane are added to the sequence, and finally, if steered emissions are made in two planes, 3-D volumetric flow can be obtained. The steered transmit sequence is used to estimate 3-D vector flow in the cross-sectional plane in a vessel. This sequence consists of one focused emission *C1* using column elements and *N* focused emissions *Ri* using row elements, where  $i = 1 \dots N$ . 3-D vector flow is

estimated in points along the  $N$  steered directions in the  $zy$ -plane. The column emission generated a plane wave within the cross sectional  $zy$ -scan plane, whereas plane waves perpendicular to the scan plane were steered in the  $zy$ -plane when using the row elements. From the row transmit event  $R_i$ , the  $v_{xi}$  and  $v_{zi}$  velocity components are estimated in points along the direction of the respective beamformed centerline. However, the  $C1$  column transmit event provides the data for beamforming the lines needed for estimating all  $v_{yi}$  and  $v_{zi}$  velocity components, as this transmit event sonifies the  $zy$  scan plane. The steered transmit sequence used is schematically written as:  $C1 \rightarrow R1 \rightarrow R2 \rightarrow R3 \rightarrow \dots RN$ , and  $C1 \rightarrow R1 \rightarrow R2 \rightarrow R3 \rightarrow \dots RN$ . The sequence can be modified to yield volumetric 3-D vector flow, if several column emissions are added. A sequence to yield volumetric 3-D vector flow could be written as:  $C1 \rightarrow R1 \rightarrow C2 \rightarrow R2 \rightarrow \dots CN \rightarrow RN$  and  $C1 \rightarrow R1 \rightarrow C2 \rightarrow R2 \rightarrow \dots CN \rightarrow RN$ . This is shown in FIGURE 13. Compared to the  $M$ -mode sequence, the steered sequence differs in two ways. First, after each column emission  $C1$ , multiple steered row emissions  $R_N$  are emitted. From each row emission three lines are beamformed according to the steering directions and  $v_x$  and  $v_z$  can be estimated along each direction. Second, from a single column emission  $C1$ , three lines are beamformed along each steering direction yielding  $v_y$  and  $v_z$  velocity estimates along the  $N$  directions. 3-D vector flow is estimated in points along directions originating from the center of the aperture and through the intersection between the focal lines. The estimation plane is obtained when interpolating the combined 3-D vector flow estimates. To achieve volumetric 3-D flow, TO beamforming is performed in multiple directions. TO beamforming is performed at all sites where the focal line from a row emission and a column emission are intersecting. Both sequences yield continuous data, which means that the distance between each identical emission type is equally distributed in time for all time. An advantage of continuous data is that very high frames rate can be obtained, and that dynamic ensemble lengths and echo canceling filters can be applied. The higher obtainable frame rate with continuous data occurs, since a sliding window can be applied on the beamformed data to generate one velocity estimate. The velocity estimate can be updated from each new similar emission, since the new data can replace the oldest data in the estimator. As briefly discussed above, in one non-limiting instance, the velocity processor 120 processes the beamformed row-column addressed echoes to estimate 2-D and/or 3-D velocity components in a volume using DTO. An example of this described next in connection with FIGURE 14. Compared to the single plane sequence of FIGURE 13, the volumetric sequence differs in at least two ways. First, after

multiple column emission CN are emitted, and second, TO beamforming is performed where ever the focal line from a row emission or a column emission are intersecting. 3-D vector flow is estimated in all points along directions originating from the center of the aperture and through the intersection between the focal lines. The estimation volume is obtained when interpolating the combined 3-D vector flow estimates. An alternative sequence could be: C1→C1→R1 →R1 → ...CN → CN → RN → RN. This gives a high velocity range and a continuous sequence. Although the sequence becomes longer however the time difference between the two sequences for every direction becomes smaller compared to the previous sequences. The following describes ultrafast vector flow estimation using line focusing emissions with a 2-D row-column array. This approach, generally, can be used on any 2-D transducer. For the following, the transducer array 102 is fixated above a tube ( $\varnothing = 12$  mm) in a distance of 3 cm from the center of the vessel. The beam-to-flow-angle between the transducer and the flow in the vessel is  $90^\circ$ . A centrifugal pump circulates a blood-mimicking fluid in the system and a long inlet ensured that a fully developed laminar flow with a parabolic profile was present at the measure site. A total of 20 frames, each consisting of 32 focused emissions are conducted. Transmit is done with the row elements and sampling is done with the column elements, which were perpendicularly oriented to the flow direction. For each emission, an entire plane is beamformed with axial dimensions running from 2 cm to 5 cm and lateral dimensions from - 0.8 cm to +0.8 cm. A spatial Hilbert transformation is performed on the beamformed image (e.g., as described in PCT/IB2015/051526) and used as input for the transverse oscillation velocity estimator. The mean transverse velocity estimated over the region of interest from one frame. The transverse estimate has a relative mean. The mean axial estimate has a relative mean bias of 5.8 % bias of 18.1 % with a mean standard deviation of  $\pm 0.039$  m/s. with a mean standard deviation of  $\pm 0.023$  m/s. The results show that without any further optimization, a parabolic flow profile is seen across the entire field of view, which spans the physical dimensions for a 2-D row-column addressed array 102 without a lens. The peak velocity is expected to be 0.55 m/s and the vessel boundary is illustrated with dotted lines at 2.6 and 3.8 cm depth. Since only one emission type was used to estimate the 2-D in plane velocities, a frame rate of half the pulse repetition frequency ( $f_{prf}$ ) is achievable if every other emission is used for B-mode imaging. If velocity estimates from several closely spaced planes are merged together, the information will provide one with the actual volume flow. This can be done by sweeping steered focused emissions over the region of interest and estimating the vector flow in each of the planes.

The number of steered directions or number of planes used for velocity estimation is denoted FN, with Frame rate =  $f_{prf} / (FN+1)$ , where the +1 comes from an emission used for B-mode imaging. An example of a transmission sequence for volume flow estimation is as discussed next. Consider a setup with a fprf of 10 kHz. A maximum depth which can be sampled is  $C / (2 * fprf) = 1540 \text{ m/s} / (2 * 10,000 \text{ s}) = 7.7 \text{ cm}$ . To cover a reasonable area, FN is set to 11. The Frame rate =  $10,000 \text{ Hz} / (11+1) = 833 \text{ Hz}$ . This approach is thus able to estimate 2-D vector flow in a volume without ECG gating at frame rates around 1 kHz. The application has been described with reference to various embodiments. Modifications and alterations will occur to others upon reading the application. It is intended that the invention be construed as including all such modifications and alterations, including insofar as they come within the scope of the appended claims and the equivalents thereof.

## CLAIMS

What is claimed is:

1. An ultrasound imaging system (100), comprising: a 2-D transducer array (102), including: a first 1-D array (104, 204) of one or more rows of transducing elements (106, 2041, ... 2046) configured to produce first ultrasound data; and a second 1-D array (104, 206) of one or more columns of transducing elements (106, 2061, ... 2066) configured to produce second ultrasound data, wherein the first and second 1-D arrays are configured for row-column addressing; a controller (112) configured to control transmission and reception of the first and second 1-D arrays; a beamformer (114) configured to beamform the received first and second echoes to produce ultrasound data; and an image processor (116) configured to process the ultrasound data to generate an image, which is displayed via a display (224).

2. The ultrasound imaging system of claim 1, wherein the controller is configured to control the first and second 1-D arrays to transmit a first ultrasound signal with the first 1-D array and receive first echoes with the first and second 1-D arrays, and subsequently transmit a second ultrasound signal with the second 1-D array and receive second echoes with the first and second 1-D arrays, and the beamformer is configured to combine the beamformed first and second echoes to produce the ultrasound data with two-way focusing in an elevation direction in transmit.

3. The ultrasound imaging system of claim 2, wherein the beamformer combines the first and second echoes by multiplying the beamformed first and second echoes.

4. The ultrasound imaging system of claim 2, wherein the beamformer combines the beamformed first and second echoes by summing the first and second echoes.

5. The ultrasound imaging system of claim 2, wherein the beamformer combines the beamformed first and second echoes by taking a minimum value of an absolute value of the first and second echoes at each point in space.

6. The ultrasound imaging system of claim 1, further comprising: a velocity processor (120) configured to process the beamform data to produce 3-D vector flow volumetric imaging data.

7. The ultrasound imaging system of claim 6, wherein the controller is configured to control transmission of the first and second 1-D arrays to produce single element transmission.

8. The ultrasound imaging system of claim 7, wherein the velocity processor is configured to process the beamformed data using a synthetic aperture and a directional transverse oscillation estimator.

9. The ultrasound imaging system of claim 6, wherein the controller is configured to control transmission of the first and second 1-D arrays to produce focused steered emission sequence.

10. The ultrasound imaging system of claim 9, wherein the velocity processor is configured to process the beamformed data using a transverse oscillation estimator to estimate 3-D vector flow at least one of a plane or a volume.

11. The ultrasound imaging system of claim 9, wherein the velocity processor is configured to process the beamformed data using directional transverse oscillation to compute at least one of a 2-D in-plane or a 3-D vector flow estimate.

12. The ultrasound imaging system of claim 9, wherein the beamformer employs directional beamforming in the flow direction estimated by directional transverse oscillation.

13. The ultrasound imaging system of any of claims 1 to 12, further comprising: a diverging lens coupled to a transducing side of the 2-D transducer array.

14. The ultrasound imaging system of any of claims 1 to 13, wherein at least one of the first 1-D array or the second 1-D array includes a curved array.

15. A method, comprising: controlling transmission and reception of first and second 1-D arrays of a 2-D transducer array, wherein the first 1-D array includes one or more rows of transducing elements configured to produce first ultrasound

data, and the second 1-D array includes one or more columns of transducing elements configured to produce second ultrasound data, wherein the first and second 1-D arrays are configured for row-column addressing; beamforming the received first and second echoes to produce ultrasound data; and processing the ultrasound data to generate an image, which is displayed via a display.

16. The method of claim 15, wherein the controlling includes controlling the first and second 1-D arrays to transmit a first ultrasound signal with the first 1-D array and receive first echoes with the first and second 1-D arrays, and subsequently transmit a second ultrasound signal with the second 1-D array and receive second echoes with the first and second 1-D arrays, and wherein the beamforming combines the first and second echoes to produce the ultrasound data with two-way focusing in an elevation direction.

17. The method of claim 16, further comprising: processing the two-way focused data to estimate and correct for motion in at least one of 1-D, 2-D or 3-D ultrasound data.

18. The method of claim 16, further comprising: controlling the transmission to produce single element transmission or constructing a virtual source transmit; and processing the received echoes using a synthetic aperture algorithm.

19. The method of claim 18, further comprising: processing the data to produce super resolution imaging using micro bubbles in at least one of 1-D, 2-D or 3-D ultrasound data.

20. The method of claim 15, further comprising: controlling the transmission to produce single element transmission or constructing a virtual source transmit; and processing the received echoes using a synthetic aperture to produce high resolution volumes.

21. The method of claim 20, further comprising: estimating flow by adding the high resolution volumes.

22. The method of claim 20, further comprising: estimating flow by multiplying the high resolution volumes.

23. The method of claim 20, further comprising: estimating flow in a row direction by processing a high resolution volume of the volumes for the flow direction; and estimating flow in a column direction by processing a high resolution volume of the volumes for the flow column.

24. The method of claim 20, further comprising: employing directional beamforming in a flow direction estimated by transverse oscillation to refine a flow estimate.

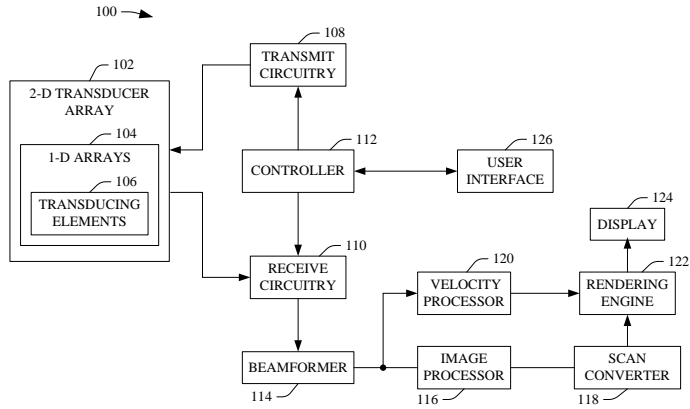
25. The method of any of claims 15 to 24, further comprising: displaying only one line in M-mode.

26. A computer readable medium encoded with non-transitory computer executable instructions which when executed by a processor causes the processor to: control transmission and reception of first and second 1-D arrays of a 2-D transducer array, wherein the first 1-D array includes one or more rows of transducing elements configured to produce first ultrasound data, and the second 1-D array includes one or more columns of transducing elements configured to produce second ultrasound data, wherein the first and second 1-D arrays are configured for row-column addressing; and at least one of beamform the received first and second echoes to produce ultrasound data with two-way focusing in elevation or process the received first and second echoes to estimate volumetric 3-D vector flow information.

## **ABSTRACT**

An ultrasound imaging system (100) includes a 2-D transducer array (102) with a first 1-D array (104, 204) of one or more rows of transducing elements (106, 2041, . . . 2046) configured to produce first ultrasound data and a second 1-D array (104, 206) of one or more columns of transducing elements (106, 2061, . . . 2066) configured to produce second ultrasound data. The first and second 1-D arrays are configured for row-column addressing. The ultrasound imaging system further includes a controller (112) configured to control transmission and reception of the first and second 1-D arrays, and a beamformer (114) configured to beamform the received first and second echoes to produce ultrasound data, and an image processor (120) configured to process the ultrasound data to generate an image, which is displayed via a display (224).

# Drawings



ANALISIS-MO  
(BKM-10-8040-PCD)

1/6

FIGURE 1

ANA1315-WO  
(BKM-10-8040-PCT)

2/6

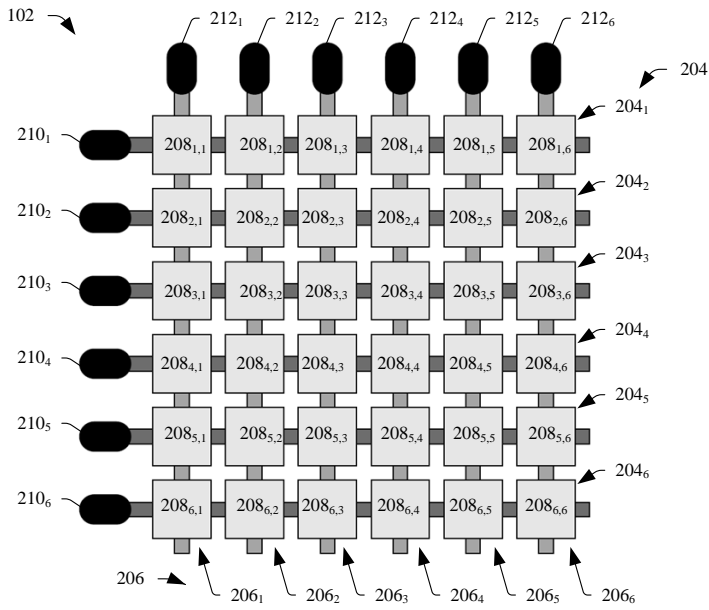


FIGURE 2

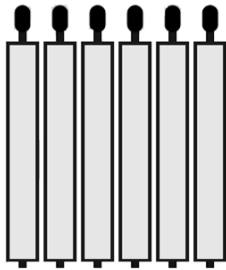


FIGURE 3

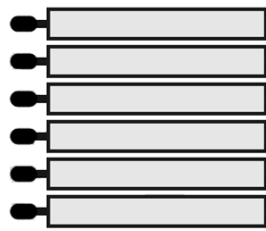


FIGURE 4

ANA1315-WO  
(BKM-10-8040-PCT)

3/6

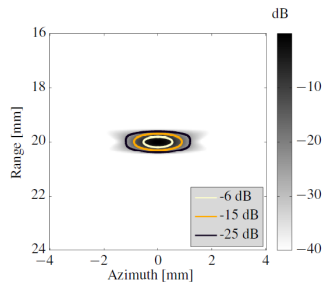


FIGURE 5

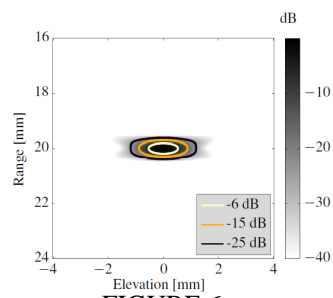


FIGURE 6

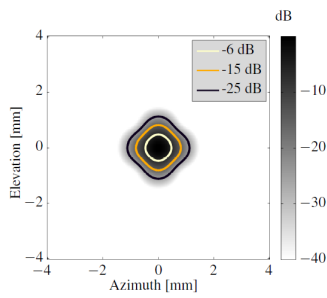


FIGURE 7

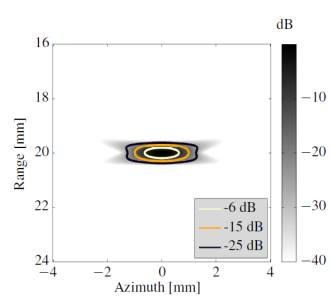


FIGURE 8

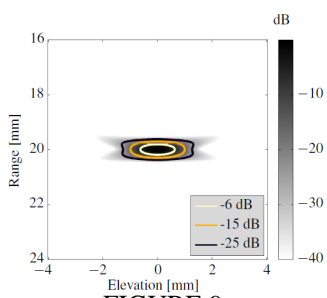


FIGURE 9

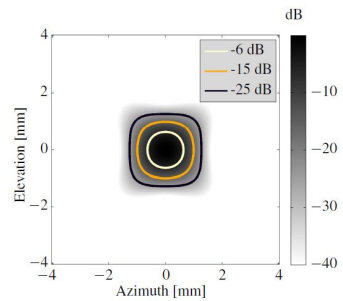
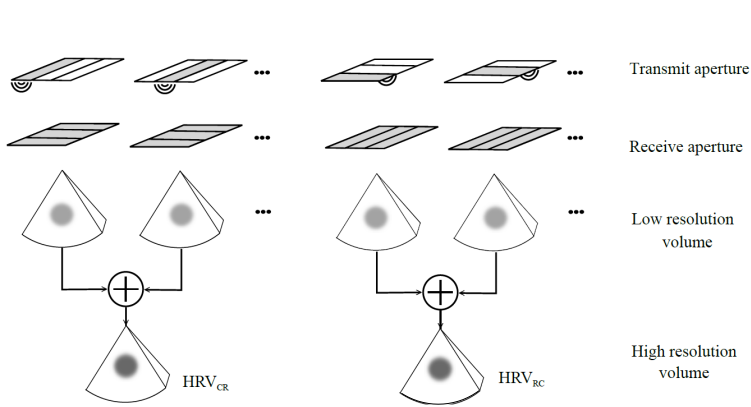


FIGURE 10



ANALISIS-WO  
(B)KM-10-5040(PCT)

4/6

FIGURE 11

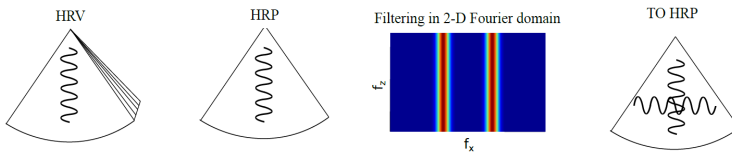


FIGURE 12

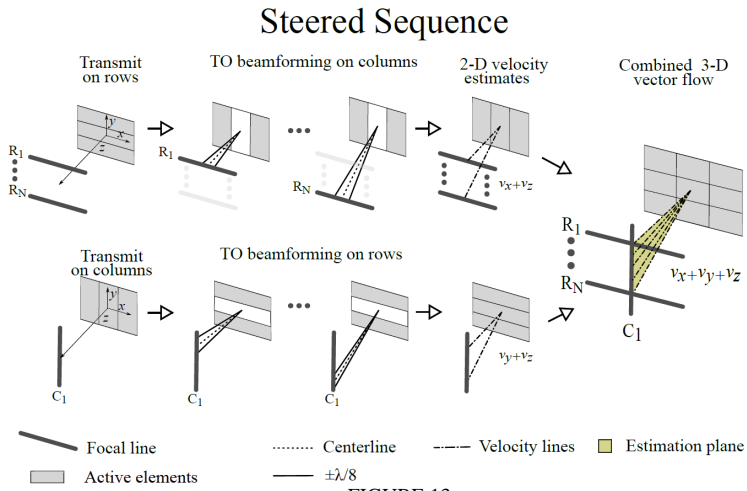


FIGURE 13

ANA1315-WO  
 (BKM-10-804/PCTD)

5/6

ANA1315-WO  
(BKM-10-8040-PCT)

6/6

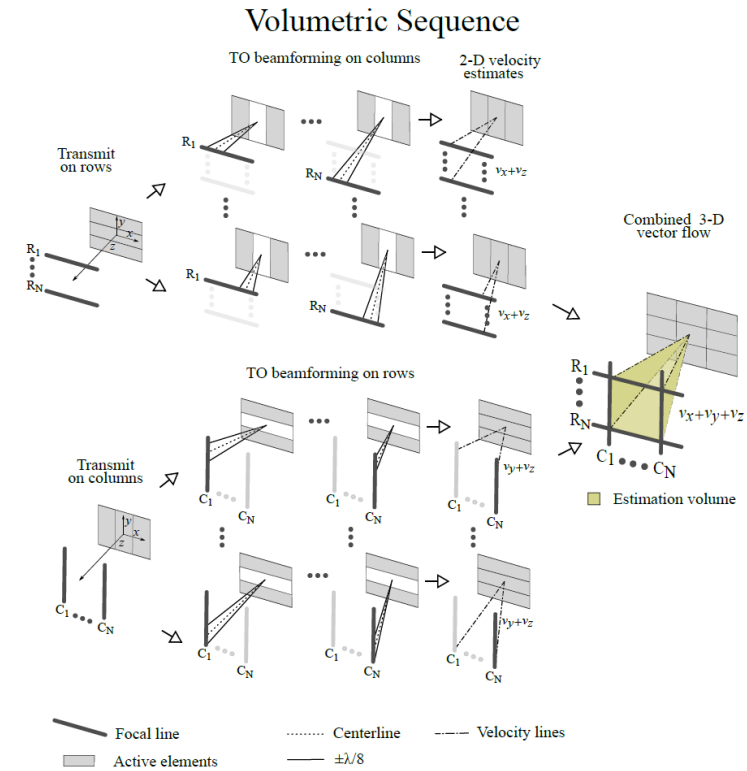


FIGURE 14

## **3-D Flow Estimation using Row-Column Addressed Transducer Arrays**

Thomas Lehrmann Christiansen, **Simon Holbek**, Morten Fischer Rasmussen, Erik Vilain Thomsen, and Jørgen Arendt Jensen.

*Patent filed January 19, 2015. US application number: 14/599,857.*

### 3-D Flow estimation using row-column addressed transducer arrays

## TECHNICAL FIELD

The following generally relates to ultrasound imaging and more particularly to 3-D flow estimation using row-column addressed transducer arrays.

## BACKGROUND

For ultrasound velocity estimation, the oscillation of the pulsed ultrasound field has been used to estimate the axial velocity component of the structure of interest. The axial component is the component of the velocity vector in the direction of propagation of ultrasound energy from the ultrasound transducer array. Several methods have been proposed in the literature to estimate the lateral components of the velocity vector (perpendicular to the axial component). For 2-D imaging using 1-D transducer arrays, these include speckle tracking, directional beamforming, and transverse oscillation (TO). In directional beamforming, the received signals are focused along the flow direction for a given depth. The signals for two emissions are then cross-correlated, and the shift between them is found. This is a shift in spatial position of the scatterers, and dividing by the time between emissions, thus, directly gives the velocity magnitude. The angle between the emitted beam and the flow direction must be known before the beamformation can be done. The angle could, e.g., be found from the B-mode image as in conventional spectral velocity estimation. For 2-D velocity vector estimation using the TO approach, an oscillation oriented transverse to that of the ultrasound pulse is introduced in the ultrasound field by applying the same transmit beam as used in conventional axial velocity estimation and adjusting the apodization of the receive aperture in such a way that the whole aperture resembles two point sources. Two point sources separated in space will give rise to two interfering fields, which creates the transverse oscillation. Using the Fraunhofer approximation, the relation between the lateral spatial wavelength and the apodization function is  $\lambda_x = 2\lambda_z z_0/d$ , where  $d$  is the distance between the two peaks in the apodization function,  $z_0$  is a depth, and  $\lambda_z$  is the axial wavelength. In axial velocity estimation, a Hilbert transform is performed to yield two  $90^\circ$  phase shifted signals; the in-phase signal and the quadrature signal. This enables the direction of the flow to be determined. The  $90^\circ$  phase shift in the transverse direction can be accomplished by having two parallel beamformers in receive. The two receive beams are steered,

so that the transverse distance between each beam is  $\lambda_x/4$ , which corresponds to a  $90^\circ$  phase shift in space. Along with these two TO lines, a center line can be beamformed by a third beamformer for conventional axial velocity estimation. For 3-D velocity vector estimation using the TO approach, 2-D transducer arrays are used to generate the TO field in both lateral dimensions allowing estimation of the velocity vector components in all three dimensions. 3-D velocity vector estimation using multiple crossed-beam ultrasound Doppler velocimetry and speckle tracking have also been proposed in the literature. There is an unresolved need for other approaches to 3-D velocity vector estimation that are applicable to arrays with a reduced number of connections, such as row-column addressed arrays.

## SUMMARY

Aspects of the application address the above matters, and others. In one aspect, an ultrasound system includes a 2-D transducer array and a velocity processor. The 2-D transducer array includes a first 1-D array of one or more rows of transducing elements configured to produce first ultrasound data. The 2-D transducer array further includes a second 1-D array of one or more columns of transducing elements configured to produce second ultrasound data. The first and second 1-D arrays are configured for row-column addressing. The velocity processor processes the first and the second ultrasound data, producing 3-D vector flow data. The 3-D vector flow data includes an axial component, a first lateral component transverse to the axial component, and a second lateral component transverse to the axial component and the first lateral component. In another aspect, a method includes employing row-column addressing with an orthogonally disposed 1-D arrays of a 2-D transducer array to produce data for determining 3-D velocity components. The method further includes processing, with a velocity processor, the data to produce the 3-D velocity components, which includes at least two lateral components, one transverse to the axial component and the other transverse to the axial component and the one lateral component. In another aspect, an ultrasound imaging system includes a pair of 1-D arrays oriented orthogonal to each other and row-column addressed. The ultrasound imaging system further includes processing components that process an output of the pair of 1-D arrays to estimate an axial and two lateral components using 2-D velocity vector estimator. Those skilled in the art will recognize still other aspects of the present application upon reading and understanding the attached description.

## BRIEF DESCRIPTION OF THE DRAWINGS

The application is illustrated by way of example and not limited by the figures of the accompanying drawings, in which like references indicate similar elements and in which: Figure 1 schematically illustrates an example ultrasound imaging system with a 2-D transducer array of row-addressed orthogonal 1-D arrays; Figure 2 schematically illustrates an example of the 2-D transducer array; Figure 3 illustrates an example method for determining 3-D vector velocity component utilizing the 2-D transducer array of row-addressed orthogonal 1-D arrays; Figures 4 and 5 schematically illustrate transmit along rows (or columns) and receive by both rows and columns; Figure 6 schematically illustrates an example beamformer and velocity processor; Figure 7 schematically illustrates a variation of the beamformer of Figure 6; Figures 8, 9, 10 and 11 schematically illustrate transmit along rows (or columns) and receive along columns (or rows), and subsequent transmit along columns (or rows) and receive along rows (or columns); Figures 12 and 13 schematically illustrate other variations of the beamformer of Figure 6; Figure 14 shows an example of the two angles used for a velocity estimator using directional beamforming; and Figure 15, 16 and 17 illustrate an example in which the 2-D array 102 includes a physical lens for fixed elevation focus.

## DETAILED DESCRIPTION

The following describes an approach to estimate the axial component and both lateral components of the 3-D velocity vector with ultrasound imaging data acquired through row-column addressing of two orthogonally oriented 1-D transducer arrays. Figure 1 schematically illustrates an example ultrasound imaging system 100. The ultrasound imaging system 100 includes a 2-D transducer array 102 with at least two one-dimensional (1-D) arrays 104 of transducing elements orthogonally arranged with respect to each other. An example of the 2-D array 102 includes N rows (or columns) and M columns (or rows) of transducing elements, where N and M are positive integers and  $N = M$  or  $N \neq M$ . The 2-D array 102 may include a 16x16, 32x32, 32x16, 64x64, larger or smaller array, a non-square/rectangular array, and/or other 2-D array. Figure 2 illustrates an example of the 2-D transducer array 102. Briefly turning to Figure 2, the example 2-D transducer array 102 is 6x6 transducer array ( $N=M=6$ ). The 2-D array 102 includes a plurality of rows 2041, 2042, 2043, 2044, 2045, and 2046, collectively referred to herein as rows 204. The 2-D array 102 also includes a plurality of columns 2061, 2062, 2063, 2064,

2065, and 2066, collectively referred to herein as columns 206. The rows 204 and columns 206 provide individual elements 2081,1, ..., 2081,6, ... 2086,1, ... 2086,6, collectively referred to herein as elements 208. The individual rows 204 and columns 206 are addressable (individually or in groups) respectively through contacts 2101, 2102, 2103, 2104, 2105, and 2106, and 2121, 2122, 2123, 2124, 2125, and 2126, collectively referred to as row contacts 210 and column contacts 212. Returning to Figure 1, multiple different types of row-column addressed array configurations are contemplated herein. One type includes a conventional row-column addressed 2-D array. This may allow volumetric imaging and estimation of all three velocity vector components in a volume. Another type includes a row-column addressed 2-D array with a physical or electronic elevation lens. This may offer two-way focused B-mode imaging and estimation of the two velocity vectors in the plane of the B-mode image in addition to the out-of-plane velocity vector. This transducer array may include a dynamic receive capability in elevation to improve B-mode image resolution. The transducing elements may include piezoelectric, capacitive micromachined ultrasonic transducer (CMUT), and/or other transducing elements. Furthermore, the transducing elements may include integrated apodization, which may be identical or different for the individual elements. An example of integrated apodization is described in international patent application serial number PCT/IB2013/002838, entitled "Ultrasound Imaging Transducer Array with Integrated Apodization," and filed December 19, 2013, the entirety of which is incorporated herein by reference. Furthermore, the 2-D array 102 may have a flat or a curved surface. Furthermore, the 2-D array 102 may include one or more lenses. Transmit circuitry 106 generates pulses that excite a predetermined set of addressed 1D arrays of the 2-D array 102 to emit one or more ultrasound beams or waves into a scan field of view. Receive circuitry 108 receives echoes or reflected waves, which are generated in response to the transmitted ultrasound beam or wave interacting with (stationary and/or flowing) structure in the scan field of view, from a predetermined set of addressed arrays of the 2-D array 102. A controller 110 controls the transmit circuitry 106 and/or the receive circuitry 108 based on a mode of operation. An example of suitable control includes row-column addressing, as well as individual element addressing. A beamformer 112 processes the echoes, for example, by applying time delays, weighting on the channels, summing, and/or otherwise beamforming received echoes. The beamformer 112 includes a plurality of beamformers (e.g., 2, 3, 4, 5, etc.) that process the echoes and produce data for determining the 3-D velocity components. As described in greater detail below, in one instance the beamform-

ers simultaneously process the echoes, and, in another instance, the beamformers sequentially process the echoes. The illustrated beamformer 112 also produces data for generating images in A-mode, B-mode, Doppler, and/or other ultrasound imaging modes. A velocity processor 114 processes the beamformed data to determine the 3-D velocity components. The velocity processor 114 employs one or more algorithms from an algorithm bank 116. A suitable algorithm includes a 2-D velocity vector estimator such as a speckle tracking, crossed-beam ultrasound Doppler velocimetry, directional beamforming, transverse oscillation (TO), and/or other estimator. An image processor 118 also processes the beamformed data. For B-mode, this includes generating a sequence of focused, coherent echo samples along focused scanlines of a scanplane. The image processor 118 may also be configured to process the scanlines to lower speckle and/or improve specular reflector delineation via spatial compounding, apply filtering such as FIR and/or IIR, etc. A scan converter 120 scan converts the output of the image processor 118 and generates data for display, for example, by converting the data to the coordinate system of the display. The scan converter 120 can be configured to employ analog and/or digital scan converting techniques. A rendering engine 122 visually presents one or more images and/or velocity information via a display monitor 124. Such presentation can be in an interactive graphical user interface (GUI), which allows the user to selectively rotate, scale, and/or manipulate the displayed data. Such interaction can be through a mouse or the like, and/or a keyboard or the like, and/or other approach for interacting with the GUI. A user interface 126 includes one or more input devices (e.g., a button, a knob, a slider, a touch pad, etc.) and/or one or more output devices (e.g., a display screen, lights, a speaker, etc.). A particular mode, scanning, and/or other function can be activated by one or more signals indicative of input from the user interface 126. For example, where the algorithm bank 116 include more than one 2-D velocity vector estimators the user interface 126 can be used to select one through a user input. The user interface 126 can also be used to set and/or change parameters such as imaging parameters, processing parameters, display parameters, etc. The beamformer 112, the velocity processor 114 and/or the image processor 118 can be implemented via a processor (e.g., a microprocessor, a CPU, a GPU, etc.) executing one or more computer readable instructions encoded or embedded on non-transitory computer readable storage medium such as physical memory. Such a processor can be part of the system 100 and/or a computing device remote from the system 100. Additionally or alternatively, the processor can execute at least one computer readable instructions carried by a carrier wave, a signal, or

other transitory medium. In one instance, the transducer array 102 is part of a probe and the transmit circuitry 106, the receive circuitry 108, the beamformer 112, the controller 110, the velocity processor 114, the image processor 118, the scan converter 120, the rendering engine 122, the user interface 126, and the display 124 are part of a separate console. Communication there between can be through a wired (e.g., a cable and electro-mechanical interfaces) and/or wireless communication channel. In this instance, console can be similar to a portable computer such as a laptop, a notebook, etc., with additional hardware and/or software for ultrasound imaging. The console can be docked to a docketing station and used. Alternatively, the console can be part (fixed or removable) of a mobile or portable cart system with wheels, casters, rollers, or the like, which can be moved around. In this instance, the display 124 may be separate from the console and connected thereto through a wired and/or wireless communication channel. Where the cart includes a docking interface, the laptop or notebook computer type console can be interfaced with the cart and used. An example of a cart system where the console can be selectively installed and removed is described in US publication 2011/0118562 A1, entitled "Portable ultrasound scanner," and filed on November 17, 2009, which is incorporated herein in its entirety by reference. Alternatively, the transducer array 102, the transmit circuitry 106, the receive circuitry 108, the beamformer 112, the controller 110, the velocity processor 114, the image processor 118, the scan converter 120, the rendering engine 122, the user interface 126, and the display 124 are housed within a hand-held ultrasound apparatus, where the housing mechanically supports and/or encloses the components therein. In this instance, the transducer 102 and/or the display 124 can be part of the housing, being structurally integrated or part of a surface or end of the hand-held ultrasound apparatus. An example of a hand-held device is described in US 7,699,776, entitled "Intuitive Ultrasonic Imaging System and Related Method Thereof," and filed on March 6, 2003, which is incorporated herein in its entirety by reference. Figure 3 illustrates a method for 3-D flow estimation using row-column addressed arrays. At 302, either the rows or the columns (or both sequentially) are used as transmit elements. Any apodization and phase delay can be applied to the transmit elements, and any number of transmit elements can be used simultaneously. Furthermore, any emission technique may be used, e.g. focused emission, plane wave emission, single element emission, synthetic transmit aperture, etc. An example of transmit along a subset of the rows or the columns 402 of the 2-D transducer array 102 is shown in Figure 4. In Figure 4, the example transmit produces a focused sound wave 404 in one line of

direction. Returning to Figure 3, at 304, echoes are subsequently received by the rows and the columns. An example of this is shown in Figure 5, which shows both rows 502 (or columns) and columns 504 (or rows) of the 2-D transducer array 102 respectively receive echoes 506 and 508. Returning to Figure 3, at 306, the echoes are processed to determine the 3-D velocity components. Depending on the velocity estimator, any subset of the received signals may be used. For example, in one instance, only the signals received by the rows are used. Furthermore, any apodization and phase delay may be applied to the receiving elements. The full 3-D velocity estimation may be performed using a single or several of such transmit-receive events, which may be combined in the estimation. In one embodiment, the controller 110 controls the transmit circuitry 106 so that either the rows or the columns emit ultrasound, and the velocity processor 114 estimates velocity by synthesizing TO fields in receive for both the rows and columns, respectively. The sequence may be repeated with the same or different transmit setup. This embodiment may be realized with a total of five beamformers 602, 604, 606, 608 and 610, as shown in Figure 6, each beamforming a line. The velocity processor 114 includes a transverse velocity processor 612, a transverse velocity processor 614, and an axial velocity processor 616. The received signals from the rows 612 are processed by beamformers 602 and 604, which are configured to produce data, which the transverse velocity processor 612 processes to determine the velocity component perpendicular to the rows. The received signals from the columns 614 are processed by beamformers 608 and 610, which are configured to produce data, which the transverse velocity processor 614 processes to determine the velocity component perpendicular to the columns. Example approaches for each of the two sets of beamformers are described in Jensen et al., "A new method for estimation of velocity vectors," *IEEE Trans. Ultrason., Ferroelec., Freq. Contr.*, vol. 45, pp. 837–851, 1998, Jensen, "A New Estimator for Vector Velocity Estimation", *IEEE Trans. Ultrason., Ferroelec., Freq. Contr.*, vol. 48, pp. 886-894, 2001, and Udesen et al., "Investigation of Transverse Oscillation Method," *IEEE Trans. Ultrason., Ferroelec., Freq. Contr.*, vol. 53, pp. 959–971, 2006, and international application publication WO/2000/068678, entitled "Estimation of Vector Velocity," and filed November 16, 2000, the entirety of which is incorporated herein by reference. The beamformer 606 is configured to produce data, which the axial velocity processor 616 processes to determine the axial velocity component. In one instance, the beamformer 606 processes the signals received by the rows 612. In another instance, the beamformer 606 processes the signals received by the columns 614. In yet another instance, the beamformer 606 processes both the signals received

by the rows 612 and the signals received by columns 614. In a variation, the beamformer 606 is omitted, and data from beamformers 602 and 604 and/or the beamformers 608 and 610 are feed to the axial velocity processor 616, as shown in Figure 7, which processes the signals to determine the axial velocity component. In a variation, columns 802 (or rows 804) emit ultrasound (Figure 8), and the TO field is synthesized in receive using the rows 804 (or the columns 802) (Figure 9). This allows estimation of the velocity component perpendicular to the rows (or columns). Subsequently, the rows 804 (or the columns 802) emit ultrasound (Figure 10), and the TO field is synthesized in receive using the columns 802 (or the rows 804) (Figure 11). This allows estimation of the velocity component perpendicular to the columns (or rows). The axial velocity component may be estimated using data from either of the two transmit-receive events. The signal processing may be done as shown in Figure 6. Alternatively, the signal processing may be done as shown in Figure 12. Figure 12 is substantially similar to Figure 6 except that the two of beamformers feeding one the transverse velocity processors are omitted. In this example, the beamformer 602 and 604, are omitted. In another example, the beamformers 608 and 610, are omitted. This can be implemented because the two transverse components of the velocity vector are estimated in two separate transmit-receive events. Hence, the same set of beamformers may be used. In a variation, the axial beamformer 606 is also omitted (Figure 13), and data from beamformers 602 and 604 and/or beamformer 608 and 610 (as shown) is used to feed the axial velocity processor 614. In another embodiment, either the rows or columns emit ultrasound, and the velocity estimation is subsequently done by performing directional beamforming in receive for both the rows and columns, respectively. The sequence may be repeated with the same or different transmit setup. In another embodiment, the rows emit ultrasound, and the velocity estimation is done by performing directional beamforming in receive for the columns. This is used to estimate the velocity component perpendicular to the columns. Subsequently, the columns emit ultrasound, and the velocity estimation is done by performing directional beamforming in receive for the rows. This is used to estimate the velocity component perpendicular to the rows. In both embodiments using directional beamforming, two angles must be predetermined. As shown in Figure 14, this includes a first angle ( $a_1$ ) 1402 between a surface 1404 of the transducer array 102 and a first projected direction of flow 1412, which is a direction of flow 1406 projected on a plane 1408 parallel to columns 1410. This also includes a second angle ( $a_2$ ) 1414 between the transducer surface 1404 and a second projected direction of flow 1420, which is the direction of

flow 1406 projected on a plane 1416 parallel to columns 1418. These angles are used to determine the line to be produced using the received data. They may be estimated e.g. from the volumetric image generated by the transducer array. Alternatively, they may be found using the TO approach and/or the methods approach disclosed in Jensen et al., "Estimation of velocity vectors in synthetic aperture ultrasound imaging." *IEEE Trans. Ultrason., Ferroelec., Freq. Contr.*, vol. 25, pp. 1637–1644, 2006, Kortbek et al., "Estimation of velocity vector angles using the directional cross-correlation method," *IEEE Trans. Ultrason., Ferroelec., Freq. Contr.*, vol. 53, pp. 2036–2049, 2006, and/or other approach. Figure 15, 16 and 17 illustrate an example in which the 2-D array 102 includes a physical lens 1502 giving fixed elevation focus. A conventional row-column addressed array using delay-and-sum beamforming can only achieve one-way focusing in each dimension. The elevation lens 1502 can be of any suitable material and can focus in any desired depth. Alternatively, an electronic lens could be used. An example of an electronic lens is described in Daft et al., "Elevation beam profile control with bias polarity patterns applied to microfabricated ultrasound transducers," in *Proc. IEEE Ultrason. Symp.*, vol. 2, 2003, pp. 1578–1581. In such a lens configuration, the row-column array essentially functions as a conventional 1-D array. From Figure 15, in the illustrated example rows 1504 oriented in the x-direction are used for transmitting. Electronic transmit focusing can then be performed in the y-direction, while the lens provides transmit focusing in the x-direction. A B-mode image can be acquired using the rows as receivers, in which case the array functions exactly like a 1-D array with elevation focus. The array may be used for estimating the 3-D velocity vector in the plane defined by the elevation lens. This is done by processing the data received on the rows and columns using an estimator discussed herein and/or other estimator for the conventional row-column addressed array. The velocity vector component in the y-direction is estimated using received data from the rows 1504 (Figure 16) and the velocity vector component in the x-direction is estimated using received data from columns 1702 (Figure 17). The z-component may be estimated using received data from either the rows or the columns, e.g., as shown in Figure 6. As such, by installing the lens 1502 on the row-column array, a two-way focused B-mode image with full 3-D velocity vector information in the plane of the B-mode image is achieved. This can be used for finding e.g. flow rate, direction of flow, peak velocities, etc., without sacrificing frame-rate nor B-mode image quality. A clinician will experience the same performance as when using a 1-D transducer for B-mode imaging in conjunction with 2-D velocity vector imaging, but with the addition

of out-of plane velocity estimation. The application has been described with reference to various embodiments. Modifications and alterations will occur to others upon reading the application. It is intended that the invention be construed as including all such modifications and alterations, including insofar as they come within the scope of the appended claims and the equivalents thereof.

## CLAIMS

What is claimed is:

1. An ultrasound system, comprising: a 2-D transducer array, including: a first 1-D array of one or more rows of transducing elements configured to produce first ultrasound data; and a second 1-D array of one or more columns of transducing elements (208) configured to produce second ultrasound data, wherein the first and second 1-D arrays are configured for row-column addressing; and a velocity processor that processes the first and the second ultrasound data, producing 3-D vector flow data, including: an axial component, a first lateral component transverse to the axial component, and a second lateral component transverse to the axial component and the first lateral component.

2. The ultrasound system of claim 1, further comprising: an algorithm bank that includes at least one algorithm from a group consisting of speckle tracking, crossed-beam ultrasound Doppler velocimetry, directional beamforming and transverse oscillation, wherein the velocity processor employs the at least one algorithm to process the first and the second ultrasound data to produce the 3-D vector flow data.

3. The ultrasound system of claim 1, further comprising: transmit circuitry; receive circuitry; and a controller that controls the transmit and receive circuitry to transmit using one of the first or second 1-D arrays and receive simultaneously from both of the first and second 1-D arrays.

4. The ultrasound system of claim 3, further comprising: first and second beamformer that process signals from one of the first or second 1-D arrays and produce first beamformed data; a first velocity processor that processes the first beamformed data, producing the velocity component perpendicular to the first or second 1-D array; third and fourth beamformer that process signals from the other of the first or second 1-D arrays and produce second beamformed data; and a second velocity processor that processes the second beamformed data, producing the velocity component perpendicular to the other of the first or second 1-D array.

5. The ultrasound system of claim 4, further comprising: a fifth beamformer that process at least one of the signal from the first or the second 1-D array and produces third beamformed data; and a third velocity processor that processes the third beamformed data, producing the axial component.

6. The ultrasound system of claim 4, further comprising: a third velocity processor that processes at least one of first beamformed data or the second beamformed data, producing the axial component.

7. The ultrasound system of claim 1, further comprising: transmit circuitry; receive circuitry; and a controller that controls the receive and transmit circuitry to transmit using one of the first or second 1-D arrays and receive using the other of the first or second 1-D arrays and subsequently to transmit using the other of the first or second 1-D arrays and receive using the one of the first or second 1-D arrays, wherein the velocity processor processes data from at least one of transmit-receive sequences to estimate the lateral velocity components.

8. The ultrasound system of claim 7, further comprising: first and second beamformer that process signals from one of the first or second 1-D arrays and produce first beamformed data; a first velocity processor that processes the first beamformed data, producing the velocity component perpendicular to the first or second 1-D array; third and fourth beamformer that process signals from the other of the first or second 1-D arrays and produce second beamformed data; and a second velocity processor that processes the second beamformed data, producing the velocity component perpendicular to the other of the first or second 1-D array.

9. The ultrasound system of claim 8, further comprising: a fifth beamformer that process at least one of the signal from the first or the second 1-D array and produces third beamformed data; and a third velocity processor that processes the third beamformed data, producing the axial component.

10. The ultrasound system of claim 8, further comprising: a third velocity processor that processes at least one of first beamformed data or the second beamformed data, producing the axial component.

11. The ultrasound system of claim 7, further comprising: a first pair of beamformers that processes signals from one of the first or second 1-D arrays and produces first or second beamformed data; a first velocity processor that processes the first beamformed data, producing the two lateral velocity components.

12. The ultrasound system of claim 11, further comprising: an axial velocity beamformer that process at least one of the signal from the first or the second 1-D array and produces third beamformed data; and a third velocity processor that processes the third beamformed data, producing the axial component.

13. The ultrasound system of claims 11, further comprising: a third velocity processor that processes at least one of first beamformed data or the second beamformed data, producing the axial component.

14. The ultrasound system of claim 1, wherein the velocity processor employs transverse oscillation to produce the first and second lateral components.

15. The ultrasound system of claim 1, wherein the velocity processor employs directional beamforming to produce the first and second lateral components.

16. The ultrasound system of claim 1, further comprising: an acoustical elevation lens affixed to the first and second 1-D arrays;

17. The ultrasound system claim 16, wherein the 2-D array is configured for two way focused B-Mode imaging, and the velocity processor estimates two velocity vectors in a plane of a B-mode image and a velocity vector out of the plane of the B-mode image.

18. A method, comprising: employing row-column addressing with a orthogonally disposed 1-D arrays of a 2-D transducer array to produce data for determining 3-D velocity components; and processing, with a velocity processor, the data to produce the 3-D velocity components, which includes at least two lateral components, one transverse to the axial component and the other transverse to the axial component and the one lateral component.

19. The method of claim 18, wherein the velocity processor employs at least one of speckle tracking, crossed-beam ultrasound Doppler velocimetry, directional beamforming and transverse oscillation to produce the 3-D velocity components.

20. The method of claim 19, further comprising: transmitting ultrasound with only one of the orthogonally disposed 1-D arrays; receiving echoes concurrently with the orthogonally disposed 1-D arrays; and processing the received echoes to produce at least the two lateral components.

21. The method of claim 19, further comprising: transmitting ultrasound with only one of the orthogonally disposed 1-D arrays and receiving echoes with only the other of the orthogonally disposed 1-D arrays; and processing the received echoes to produce at least the two lateral components.

22. The method of claim 21, further comprising: transmitting ultrasound with only the other of the orthogonally disposed 1-D arrays and receiving echoes with only the one of the orthogonally disposed 1-D arrays; and processing the echoes received by the one and the other one of the 1-D arrays to produce at least the two lateral components.

23. The method of claim 18, further comprising: applying apodization for the transmitting.

24. The method of claim 23, wherein the apodization is integrated into transducer elements of the 1-D arrays.

25. The method of claim 18, further comprising: applying a phase delay for the transmitting.

26. The method of claim 18, further comprising: utilizing at least one of focused emission, plane wave emission, single element emission, or synthetic transmit aperture for transmitting.

27. The method of claim 18, further comprising: providing one-way focusing in both lateral directions.

28. The method of claim 18, further comprising: employing a lens having a fixed elevation focus with the orthogonally disposed 1-D arrays.

29. The method of claim 28, wherein the lens is a physical lens.

30. The method of claim 29, wherein the lens is an electronic lens.

31. The method of claim 28, further comprising: providing two-way focusing in a plane of the orthogonally disposed 1-D arrays.

32. An ultrasound imaging system, comprising: a pair of 1-D arrays oriented orthogonal to each other and row-column addressed; and processing components that process an output of the pair of 1-D arrays to estimate an axial and two lateral components using 2-D velocity vector estimator.

## ABSTRACT

An ultrasound system includes a 2-D transducer array and a velocity processor. The 2-D transducer array includes a first 1-D array of one or more rows of transducing elements configured to produce first ultrasound data. The 2-D transducer array further includes a second 1-D array of one or more columns of transducing elements configured to produce second ultrasound data. The first and second 1-D arrays are configured for row-column addressing. The velocity processor processes the first and the second ultrasound data, producing 3-D vector flow data. The 3-D vector flow data includes an axial component, a first lateral component transverse to the axial component, and a second lateral component transverse to the axial component and the first lateral component.

Drawings

1/10

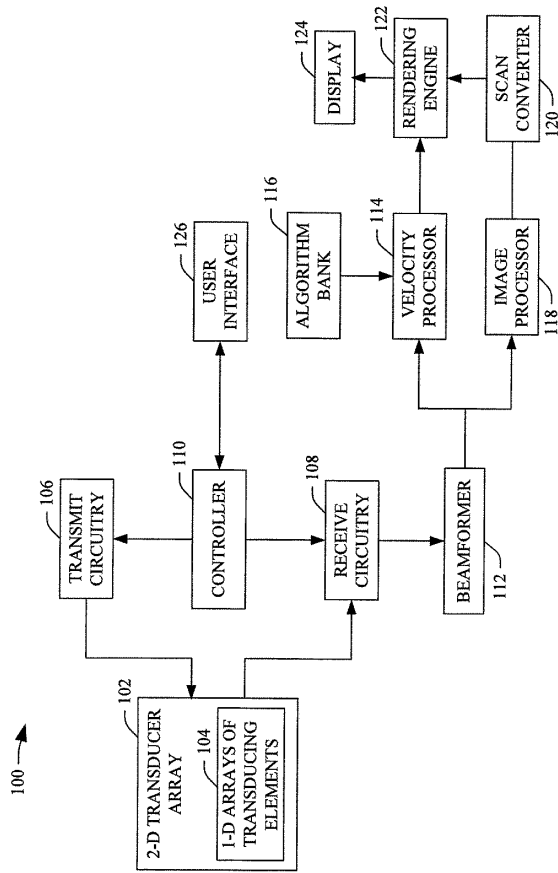


FIGURE 1

2/10

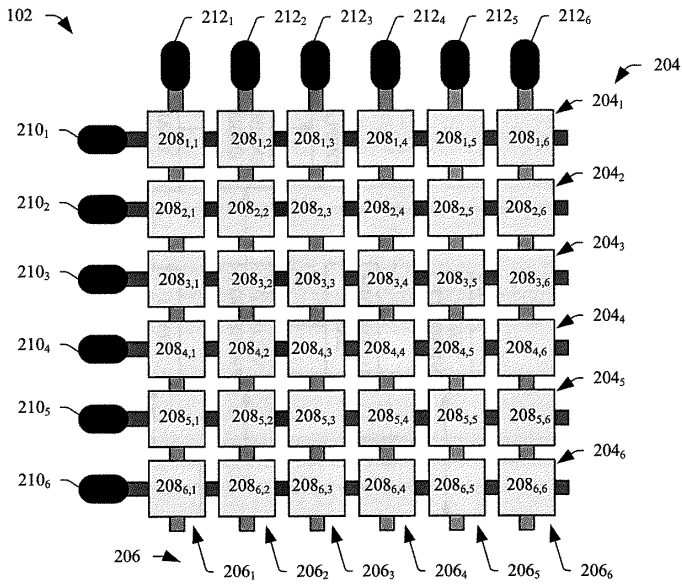


FIGURE 2

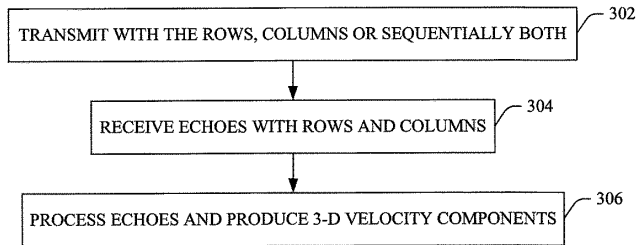


FIGURE 3

3/10

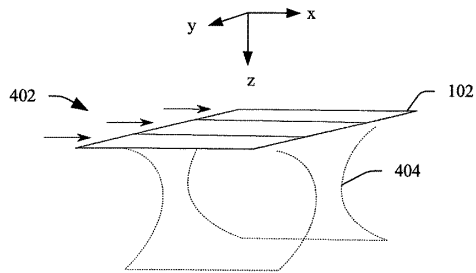


FIGURE 4

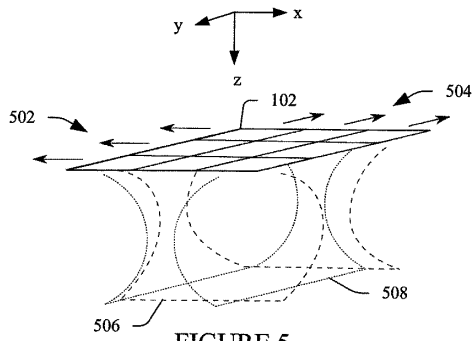


FIGURE 5

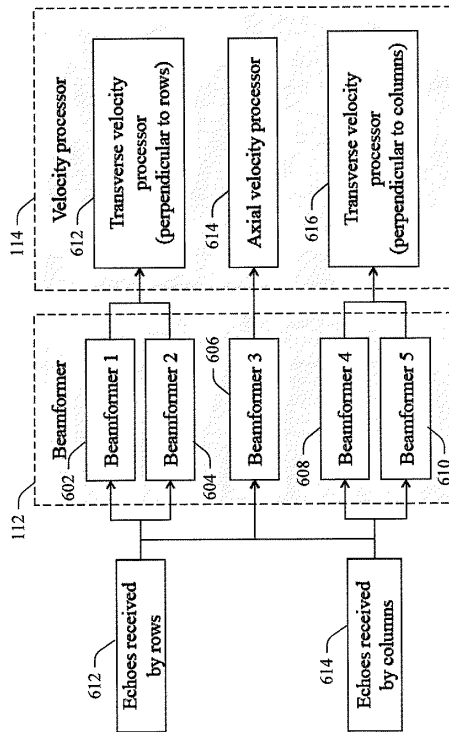


FIGURE 6

5/10

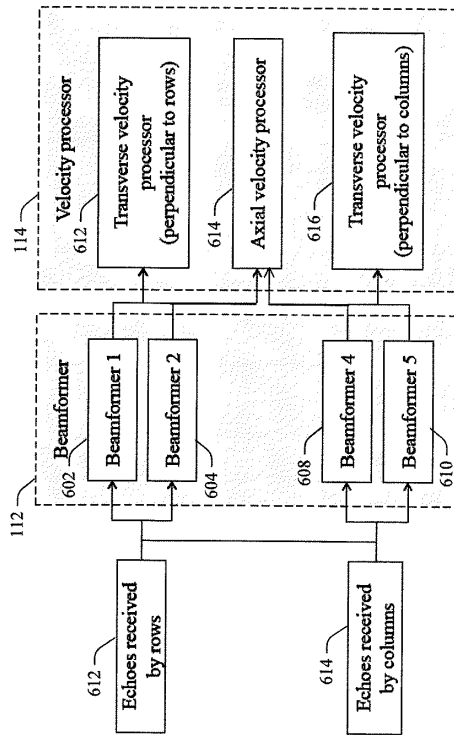


FIGURE 7

6/10

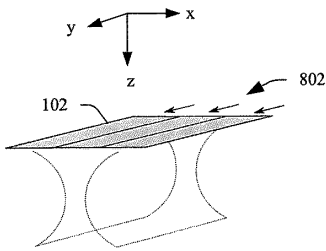


FIGURE 8

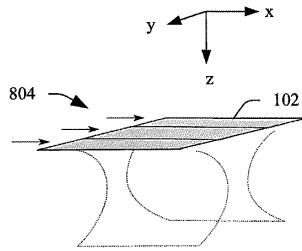


FIGURE 10

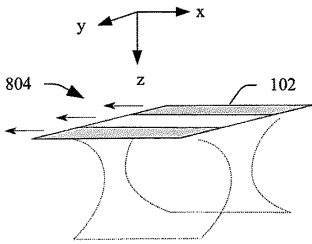


FIGURE 9

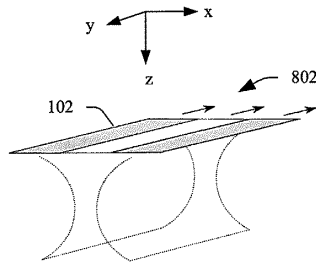


FIGURE 11

7/10

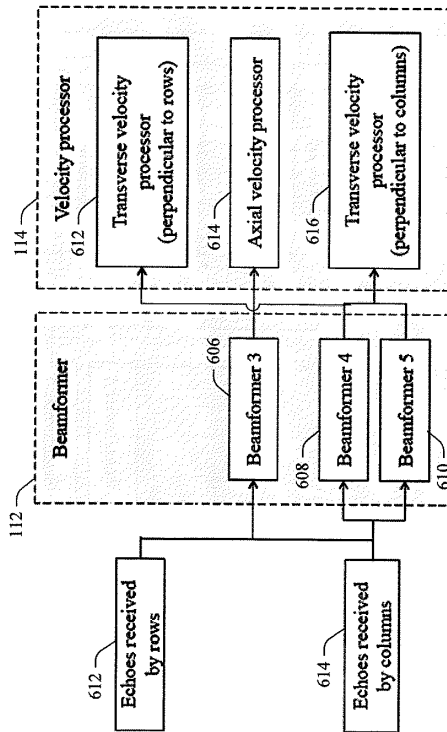


FIGURE 12

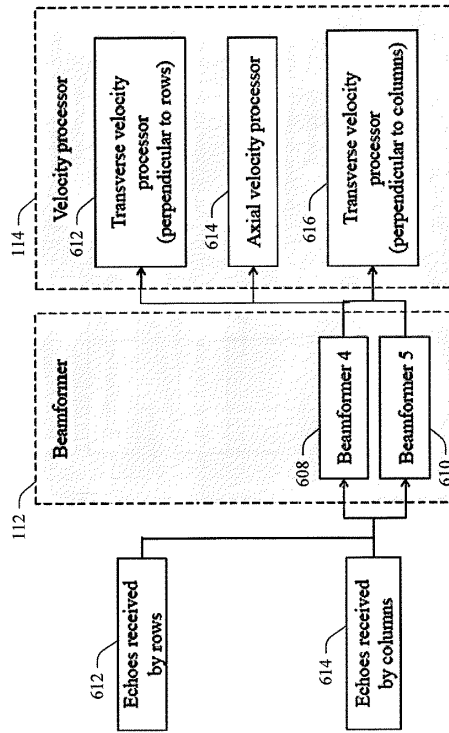


FIGURE 13

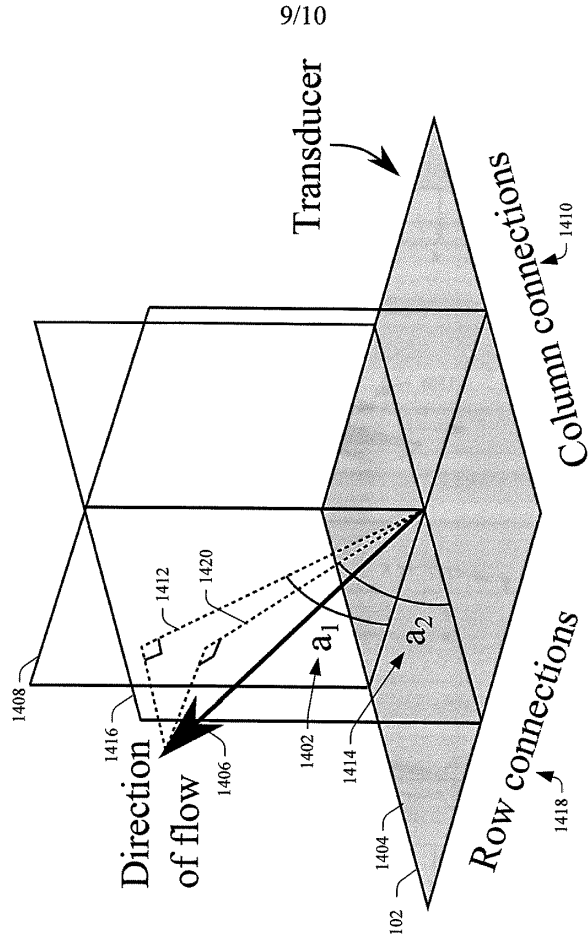


FIGURE 14

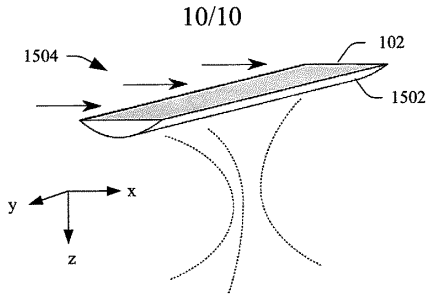


FIGURE 15

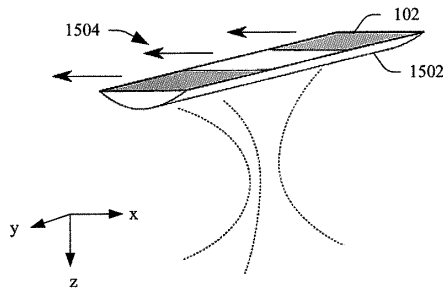


FIGURE 16

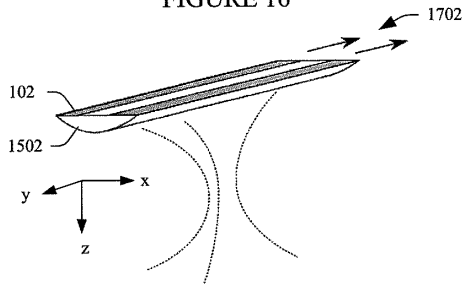


FIGURE 17

## **Row-column Addressed 2-D Array with a Double Curved Surface**

Hamed Bouzari, **Simon Holbek**, Thomas Lehrmann Christiansen, Matthias Bo Stuart, Erik Villain Thomsen, and Jørgen Arendt Jensen.

*Patent filed June 8, 2016. Patent number: PCT/IB2016/053367*

## Technical Field

The following generally relates to ultrasound imaging and more particularly to a row-column addressed 2-D with a double curved surface and/or 3-D imaging with the row-column addressed 2-D with the double curved surface.

## Background

An ultrasound imaging system includes a transducer array, which includes a one-dimensional (1-D) or a two-dimensional (2-D) array of transducing elements. For three dimensional (3-D) imaging with a 2-D array, the elements can be individually addressed or group-wise addressed using row-column addressing where the elements are accessed by their row or column index, and each row and column in the array thereby acts as one large element. With individual addressing, an  $N \times N$  array would require  $N^2$  electrical connections and channels to fully address the array. As a result, 2-D arrays in the medical environment have been small with small fields of view, which are not well-suited for applications such as abdominal, breast, vascular, etc. examinations. With row-column addressing, the  $N \times N$  array would require only  $2N$  electrical connections and channels to fully address the array.

Figure 1 schematically illustrates an example 6x6 flat array 102 configured for row-column addressing. Each column 106 includes an electrically conductive trace or path 108 in electrical communication with each element 104 of the column 106. The column 106 also includes an electrode 110, in electrical communication with the electrically conductive trace or path 108, which is used to excite the column 106. Each row 112 includes an electrically conductive trace or path 114 in electrical communication with the elements 104 of the row 112. The row 112 also includes an electrode 116, in electrical communication with the electrically conductive trace or path 114, which is used to excite the row 112. The row-column addressing of the array 102 effectively transforms the 36-element 2-D array into a 6-element 1-D flat column array 118 and a 6-element 1-D flat row array 120.

For 3-D imaging, one of the 1-D arrays transmits waves into an object under evaluation and the other 1-D arrays receives echoes scattered from the insonified region. Both of the 1-D arrays can be focused in the lateral and elevation directions separately, and each of the 1-D arrays can electronically focus in one lateral dimension when delays are applied to the elements in the array. For example, the 1-D array 118 is able to focus the beam in x- and z-directions, but not in a

y-direction. As a result, the emitted ultrasound is focused along a line segment or arc parallel to the y-direction. By adjusting the delays on the transmit elements, this focal line may be translated to any position in the xz-plane. The 1-D array 120 receives the echoes, and by applying delays, the received signals can be focused in a line segment or arc normal to any position in the yz-plane.

The 2-D array 102 can be used for phased array imaging. However, due to the 1-D arrays being flat, when transmitting plane waves, only a rectilinear forward-looking volume region can be imaged. Although it is possible to focus the ultrasound wavefronts curvilinearly, the pulse-echo field is limited only to a forward-looking volume region. This can be seen in Figure 2, which shows the transmit and receive pressure fields 202 and 204 when steering the transmit and receive beams by  $\pm 45^\circ$  with a same radial distance. The imaging area is the intersection of these two fields, which, unfortunately, is limited to a rectilinear forward-looking boxed-shaped region 206 in front of the transducer 102. Furthermore, it is only possible to use each 1-D flat array either in transmit or receive focusing to jointly target a single point in 3-D space.

## Summary

Aspects of the application address the above matters, and others. In one aspect, a transducer array for an ultrasound imaging system includes a row-column addressed 2-D array of transducer elements. The row-column addressed 2-D array includes a first array of 1-D arrays of elements, a second array of 1-D arrays of elements, which is orthogonal to the first array, and a double-curved surface. In another aspect, an apparatus includes a transducer array with an array-wise addressable 2-D array with a curved surface. The 2-D array includes a set of 1-D column array elements and a set of 1-D row array elements. The apparatus further includes transmit circuitry that conveys an excitation pulse to the transducer array, receive circuitry that receives a signal indicative of an ultrasound echo from the transducer array, and a beamformer that processes the received signal, generating ultrasound image data. In another aspect, a method includes transmitting an ultrasound signal with 2-D row-column addressed transducer array with a curved surface, transmitting an echo signal with the 2-D row-column addressed transducer array with a curved surface, beamforming the echo signal to create an image, and displaying the image. Those skilled in the art will recognize still other aspects of the present application upon reading and understanding the attached description.

## Brief Description of the Drawings

The application is illustrated by way of example and not limited by the figures of the accompanying drawings, in which like references indicate similar elements and in which: Figure 1 schematically illustrates a 2-D array configured for row-column addressing;

Figure 2 schematically illustrates a rectilinear forward-looking imaging region of the prior art 2-D array of Figure 1;

Figure 3 schematically illustrates an example ultrasound imaging system with a row-column addressed transducer array with a curved surface;

Figure 4 schematically illustrates an example row-column addressed transducer array for the configuration of Figure 3;

Figure 5 schematically illustrates another example row-column addressed transducer array for the configuration of Figure 3;

Figure 6 schematically illustrates an example of the curved surface of the row-column addressed transducer array;

Figure 7 schematically illustrates a field of view for the row-column addressed transducer array with the curved surface;

Figure 8 shows the intersection of transmitted wavefronts with the row-column addressed transducer array with the curved surface is a point;

Figure 9 shows wavefronts that create two focus points using the row-column addressed transducer array with the curved surface;

Figure 10 provides a diagram showing how to extend beamforming to calculate a time-of-flight in dynamic receive focusing with the curved surface for single element transmissions;

Figure 11 shows a beamformed B-mode image of a point scatterer imaged with the curved surface as the system's point spread function;

Figure 12 shows a beamformed B-mode image of a point scatterer imaged without the curved surface as the system's point spread function;

Figure 13 shows a beamformed B-mode image of point scatterers imaged with the curved surface;

Figure 14 shows a beamformed B-mode image of point scatterers imaged without the curved surface;

Figure 15 graphically shows pulse-echo energy as a function of steering angles for different f#s and without the curved surface; and

Figure 16 illustrates an example method in accordance with an embodiment herein.

## Detailed Description

Figure 3 schematically illustrates an example ultrasound imaging system 300. The ultrasound imaging system 300 includes a 2-D transducer array 302 configured for row-column addressing. The 2-D array 302 include a plurality of detector elements arranged in a  $N \times M$  matrix of  $N$  rows and  $M$  columns, where  $N$  and  $M$  are positive integers and  $N=M$  or  $N \neq M$  (e.g.,  $N > M$  or  $N < M$ ). Examples of square arrays include  $64 \times 64$ ,  $192 \times 192$ ,  $256 \times 256$ ,  $512 \times 512$  and/or other arrays, including larger and/or smaller arrays. Examples also include non-square arrays such as rectangular, circular, irregular and/or other shaped arrays. The elements can be piezoelectric (PZT), capacitive micromachined ultrasonic transducer (CMUT) elements, and/or other transducing elements.

Figure 4 schematically illustrates a non-limiting example of the row-column addressed array 304. Each column 402 includes an electrically conductive trace or path 404 in electrical communication with the elements 404 of the column 402. The column 402 also includes an electrode 408, in electrical communication with the electrically conductive trace or path 404, which is used to excite the column 104. Each row 410 includes an electrically conductive trace or path 412 in electrical communication with the elements 406 of the row 410. The row 410 also includes an electrode 414, in electrical communication with the electrically conductive trace or path 412, which is used to excite the row 110.

Either the rows 410 or the columns 402 transmit while the other receives. In this example, the elements 406 of the column 402 are arranged in a first or “y” direction of an “x-y” plane, and the elements 406 of the row 410 are arranged in a second or “x” direction of the “x-y” plane. The elements 406 of the column 402 are configured to transmit, in response to being excited with an electrical pulse, a pressure wave in a “z-x” plane, and the elements 406 of the rows 410 are configured to receive echoes, produced in response to the transmitted pressure wave interacting with matter, in a “z-y” plane. In this example, “x,” “y,” and “z” are axes of the Cartesian coordinate system 416.

A geometry of the elements 406 in Figure 4 are square and/or rectangular. Figure 5 schematically illustrates a variation of Figure 4 in which a geometry of outer or perimeter elements 502 are not square and/or rectangular, and elements at corners 504 are omitted. The triangular elements 502 provide integrated apodization that linearly scales (rather than discretely scales, as shown in Figure 4) the output pressure transmitted by (during transmit) and the electrical signal generated by (during receive) of the elements of the periphery. The illustrated apodization

decreases in a direction towards the periphery and away from the center region. Other geometries (e.g., hexagon, circle, etc.) are also contemplated herein.

The examples discussed in connection with Figures 4 and 5 and/or other examples of row-column addressed 2-D arrays are described in international application serial number PCT/IB2013/002838, filed on December 20, 2013, and entitled "Ultrasound Imaging Transducer Array with Integrated Apodization," the entirety of which is incorporated herein by reference. An example in international application PCT/IB2013/002838 includes PZT transducer elements. Another example in international application PCT/IB2013/002838 includes CMUT elements. Other configurations of the row-column addressed 2-D array 102 are also contemplated herein.

Returning to Figure 3, the transducer array 302 further includes a curved surface 306. In one instance, the curved surface 306 is a diverging lens disposed in front of an active transducing surface of the 2-D array 304. In another instance, the curved surface 306 is the active transducing surface of the 2-D array 304. In yet another instance, the curved surface 306 is a combination of the diverging lens and the active transducing surface. As described in greater detail below, the curved surface 306 disperses the transmit and receive fields so that they overlap in an area that is larger than the forward-looking volume region of the 2-D array 304. Also described in greater detail below, the curved surface 306 allows for two-way focusing by focusing at any point in the 3-D space both in transmit and in receive separately. As a result, at least two elements are enough to image a whole curvilinear volume.

Transmit circuitry 308 generates pulses that excite a predetermined set of the addressed columns (or rows) to emit one or more ultrasound beams or waves. Receive circuitry 310 receives signals indicative echoes or reflected waves, which are generated in response to the transmitted ultrasound beam or wave interacting with (stationary and/or flowing), from a predetermined set of addressed rows (or columns). The receive circuitry 310 may also pre-process and/or condition the received signals, e.g., by amplifying, digitizing, etc. the signals. A switch 312 switches between the transmit circuitry 308 and the receive circuitry 310, depending on whether the transducer array 302 is in transmit or receive mode.

A beamformer 312 processes the received echoes, for example, by applying time delays and weights, summing, and/or otherwise processing the received echoes. Alternatively, the beamformer 312 can process the received echoes by applying spatial matched filtering to focus the RF-data at any time and location in space. An example of this is described in Jensen, & Gori. (2001), "Spatial filters

for focusing ultrasound images,” 2, 1507–1511 vol.2. doi:10.1109/ULTSYM.

A display 316 is configured to visually display images and/or other information. A scan converter 318 scan converts the beamformed data, converting the beamformed data (e.g., images or volumes) into the coordinate system of the display 316, which visually displays the images. In one instance, the data is visually displayed in an interactive graphical user interface (GUI), which allows the user to selectively rotate, scale, and/or manipulate the displayed data through a mouse, a keyboard, touch-screen controls, etc.

A controller 320 controls one or more of the components of the system 300 such as at least one of the transmit circuitry 308 or receive circuitry 310, the switch 312, and the beamformer 314. Such control can be based on the mode of operation (e.g., B-mode, etc.) of the system 300 and/or otherwise. A user interface 322 includes include an input device (e.g., a physical control, a touch-sensitive surface, etc.) and/or an output device (e.g., a display screen, etc.). A mode, scanning, and/or other function can be activated by a signal indicative of input from the user interface 322.

In one instance, the transducer array 302 is part of a probe and the transmit circuitry 308, the receive circuitry 310, the switch 312, the beamformer 314, the scan converter 318, the controller 320, the user interface 322, and the display 816 are part of a console. Communication there between can be through a wired (e.g., a cable and electro-mechanical interfaces) and/or wireless communication channel. In this instance, console can be a portable computer such as a laptop, a notebook, etc., with additional hardware and/or software for ultrasound imaging. The console can be docked to a docking station and used.

Alternatively, the console can be part (fixed or removable) of a mobile or portable cart system with wheels, casters, rollers, or the like, which can be moved around. In this instance, the display 316 may be separate from the console and connected thereto through a wired and/or wireless communication channel. Where the cart includes a docking interface, the console can be interfaced with the cart and used. An example of such a system is described in US publication 2011/0118562 A1, entitled “Portable ultrasound scanner,” and filed on November 17, 2009, which is incorporated herein in its entirety by reference.

Alternatively, the transducer array 302, the transmit circuitry 308, the receive circuitry 310, the switch 312, the beamformer 314, the scan converter 318, the controller 320, the user interface 322, and the display 316 are all housed by and enclosed within a hand-held ultrasound apparatus, with a housing that mechanically supports and/or shields the components within. In this instance, the 2-D array 304

is structurally integrated as part of the housing. An example of a hand-held device is described in US patent 7,699,776, entitled “Intuitive Ultrasonic Imaging System and Related Method Thereof,” and filed on March 6, 2003, which is incorporated herein in its entirety by reference.

As briefly discussed above, the transducer array 302 includes the curved surface 306. Figure 6 illustrates a representation of the curved surface 306 in connection with the row-column addressed 2-D array 304 of Figure 5. However, it is to be understood that the curved surface 306 can be employed with the row-column addressed 2-D array 304 of Figure 4 and/or other row-column addressed 2-D array. As discussed herein, the curved surface 306 can be a diverging lens disposed adjacent to the transmitting/receiving side of the row-column addressed 2-D array. Examples of suitable lenses include a spherical, cylindrical, Fresnel, and/or other lens. In a variation, the curved surface 306 is the active transducing surface of the 2-D array 304. The curved surface 306 may or may not have integrated apodization.

The illustrated curved surface 306 is a double-curved (i.e., curved in the x-z and y-z planes) convex surface. In one instance, the curvature is the same in the x-z and x-y planes. In another instance, the curvature is different in the x-z and x-y planes. The curved surface 306 has a first thickness at peripheral regions 602 and a second thickness at a center region 604, where the first thickness is greater than the second thickness. The thickness of a region controls the delay provided by that region and hence the divergence.

A non-limiting example of suitable thicknesses includes a thickness in a range of 0 to 5 mm for a lens with  $f\# = -0.7$  and a speed of sound of 1400 m/s, which corresponds to a delay range of 0 to 3.5  $\mu\text{s}$ . The  $f\#$  is defined as a ratio between a focal distance to a diameter of the lens. A non-limiting example of a suitable material of the curved surface 306 is Sylgard® 170 (PDMS) with a density of 1000 and a speed of sound of 1400 m/s and attenuation of 3.7. Sylgard® 170 is a product of Dow Corning Corporation, MI, USA. The curved surface 306 can be disposed centered over the 2-D array 304 or disposed off-center, e.g., at a corner region.

The curved surface 306 disperses the transmit and receive fields so that they overlap in a larger area relative to the forward-looking region of the 2-D array 304. Generally, for the flat 2-D array 102 of Figure 1, each line element produces a cylindrical wave in one direction and a plane wave in the other direction, which restricts the width in the other direction to a line segment having the width of the element. In contrast, the curved surface 306 produces a spherical wave, which

originates from a virtual point source, located behind the array, which propagates in a larger field of view. This can be seen by comparing Figures 2 and 7. In Figure 2, the transmit and receive pressure fields 202 and 204 intersect and provide the rectilinear forward-looking region 206. In Figure 7, diverging transmit and receive pressure fields 702 and 704 intersect and provide a larger intersecting and thus larger imaging region 706, which is larger than the rectilinear forward-looking region 206 of Figure 2. In the example of Figure 7, the overlapped transmit and receive region 706, compared to Figure 2, increases to  $\pm 26.5^\circ$  in both directions.

With the 2-D flat array 102 of Figure 1, the intersection of transmitted wavefronts has a shape of a line segment. With the configuration shown in Figures 3 and 6, with the curved surface 306, the intersection of the transmitted wavefronts is not a line segment but a point. This can be seen in Figure 8, which shows how the intersection of multiple wavefronts creates a curved line instead of a straight line. Each curved line 802, 804 and 806 is an intersection of two spherical wavefronts. Depending on a distance of each element to a focusing point, each wavefront has a different curvature and therefore all the wavefronts contact at only one point 808. With the 2-D flat array 102 of Figure 1, focusing is not possible in the orthogonal plane to the transmit steering direction.

With the curved surface 306, focusing in transmit direction can be achieved by delaying the wavefronts so that they pass the first point of contact and generate two focus points. This can be seen in Figure 9, which shows curved lines 902, 904 and 906 and two focus points 908 and 910. This allows for not only focusing in the transmit plane but also in the orthogonal plane. In conventional ultrasound imaging it will be a tedious process to transmit for each steering angle so many times to cover the whole volume. However, this can be done with the approached described herein, e.g., by employing a synthetic aperture imaging (SAI) algorithm, which allows all the delay calculations to be done after data acquisition. Furthermore, since it is possible to focus at any point in the 3-D space both in transmit and in receive separately, two-way focusing can be achieved.

An example beamforming algorithm is described next. The example first explains flat row-column beamforming and then extends this to row-column beamforming for the curved surface 306.

Delay-and-sum (DAS) beamformers usually assume the geometry of the sound sources and receivers to be points. However, by row-column addressing the elements on a 2-D matrix array, each row and column is acoustically equivalent to a line-element. Furthermore, the emitted wavefront of a line-element has the shape of a cylinder, i.e. it is a plane wave in the plane aligned along the line-element and

a circle arc in the plane orthogonal to the line-element. Assuming the geometry of the line-elements to be points is therefore a poor approximation. A better approximation assumes the line-elements to be line segments instead of points. At the focal zone where an array of line-elements is focused, the geometry is also a line segment.

Calculating the distances between the line-elements and a given point should therefore be calculated as the distance between a line segment and a point. For beamforming with line-segment virtual sources, the time-of-flight for the sound propagating through the media can be calculated as shown in Equation 1:

Equation 1:

$$t_{ToF} = \frac{|r_{fp} - r_{xmt}| \pm d(AB_{fp}, P) + d(CD_{rcv}, P)}{c},$$

where  $r_{xmt}$  and  $r_{fp}$  are vectors from a center of the 2-D array to a center of each transmit line-element and also to a center of a focal line-segment,  $P$  is a position vector of any beamforming point,  $AB_{fp}$  is a vector from one end to another end of a focal line-segment,  $CD_{rcv}$  is a vector from one end to another end of each receive line element,  $d(;;)$  calculates a shortest distance between the point  $P$  and each of the transmit or receive line-elements which finds a minimum distance between a point and a line-segment, and  $\pm$  refers to whether the point  $P$  is in between a focal line-segment and a surface of the transducer, i.e. -, or the point  $P$  is located after the focal line-segment, i.e. +. The minimum distance between the point  $P$  and the line segment  $AB$  can be calculated as shown in Equation 2:

Equation 2:

$$d(AB, P) = \begin{cases} \frac{\|AB \times AP\|}{\|AB\|} & \text{if } 0 \leq \frac{AB \cdot AP}{\|AB\|^2} \leq 1 \\ \|AP\| & \text{if } \frac{AB \cdot AP}{\|AB\|^2} < 0 \\ \|BP\| & \text{if } \frac{AB \cdot AP}{\|AB\|^2} > 1 \end{cases},$$

Figure 10 is used to explain how to extend the above to calculate the time-of-flight in dynamic receive focusing with the curved surface 306 for single element transmissions. The curved surface 306 is not shown for sake of clarity, and is located above or on top of the 2-D array 304. A shortest path 1002 from a source line-element 1004 to an imaging point  $P$  1006 is in a plane 1008 that goes through a curved surface center 1012 and the point  $P$  1006 and that is orthogonal to a

transmit plane B 1010, which goes through the transmit element 1004 and the curved surface center 1012.

To calculate the distance from the transmit element 1004 to the imaging point  $P$  1006,  $(\overline{BP})$ , a perpendicular projection  $P_{TX_{proj}}$  1014 of the point  $P$  1006 is located on the plane 1010. An intersection 1016 of the plane B 1008 (which goes through the point  $P$  1006,  $P_{TX_{proj}}$  1014 and the center 1012), with the transmitting element 1004, is identified at a point B 1018.  $\overline{BP}$  is then calculated as shown in Equation 3:

Equation 3:

$$\overline{BP} = \sqrt{BP_{TX_{proj}}^2 + P_{TX_{proj}}^2},$$

where  $\overline{P_{TX_{proj}}P}$  is a line segment from  $P_{TX_{proj}}$  1014 to  $P$  1006, and  $BP_{TX_{proj}}$  is a line segment, which is computed by subtracting the vector which is pointing from the center 1012 to the  $P_{TX_{proj}}$  1014 by the radius of the curved surface 306, which is fixed. This approach is also used to calculate  $\overline{AP}$  1024, using a perpendicular projection  $P_{RX_{proj}}$  1026 and a point A 1028 on a receive segment 1030, as shown in Equation 4:

Equation 4:

$$\overline{PA} = \sqrt{AP_{RX_{proj}}^2 + P_{RX_{proj}}^2},$$

where  $\overline{P_{RX_{proj}}P}$  is a line segment from  $P_{RX_{proj}}$  1014 to the  $P$  1106, and  $AP_{RX_{proj}}$  is a line segment, which is computed by subtracting the line segment from the center 1012 to the  $P_{RX_{proj}}$  1026 by the radius of the curved surface 306.

A total distance is computed as shown in Equation 5:

Equation 5:

$$\overline{BP} + \overline{PA}.$$

This is repeated for the other columns of the 2-D array 304 for the point  $P$  1006. The computed shortest distances for all of the columns to the point  $P$  1006 provide the data to beamform the point  $P$  1006. This can be achieved using a synthetic aperture imaging and/or other algorithm. In synthetic transmit aperture imaging, by taking advantage of the superposition theorem, the transmit focus may be synthesized in every location by delaying and summing a plurality of datasets (before or after conventional beamforming) acquired from successive transmissions.

In synthetic transmit aperture imaging with a linear array with  $N$  elements, for each image point  $(r, \theta)$ , the A-scan signal is as shown in Equation 6:

Equation 6:

$$A_{STA}(r, \theta) = \sum_{n=0}^{N-1} \sum_{m=0}^{N-1} S_{m,n} \left( \frac{2r}{c} - \tau_n - \tau_m \right),$$

where  $S_{m,n}$  is the echo signal. The first and second summations correspond to transmit and receive beamforming.  $\tau_n$  and  $\tau_m$  are beamforming delays for transmit  $m$  and receive  $n$  element combination shown in Equations 7 and 8:

Equation 7:

$$\tau_m = \frac{1}{c} \left( r - \sqrt{x_m^2 - r^2 - 2x_m r \sin\theta} \right) \text{ and}$$

Equation 8:

$$\tau_n = \frac{1}{c} \left( r - \sqrt{x_n^2 - r^2 - 2x_n r \sin\theta} \right).$$

An example of this is described in Jensen, J. A., Nikolov, S., Gammelmark, K. L., & Pedersen, M. H. (2006), "Synthetic Aperture Ultrasound Imaging. Ultrasonics," 44(SUPPL.), e5–e15, e5–e15. doi:10.1016/j.ultras.2006.07.017. The above shortest distance calculation is repeated for all the points of interest in the field of view or region 706. The points can be inside the planes, outside of the planes and/or on a plane(s).

Figures 11 and 12 respectively show two beamformed B-mode images of a point scatterer imaged with the curved surface 306 (Figure 11) and without the curved surface 306 (Figure 12). The point scatterer is positioned at eighty (80) millimeters (mm) distance from the 2-D array 304. The origin corresponds to the center of the transducer surface. Data was generated using synthetic aperture imaging with 62 single-element transmissions, emitting a 2-cycle sinusoidal excitation pulse with every row of elements at a time and receiving the echoes with all column elements. These figures show how energy falls off with angle with and without the curved surface 306.

Figures 13 and 14 respectively show two beamformed B-mode images for multiple point scatterers imaged with the curved surface 306 (Figure 13) and without the curved surface 306 (Figure 14). For these images, seven scatterers 1301, 1302, 1303, 1304, 1305, 1306 and 1307 are positioned at forty (40) mm distance from the 2-D array 304 within  $\pm 45^\circ$  in the elevation plane. One 1-D array includes sixty-two columns, and the other 1-D array includes sixty-two rows. The receive array is rotated  $90^\circ$  with respect to the transmit array. The parameters as shown in Table 1.

Table 1  
Parameters

Parameter name	Notation	Value	Unit
Number of elements	–	62+62	–
Center frequency	$f_0$	3.0	MHz
Speed of sound	$c$	1480	$\text{m s}^{-1}$
Wave length	$\lambda$	493.3	$\mu\text{m}$
Array pitch - $x$	$d_x$	$\lambda/2 = 246.6$	$\mu\text{m}$
Array pitch - $y$	$d_y$	$\lambda/2 = 246.6$	$\mu\text{m}$
Sampling frequency	$f_s$	120	MHz
Emission pulse	–	2-cycles, Hann-weighted	–
Lens focal ratio	$f_{\#}$	-1	–

Figure 13 shows all of the scatterers 1301, 1302, 1303, 1304, 1305, 1306 and 1307, including those (1301, 1302, 1306 and 1307) beyond the forward-looking region 206, which are in the larger area 706. Figure 14 shows the scatterers within the forward-looking region 206 of the 2-D array 304, which include scatterers 1303, 1304 and 1305. Using a diverging lens can thus enable imaging a large field of view.

Figure 15 graphically shows a comparison of the normalized pulse-echo energy as a function of steering angle from center to one side of the array with and without the curved surface 306. The points are located on an arc with radii of eighty (80) millimeters (mm) away from the center of the 2-D array 304 and spanned from  $0^\circ$  to  $80^\circ$ . A curve 1502 shows the pulse-echo energy without the curved surface 306. The curves 1504, 1506, 1508 and 1510 respectively show the pulse-echo energy with the curved surface 306 for a decreasing  $f_{\#}$ , which shows an increasing imaging region. For example, at -40 dB a lens increases the pulse-echo field-of-view up to 70 degrees for a lens with  $f_{\#} = -0.5$ .

Figure 16 illustrates an example method. At 1600, the transducer array 302 is used to scan a subject. As described herein the transducer array 302 includes the row-addressed 2-D array 304 with the curved surface 306. Two-way focusing may be employed. The curved surface 306 may be configured with integrated apodization. At 1602, the acquired data is beamformed as described herein. At 1604, the beamformed data is processed to generate an image. At 1606, the image is displayed.

The functions described herein may be implemented via one or more hardware and/or software computer processors (e.g., a micro-processor, a central processing

unit (CPU), etc.) executing one or more computer readable instructions encoded or embodied on computer readable storage medium (which excludes transitory medium) such as physical memory which causes the one or more processors to carry out the various acts and/or other functions and/or acts. Additionally, or alternatively, the one or more processors can execute instructions carried by transitory medium such as a signal or carrier wave.

The application has been described with reference to various embodiments. Modifications and alterations will occur to others upon reading the application. It is intended that the invention be construed as including all such modifications and alterations, including insofar as they come within the scope of the appended claims and the equivalents thereof.

## Claims

What is claimed is:

1. A transducer array (302) for an ultrasound imaging system (300), the transducer array comprising: a row-column addressed 2-D array of transducer elements (304), wherein the row-column addressed 2-D array comprises: a first array of 1-D arrays of elements; a second array of 1-D arrays of elements, which is orthogonal to the first array; and a double-curved surface (306).
2. The transducer array of claim 1, wherein the double-curved surface is a lens.
3. The transducer array of claim 2, wherein the lens is a convex lens.
4. The transducer array of claim 3, wherein the convex lens is a spherical lens.
5. The transducer array of any of claims 2 to 4, wherein the lens has a same curvature in two orthogonal directions.
6. The transducer array of any of claims 2 to 4, wherein the lens has a first curvature in a direction of the first array and a second curvature in a direction of the second array, wherein the first and second curvatures are different.
7. The transducer array of any of claims 2 to 6, wherein the lens has a first thickness at a periphery and a second thickness at a center region, and the first thickness is greater than the second thickness.
8. The transducer array of any of claims 2 to 6, wherein the lens is centered over the 2-D array.
9. The transducer array of any of claims 2 to 6, wherein the lens is disposed off-center with respect to the 2-D array.

10. The transducer array of any of claims 2 to 6, wherein the 2-D array has a first imaging region (206) and the combination of the 2-D array and the lens has a second imaging region (706), and the second imaging region is larger than the first imaging region.

11. The transducer array of any of claims 2 to 10, wherein the lens has integrated apodization.

12. The transducer array of any of claims 2 to 11, wherein the lens is a Fresnel lens.

13. The transducer array of claim 1, wherein the curved surface is an active transducing surface of the 2-D array.

14. The transducer array of any of claims 1 to 13, wherein the 2-D array includes piezoelectric or capacitive micromachined ultrasonic transducer transducing elements.

15. An apparatus (300), comprising: a transducer array (302) with an array-wise addressable 2-D array with a curved surface, wherein the 2-D array includes a set of 1-D column array elements and a set of 1-D row array elements; transmit circuitry (308) that conveys an excitation pulse to the transducer array; receive circuitry (310) that receives a signal indicative of an ultrasound echo from the transducer array; and a beamformer (314) that processes the received signal, generating ultrasound image data.

16. The apparatus of claim 15, further comprising: a controller (320) configured to control the transmit circuitry for two-way focusing to focus the set of 1-D column array elements or the set of 1-D row array elements.

17. The apparatus of claim 16, wherein the beamformer is configured to determine a shortest distance from a source to a point to a drain for each column and each row for a plurality of points in an imaging field of view.

18. The apparatus of claim 17, wherein the beamformer sums coherently low resolution beamformed images for a point for all transmissions.

19. The apparatus of any of claims 17 to 18, wherein the point is The points can be inside the planes, outside of the planes and/or on a plane(s).

20. A method, comprising: transmitting an ultrasound signal with 2-D row-column addressed transducer array with a curved surface; transmitting an echo signal with the 2-D row-column addressed transducer array with a curved surface; beamforming the echo signal to create an image; and displaying the image.

**Abstract**

A transducer array (302) for an ultrasound imaging system (300) includes a row-column addressed 2-D array of transducer elements (304). The row-column addressed 2-D includes a first array of 1-D arrays of elements, a second array of 1-D arrays of elements, which is orthogonal to the first array, and a double-curved surface (306). In another aspect, an apparatus includes a transducer array with an array-wise addressable 2-D array with a curved surface. The 2-D array includes a set of 1-D column array elements and a set of 1-D row array elements. The apparatus further includes transmit circuitry (308) that conveys an excitation pulse to the transducer array, receive circuitry (308) that receives a signal indicative of an ultrasound echo from the transducer array, and a beamformer (314) that processes the received signal, generating ultrasound image data.

### Drawings

ANA1304-WO  
(BKM-10-7958-PCT)

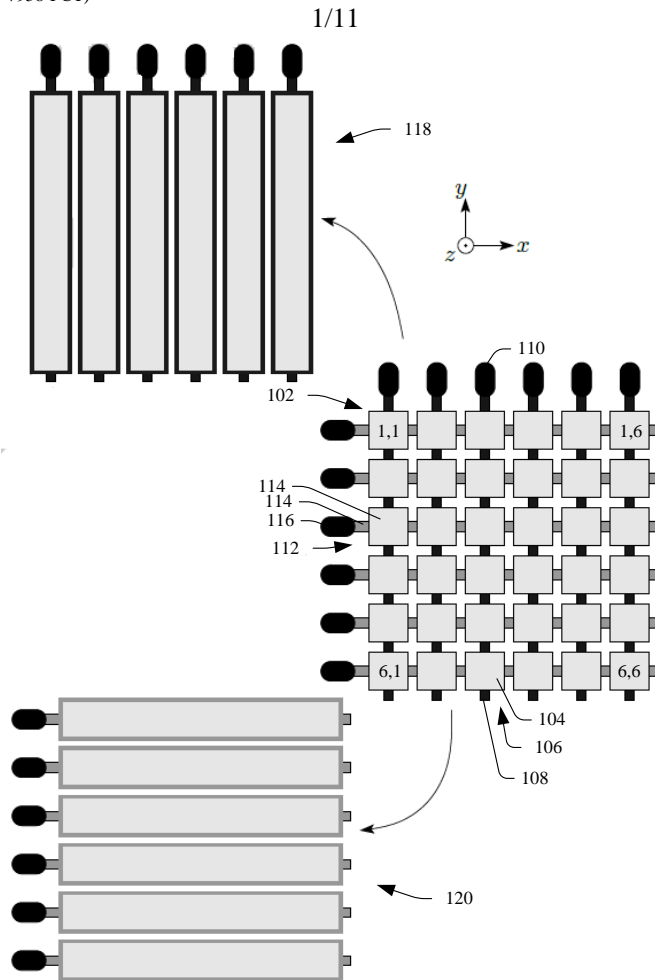


FIGURE 1

ANA1304-WO  
(BKM-10-7958-PCT)

2/11

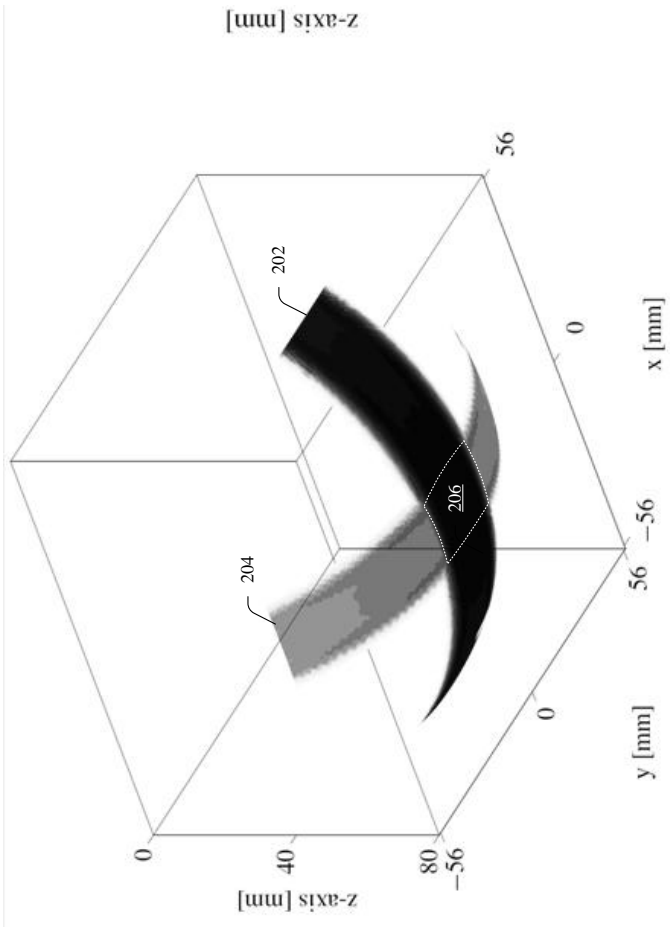


FIGURE 2

ANA1304-WO  
(BKM-10-7958-PCT)

3/11

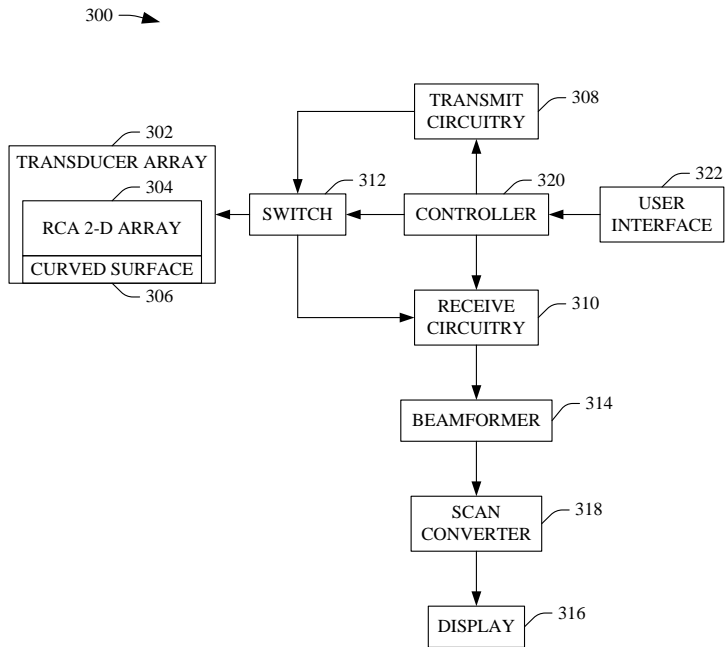


FIGURE 3

ANA1304-WO  
(BKM-10-7958-PCT)

4/11

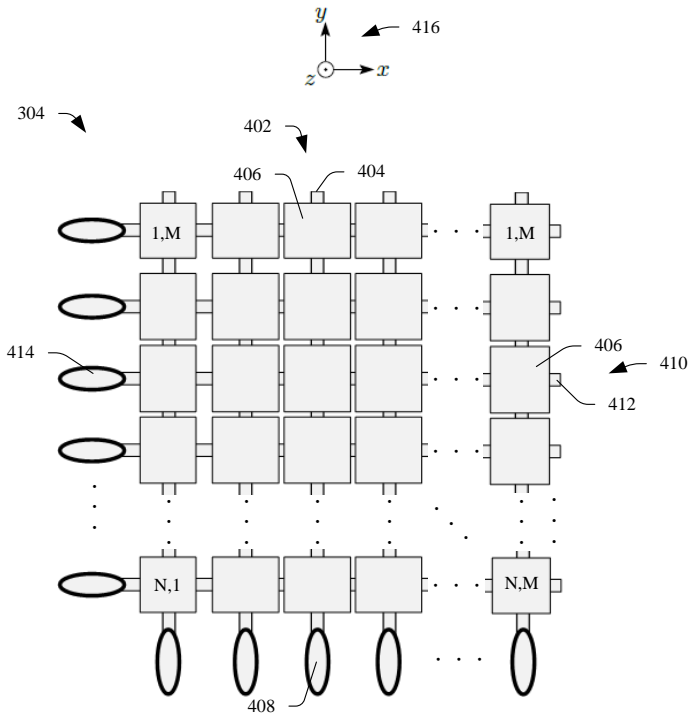


FIGURE 4

ANA1304-WO  
(BKM-10-7958-PCT)

5/11

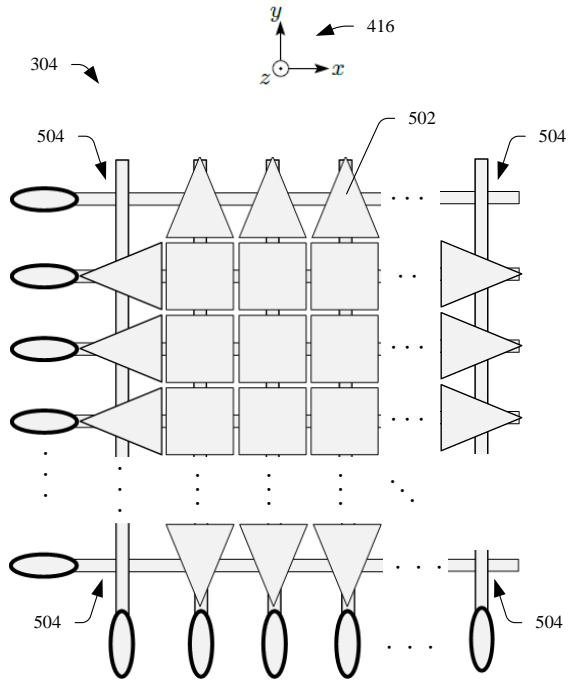


FIGURE 5

ANA1304-WO  
(BKM-10-7958-PCT)

6/11

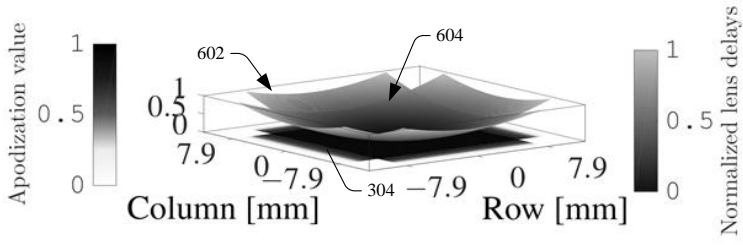


FIGURE 6

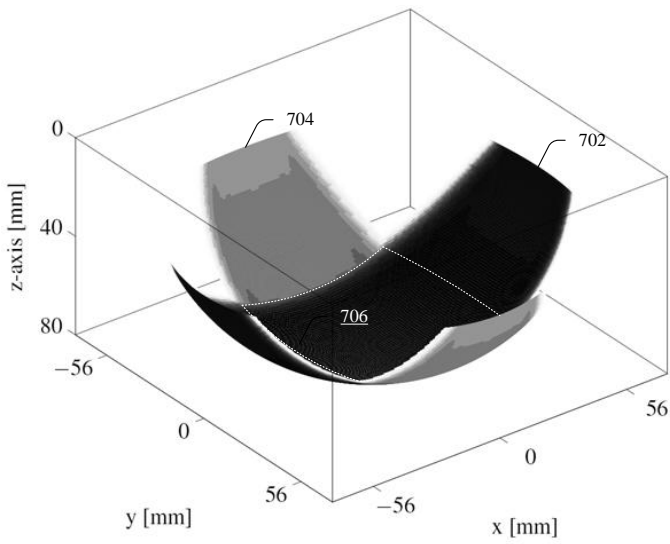


FIGURE 7

ANA1304-WO  
(BKM-10-7958-PCT)

7/11

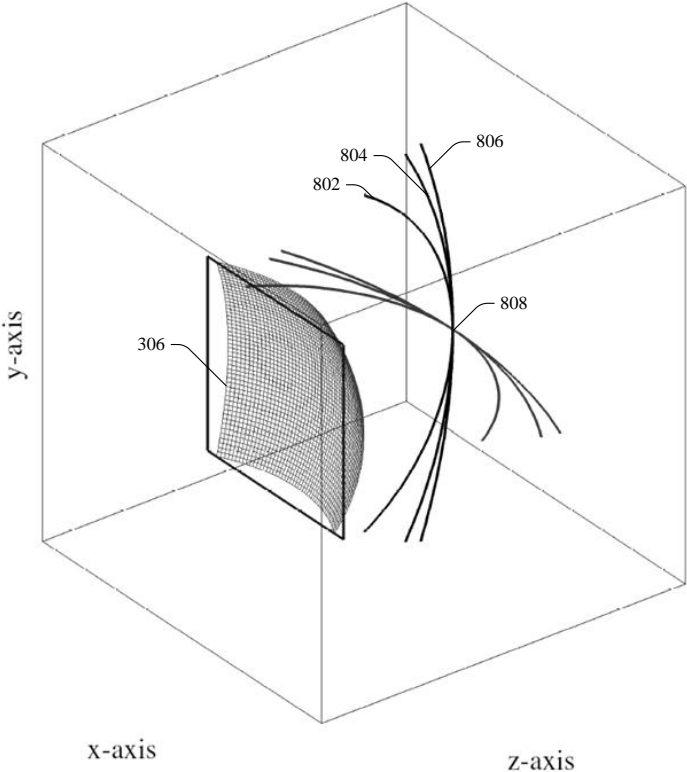


FIGURE 8

ANA1304-WO  
(BKM-10-7958-PCT)

8/11

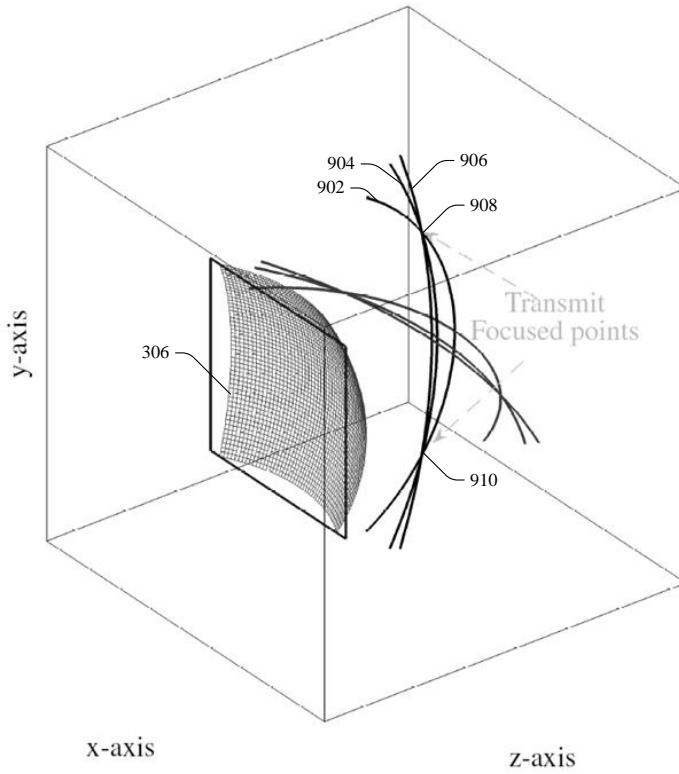


FIGURE 9

ANA1304-WO  
(BKM-10-7958-PCT)

9/11

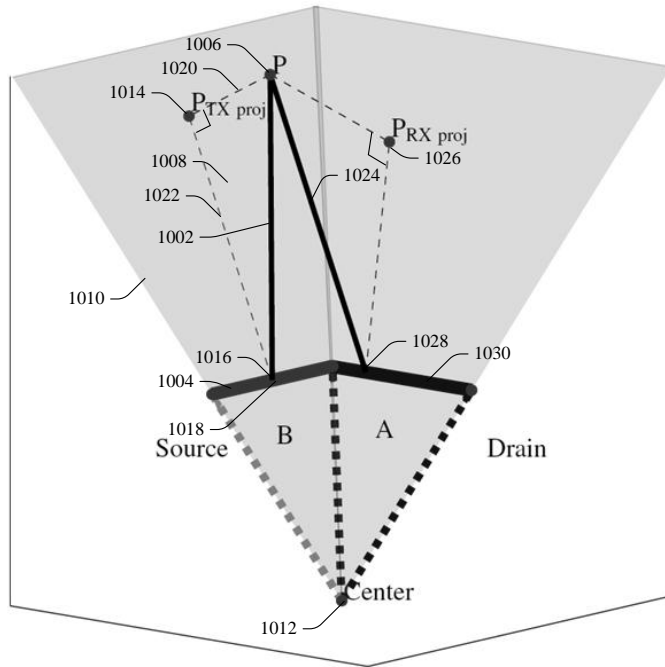


FIGURE 10

ANA1304-WO  
(BKM-10-7958-PCT)

10/11

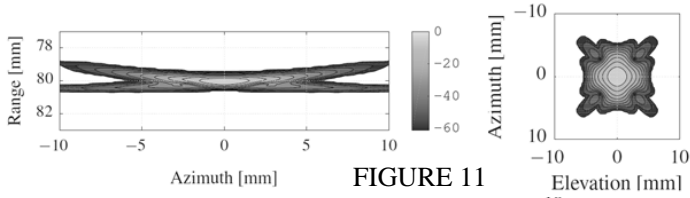


FIGURE 11

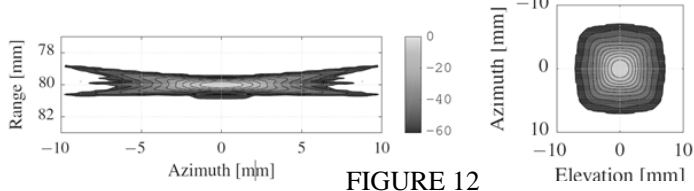


FIGURE 12

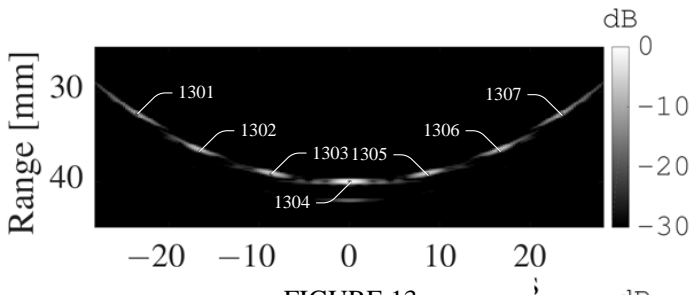


FIGURE 13

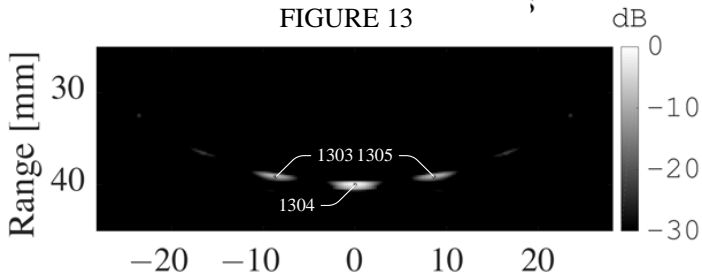


FIGURE 13

ANA1304-WO  
(BKM-10-7958-PCT)

11/11

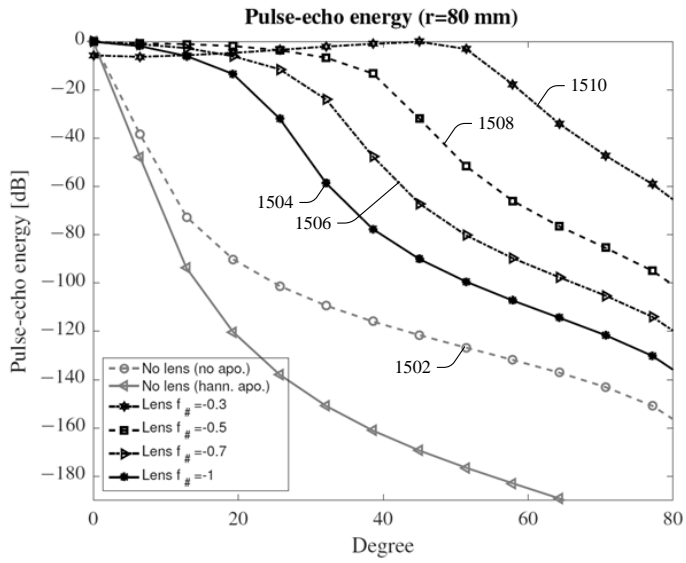


FIGURE 15

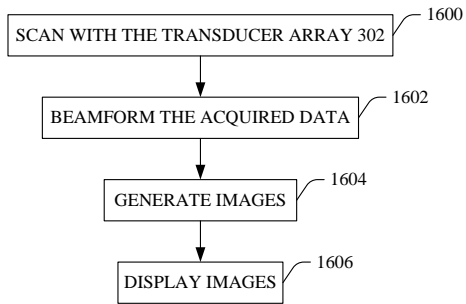


FIGURE 16

